Targeting non-canonical NF-κB signalling in CYLD defective tumours

Kirsty Hodgson

Thesis submitted for the degree of Doctor of Philosophy

Newcastle University

Faculty of Medical Sciences

Translational and Clinical Research Institute

April 2021

Abstract

CYLD cutaneous syndrome (CCS) is a rare, autosomal dominant, hair follicle tumour predisposition syndrome where non-surgical therapeutics are needed. In this thesis I delineate non-canonical NF-κB signalling in CYLD defective tumours and evaluate the utility of targeting this pathway with novel small molecule IKKα inhibitors. Such information may underpin the potential development of non-surgical approaches for CCS.

First, I sought to establish the genetic landscape of tumours in CCS. Using whole genome sequencing, I showed that biallelic mutation of the cylindromatosis gene (*CYLD*) was present in almost all tumours studied. In addition, I discovered that a subset of tumours had mutations in epigenetic modifiers that modulate Wnt signalling, a known oncogenic dependency in these tumour cells.

CCS has not been successfully modelled in mice, limiting mechanistic insight into how truncating mutations in *CYLD* result in a skin tumour phenotype. To overcome this, I explored both the canonical and non-canonical NF-κB signalling pathways in CCS whole tumour tissue. I also developed a patient-derived tumour spheroid model that recapitulated in vivo deregulation of both NF-κB signalling pathways. In the non-canonical pathway, I showed processing of the p52 precursor p100 was altered in CCS tumour tissue and spheroids. Given non-canonical NF-κB signalling is targetable by inhibiting IKKα, I inhibited IKKα in CCS spheroids with a novel compound, designated Compound Z, and showed reduction in viability following treatment.

To determine the impact of biallelic *CYLD* truncating mutations on the transcriptome, I used a CD45 depletion method to isolate CD45- CCS tumour keratinocytes by FACS. RNA-sequencing of tumour keratinocytes identified the ectodysplasin a receptor *EDAR* as highly differentially expressed. Measurement of gene expression after treatment with Compound Z confirmed that *EDAR* overexpression is IKKα-dependent in CCS spheroids.

In summary, I have highlighted the oncogenic dependency of CCS tumour cells on non-canonical NF-κB signalling and demonstrate the effectiveness of targeting IKKα for the treatment of CYLD cutaneous syndrome.

Acknowledgements

I would like to firstly offer my sincere thanks to my principal supervisor Dr Neil Rajan for his kindness and support at every stage of this project. I could not have asked for a better mentor. I am also extremely grateful to my supervisor Dr Iglika Ivanova for her invaluable teaching and advice, and to my supervisor Prof. Neil Perkins for sharing his knowledge and experience.

Thank you to my colleagues Dr Naomi Sinclair, Dr Majid Arefi, Dr Siobhan Muthiah, Dr Marina Danilenko, Dr Jill Hunter, Dr Adrian Yemm, Dr George Schlossmacher, Dr Ling-i Su, Dr Nicola Hannaway and Emma Corbin for your help and for making my time in the lab such an enjoyable experience!

Many thanks to Prof. Simon Mackay and Dr Andrew Paul for providing the novel IKKα inhibitors used in this study. Thank you to Dr Helen Davies, Dr Serena Nik-Zainal and all involved with the Nature Communications paper for inviting me to contribute. Thanks also to Dr Lutz Langbein for the CK77 antibody and Prof. Ramin Massoumi for the CYLD antibody. I would also like to thank Dr Andrew Filby and team at the Newcastle University Flow Cytometry Core Facility, Dr Simon Cockell and Dr Jonathan Coxhead for their technical support.

This thesis is dedicated to the patients that made this research possible. I am also incredibly grateful to the British Skin Foundation for funding this PhD. Finally, I would like to express my gratitude to my family, especially my daughter Lily and Margaret, for their patience and unwavering support.

Declaration

I, Kirsty Hodgson, declare that no portion of the work compiled in this thesis has been submitted in support of another degree or qualification at this or any other University or Institute of Learning. This thesis includes nothing that is the work of others, nor the outcomes of work done in collaboration, except where otherwise stated.

Kirsty Hodgson

Table of Contents

List of Figures

List of Tables

Abbreviations

A20	TNF Alpha Induced Protein 3 (syn. TNFAIP3)
ADD	ATRX-DNMT3-DNMT3L domain
AKT1	AKT Serine/Threonine Kinase 1
AML	Acute myeloid leukaemia
APPRIS	Database of annotations of human splice isoforms
ASCAT	Allele-specific copy number analysis of tumours
BAFFR	B Cell-Activating Factor Receptor (syn. TNFRSF13C)
BBD	BCL6 binding domain
BCAC-LG	Basal cell adenocarcinoma-low grade
BCC	Basal cell carcinoma
BCL10	BCL10 Immune Signaling Adaptor
BCL3	B-cell CLL/lymphoma 3
BCL6	BCL6 Transcription Repressor
BCOR	BCL6 Corepressor
BCORL	BCL6 Corepressor Like 1
BCR	B cell receptor
BSS	Brooke-Spiegler syndrome
C-REL	REL Proto-Oncogene, NF-KB Subunit, syn. REL
$CaCl_2$	Calcium chloride
CAP-Gly	Cytoskeletal-associated protein-glycine-conserved domain
CARMA1	Caspase Recruitment Domain Family Member 11 (syn. CARD11)
CASPASE	Cysteine-aspartic acid protease
CBM	CARD11/BCL10/MALT1 complex
CCD1106	Human keratinocyte cell line
CCS	CYLD cutaneous syndrome
CD40	CD40 Molecule, TNF Receptor Superfamily Member 5
CD45	Lymphocyte common antigen
ChIP	Chromatin immunoprecipitation
cIAP	Cellular Inhibitor of Apoptosis, syn. BIRC
CK	Cytokeratin
CLL	Chronic lymphocytic leukaemia

CNV	Copy number variation
CORUM	The comprehensive resource of mammalian protein complexes
CPCC	Cylindroma primary cell culture
CRC	Colorectal cancer
CTNNB1	Catenin Beta 1, syn. β-catenin
CYLD	CYLD Lysine 63 Deubiquitinase, syn. Cylindromatosis
DAPI	4′,6-diamidino-2-phenylindole
DEG	Differentially expressed gene
DKK2	Dickkopf WNT Signaling Pathway Inhibitor 2
DLRP	Database of Ligand-Receptor Partners
DMEM	Dulbecco’s modified eagle medium
DMSO	Dimethyl sulfoxide
DNMT1	DNA Methyltransferase 1
DNMT3A	DNA Methyltransferase 3 Alpha
DNMT3B	DNA Methyltransferase 3 Beta
DNMT3L	DNA Methyltransferase 3 Like
DP	Ductal portion
DVL1	Dishevelled Segment Polarity Protein 1
ECM	Extracellular matrix
EDA	Ectodysplasin A
EDAR	Ectodysplasin A Receptor
EDARADD	EDAR Associated Death Domain
EDTA	Ethylenediaminetetraacetic acid
EKO	Epidermis-specific knockout
EpSC	Epidermal stem cell
ESC	Embryonic stem cell
FACS	Fluorescence activated cell sorting
FBS	Fetal bovine serum
FC	Fold change
FITC	Fluorescein isothiocyanate
FL	Full length
GAPDH	Glyceraldehyde-3-Phosphate Dehydrogenase
GFP	Green fluorescent protein
GNP	Granule neuron progenitors

GO	Gene Ontology
H2A	Histone H2A
H3	Histone H3
HaCaT	Human epidermal keratinocyte cell line
HDAC6	Histone Deacetylase 6
HED	Hypohidrotic ectodermal dysplasia
HEK293	Human embryonic kidney cell line
HF	Hair follicle
HLA	Human leukocyte antigen
HOIL-1	Heme-Oxidized IRP2 Ubiquitin Ligase 1 syn. RBCK1
HOIP	HOIL-1-Interacting Protein, syn. RNF31
HOX	Homeobox
HP	Human Phenotype Ontology
HPA	Human Protein Atlas
HRP	Horseradish peroxidase
HSC	Haematopoietic stem cell
IC_{50}	Half maximal inhibitory concentration
IFNG	Interferon Gamma
IGV	Integrative Genomics Viewer
IKBKB	Inhibitor of Nuclear Factor Kappa B Kinase Subunit Beta, syn. IKKβ
IKBKG	Inhibitor of Nuclear Factor Kappa B Kinase Regulatory Subunit Gamma, syn. NEMO
IKKα	Inhibitor of Nuclear Factor Kappa-B Kinase Subunit Alpha
IKKβ	Inhibitor of Nuclear Factor Kappa B Kinase Subunit Beta
IKKε	Inhibitor of Nuclear Factor Kappa B Kinase Subunit Epsilon
IL	Interleukin
IRAK	Interleukin 1 Receptor Associated Kinase
IRF	Interferon regulatory factor
IRS	Inner root sheath
IUPHAR/BPS	International Union of Basic and Clinical Pharmacology/British Pharmacological Society
IκBα	NFKB Inhibitor Alpha, syn. NFKBIA
JAG	Jagged Canonical Notch Ligand
JNK	c-Jun NH2-terminal kinase, syn. MAPK8

K63	Lysine 63
KEGG	Kyoto Encyclopaedia of Genes and Genomes
KREMEN2	Kringle Containing Transmembrane Protein 2
KRT	Keratin
KSFM	Keratinocyte serum-free medium
LOH	Loss of heterozygosity
LPS	Lipopolysaccharides
LTβR	Lymphotoxin Beta Receptor
LUBAC	Linear ubiquitin assembly complex
MALT1	Mucosa-associated lymphoid tissue 1
MBD	MLLT3 binding domain
MBD4	Methyl-CpG Binding Domain 4, DNA Glycosylase
MDS	Myelodysplastic syndrome
Met1	Methionine 1
MFT	Multiple familial trichoepithelioma
MIB2	MIB E3 Ubiquitin Protein Ligase 2
MMP	Matrix metalloproteinase
MTase	Methyltransferase
MYB	MYB Proto-Oncogene, Transcription Factor
MYD88	MYD88 Innate Immune Signal Transduction Adaptor
NEMO	NF-Kappa-B Essential Modulator, syn. IKBKG
NF-κB	Nuclear factor binding near the κ light chain gene in B cells
NFIB	Nuclear Factor I B
NFKB1	Nuclear Factor Kappa B Subunit 1, syn. p105/p50
NFKB2	Nuclear Factor Kappa B Subunit 2 , syn. p100/p52
NGF	Nerve Growth Factor
NGS	Next generation sequencing
NIK	NF-Kappa-Beta-Inducing Kinase, syn. MAP3K14
NLS	Nuclear localisation sequence
NMD	Nonsense mediated decay
NOTCH	Notch Receptor
NTRK	Neurotrophic tyrosine kinase
OFCD	Oculofaciocardiodental syndrome
OMIM	Online Mendelian Inheritance in Man

ORS	Outer root sheath
OTUD7B	OTU Deubiquitinase 7B, syn. Cezanne
OTULIN	OTU Deubiquitinase With Linear Linkage Specificity
PAGE	Polyacrylamide Gel Electrophoresis
PBS	Phosphate-buffered saline
PCA	Principal component analysis
PCGF	Polycomb-group RING finger
PCR	Polymerase chain reaction
PDX	Patient-derived xenograft
PI3K	Phosphatidylinositol-3-kinase
PKC	Protein kinase C
PLK1	Polo-like kinase
PR	Proline Rich
PRC1.1	Polycomb repressive complex 1.1
PTC	Premature termination codon
PTM	Post translational modification
PUFD	Polycomb-group RING finger Ub-like fold discriminator
PUM1	Pumilio RNA Binding Family Member 1
PVDF	Polyvinylidene fluoride
PWM	Position weight matrix
PWWP	Proline-tryptophan-tryptophan-proline
RANK	Receptor Activator of Nuclear Factor-Kappa B, syn. TNFRSF11A
RANKL	Receptor activator of nuclear factor κB ligand, syn. TNFSF11
REAC	Reactome
RELA	RELA Proto-Oncogene, NF-KB Subunit, syn. p65
RELB	RELB Proto-Oncogene, NF-KB Subunit
RHD	Rel homology domain
RIPK	Receptor Interacting Serine/Threonine Kinase
RPKM	Reads per kilobase per million mapped reads
RT-qPCR	Quantitative reverse transcription polymerase chain reaction
SAA1	Serum Amyloid A1
SCC	Squamous cell carcinoma
SCF	Skp-Cullin1-F-box protein
SFRP	Secreted Frizzled Related Protein

SMAD	SMAD Family Member
SOX	SRY-Box Transcription Factor
SPATA2	Spermatogenesis Associated 2
TAB	TGF-Beta Activated Kinase 1 (MAP3K7) Binding Protein
TAD	Transactivation domain
TAK1	TGF-Beta Activated Kinase 1, syn. MAP3K7
TAM	Tumour associated macrophage
TBRS	Tatton-Brown-Rahman syndrome
TBST	Tris-buffered saline Tween-20
TCF/LEF	T-cell factor/lymphoid enhancer-binding factor
TCR	T-cell receptor
TDS	Targeted deep sequencing
TF	Transcription factor
TFBS	Transcription factor binding site
TGF-β	Transforming growth factor-β
TIL	Tumour infiltrating leukocyte
TIME	Tumour immune microenvironment
TLR	Toll Like Receptor
TME	Tumour microenvironment
TMM	Trimmed mean of M values
TNF	Tumour Necrosis Factor
TNFR1	TNF Receptor Superfamily Member 1A, syn. TNFRSF1A
TNFRSF18	TNF Receptor Superfamily Member 18, syn. GITR
TNFSF18	TNF Superfamily Member 18, syn. GITRL
TPA	12-O-tetradecanoylphorbol-13 acetate
TPCA-1	5-(p-Fluorophenyl)-2-ureido]thiophene-3-carboxamide
TRAC	Tropomyosin Receptor Antagonism in Cylindromatosis
TRADD	TNFRSF1A Associated Via Death Domain
TRAF	TNF Receptor Associated Factor
TRANSFAC	Database of eukaryotic transcription factors and their binding sites
TRCP	Beta-Transducin Repeat Containing, syn. BTRC
TRK	Tropomyosin receptor kinase
TSS	Transcription start site
USP	Ubiquitin specific protease

UTR	Untranslated region
VAF	Variant allele frequency
WES	Whole exome sequencing
WGBS	Whole-genome bisulphite sequencing
WGS	Whole genome sequencing
WNT	Wingless
WNT10B	Wnt family member 10B
ZNF	Zinc finger

Chapter 1. Introduction

1.1 CYLD Cutaneous Syndrome

Brooke-Spiegler syndrome (BSS, OMIM 605041) is a rare autosomal dominant disorder caused by germline mutations in the CYLD lysine 63 deubiquitinase gene (syn. Cylindromatosis gene, *CYLD*)(Biggs et al., 1995, Bignell et al., 2000, Zhang et al., 2004). The disease is characterised by the appearance of benign hair follicle related tumours, specifically cylindromas, spiradenomas and trichoepitheliomas. Cylindromas and trichoepitheliomas are also associated with the hereditary skin diseases familial cylindromatosis (OMIM 132700) and multiple familial trichoepithelioma (MFT, OMIM 601606), respectively. Patients with MFT or familial cylindromatosis develop the eponymous tumour type only, whereas BSS patients may present with a mixture of all three. It is now widely recognized that these disorders have the same genetic basis, prompting the suggestion that BSS, familial cylindromatosis and MFT should come under the collective name 'CYLD cutaneous syndrome' (CCS)(Rajan et al., 2009).

1.1.1 Clinical and histological phenotype

CCS patients typically begin to develop skin appendage tumours after puberty that will accumulate throughout adulthood(Rajan et al., 2009). Although *CYLD* mutations affect males and females equally, penetrance can vary and tumours may occur more severely in women(van Balkom and Hennekam, 1994).

Cylindromas predominantly affect the face and scalp but may also occur on the trunk and pubic area. They are slow growing, benign, painless pink tumours that can grow to over 5 cm (Figure 1-1a)(Dubois et al., 2017). Spiradenomas are bluish in colour and may grow up to 10 cm in diameter with a similar distribution as cylindromas (Figure 1-1b). Although they are benign, patients often report spiradenomas as painful. Trichoepitheliomas are small, benign skin coloured papules that occur most commonly on the face at nasolabial folds (Figure 1-1c).

Histologically, cylindromas are characterised by tumour islands arranged in a jigsaw pattern that resemble cylinders in cross section (Figure 1-1d). The tumour islands

consist of an eosinophilic hyaline sheath enclosing basaloid cells with small nuclei at the periphery and more differentiated cells with larger nuclei at the centre. Spiradenomas have a highly disorganised histology with a large number of infiltrating immune cells (Figure 1-1e). Trichoepitheliomas are characterised by irregular islands of basaloid cells, horn cysts and follicular differentiation (Figure 1-1f).

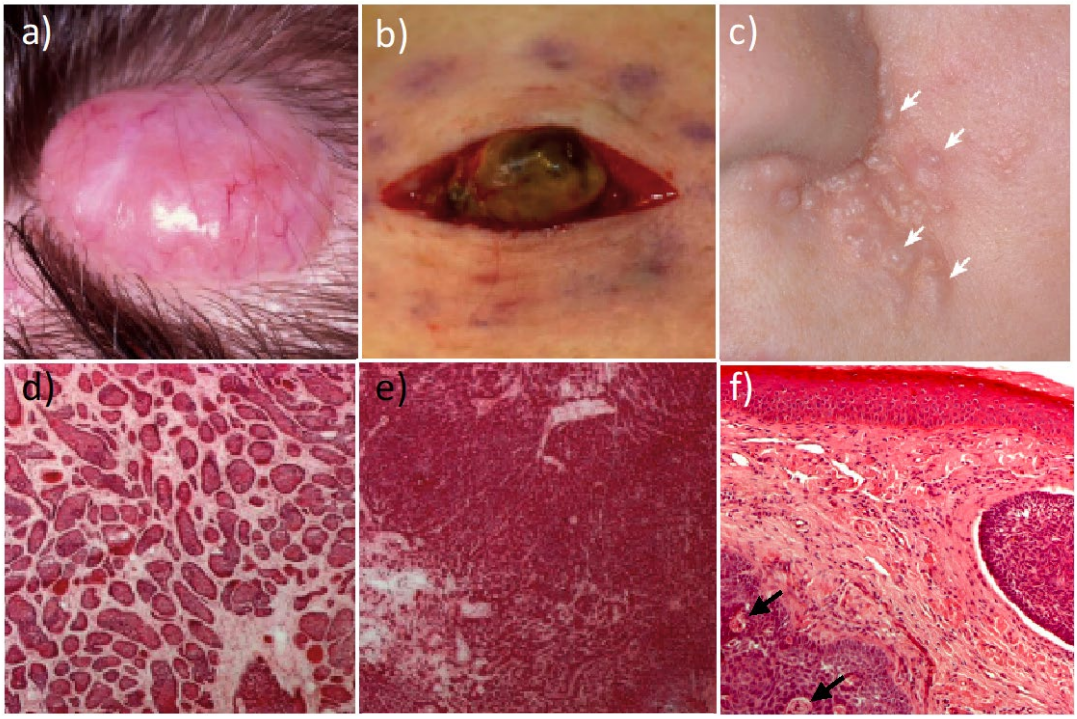

Figure 1-1. Histology of cylindroma, spiradenoma and trichoepithelioma. a) Macroscopic picture of a cylindroma, on the scalp. b) A spiradenoma at surgery. c) Multiple trichoepithelioma (white arrows). d) Cylindroma histology showing irregular tumour islands in the characteristic jigsaw pattern. e) The highly disorganised histology of spiradenoma. f) Trichoepithelioma histology showing two islands of basaloid cells and abortive hair cysts (black arrows). Adapted from (Rajan et al., 2011a) and (Dubois et al., 2017).

Histological examination of a single tumour may reveal tissue-patterning features consistent with both cylindromas and spiradenomas(1999). Such lesions, called spiradenocylindromas, provide evidence that highly organised cylindroma tissue can transition into spiradenoma. A study investigating this transition uncovered a correlation between reduced expression of Dickkopf WNT Signaling Pathway Inhibitor 2 (DKK2) and the extent of tumour tissue disorganization in spiradenomas(Rajan et al., 2011a).

DKK2 is a Wnt antagonist that is downregulated in renal cell, colorectal and ovarian carcinoma due to epigenetic silencing(Sato et al., 2007, Hirata et al., 2009, Zhu et al.,

2012). In spiradenocylindromas, DNA methylation of the DKK2 promotor region increased with increasing tumour disorganisation suggesting that in CCS tumours, epigenetic silencing of DKK2 may contribute to loss of cylindroma tissue patterning.

1.1.2 Histogenesis

The occurrence of papillary mesenchymal bodies in trichoepitheliomas, which induce the development of hair follicle dermal papilla in normal skin, suggests that these tumours arise from the hair follicle(Brooke et al., 1989). There has however been disagreement in the literature regarding the histogenesis of cylindromas and spiradenomas. These have been reported as both apocrine and eccrine in origin due to apocrine or eccrine differentiation and the immunohistochemical detection of antigens known to be expressed in and around the eccrine coil, such as nerve growth factor, CD44, CD34 and Leu-7(Kanitakis et al., 1987, Penneys and Kaiser, 1993) or markers of apocrine differentiation such as Human milk fat globulin and lysozyme(Meybehm and Fischer, 1997).

As cylindromas and spiradenomas primarily occur at hair bearing sites and are not found on the hands or feet (which are rich in eccrine glands), it has logically been argued that these tumours may arise from the hair follicle. In support of this theory, cylindroma have been shown to express the hair follicle keratins K17, K6irs1 and K6Hf by immunofluorescence(Massoumi et al., 2006b). In 2015, Sellheyer found evidence that both cylindromas and spiradenomas arise from the folliculosebaceous-apocrine unit (Figure 1-2)(Sellheyer, 2015). In this immunohistochemical study of 97 tumours, all spiradenomas and cylindromas expressed the hair follicle stem cell marker CD200 whereas tumours of eccrine origin did not.

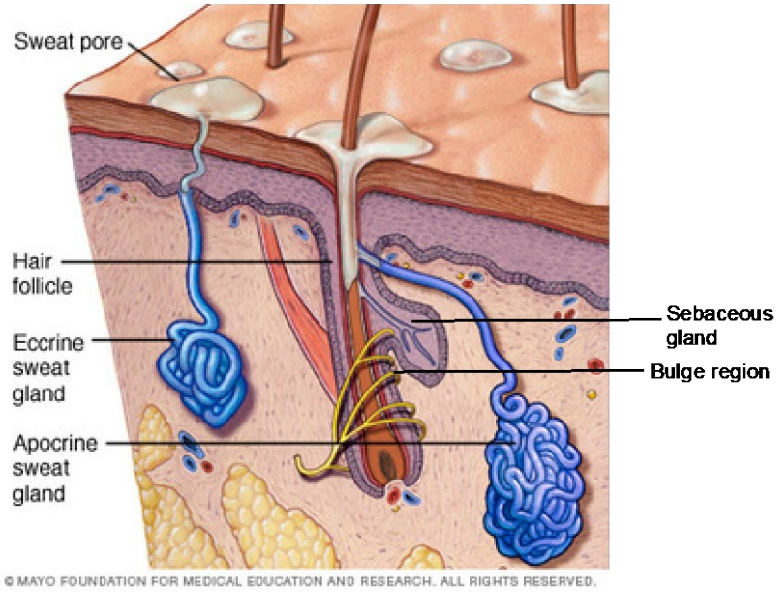

Figure 1-2. Schematic of the folliculosebaceous-apocrine unit and eccrine sweat gland. The hair follicle bulge region, which contains stem cells thought to be the origin of cylindromas and spiradenomas, is located beneath the sebaceous gland. Adapted from www.mayoclinic.org.

1.1.3 Sporadic tumours

Trichoepitheliomas, cylindromas and spiradenomas may occur sporadically as solitary lesions in patients that do not have a germ-line mutation in the *CYLD* gene. Loss of the CYLD protein due to somatic mutations and/or loss of heterozygosity at 16q as seen in CCS has been reported in sporadic tumours(Leonard et al., 2001). In 2011, a study of 12 cases of sporadic cylindromas found that 6 tumours expressed a *MYB-NFIB* fusion transcript predicted to increase *MYB* target gene activation. In addition, two tumours that did not express the fusion transcript stained positive by immunohistochemistry for nuclear MYB expression(Fehr et al., 2011). The *MYB-NFIB* transcript had previously been discovered to recur in adenoid cystic carcinomas, malignant tumours of secretory glands that share histological similarities with cylindromas.

The *MYB* transcription factor is a crucial regulator of hematopoietic stem cell proliferation and differentiation(Ramsay, 2005). It is also recognised as an important oncogene in leukaemia and other cancers(Ramsay and Gonda, 2008). An investigation into aberrant *MYB* expression in 23 CYLD defective tumours from CCS patients did not detect the *MYB-NFIB* fusion transcript by fluorescent in situ hybridisation(Rajan et al., 2016). *MYB* expression was however increased at both

the RNA and protein level in 69% of the tumours, suggesting that aberrant *MYB* activation is a pathogenic feature of both sporadic and inherited CYLD defective tumours. Recently, *ALPK1* has been shown to be mutated in spiradenoma and spiradenocarcinoma(Rashid et al., 2019).

1.1.4 Malignant transformation of CYLD defective tumours

Malignant transformation of cylindromas and spiradenomas may occur in solitary tumours and those arising due to CCS, although instances are rare(Kazakov et al., 2009). A meta-analysis of malignant spiradenoma in 2011 found 102 cases reported in the English literature(Andreoli and Itani, 2011) while less than 50 well documented cases exist of malignant cylindroma(Bansal et al., 2012). Transformed spiradenoma and cylindroma exhibit rapid growth relative to their benign counterparts and may display bleeding, colour change and ulceration. They are locally invasive and may metastasise to lymph nodes, lung, bones, skin, stomach, thyroid and brain. Trichoepitheliomas may transform into basal cell carcinoma (BCC), although it is not always certain that the BCC developed directly from the benign neoplasm or independently(Johnson and Bennett, 1993, Kallam et al., 2016, Agarwal et al., 2015).

Very rarely, other benign tumours not relating to the skin may arise alongside CYLD defective tumours. Less than 5% of CCS patients develop the most common associated tumour, membranous basal cell adenoma of the salivary gland(Jungehulsing et al., 1999, Scott et al., 2010).

1.1.5 Treatment of CYLD cutaneous syndrome

There is no current medical treatment available for CCS apart from repeated surgeries to relieve tumour burden. Reasons for tumour removal may include pain, bleeding, ulceration and sexual dysfunction(Rajan et al., 2009). In very severe cases, cylindromas on the scalp may become confluent and entire scalp removal is necessary (Figure 1-3).

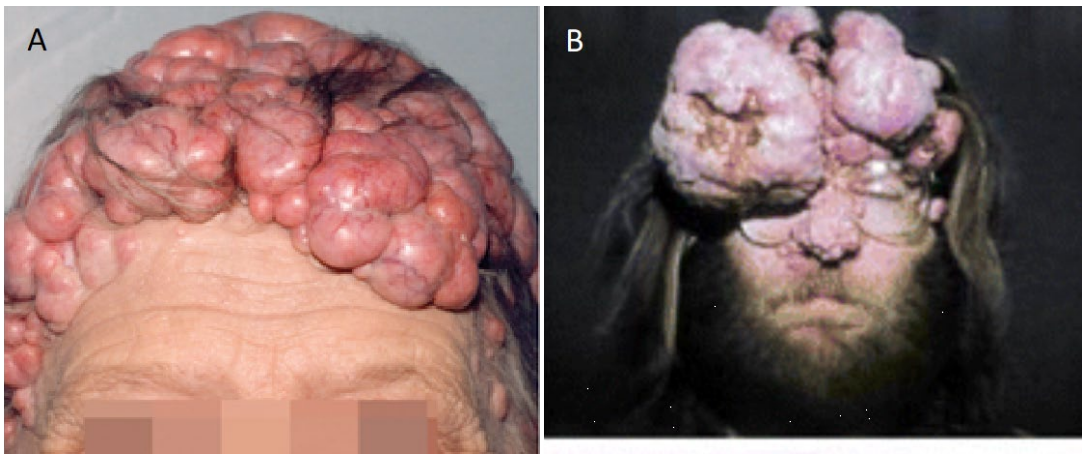

Figure 1-3. CYLD cutaneous syndrome. A) A female CCS patient with multiple cylindromas on the scalp, image from (Rajan and Ashworth, 2015). B) A male CCS patient with multiple cylindromas on the scalp and face, image from (Bignell et al., 2000).

The discovery of the causative gene for CCS in 2000 and later elucidation of the role of CYLD as a negative regulator of NF-κB signalling led to a pilot study of topically applied salicylic acid, an inhibitor of IKKβ, as a potential treatment for CCS. Out of 12 tumours, 2 had complete remission and 8 responded to treatment, however the response was not sufficient to take the trial forward(Oosterkamp et al., 2006).

More recently, an early phase trial was carried out to test the topical use of a tropomyosin-related kinase (TRK) inhibitor (Pegcantratinib) after deregulation of the TRK signalling pathway was uncovered in CCS tumours(Rajan et al., 2011b, Danilenko et al., 2018). The TRK family of receptor tyrosine kinases consists of TRKA, TRKB and TRKC. Binding of neurotrophins to TRK receptors activates signalling pathways involved in neuronal differentiation, growth and survival(Skaper, 2012). Transcriptomic profiling of 32 CCS tumours and 10 perilesional controls indicated an upregulation of both TRKB and TRKC in tumours relative to normal skin(Rajan et al., 2011b). While the phase 2 trial demonstrated safety of application and penetration of Pegcantratinib into treated tumours at low concentrations, a further trial phase was not carried out at the same highest available dose as the number of tumours showing a response compared to placebo did not meet the predefined critical number.

1.2 The cylindromatosis gene (*CYLD*)

1.2.1 Discovery of CYLD as the causative gene of familial cylindromatosis

The first evidence suggesting a tumour-suppressor gene may be responsible for familial cylindromatosis was provided by linkage analysis using the genomes of two families in the northeast of England in 1995(Biggs et al., 1995). The causative gene was mapped to loci at chromosome 16q12-13 and loss of heterozygosity (LOH) due to deletion or recombination at chromosome 16 involving all or part of the long q arm was confirmed in 19 out of 25 tumours examined. In all instances the wild-type allele from the unaffected parent was lost, consistent with Knudson's two hit model for tumour development(Knudson, 2001). In 2000, Bignell *et al.* used fine-mapping and positional cloning to identify the susceptibility gene, named '*CYLD'(Bignell et al., 2000).* It was later confirmed by Zhang *et al*. that mutation of *CYLD* is also responsible for MFT(Zhang et al., 2004).

1.2.2 Characterisation of CYLD

The *CYLD* gene is composed of 20 exons, the first three of which are untranslated. The CYLD protein contains three N-terminal cytoskeletal-associated protein-glycine-conserved (CAP-Gly) domains and one C-terminal ubiquitin-specific protease (USP) domain (Figure 1-4)(Bignell et al., 2000). The CAP-Gly domains allow CYLD to interact with microtubules and other proteins during the regulation of cell processes such as cell division and migration(Gao et al., 2008, Wickstrom et al., 2010).

The USP domain is responsible for the deubiquitinating (DUB) activity of CYLD. This crystal structure of this catalytic domain was resolved in 2008 by Komander et al. to consist of thumb, truncated fingers and palm subdomains with a small zinc binding B-box at the core(Komander et al., 2008). The B-box is thought to facilitate intermolecular interaction and retention of CYLD in the cytoplasm(Xie et al., 2017). The binding sites of some substrates of CYLD have been determined. The TNF receptor-associated factor 2 (TRAF2) binding site is adjacent to the NF-Kappa-B Essential Modulator (NEMO, also known as IKKγ) binding site, which is located partially within the third CAP-Gly domain(Kovalenko et al., 2003, Saito et al., 2004). There are thirteen protein coding transcript variants of the human *CYLD* gene

(www.emsembl.org), with isoforms ranging in size from 956 amino acids to 33 amino acids.

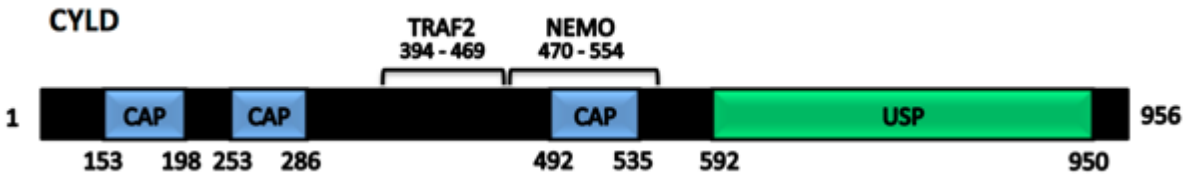

Figure 1-4. Domain structure of the full-length human CYLD protein. CAP, CAP-Gly domain; USP, Ubiquitin specific protease domain; TRAF2, TRAF2 binding site; NEMO, NEMO binding site.

1.2.3 CYLD mutations associated with CYLD cutaneous syndrome

A 2015 literature review found 95 published *CYLD* gene mutations including missense, nonsense, splice-site and frameshift mutations(Nagy et al., 2015). The most common types of mutation, frameshifts (48%) and nonsense (27%), result in truncation of the CYLD protein due to the introduction of a premature stop codon. The majority of mutations (99%) occurred within exons 9 – 20, which contain the TRAF2 and NEMO binding sites and the catalytic USP domain (Figure 1-5). The mutations responsible for CCS are therefore predicted to result in loss of function and impair the catalytic ability of CYLD to remove ubiquitin from target substrates. Conversely, one missense mutation in *CYLD* that causes frontotemporal dementia-amyotrophic lateral sclerosis (c.2155A>G, p.M719V) has been reported to result in enhanced CYLD catalytic activity(Dobson-Stone et al., 2020).

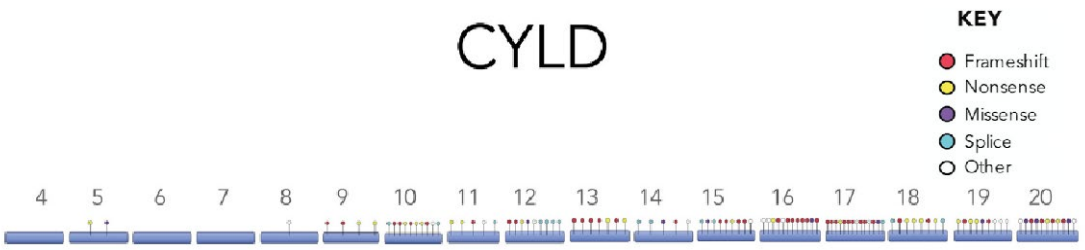

Figure 1-5. . The locations of reported mutations in the *CYLD* gene of patients with CYLD cutaneous syndrome.Untranslated exons (1 - 3) are not shown; exons 4 - 20 are not drawn to scale. Adapted from(Dubois et al., 2017).***CYLD expression***

In humans, *CYLD* RNA is ubiquitously expressed in all tissues. Expression is highest in brain, endocrine tissues, muscle, blood, bone marrow and lymphoid tissues (www.proteinatlas.org). In human skin appendages, CYLD protein is expressed in

eccrine sweat glands and the inner root sheath of the hair follicle(Massoumi et al., 2006b, Zuo et al., 2007).

1.2.5 CYLD function

1.2.5.1 Deubiquitination

Ubiquitination is a posttranslational modification (PTM) involving the attachment of ubiquitin, a small 76 aa protein, to substrate proteins. The process involves the coordination of an E1 ubiquitin activating enzyme, an E2 ubiquitin-conjugation enzyme and substrate recognition by an E3 ubiquitin ligase. Ubiquitin contains seven lysine residues (K6, K11, K27, K29, K33, K48 and K63) at which another ubiquitin may be attached. The specific lysine residue that joins the C-terminus of the next ubiquitin in the chain determines the role of the PTM. For example, K11 and K48-linked ubiquitin chains target the substrate for degradation by the proteosome, whereas K63-linked chains facilitate protein complex assembly(Komander and Rape, 2012).

Polyubiquitin chains may be linked at the same lysine residue (homotypic) or a mixture of different lysine residues (heterotypic). Linear chains are produced by linking the N-terminal methionine (Met1) of one ubiquitin to the C-terminal glycine residue of the next ubiquitin(Komander and Rape, 2012, Rape, 2017). The process of ubiquitination can be reversed by the removal of ubiquitin by deubiquitinating enzymes (DUBs). CYLD is a DUB that specifically hydrolyses K63- and Met1-linked polyubiquitin chains from substrates via its catalytic USP domain(Komander et al., 2008, Hrdinka et al., 2016).

CYLD is recognised as a key negative regulator of the NF-κB signalling pathway(Kovalenko et al., 2003, Trompouki et al., 2003, Brummelkamp et al., 2003). The DUBs A20 (syn. TNFAIP3) and Otulin have also been shown to negatively regulate NF-κB signalling(Lork et al., 2017). Although CYLD, A20 and Otulin have many overlapping substrates, each prefers distinct polyubiquitin chains; Otulin exclusively removes Met1-linked ubiquitin chains, while A20 hydrolyses K63-linked chains and mediates the addition of K48-linked chains to some substrates. Differing phenotypes displayed by CYLD, A20 and Otulin knockout mice suggest that non-redundant functions of these DUBS exist(Lork et al., 2017).

Since its discovery as a DUB that negatively regulates NF-κB signalling in 2003, this function of CYLD is now known to mediate diverse biological processes such as spermatogenesis(Wright et al., 2007), osteoclastogenesis(Jin et al., 2008), ciliogenesis(Yang et al., 2014) and cell death signalling(Lork et al., 2017).

1.2.5.2 Microtubule dynamics and cell cycle regulation

In addition to its DUB role, CYLD interacts with and regulates microtubule dynamics(Gao et al., 2008). This function of CYLD is mediated by its first and second CAP-Gly domains, which can bind directly to tubulin and enhance tubulin polymerization.

Tubulin is a dimer made up of α-tubulin and β-tubulin, which polymerize to form microtubules. Acetylation is a PTM of α-tubulin that stabilises microtubules after formation. CYLD inhibits deacetylation of α-tubulin via an interaction between the N-terminal domain of CYLD and the catalytic site of histone deacetylase-6 (HDAC6)(Wickstrom et al., 2010). This results in the accumulation of acetylated α-tubulin around the nucleus. Perinuclear co-localisation of CYLD with acetylated α-tubulin led to a delay in the G_1-to-S-phase transition in mouse keratinocytes, suggesting a role for CYLD in the regulation of cell cycle duration(Wickstrom et al., 2010).

A short hairpin RNA screen for cell-cycle regulators also identified CYLD in human cells. CYLD was subsequently found to delay entry to mitosis by removing K63-linked ubiquitin chains from the polo-like kinase (PLK1), a critical regulator of cytokinesis(Stegmeier et al., 2007).

1.2.6 Deregulation of CYLD in cancer

CYLD down-regulation or the loss of CYLD deubiquitination function has been reported in multiple human tumours including breast(Hutti et al., 2009), melanoma(Massoumi et al., 2009), hepatocellular and colon(Hellerbrand et al., 2007, Pannem et al., 2014) and adenoid cystic carcinoma(Stephens et al., 2013). Deletion of the CYLD locus has also been found in association with upregulation of NF-κB signalling in multiple myeloma patient tissues(Annunziata et al., 2007). Somatic mutations in *CYLD* have been found to occur in human papillomavirus-associated

head and neck carcinomas that display cylindroma-like histology(Cui et al., 2021, Williams et al., 2021).

Recently, Hahn *et al.* used a condition *CYLD* mouse model to investigate underlying mechanisms of constitutive NF-κB activation in chronic lymphocytic leukaemia (CLL)(Hahn et al., 2018). Mice with targeted mutation of *CYLD* in B cells lack full length CYLD and overexpress a shorter isoform of CYLD (sCYLD) that lacks the ability to bind to the NF-κB substrates TRAF2 and NEMO. Mice overexpressing sCYLD spontaneously develop $CD5^+$ B-cell hyperproliferation, a characteristic of CLL. Expression of sCYLD was confirmed in CLL-patient samples, suggesting that alternative splicing of *CYLD* may promote the development of CLL.

1.3 The role of CYLD in NF-κB signalling

1.3.1 Introduction to NF-κB

Since its discovery in 1986 by Sen and Baltimore, Nuclear factor binding near the κ light chain gene in B cells (NF-κB) has emerged as not one but five related transcription factor proteins present in almost all cells(Sen and Baltimore, 1986b, Sen and Baltimore, 1986a, Zhang et al., 2017). These proteins regulate genes with diverse roles in adaptive and innate immune response, inflammation, lymphoid organogenesis, regulation of T and B cell development, survival, differentiation and proliferation(Beg and Baltimore, 1996, Gerondakis et al., 2006).

The NF-κB/Rel family of transcription factors consisting of RelA (p65), RelB, c-Rel, p50 and p52 can potentially form 15 homo- or heterodimers to activate or repress hundreds of genes(Smale, 2012). NF-κB dimers bind to target genes at the ‘kB’ consensus DNA sequence 5’-GGGRNWYYCC-3’ where R is purine, N is any base, W is adenine or thymine and Y is pyrimidine(Sen and Baltimore, 1986b).

All five proteins share an N-terminal Rel homology domain (RHD) that is structurally similar to the v-Rel oncogene product of the avian Reticuloendotheliosis virus REV-T and a nuclear localisation sequence (NLS) (Figure 1-6A)(Zhang et al., 2017). The RHD is responsible for DNA sequence recognition and binding via its N-terminal subdomain. The C-terminal RHD subdomain binds to inhibitory proteins and facilitates dimerization(Hayden and Ghosh, 2012, Smale, 2012). RelA, RelB and c-

Rel proteins contain a transcription transactivation domain (TAD) and are synthesized as mature proteins. Dimers containing one of these TAD monomers are transcriptional activators.

p105 (NFKB1) and p100 (NFKB2) are translated as precursor proteins containing multiple tandem ankyrin repeats (AnkR) and a C-terminal death domain (DD)(Zhang et al., 2017). The precursor proteins are post-translationally cleaved between the NLS and first AnkR into p50 and p52. Processing of p105 to p50 is constitutive while p100 processing to p52 requires signalling activation. Functionally, p50 and p52 homodimers are transcriptional repressors unless bound to a co-activator protein.

Cleaved p105 and p100 retain the ability to bind to the RHD of all five NF-κB transcription factors, inhibiting their nuclear localisation by masking the NLS domain. Consequently, p105 and p100 are considered to be members of the inhibitors of κB (IκB) family (Figure 1-6B). The eight members of the IκB family of proteins, IκBα, IκBβ, IκBε, BCL3, IκBζ, IκBNS, IκBγ (p105) and IκBδ (p100), contain five to seven AnkR repeats which bind to the RHD of NF-κB(Zhang et al., 2017). The resulting conformation conceals the NF-κB NLS, preventing nuclear localisation and gene transcription or repression until the signalling pathway is activated. Activation of NF-κB occurs via two distinct pathways; the ‘canonical pathway’ and ‘non-canonical’ or ‘alternative pathway’.

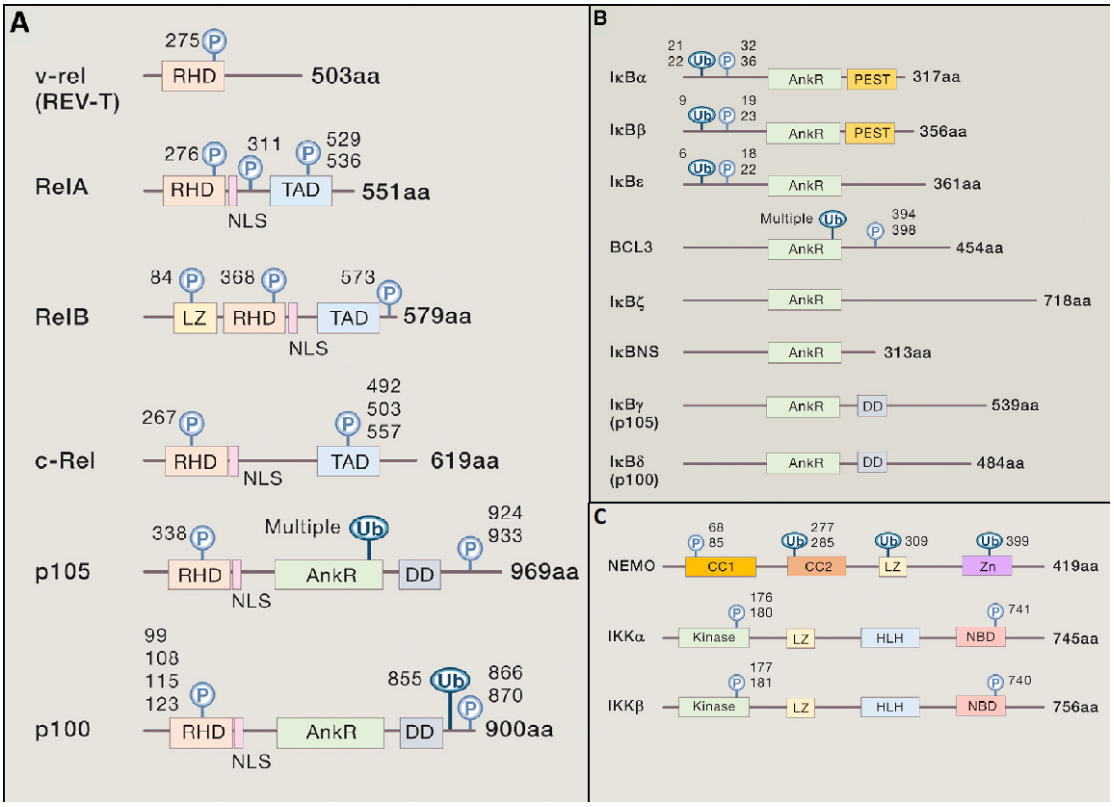

Figure 1-6. NF-κB subunits and related proteins. A) The NF-κB transcription factors RelA, RelB, c-Rel, p105 and p100 share homology with the v-rel oncogene product from the avian reticuloendotheliosis virus strain T. The precursor proteins p105 and p100 are post-translationally processed into p50 and p52, respectively. RHD, rel homology domain; NLS, nuclear localisation sequence; TAD, transactivation domain; AnkR, tandem ankyrin repeats; DD, death domain; LZ, leucine zipper; Ub, ubiquitination site; P, phosphorylation site. B) The eight members of the Inhibitor of κB (IκB) family harbour tandem ankyrin repeats that inhibit nuclear localisation of NF-κB by binding to the RHD and masking the NLS. PEST; proline, glutamic acid, serine and threonine rich region. C) The subunits of the IKK complex. CC1, coiled–coil domain 1; CC2, coiled-coil domain2, Zn, zinc-finger; Kinase, kinase domain, HLH, helix-loop-helix region; NBD, NEMO-binding domain. Adapted from Hayden and Ghosh (2008, 2012) and Zhang et al. (2017).

In the remainder of this section, I will describe known NF-κB signalling mechanisms in immune cells. I will then highlight skin specific NF-κB signalling.

1.3.2 Canonical NF-κB signalling

In resting cells, NF-κB dimers shuttle in and out of the nucleus while bound to IκBs(Hayden and Ghosh, 2004). Antigens and proinflammatory cytokines such as TNF and IL1 activate the canonical pathway to generate a rapid response to immune insults. The canonical pathway may be stimulated via multiple receptors (TNFR, TCR, BCR, IL-1R and TLRs) which all converge on activation of the IKK complex (Figure 1-7).

The IKK complex consists of two kinases, IKKα and IKKβ, plus the non-catalytic regulatory subunit NEMO (Figure 1-6C). Activation of the IKK complex is facilitated by the ubiquitin-mediated connection of NEMO to upstream signalling complexes and the phosphorylation of IKKs by TAK1, an ubiquitin-dependent kinase that forms a complex with TAK1-binding (TAB) proteins(Wang et al., 2001, Hirata et al., 2017, Krappmann and Scheidereit, 2005) (Figure 1-7). The activated IKK complex phosphorylates IκBs, resulting in their degradation by the proteasome. This frees NF-κB dimers to translocate to the nucleus and bind to κB consensus sites.

In canonical NF-κB signalling, RelA/p50 is the classic heterodimer and IκBα is the prototypical inhibitor. IκBα is phosphorylated at serines 32 and 36 by the IKKβ subunit of the activated IKK complex. In response IκBα is rapidly polyubiquitinated by the $SCF^{\beta\text{-}TrCP}$ E3 ubiquitin ligase complex and degraded by the 26S proteasome, allowing the nuclear localisation of RelA/p50 to activate proinflammatory target genes (Figure 1-7).

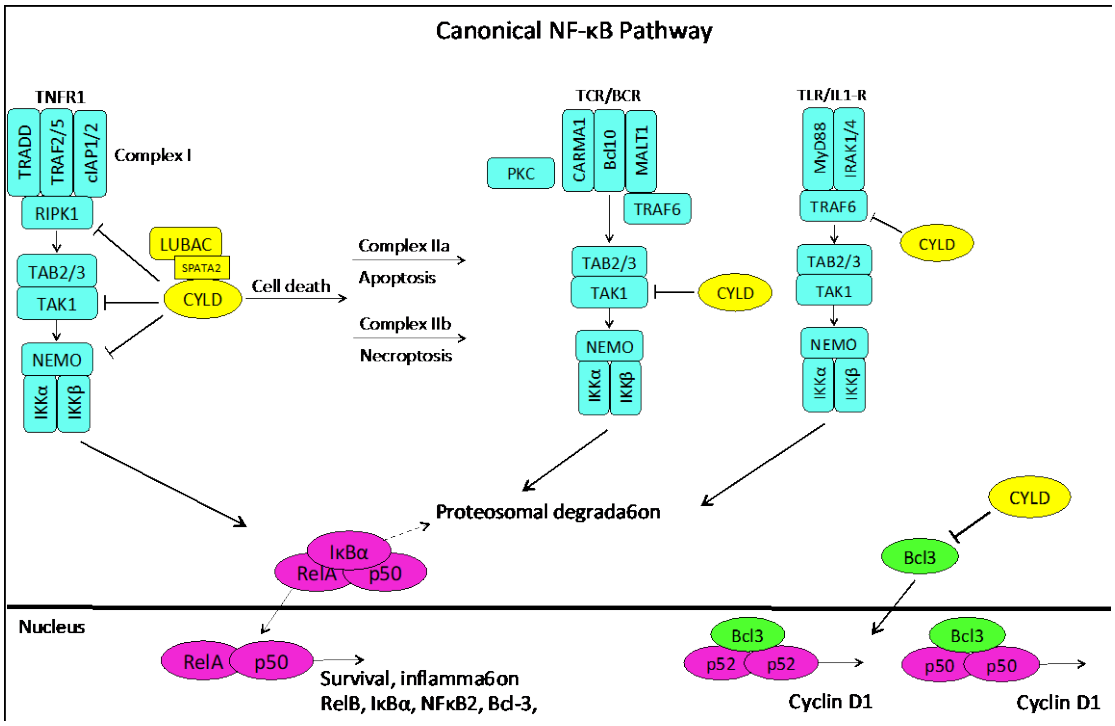

Figure 1-7. The canonical NF-κB signalling pathway. TNFR1 stimulation induces complex I formation. TRAF2 mediated K63-linked ubiquitination (K63-Ub) of RIPK1 recruits TAB2/3 and TAK1. LUBAC is recruited to generate Met1-linked ubiquitin chains on substrates in complex I, which recruit the IKK complex via NEMO. The IKK complex is activated by TAK1, leading to phosphorylation and degradation of IκBα and release of canonical NF-κB dimers. CYLD is also recruited to complex I via SPATA2 and LUBAC. CYLD negatively regulates NF-κB signalling by removing K63-Ub from complex I, TAK1 and NEMO. Destabilisation of complex I attenuates pro-survival signalling and favours complex IIa driven apoptosis. In the

presence of RIPK1 and RIPK3 and in the absence of Caspases, complex IIb is formed resulting in necrotic cell death. Stimulation of TCR/BCR results in phosphorylation of CARMA1 by PKC and formation of the CBM complex. MALT1 binds TRAF6 to the CBM, which stimulates the K63-Ub of BCL10 and MALT1 and recruitment of the IKK complex via NEMO(Thome et al., 2010). The IKK complex is activated by TAK1 and IκBα is degraded. Stimulation of TLRs recruits MyD88, the IRAK1/4 kinases and TRAF6. TRAF6 promotes K63-Ub of IRAK1/4 and itself, resulting in recruitment of TAB2/3/TAK1 and downstream IKK activation. CYLD prevents the nuclear translocation of BCL3-p50/BCL3-p52 complexes by removing K63-linked ubiquitin chains from BCL3.

1.3.3 The function of CYLD in canonical NF-κB signaling in immune cells

Inflammatory signalling via TNFR1 is a well-studied route of NF-κB activation. Stimulation of TNFR1 induces the formation of complex I, consisting of TRADD, TRAF2/5, cIAP1/2 and RIPK1 (Figure 1-7). TRAF2 has E3 ubiquitin ligase activity for the attachment of K63-linked ubiquitin chains to substrates. TRAF2 and cIAP1/2 mediated polyubiquitination of RIPK1 results in the recruitment of the adaptors TAB2/3 and the kinase TAK1. The linear ubiquitin assembly complex (LUBAC) is also recruited to the K-63 linked chains generated by TRAF2 and cIAP1/2(Schlicher et al., 2017). LUBAC consists of the subunits HOIP (an E3 ubiquitin ligase), HOIL-1 and SHARPIN. HOIP then generates Met1-linked ubiquitin chains on substrates within complex I, which recruit the IKK complex via NEMO(Rahighi et al., 2009). The IKK complex is subsequently activated by phosphorylation of IKKβ by TAK1.

The role of CYLD as a DUB that negatively regulates canonical NF-κB signalling was discovered *in vitro* using yeast two-hybrid screening and RNA interference approaches(Kovalenko et al., 2003, Trompouki et al., 2003, Brummelkamp et al., 2003). This role was first elucidated in the NF-κB TNF inflammatory signalling pathway. Overexpressed CYLD in transfected cells was shown to bind to NEMO and remove ubiquitin from TRAF2 after stimulation with TNFR ligands. Constitutive activation of NF-κB due to loss of CYLD is predicted to contribute to tumourigenesis due to the upregulation of proinflammatory and anti-apoptotic genes.

Recently, it was shown that SPATA2 is a ‘bridging’ protein between CYLD and the HOIP component of LUBAC(Wagner et al., 2016, Schlicher et al., 2016, Kupka et al., 2016, Elliott et al., 2016). CYLD, which is bound to LUBAC by SPATA2, is recruited with LUBAC to complex I where it attenuates NF-κB signalling by removing Met1- and K63-linked polyubiquitin chains from TRADD, RIPK1 and TNFR1(Draber et al., 2015, Schlicher et al., 2017). This negative regulation by CYLD favours the formation

of complex IIa or b, which lead to apoptosis or necroptosis respectively (Figure 1-7)(Lork et al., 2017).

In lymphocytes, stimulation of TCR and BCR by antigens results in the formation of the CARMA1/BCL10/MALT1 (CBM) complex (Figure 1-7). Upon phosphorylation by protein kinase C (PKC), CARMA1 recruits BCl-10 and the paracaspase MALT1. MALT1 binds TRAF6 to the CBM, which stimulates the K63-linked polyubiquitination of BCL10 and MALT1 and recruitment of the IKK complex via NEMO(Thome et al., 2010). TRAF6 also undergoes auto-ubiquitination, with the K63-linked polyubiquitin chains acting as a scaffold for TAB2/3(Hirata et al., 2017). The MALT1 protease simultaneously cleaves the DUB A20, culminating in the activation of the IKK complex by TAK1(Wang et al., 2001). In primary T-cells, upon TCR stimulation CYLD negatively regulates TAK1 directly by preventing its ubiquitination and downstream activation of the IKK complex(Reiley et al., 2007a).

Toll-like receptors (TLRs) mediate immune and inflammatory responses to pathogen invasion. Stimulation of this pathway recruits the adaptor protein MyD88, the IRAK1/4 kinases and the E3 ubiquitin ligase TRAF6 (Figure 1-7). TRAF6 promotes the K63-linked polyubiquitination of IRAK1/4 and itself, resulting in recruitment of TAB2/3/TAK1 and downstream IKK activation. In HEK293 cells stably transfected with TLR2, stimulation with TLR2 ligands induced the transcription of proinflammatory cytokines (TNF-α, IL1β, IL8) and CYLD(Yoshida et al., 2005). CYLD knockdown by siRNA enhanced NF-κB activation in response to specific TLR2 ligands, suggesting an auto-regulatory feedback loop that prevents excessive inflammation. Negative regulation by CYLD was via a direct interaction with TRAF6 and TRAF7, suggesting deubiquitination as the mechanism of inhibition.

1.3.4 Non-canonical NF-κB signaling

While canonical NF-κB activation occurs rapidly and transiently, the non-canonical pathway responds relative slowly and is sustained for longer(Sun, 2011, Zhang et al., 2017). Signalling is induced by TRAF-interacting receptors that mediate specific biological functions, including B-cell survival (BAFFR), B-cell maturation (CD40), development of peripheral lymphoid organs (LTβR) and osteoclastogenesis (RANK).

In the non-canonical pathway, the RelB/p52 heterodimer is freed to enter the nucleus by the IKKα induced processing of p100. This processing of p100 is regulated by the NF-κB inducing kinase (NIK)(Xiao et al., 2001). Under normal conditions, TRAF2/3 and cIAP1/2 mediate the constant K48-linked ubiquitination and proteasomal degradation of NIK. When the TRAF2/3-cIAP1/2 complex is recruited to the receptor after ligand stimulation, cIAP1/2 ubiquitinates TRAF2 and TRAF3 with K48-linked chains. These in turn are degraded, allowing the stabilisation of NIK (Figure 1-8).

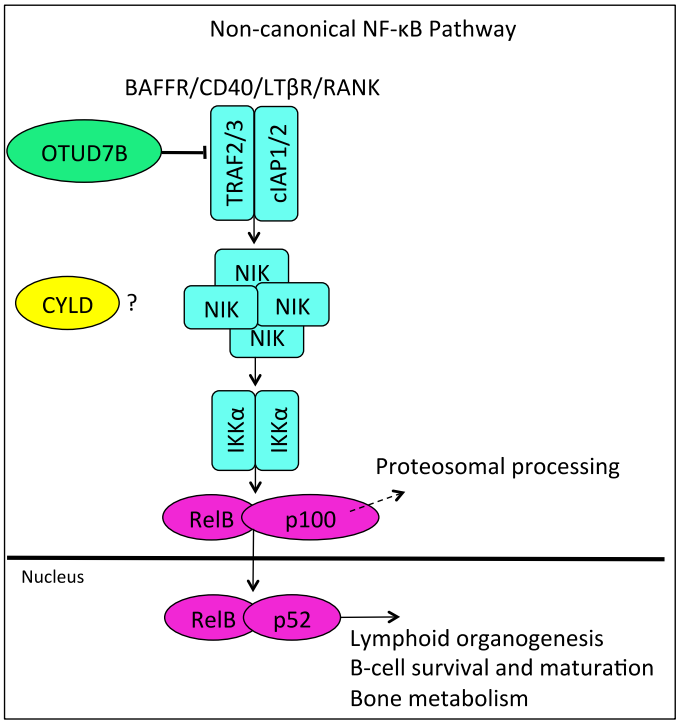

Figure 1-8. The non-canonical NF-κB signalling pathway. TRAF2/3 and cIAP1/2 mediate the constant K48-linked ubiquitination (K48-Ub) and proteasomal degradation of NIK. Upon receptor stimulation, TRAF2/3 are K48-Ub by cIAP1/2 and degraded. Stabilised NIK phosphorylates IKKα homodimers, which phosphorylate p100. P100 is partially processed by the proteasome into p52 and the RelB/p52 heterodimer is freed to enter the nucleus. OTUD7B negatively regulates non-canonical NF-κB signalling by removing K48-Ub from TRAF3. CYLD is not thought to have a role in non-canonical NF-κB signalling.

NIK accumulates and phosphorylates IKKα homodimers, which phosphorylate p100 at serines 866 and 870. The ubiquitin ligase SCFβ^{Trcp} binds to p100 within the phosphorylated serine residues. P100 is subsequently ubiquitinated at K856 with K48-linked chains and partially processed into p52 by the proteasome. The deubiquitinase OTUD7B (also known as Cezanne) negatively regulates this process by removing K48-linked ubiquitin chains from TRAF3, preventing its degradation and subsequent accumulation of NIK(Hu et al., 2013).

Based on *in vitro* studies of transfected cell lines, CYLD is not currently thought to influence non-canonical NF-κB signalling. Studies of CYLD deficient mice however suggest that *in vivo*, CYLD function may be cell type and stimulation specific(Massoumi et al., 2006a, Reiley et al., 2006, Hovelmeyer et al., 2007). A physiological role for CYLD in the non-canonical NF-κB signalling pathway cannot therefore be ruled out, particularly in CYLD defective tumours for which there are no mouse models available that develop the CCS tumour phenotype.

1.3.5 NF-κB in skin

Multiple NF-κB knockout mice develop cutaneous defects, for example IKKα deficient mice display defects in epidermal differentiation(Hu et al., 1999). Control of epidermis formation was however shown to be independent of IKKα's NF-κB kinase activity(Hu et al., 2001). Conditional deletion of *IKBKB*, the gene encoding IKKβ, in epidermal keratinocytes inhibits NF-κB activity but does not alter differentiation or proliferation. These mice developed a severe inflammatory skin disease, suggesting canonical NF-κB maintains the immune homeostasis of the skin(Pasparakis et al., 2002). Further supporting this role, CRE-mediated deletion of both *c-Rel* and *RelA* in keratinocytes resulted in severe dermatitis with partial histological similarity to human psoriasis(Grinberg-Bleyer et al., 2015, Schmidt-Supprian et al., 2000). Mice deficient in RelB and IκBα also develop skin lesions due to inflammation(Barton et al., 2000). The heterozygous *IKBKG* (NEMO) knockout mouse is a model for the male-lethal skin disorder incontinentia pigmenti, which is caused by mutation of *IKBKG* in humans(Schmidt-Supprian et al., 2000).

As RelA, IKKβ and NEMO knockout mice are embryonic lethal, Schmidt-Ullrich *et al.* used systemic repression of NF-κB signalling via ubiquitous expression of an IkBα mutant to investigate the role of NF-κB in adult mice(Schmidt-Ullrich et al., 2001). These mice had severe defects in skin appendage development due to increased apoptosis, while NF-κB was strongly expressed in wild-type skin appendages including the hair follicle bulge region.

In murine keratinocytes stimulated with UV light or 12-O-tetradecanoylphorbol-13 acetate (TPA), CYLD binds to and deubiquitinates B-cell CLL/lymphoma 3 (BCL3) in the perinuclear region(Massoumi et al., 2006a). BCL3 is a transcriptional co-activator that associates with p50 and p52 homodimers in the nucleus (Figure 1-7). BCL-p50

and BCL-p52 complexes have been implicated in breast cancer, melanoma and hepatocellular carcinoma due to aberrant expression of the target gene cyclin D1 (*CCND1*)(Cogswell et al., 2000, Massoumi et al., 2009, Park et al., 2006). Removal of K63-linked ubiquitin chains from BCL3 by CYLD prevented the nuclear translocation of BCL3-p50/BCL3-p52 complexes. In agreement, CYLD-deficient mice were more susceptible to chemically induced skin tumours than wild-type controls(Massoumi et al., 2006a). Analysis of tumours cells after the application of TPA showed increased proliferation and cyclin D1 expression. Taken together, this data suggests that negative regulation of BCL3 by CYLD inhibits cell proliferation and tumourigenesis.

Relative to the other NF-κB subunits, little is known regarding p52 in skin. P52-deficent mice do not develop any overt epidermal defects, while limited data exists regarding p52 mRNA expression in keratinocytes or p52 protein expression in skin(Lorenz et al., 2016).

1.4 The role of CYLD in other cell signalling pathways

1.4.1 JNK signalling

TNFR signalling can result in the selective activation of multiple pathways, including the c-Jun NH_2-terminal kinase (JNK) and p38 subsets of mitogen-activated protein (MAP) kinases(Lee et al., 1997). In the JNK signalling pathway, membrane proximal MAPKKKs are activated upon receptor stimulation. MAPKKKs phosphorylate MKK4 or MKK7, which in turn activate JNK. Activated JNK translocates to the nucleus where it regulates numerous transcription factors(Davies and Tournier, 2012). Like IKK, TNFR induced JNK activation involves the upstream K63-linked ubiquitination of TRAF2(Lee et al., 1997).

In vitro and in vivo studies suggest that CYLD is a negative regulator of JNK signalling(Reiley et al., 2004), (Zhang et al., 2006). JNK activation was markedly enhanced in TNFα, CD40L, LPS and IL1-β stimulated cell lines with RNA interference mediated knockdown of CYLD(Reiley et al., 2004). In vivo, macrophages from CYLD-deficient mice displaying increased TRAF2 ubiquitination and JNK activation compared to controls(Zhang et al., 2006). More recently, it was shown *in*

vitro that cleavage of CYLD by the paracaspase MALT1 is required for TCR-induced JNK pathway activation(Staal et al., 2011).

1.4.2 TGF-β signalling

Transforming growth factor-β (TGF-β) family members are secreted polypeptide factors that regulate genes involved in developmental processes and maintaining tissue homeostasis(Attisano and Wrana, 2002). In TGF-β signalling, two receptors are required for pathway activation (type I and type II). TGF-β ligands bind to type II receptors, which associate with and phosphorylate a type I receptor to activate its kinase domain. The activated receptor then phosphorylates SMAD proteins, of which there are eight family members in mammals.

Only five Smads are receptor activated (Smads 1, 2, 3, 5 and 8) and hence known as R-Smads(Attisano and Wrana, 2002). Phosphorylated R-Smads are released from the receptor complex to accumulate in the nucleus where they form heteromeric complexes with Smad4, the only family member described as a Co-Smad. In the nucleus, the Smad complexes interact with DNA binding proteins and transcriptional co-activators or repressors to regulate gene expression. The two remaining Smads (Smads 6 & 7) inhibit TGF-β signalling by supressing the activity of R-Smads. Smad-independent TGF-β pathways have also been reported, including phosphatidylinositol-3-kinase (PI3K)/AKT and JNK/p38 signalling(Zhang, 2009).

TGF-β stimulation of CYLD-deficient mouse primary T-cells resulted in enhanced ubiquitination of Smad7. Furthermore, endogenous CYLD was shown to deubiquitinate Smad7 at specific lysine residues and ubiquitination at these residues was required for downstream TAK1 and p38 MAP kinase activation. Negative regulation of TGF-β signalling via deubiquitination of Smad7 by CYLD may regulate T regulatory cell (Treg) development, as CYLD-deficient mice display an increased number of Tregs in peripheral lymph nodes than controls(Zhao et al., 2011).

In addition to TGF-β-mediated activation of p38 MAP kinase signalling, CYLD negatively regulates TGF-β signalling via direct deubiquitination of Akt. Infection of CYLD-deficient mice with *Streptococcus pneumoniae* results in lung fibrosis due to excessive wound healing(Lim et al., 2012). Lim *et al.* showed that removal of K63-

linked polyubiquitin chains from Akt decreased the stability of Smad3 and prevented TGF-β mediated lung fibrosis.

1.4.3 Notch signalling

The Notch signalling pathway regulates cell fate decisions after cell-cell interactions(Miele, 2006). In mammals, there are four transmembrane Notch receptors (Notch1 - 4) that are proteolytically cleaved upon binding to ligands expressed on neighbouring cells. The five Notch ligands can be divided into 'Jagged' (JAG1 and 2) and 'Delta-like' (DLL1, 3 and 4). The intracellular domain of the Notch receptor (Notch intracellular domain, NICD) is freed upon cleavage to enter the nucleus and modulate gene expression via binding to CBF1, Suppressor of Hairless, Lag-1 (CSL) transcription factors. Notch1 has been shown to orchestrate differentiation in a number of cell types, including T-cells, keratinocytes and hair follicles(Kopan and Weintraub, 1993, Nickoloff et al., 2002, Pui et al., 1999).

A proteomics screen using CYLD as bait identified an interaction between mind bomb homologue 2 (MIB2) and CYLD(Rajan et al., 2014). MIB2 is an E3 ubiquitin ligase that mediates the intracellular ubiquitination of the Notch1 ligand JAG2. Ubiquitination of intracellular Notch ligands is thought to facilitate endocytosis, thereby enhancing Notch1 signalling(Koo et al., 2007). Knockdown of CYLD with siRNA resulted in increased expression of JAG2 and Notch1 target genes. Similarly, JAG2 and Notch1 target genes were upregulated in array data from 32 CYLD defective tumours from CCS patients compared to control skin. These results suggest that CYLD negatively regulates JAG2 mediated Notch signalling via a direct interaction with MIB2.

1.4.4 Wnt signalling

Like Notch and TGF-β, the Wnt/β-catenin pathway is a highly evolutionarily conserved developmental signalling pathway(Clevers, 2006). Genes regulated by Wnt signalling are critical for tissue patterning during development. In resting cells, β-catenin is constantly turned over in the cytoplasm. Upon binding of Wnt to its receptor, Frizzled (Fz), and co-receptor LDL Receptor Related Protein (LRP)5/6, a signalling cascade ensues that disrupts the degradation of β-catenin. Nuclear

translocation of stabilised β-catenin then mediates the transcription of Wnt target genes.

A screen of 50 DUBs of the USP family in HEK293T cells using shRNA identified CYLD as a negative regulator of Wnt signalling(Tauriello et al., 2010). Furthermore, CYLD was shown to remove K63-linked polyubiquitin chains from the DIX domain of Dishevelled (Dvl). Dvl is a core component of Wnt signalling that forms a complex with Fz early in the cascade. Hyper-ubiquitination of Dvl and activation of the Wnt pathway was observed due to loss of CYLD in transfected cells. In agreement, CYLD defective tumours stained positive for markers of Wnt pathway activation including nuclear β-catenin.

1.5 Regulation of CYLD

1.5.1 Transcriptional regulation

CYLD is subject to multiple mechanisms of regulation at the post-transcriptional and post-translational level(Sun, 2010). At the gene level, down-regulation of *CYLD* expression by numerous miRNAs in cancer has been reported. These include miR-19 in T-cell acute lymphoblastic leukemia (T-all), miR-362-5p in hepatocellular carcinoma, miRNA-362 in gastric cancer and miRNA-181b in thyroid papillary cancer(Ye et al., 2012a, Ni et al., 2015, Xia et al., 2014). Down-regulation of CYLD expression by the transcription factor Snail has also been reported in malignant melanoma(Massoumi et al., 2009). Upregulation of *CYLD* gene transcription is induced by canonical NF-κB pathway activation, providing an auto-regulatory feedback mechanism to terminate inflammatory NF-κB signalling(Jono et al., 2004).

1.5.2 Phosphorylation

At the protein level, Reiley *et al.* showed that CYLD is phosphorylated at a cluster of serine residues between amino acids 418 and 444 by recombinant IKKα and IKKβ in a NEMO dependent manner. Site directed mutagenesis of all serines to alanine within the cluster abolished CYLD phosphorylation by IKK. Phosphorylation of CYLD in response to inducers of NF-κB prevented the deubiquitination of TRAF2, suggesting that phosphorylation attenuates the DUB function of CYLD(Reiley et al., 2005).

A proteomics screen for likely substrates of the IKK family member IκB kinase epsilon (IKKε) uncovered CYLD as a possible target(Hutti et al., 2009). In TNF-α stimulated HEK293T cells, IKKε directly phosphorylated CYLD at serine 418. In agreement with Reiley *et al.*, phosphorylation reduced the ability of CYLD to deubiquitinate TRAF2.

Phosphorylation of CYLD by IKKα and IKKβ has also been reported to regulate CYLD abundance. In osteoclast precursor cells, phosphorylation at Ser432/Ser436 led to the $SCF^{\beta\text{-}TrCP}$ mediated K48-linked ubiquitination of CYLD and its subsequent degradation by the proteasome(Wu et al., 2014).

1.5.3 Proteolytic cleavage

In vitro experiments suggest that caspase-8 cleaves CYLD at aspartic acid 215, generating an N-terminal fragment detectable by immunoblot(O'Donnell et al., 2011). The C-terminal fragment containing the catalytic USP domain is thought to be unstable and degraded by the proteasome. A major role of caspase-8 is to repress programmed necrosis, which is mediated by the formation of complex IIb (also known as the necrosome) containing RIPK1 and RIPK3 in response to TNF stimulation (Figure 1-7)(O'Donnell et al., 2011).

Negative regulation of CYLD by caspase-8 prevents the deubiquitination of RIPK1, both at the TNFR complex 1 and the necrosome(Lork et al., 2017). At complex 1, this has a pro-survival effect via NF-κB pathway activation. In an autoregulatory feedback mechanism, transcription of *CYLD* is induced by NF-κB and this in turn leads to down-regulation of NF-κB signalling(Jono et al., 2004). Deubiquitination of RIPK1 by CYLD ensues, favouring the formation of complex IIa leading to apoptosis. Activation of caspase-8 in the apoptotic process resumes proteolytic cleavage of CYLD and restores NF-κB signalling. Importantly, inhibition of caspases and the presence of RIPK3 results in the formation of complex IIb, where deubiquitination of RIPK1 by CYLD facilitates necroptosis(Lork et al., 2017),(O'Donnell et al., 2011).

Further regulation of the CYLD protein occurs via proteolytic cleavage at arginine 324 by MALT1(Staal et al., 2011). Cleavage of CYLD by MALT1 in response to T cell or B cell receptor stimulation occurs between the second and third CAP-Gly domain, resulting in an N-terminal 40kDa fragment and a 70kDa C-terminal fragment. Inactivation of CYLD by this mechanism is necessary for TCR-induced JNK activation

and is not thought to affect the role of CYLD in NF-κB signalling. MALT1 is a paracaspase known to positively regulate NF-κB, both through its proteolysis of A20 and RelB and via its function in the CARD11-MALT1-BCL10 complex (Hailfinger et al., 2011, Coornaert et al., 2008).

1.6 CYLD-deficient mouse models

1.6.1 CYLD knockout mice

1.6.1.1 Immune regulation

Despite the diverse biological functions of CYLD, mice with complete *CYLD* knockout are viable and appear healthy at birth. Around 10 months of age, lymphocytic inflammatory infiltrate is observed in liver, lungs, salivary glands and spleen(Zhang et al., 2006).

CYLD-deficient mice generated by Reiley *et al.* had fewer mature thymocytes (T-cell progenitor cells) and peripheral T-cells than controls, suggesting a role for CYLD in T-cell development(Reiley et al., 2006). Investigation revealed that in thymocytes, CYLD positively regulates TCR signalling by promoting the association of activated Lck kinase with its target, Zap70. The Lck kinase is an essential activator of TCR signalling in thymocytes. Interestingly, CYLD removed both K63-linked and K48-linked chains from Lck *in vitro*.

This mouse model also developed spontaneous colonic inflammation and autoimmune symptoms(Reiley et al., 2007b). Primary mouse T-cells were hyperresponsive to TCR stimulation *in vitro* and had constitutively activated TAK1, IKKβ and JNK. Furthermore, CYLD was shown to directly remove K63-linked ubiquitin chains from TAK1. This evidence suggests that in T-cells, deubiquitination of TAK1 by CYLD negatively regulates NF-κB and JNK signalling to maintain normal T-cell responses to TCR stimulation.

CYLD was also shown to negatively regulate NF-κB in B-cells *in vivo(Jin et al., 2007)*. CYLD-deficient mice developed enlarged mesenteric lymph nodes and B-cell hyperplasia. B-cells derived from the CYLD-deficient mice displayed elevated constitutive NF-κB activation compared to wild-type controls, consistent with the hyperproliferative phenotype.

1.6.1.2 Tumourigenesis

CYLD knockout mice are more prone to developing chemically induced tumours than wild-type controls. In a colitis-associated cancer model, mice injected with a DNA-alkylating agent to induce colonic mutations followed by cycles of inflammation-causing dextran sulphate sodium (DSS) developed more colon tumours than controls(Zhang et al., 2006). As previously mentioned, mice generated by the Massoumi lab were prone to chemically induced skin papillomas due to upregulation of Cyclin D1 in keratinocytes via nuclear BCL3(Massoumi et al., 2006a).

1.6.1.3 Ciliogenesis

CYLD knockout mice also develop phenotypes consistent with defects in ciliogenesis such as polydactyly(Yang et al., 2014). Investigation into the regulatory role of CYLD in ciliogenesis revealed that both the DUB and CAP-Gly domains are required. CYLD positively regulates ciliogenesis by deubiquitinating centrosomal protein of 70 kDa (Cep70), which promotes the interaction of Cep70 with γ-tubulin at the centrosome, while inhibition of HDAC6 via the first two CAP-Gly domains of CYLD also promoted ciliogenesis. Importantly, HDAC6 inhibitors partially rescued the defects in ciliary length in *CYLD* knockout mice.

1.6.1.4 Osteoclastogenesis

In addition to ciliopathies, CYLD-deficient mice also display an osteoporosis phenotype with low bone density(Jin et al., 2008). Osteoclast precursor cells derived from these mice were more sensitive to differentiation induced by RANKL (receptor activator of nuclear factor κB ligand), a non-canonical NF-κB pathway ligand. CYLD was found to associate with the adaptor protein p62 in preosteoclasts, which promoted binding of CYLD to TRAF6. Subsequent deubiquitination of TRAF6 by CYLD negatively regulated RANK induced signalling and osteoclastogenesis.

1.6.1.5 Spermatogenesis

Male CYLD-deficient mice are sterile and display testicular atrophy. This developmental defect prompted investigation of CYLD function in testicular cells(Wright et al., 2007). Loss of CYLD in mice prevents the early germ cell

apoptosis necessary for spermatogenesis. Direct interaction of CYLD with RIPK1 was discovered in this study, as loss of CYLD resulted in enhanced ubiquitination of RIPK1 and constitutive activation of IKK. CYLD therefore regulates spermatogenesis via the negative regulation of RIPK1 and NF-κB.

1.6.2 Conditional CYLD-deficient mouse models

1.6.2.1 Liver

Homozygous deletion of *CYLD* exon 9 (*CYLD*ex9) results in a truncation of CYLD with loss of DUB activity, similar to human mutations in CCS(Trompouki et al., 2009). As *CYLD*ex9 mice die shortly after birth due to impaired lung maturation, it was necessary to generate mice with tissue specific expression of the *CYLD*ex9 mutation to investigate the effects of truncating *CYLD* mutations. The first conditional model of *CYLD*ex9 targeted hepatocytes and resulted in the development of hepatocellular carcinoma due to the chronic activation of TAK1 and JNK(Nikolaou et al., 2012).

1.6.2.2 Intestine

When *CYLD* was conditionally inactivated in intestinal epithelial cells via deletion of exon 9 (IEC-*CYLD*ex9), mice did not spontaneously develop intestinal abnormalities and both JNK and NF-κB were not deregulated under physiological conditions(Karatzas et al., 2016). Upon chemical challenge with proinflammatory or genotoxic agents, IEC-*CYLD*ex9 mice developed more adenomas than control mice.

1.6.2.3 Skin

Mice with keratin 14 (K14)-Cre mediated deletion of *CYLD* exon 9 in the epidermis developed sebaceous gland, hair and dental defects(Jin et al., 2016). When topically challenged with TPA the mice developed sebaceous gland and basaloid tumours, which are not part of the CCS phenotype. Sebaceous gland, hair and dental defects were not seen in a mouse with conditional knock in of a CCS mutation that causes a premature termination codon at amino acid 932 under the K14-promoter in the epidermis(Miliani de Marval et al., 2011). These mice were more sensitive than wild type mice to the development of skin tumours with features of squamous cell carcinoma (SCC) in response to chemical challenge with 7,12-

dimethylbenz[alpha]anthracene (DMBA) and TPA(Miliani de Marval et al., 2011). More recently, a mouse expressing catalytically dead *CYLD* under the control of the K5-promoter, which is expressed in other tissues as well as skin, developed similar skin appendage defects to the *CYLD*ex9 conditional K14 mouse(Alameda et al., 2019). These mice spontaneously developed a range of tumour types in different tissues, including a hair follicle derived tumour (trichofolliculoma) and SCC. This study revealed a role for CYLD in the maintenance of the hair follicle cycle, as well as a protective role against the effects of aging and cancer. Functionally, defects in epidermal keratinocyte differentiation were attributed to increased JNK signalling, while symptoms of premature aging were attributed to constitutive NF-κB activation and consequent inflammation.

1.6.2.4 B-cells

As previously described, the *CYLD*(ex7/8) mouse generated by Hovelmeyer *et al.* solely expresses a naturally occurring shorter isoform of CYLD (sCYLD) in B-cells(Hovelmeyer et al., 2007). sCYLD does not contain the NEMO and TRAF2 binding sites but retains the ability to bind to BCL3. In contrast to complete *CYLD* knockout models, populations of mature B-cells are increased in all peripheral lymphoid organs of *CYLD*(ex7/8) mice. *CYLD*(ex7/8) B-cells also accumulate more of the non-canonical NF-κB subunits p100 and RelB, as well as more nuclear BCL3. This suggests that CYLD splice variants can differentially regulate B-cell homeostasis *in vivo*.

1.7 Tumour microenvironment

Solid tumours are a heterogeneous mixture of tumour cells and stromal cells, including cancer-associated fibroblasts, endothelial cells that make up the tumour vasculature, cancer stem cells and infiltrating immune cells, which together make up the tumour microenvironment(Hanahan and Weinberg, 2011). The individual cell types and signalling interactions between these cells must be studied in order to understand the tumour as a whole. The tumour immune microenvironment (TIME) is of particular importance, as the unique subsets of resident and infiltrating immune calls within a patient’s tumour may predict response to immunotherapies such as immune-checkpoint blockade(Binnewies et al., 2018). Infiltrating immune cells can

have both pro- and anti-tumour effects. M1 type tumour-associated macrophages (TAMs) induce a type 1 immune response whereas M2 type TAMs have an immune-suppressive effect and promote tumour progression. In skin cancers, M2 type macrophages are one of the main immune subsets within tumours. They are thought to maintain an immunosuppressive tumour microenvironment in part through the suppression of cytotoxic ($CD8^+$) T cell proliferation(Fujimura et al., 2016). T regulatory cells (Tregs) also contribute to skin tumour immune escape, and the ratio of Tregs to $CD8^+$ T cells in the melanoma tumour microenvironment is predictive for patient survival(Jacobs et al., 2012).

The extracellular matrix (ECM) surrounding the tumour is an important structural component of the tumour microenvironment made up of polysaccharides, glycoproteins, proteoglycans and fibrous proteins such as collagens. The tumour ECM can influence immune cell recruitment, modulate cancer stem cell behaviour and act as a physical barrier to drug penetration(Nallanthighal et al., 2019). Cells within the tumour microenvironment constantly make and remodel the ECM by releasing matrix degrading proteases and growth factors, thus influencing tumour progression. Aberrant degradation of the tumour ECM and basement membranes by matrix metalloproteinases (MMPs) facilitates angiogenesis, invasion and metastasis. In skin cancer biology, it is postulated that differential expression of MMPs may influence the generally non-invasive phenotype of basal cell carcinoma (BCC) and the relatively higher metastatic potential of squamous cell carcinoma (SCC)(Kerkelä and Saarialho-Kere, 2003). In melanoma, the vertical growth phase that culminates in lethal metastatic disease is characterised by a loss of E-cadherin expression and induction of MMP2, which degrades the basement membrane and permits tumour expansion through the dermis.

Methods such as magnetic cell separation and fluorescence-activated cell sorting (FACS) can be used to isolate and study a specific population of cells within a heterogeneous mixture like the tumour microenvironment. Immune cell isolation refers to methods that use antibody recognition of cell-surface antigens to enrich a specific subset of immune cells, followed by a separation technique like FACS. CD45 is a commonly used marker for bulk immune cell isolation, as it is expressed on the surface of all cells of hematopoietic lineage(Woodford-Thomas and Thomas, 1993, Antignano et al., 2020). In silico methods to parse the immune context of the tumour

microenvironment include the deconvolution of gene expression data using the webtool CIBERSORTx and xCell, which uses a combination of deconvolution and gene set enrichment to determine cellular subsets(Aran et al., 2017, Steen et al., 2020). To better understand the CCS tumour microenvironment, in this project I use a CD45 immune cell isolation method to separate infiltrating immune cells and CCS tumour keratinocytes with flow cytometry followed by transcriptomic profiling of both cell populations with RNA-seq. This novel approach allowed me to investigate deregulated NF-κB signalling in purified CYLD-defective tumour keratinocytes and use bioinformatics tools to interrogate the tumour infiltrating leukocytes (TILs) within the CCS tumour microenvironment.

1.8 Genomics, transcriptomics and methylomics

Comprehensive profiling of genomic, transcriptomic and epigenomic changes in tumours is fundamental to understanding cancer(Manzoni et al., 2018). Using next generation technologies, it is now possible to acquire omics data at multiple levels to investigate mechanisms of tumourigenesis. In this project we try to leverage these technologies in a rare condition to uncover DNA, RNA and methylation changes in CCS tumour cells to discover potential oncogenic dependencies.

Next-generation sequencing (NGS) methods involve the alignment of fragmented and sequenced genomic DNA to a reference genome(van Dijk et al., 2014). Whole genome sequencing (WGS) allows the identification of novel single nucleotide variants, large and small insertions and deletions (indels) and copy number variations (CNV) across the whole genome including non-coding regions. Whole exome sequencing (WES) provides a more targeted approach to coding regions only, where the majority of known disease-causing variants occur. Both methods have disadvantages; WGS is relatively expensive and requires intensive data processing while WES may miss disease-causing variants outside of the exome. In this project, we use both technologies to capture all genomic information from 11 tumours from 2 CCS patients and screen the exomes of 31 tumours from 13 patients.

NGS methods have also revolutionised the field of transcriptomics(Wang et al., 2009). Unlike RNA-microarray technology, RNA-sequencing (RNA-seq) does not require previous knowledge of the genome. After mRNA is isolated and converted to

cDNA, it is fragmented and sequenced before alignment to a reference sequence. Using this method, it is possible to detect and quantify both known and novel transcripts and novel splice isoforms across the entire transcriptome. Although RNA sequenced from bulk tissue may be contaminated with different cell types, single cell RNA-seq (scRNA-seq) technology is now widely used to overcome this disadvantage. In this project, we use RNA-seq to investigate differential gene expression between bulk CCS tumour samples and perilesional skin or healthy normal skin and the alternative splicing of genes of interest. In addition, RNA-seq was used to analyse the transcriptomes of CCS tumour and normal skin samples separated by FACS into purified populations of $CD45^+$ immune cells and $CD45^-$ keratinocytes.

Epigenetic mechanisms, such as DNA methylation, histone modifications and nucleosome positioning, regulate gene expression in cells without changing the underlying DNA sequence. DNA methylation involves the addition of a methyl group (CH_3) by a DNA methyltransferase enzyme to the carbon 5 position of the cytosine nucleotide (5-meC). In eukaryotes, this occurs at cytosine-phosphate-guanine dinucleotides (CpGs) at promoters, where CpGs cluster in ‘islands’, CpG island ‘shores’ which are located up to 2 kb upstream of CpG islands, within gene bodies and at repetitive sequences (Portela and Esteller, 2010). Methylation of CpG islands and shores is associated with gene silencing, while methylation at gene bodies facilitates transcription. Aberrant DNA methylation leads to disease due to dysregulated gene expression and is a well-known feature of cancer(Das and Singal, 2004).

Whole-genome bisulphite sequencing (WGBS), where the whole genome is sequenced after sodium bisulphite conversion of unmethylated cytosines to uracil, is the gold standard in methylomic profiling(Stirzaker et al., 2014). However, like WGS, WGBS is costly and requires intensive data processing. Illumina Infinium BeadChips are a cost-effective alternative that use probes on a microarray after sodium bisulphite DNA conversion to genotype targeted CpG sites. The Illumina EPIC methylation array platform supersedes the HumanMethylation450 (HM450) BeadChip and covers >850,000 CpG sites, including >350,000 CpGs at enhancers and distal regulatory elements(Pidsley et al., 2016). We use this technology to analyse methylation patterns of eight CCS tumour samples genotyped for somatic

mutations in the methyl transferase gene *DNMT3A*, to assess the impact of these mutations on the CCS tumour methylome.

1.9 Small molecule inhibitors

The two main approaches for targeted drug therapies are small molecule inhibitors and monoclonal antibodies (mAbs)(Imai and Takaoka, 2006). mAbs are relatively large proteins that target extracellular molecules such as ligands and receptors while small molecule inhibitors can cross the plasma membrane and target any molecule within a cell. Given that dysregulated NF-κB signalling is a feature of multiple chronic inflammatory diseases and cancer, small molecule inhibitors have been designed to target both the canonical and non-canonical pathways at multiple levels(Ramadass et al., 2020). While mAbs targeting the NF-κB ligand TNF have been approved for the treatment of psoriasis, arthritis and other inflammatory diseases, no small molecule inhibitors targeting TNFR have passed the preclinical stage. NF-κB small molecule inhibitors that target Toll like receptors (TLR)s, the adaptor protein Bruton tyrosine kinase, cIAP1/2/XIAP and IRAK have successfully entered clinical trials. No pan-IKK or selective IKKβ inhibitors have passed phase 2 clinical trials due to problems with toxicity and there are doubts as to the safety of long-term inhibition of IKKβ(Baud and Karin, 2009, Ramadass et al., 2020).

Small molecule inhibitors of the proteasome are not specific to NF-κB but inhibit NF-κB signalling by blocking degradation of IκBα and partial p100 processing. A number of these have been approved for clinical use (Disulfiram, Bortezomib, Ixazomib and Carfilzomib). Other small molecule NF-κB targets include selective inhibitors of nuclear export, DNA binding and NF-κB transcriptional activation. A range of NF-κB small molecule inhibitors that are not in clinic, including NIK inhibitors, are available as research tools. A selection of commercially available small molecule inhibitors targeting NF-κB for research purposes is given in Table 1-1.

Table 1-1. Commercially available NF-κB small molecule inhibitors from Abcam.
Adapted from https://www.abcam.com/reagents/nf-kb-small-molecule-guide.

Classification	Small molecule	Activity
IKK complex inhibitor	TPCA-1	IKKβ inhibitor that blocks IκB degradation and IL-8 expression

	NF-κB Activation Inhibitor VI (BOT-64)	IKKβ inhibitor and suppressor of NOS, COX-2, IL-1β, IL-6 expression
	BMS 345541	Dual IKK inhibitor
	Amlexanox	IKKε and TBK-1 inhibitor with therapeutic uses
	SC-514 (GK 01140)	Selective, reversible and ATP competitive IKKβ inhibitor
	IMD 0354	Potent, selective, IKKβ inhibitor
	IKK-16	Potent, selective IKK inhibitor and suppressor of NOS expression
IκB degradation inhibitor	BAY 11-7082	Inhibits ubiquitin conjugating ligases
	MG-115 & MG-132	Potent, reversible proteasome inhibitor disrupts RANKL signaling
	Lactacystin & Epoxomicin	Potent, irreversible, selective 20S proteasome inhibitor
	Parthenolide	Inhibits IκBα degradation and IKK complex activity
	Carfilzomib	Potent, irreversible 26S proteasome inhibitor
	MLN-4924 (Pevonedistat)	Modulates a ubiquitin-like protein (Nedd-8) activating enzyme
NF-κB nuclear translocation inhibitor	JSH-23	Exhibits translocation inhibition in vivo and in LPS-induced RAW264.7 cells
	Rolipram	Exhibits translocation inhibition in LPS-induced chorionic cells
p65 acetylation inhibitor	Gallic acid	Prevents p65 acetylation in LPS-induced A549 cells
	Anacardic acid	Inhibits p65 acetylation in TNF-induced KBM-5 cells (at 4 μM)
NF-κB-DNA binding	GYY 4137	Reduces NF-κB binding to RANTES and IL-8 promoter
	p-XSC	Inhibits NF-κB binding by covalent modification of p50 Cys62
	CV 3988	PAFR antagonist that inhibits p65 DNA binding
	Prostaglandin E2 (PGE2)	Dissociates nuclear trafficking of p50-p65 subunits

NF-κB transactivation inhibitor	LY 294002 & Wortmannin	Blocks NF-κB-dependent transactivation following IL-1 stimulation
	Mesalamine	Blocks p65-dependent transactivation
p53 induction	Quinacrine	Downregulates NF-κB and downstream transcriptional targets
	Flavopiridol	Inhibits TNFα-induced NF-κB activation

In this project, I use novel selective IKKα small molecule inhibitors as well as commercially available pan-IKK and IKKβ inhibitors to therapeutically target canonical and non-canonical NF-κB signalling in a preclinical patient-derived CCS tumour spheroid model. Selective targeting of IKKα in tumours with an oncogenic dependency on non-canonical NF-κB signalling may overcome some of the toxicities associated with IKKβ inhibition. An advantage of this project is that topical application to the skin is available as a route to drug administration. The effects of cutaneous topical application are local and therefore predicted to avoid systemic side effects. The Rajan laboratory has previously carried an early-phase exploratory trial of a topically applied TRK inhibitor (pegcantratinib) to CCS tumours and demonstrated drug penetration by molecular analysis of biopsy material(Danilenko et al., 2018, Danilenko et al., 2019). The preclinical data obtained in this study may therefore have future translational relevance for the targeted treatment of CYLD cutaneous syndrome.

1.10 Research aims and objectives

A non-invasive targeted therapy is urgently needed for CYLD cutaneous syndrome (CCS). Although CYLD deficiency has been studied extensively in vitro and in murine models, studies in patient derived tumours are lacking. The expression of NF-κB subunits in patient derived CCS tumours has not been characterised to date. Furthermore, effects of CYLD deficiency on the non-canonical NF-κB pathway have not been fully investigated.

The aims of this project were firstly to establish the genetic landscape of tumours in CCS using genomic, transcriptomic and methylomic analyses. Secondly, I aimed to characterise NF-κB signaling in CCS tumour cells using a CD45 cell isolation method

to separate the mixed populations of tumour keratinocytes and tumour infiltrating leukocytes found in fresh tumour tissue. Finally, I aimed to develop a patient derived CCS tumour spheroid model in which to validate tumour specific changes in NF-κB target gene expression and explore the therapeutic potential of novel small molecule IKKα inhibitors.

Chapter 2. Materials and Methods

2.1 Ethical approval

Patient samples used in this study were obtained with signed, informed consent. Ethical approval was obtained from the North East – Newcastle and North Tyneside 1 Research Ethics Committee (REC Ref: 06/Q1001/59) and the Hartlepool Research Ethics Committee (REC Ref: 08/H0906/95 + 5).

2.2 Cell culture experiments

2.2.1 CCS tumour primary cell culture

Fresh tumours were collected in complete Dulbecco's modified eagle medium (DMEM)/10% fetal bovine serum (FBS) immediately after surgery, transported to a class II cell culture hood, cut up into ~1mm^3 pieces in 6 cm petri dishes and transferred into 15 ml falcon tubes. One T75 flask per tumour was coated with collagen (R011K Gibco) and incubated at room temperature during sample preparation. After centrifugation at 900 x g and decanting the supernatant, tumours were digested in 5 ml 2.5% trypsin for 40 minutes in a 37°C water bath with gentle manual agitation every 20 minutes. Tumours were centrifuged at 900 x g to allow aspiration of 3 ml trypsin. The soft pellets were incubated in 5 ml collagenase (1 mg/ml) for 70 minutes in a 37°C water bath with gentle manual agitation every 20 minutes. The dissociated tumours in 7 ml trypsin/collagenase were transferred to 50 ml falcons and 3 volumes of DMEM added (21 ml) before filtering at 40 um into new 50 ml falcon tubes. From the 28 ml cell suspension, 7 ml was taken in a 15 ml falcon, centrifuged at 900 x g, resuspended in complete defined keratinocyte serum free medium (KSFM Gibco 10744019)/0.2% penicillin-streptomycin (5000 U/ml)/1% L-glutamine (200 mM)/0.04% Amphotericin B (250 µg/ml) and seeded in a collagen coated T75 flask. The remaining suspension was centrifuged at 1100 x g for 8 minutes, resuspended in 3 ml 10% dimethyl sulfoxide (DMSO)/FBS and cryopreserved in 1 ml aliquots at -80°C. Cells in culture were maintained in complete KSFM supplemented with 10 µM rho kinase inhibitor (Y-27632 Tocris) and passaged when ~80% confluent.

2.2.2 Normal skin primary cell culture

Immediately after surgery for non-CCS related conditions, donated skin was collected in complete DMEM with Dispase II (final concentration 1 U/ml) and incubated on a roller at 4°C overnight. One T25 flask per sample was coated with collagen (R011K Gibco) and incubated at room temperature during sample preparation. The epidermis was peeled from the dermis with fine forceps, transferred to a 15 ml falcon tube containing 5 ml 0.05% Trypsin-EDTA and incubated for 30 minutes in a 37°C water bath with gentle agitation by pipetting up and down every 15 minutes. After adding 5 ml complete DMEM and centrifugation at 300 x g for 5 minutes, the supernatant was aspirated and the pellet resuspended in complete Epilife medium (Gibco MEPI500CA))/0.2% penicillin-streptomycin (5000 U/ml)/1% L-glutamine (200 mM)/0.04% Amphotericin B (250 µg/ml). Cells were seeded onto a collagen coated T25 and passaged when 80% confluent. Cells were maintained in complete Epilife supplemented with 10 µM rho kinase inhibitor (Y-27632 Tocris). Stock vials were cryopreserved at passage 3 in 10%DMSO/FBS.

2.2.3 Keratinocyte cell line culture

HaCaT and CCD1106 human keratinocyte cell lines were cultured in complete Epilife (Gibco MEPI500CA) and complete Defined KSFM (Gibco 10744019) supplemented with 30 ng/ml epidermal growth factor (Peprotech AF-100-15), respectively.

2.2.4 2D Cell passage and harvesting for protein

Cell were passaged by washing once with 1X phosphate-buffered saline (PBS), incubating in versene (Gibco 15040-066) at 37°C for 5 minutes then incubating in 0.05% Trypsin-EDTA at 37°C until dissociated. After quenching with complete DMEM, cells were centrifuged at 900 x g and resuspended in 1 ml 1X PBS. Flasks were reseeded with 20% of the cell suspension per T75 and the remaining cells were transferred to an Eppendorf and centrifuged at 17,000 x g. The supernatant was completely aspirated, and pellets were frozen on dry ice immediately and stored at -80°C for downstream protein extraction.

2.2.5 IKK inhibition of 2D primary cells

Cells were grown in 6 well plates until confluent then incubated with small molecule IKK inhibitors at the concentrations shown in Table 2-1 for 24 hours. DMSO was added to a control well at the same volume as TPCA-1 and BMS345541. Concentrations of the inhibitors were derived from CCS spheroid dose-response assay generated IC_{50}s (see section 2.2.11).

Table 2-1. Concentrations of small molecule IKK inhibitors used in 2D primary cell assays. IC_{50} values were determined by spheroid dose response assays.

Well	Treatment	IC_{50} (µM)	Concentration (µM)
1	DMSO	N/A	N/A
2	TPCA-1	5.8	6
3	BMS345541	5.6	6
4	Compound Y	1.3	1
5	Compound Z	2.7	2
6	Compound Z	2.7	3

Cells were harvested by washing once with 1XPBS and adding 40 µl 8M Urea lysis buffer (8M Urea, 50 mM Tris pH 8, 300 mM NaCl, 50 mM Na2HPO4, 0.5% NP-40) to the middle of each well. Cells were scraped, collected into Eppendorf tubes and centrifuged at 4°C for 5 minutes at 20,000 x g. Samples were sonicated for 3 x 15 seconds at 30% amplitude then centrifuged at 20,000 x g for 10 minutes at 4°C to pellet cell debris. The supernatant was transferred to a new Eppendorf and protein concentration was measured with the Pierce™ BCA protein assay kit (Thermo Fisher Scientific).

The BCA assay is a colourimetric assay where addition of bicinchoninic acid (BCA) to protein in an alkaline environment containing sodium potassium tartrate results in a measurable colour change from light blue to purple. The BCA reaction has a linear absorbance at 562 nm with increasing protein concentrations. Bovine serum albumin

(BSA) protein standards in 8M Urea lysis buffer at known concentrations (0, 0.25, 0.5, 1, 1.5 and 2 µg/µl) were used to generate a standard curve from which the protein concentrations of samples could be interpolated. In a 96 well plate, 2 µl BSA standard or sample were incubated with 100 µl BCA reagent working solution for 30 minutes at 37°C. Absorbance at 562 nm was recorded with a Varioskan™ LUX microplate reader and a linear regression line was generated in Microsoft excel by plotting the absorbance of each BSA standard on the Y-axis against its known concentration on the X-axis. The equation y=mx+c was rearranged to solve for x (x=(y-c)/m), where x is estimated protein concentration, y is the measured absorbance of the sample and m and c are calculated by Microsoft excel from the linear regression line.

2.2.6 EDA-A1 stimulation of 2D primary cells

The same 6 well plate method described above for IKK inhibition was used to stimulate 2D primary cells with recombinant EDA-A1 (R&D Systems 3944-ED-010) at 0, 10, 25, 50, 75 and 100 ng/ml for 24 hours and harvest protein for analysis by immunoblot. This 6 well plate assay was also used to stimulate cells with 10 ng/ml recombinant Eda-A1 and harvest each well at different time points (0, 2, 4, 8, 24 and 48 hours).

2.2.7 Spheroid primary cell culture

Aggrewell400™ 6 well plates containing 7000 microwells per well (Stemcell Technologies) were prepared with 2 ml/well anti-adherence rinsing solution (Stemcell Technologies 07010), centrifuged at 1300 x g for 5 minutes and rinsed with warm cell culture medium (complete KSFM for CCS primary cells or complete Epilife for normal primary cells). Cell culture medium supplemented with 1.5 mM $CaCl_2$ and 10 µM rho kinase inhibitor (ROCKi) was added at 2 ml/well.

Two confluent T75 flasks of 2D primary cells from the same tumour or normal skin sample were trypsinised as previously described, pooled together and counted in 6 ml media/1.5 mM $CaCl_2$/10 µM ROCKi. One ml of cell suspension was added to each Aggrewell and gently mixed by pipetting. After centrifuging the Aggrewell plate at 100 x g for 3 minutes, wells were topped up to 5 ml with media/1.5 mM $CaCl_2$/10 µM

ROCKi. Media was changed at 48 hours by aspirating and replacing 2.5 ml media/1.5 mM $CaCl_2$.

2.2.8 Harvesting spheroids for protein

At day 4, 2.5 ml media was removed per well of the 6 well Agrewell400™ plate and the remaining media pipetted firmly up and down to dislodge the spheroids from the microwells. The media from all 6 wells containing the spheroids was passed through a 40 um cell strainer over a 50 ml falcon to remove single cells. Cell culture medium (1 ml) supplemented with 1.5 mM $CaCl_2$ and 5 mM EDTA was used to wash each well twice and each wash was passed through the filter. The filter was then turned upside down over a new falcon tube and spheroids were recovered by rinsing the filter with 5 ml media/1.5 mM $CaCl_2$/5 mM EDTA. The spheroid suspension was decanted into a 15 ml falcon, centrifuged at 2000 x g for 5 minutes and the media completely aspirated. The spheroid pellet was frozen immediately on dry ice and stored at -80°C for downstream protein extraction.

2.2.9 EDA-A1 stimulation and IKK inhibition of spheroids

Aggrewell400™ 6 well plates were seeded as described above. At day 4, recombinant EDA-A1 (100 ng/ml) or Compound Z (3 μM) was added to the bottom 3 wells of the plate. An equivalent amount of DMSO (Compound Z plates) or PBS (EDA-A1 plates) was added to the top 3 control wells of the plate.

After 24 hours incubation, cells were harvested by pooling the three control wells and the three treated wells separately, as described above, but with an added RNA recovery step. Before decanting the spheroid suspension into a 15 ml falcon tube, 1 ml of the suspension was transferred to an Eppendorf, centrifuged at 17,000 x g for 5 minutes. After complete aspiration of the media, the pellet was frozen immediately on dry ice for downstream RNA extraction. RNA was extracted with the RNeasy Micro Kit (Qiagen 74004) following the manufacturer's protocol. RNA was quantified with the Qubit™ RNA High Sensitivity Assay Kit (Thermo Fisher Scientific Q32852) following the manufacturer's protocol and measured with the Qubit™ Fluorometer.

2.2.10 TaqMan™ gene expression assay (RT-qPCR)

TaqMan Gene Expression Assays contain a pair of forward and reverse primers and a probe labelled with a fluorescent reporter dye (FAM or VIC) at the 5' end and a non-fluorescent quencher (NFQ) at the 3' end. During qPCR thermal cycling, when the cDNA template double-strand is denatured, the probe reporter signal is quenched by the NFQ. When the temperature is lowered, the primers and probe anneal to the target gene of interest on the separated single cDNA strands. During the extension step, Taq DNA polymerase synthesises new a new complementary DNA strand from the template until it reaches the bound TaqMan probe. Here, it cleaves the reporter dye from the quencher with its endogenous 5' nuclease activity. A fluorescent signal is therefore generated that is proportional to the amount of amplified qPCR product.

cDNA was generated from CCS spheroid RNA with the High-Capacity cDNA Reverse Transcription Kit (Applied Biosystems 4368814). To increase the volume of cDNA samples and enable more RT-qPCR experiments, the TaqMan PreAmp Master Mix Kit (Applied Biosystems 4391128) was used. All sets of TaqMan primers/probes in Table 2-2 were pooled in a total volume of 500 µl at a final concentration of 0.2X in ATE buffer. A preamplification reaction was prepared for each sample (see Table 2-3) and the PCR was run with the thermal cycling conditions in Table 2-4.

Table 2-2. TaqMan primer/probe IDs.

Gene	TaqMan probe ID
EDAR	Hs00223468_m1
KREMEN2	Hs00225867_m1
SOX21	Hs01072517_s1
COL22A1	Hs01377218_m1
GAPDH	Hs03929097_g1

Table 2-3. TaqMan preamplification reaction components.

Component	Volume per reaction	Final concentration
TaqMan PreAmp Master Mix (2X)	10 µl	1X
Pooled primer mix (0.2X each assay)	5 µl	0.05X (each assay)
1 – 250 ng cDNA sample + nuclease-free water	5 µl	0.02 – 5 ng/µl
Total	20 µl	

Table 2-4. TaqMan preamplification reaction thermal cycling conditions.

Step	Temperature	Time	Cycles
Enzyme activation	95°C	10 minutes	Hold
Denature	95°C	15 seconds	10
Anneal/Extend	60°C	4 minutes	
Enzyme inactivation	99°C	10 minutes	Hold

The preamplification products were diluted 1:5 in ATE buffer to a final volume of 100 µl. A master mix was prepared for each TaqMan primer/probe set with TaqMan Gene Expression Master Mix according to Table 2-5 at a sufficient volume to allow reactions to be run in quadruplicate for each sample and probe/primer pair at a final volume of 10 µl per well in a 384 well plate. The plate was sealed and centrifuged at 100 x g for 3 minutes to eliminate bubbles, then run on a QuantStudio 7 Flex System

(Applied Biosystems) with QuantStudio 6 and 7 Flex Real Time PCR System Software v1.0 at the conditions shown in Table 2-6.

Table 2-5. Reaction components for 384-well TaqMan Gene Expression Assay RT-qPCR

Component	Volume per well
TaqMan Gene Expression Master Mix (2X)	5 µl
TaqMan Gene Expression Assay primer and probe (20X)	0.5 µl
Pre-amplified cDNA (diluted 1:5)	2.5 µl
Nuclease free water	2
Total	10 µl

Table 2-6. TaqMan Gene Expression Assay RT-qPCR thermal cycling conditions.

Step	Temperature	Time	Cycles
Uracil-DNA glycosylase (UDG) incubation	50°C	2 minutes	1
AmpliTaq Gold DNA polymerase activation	95°C	10 minutes	1
Denature	95°C	15 seconds	40
Anneal/Extend	60°C	1 minute	

2.2.11 Spheroid dose response assay

Adherent primary cells were detached from T75 flasks when confluent with versene and trypsin as previously described. 96 well spheroid microplates (Corning 4520) were seeded at 30,000 cells per well in 280 µl complete KSFM or Epilife supplemented with 1.5 mM $CaCl_2$. Media was changed after 24 and 72 hours and cells were drugged after one week in culture (see Table 2-7). Each drug concentration was replicated in 3 wells. After 72 hours incubation with the inhibitor, cell viability was assessed with the CellTiter-Glo® Luminescent Cell Viability Assay (Promega). Addition of the CellTiter-Glo® reagent results in cell lysis and the generation of a luminescent signal proportional to quantity of ATP present, which is directly proportional to the number of metabolically active cells. Luminescence was recorded with the Varioskan™ LUX microplate reader. This protocol was shortened

for Compound Z to addition of the inhibitor at day 3 and cell viability assay after 48 hours incubation with the inhibitor. Dose response curves were generated using GraphPad PRISM version 9. Data was normalised and curves were constrained to a constant value of 0.0 at the bottom and 100.0 at the top.

Table 2-7. Concentrations of small molecule IKK inhibitors in spheroid dose-response assays. Inhibitors were added to spheroids at 10 concentrations in 10 wells of a 96 well plate. TPCA-1 (2559) and BMS345541 (4806/10) were purchased from Tocris. Compounds X, Y and Z were provided by Prof. Simon Mackay, Strathclyde University.

Well	Small molecule IKK inhibitor concentrations per well (μM)				
	TPCA-1	BMS345541*	Compound X	Compound Y	Compound Z
1	0	0	0	0	0
2	0.1	3	0.1	0.1	0.1
3	0.3	6	0.3	0.3	0.3
4	1	8	1	1	1
5	3	10	3	3	3
6	6	12	6	6	6
7	10	14	10	10	10
8	18	16	18	18	18
9	33	18	25	25	25
10	66	25	33	33	33

* Based on the steep dose response curves initially obtained for BMS345541 using the same concentrations as TPCA-1, concentrations of this inhibitor were amended.

2.2.12 Lentiviral mediated shRNA knockdown of CYLD

Lentivirus packaging and production was carried out by Dr Naomi Sinclair and Dr Neil Rajan using the Trans-Lentiviral packaging mix (Open Biosystems). This process involved using lentiviral vectors to deliver pGIPz short hairpin RNA (shRNA) vectors targeting *CYLD* (shCyl1 and shCyl2) to HEK293T packaging cells (Figure 2-1). As empty vector or non-silencing shRNA vector controls were not available, non-*CYLD* targeting shRNA vectors against *DKK2*, *NTRK2*, *NTRK3* and *PLK1* (that would not be predicted to affect *CYLD* expression) were used as controls. A liposomal transfection technique was used to transfect the HEK293T cells in serum-free DMEM, with media changed to complete DMEM the next day. Cells were cultured for

a further 48 hours before lentiviral particle-containing media was harvested, filtered at 0.45 µm, aliquoted and stored at -80°C.

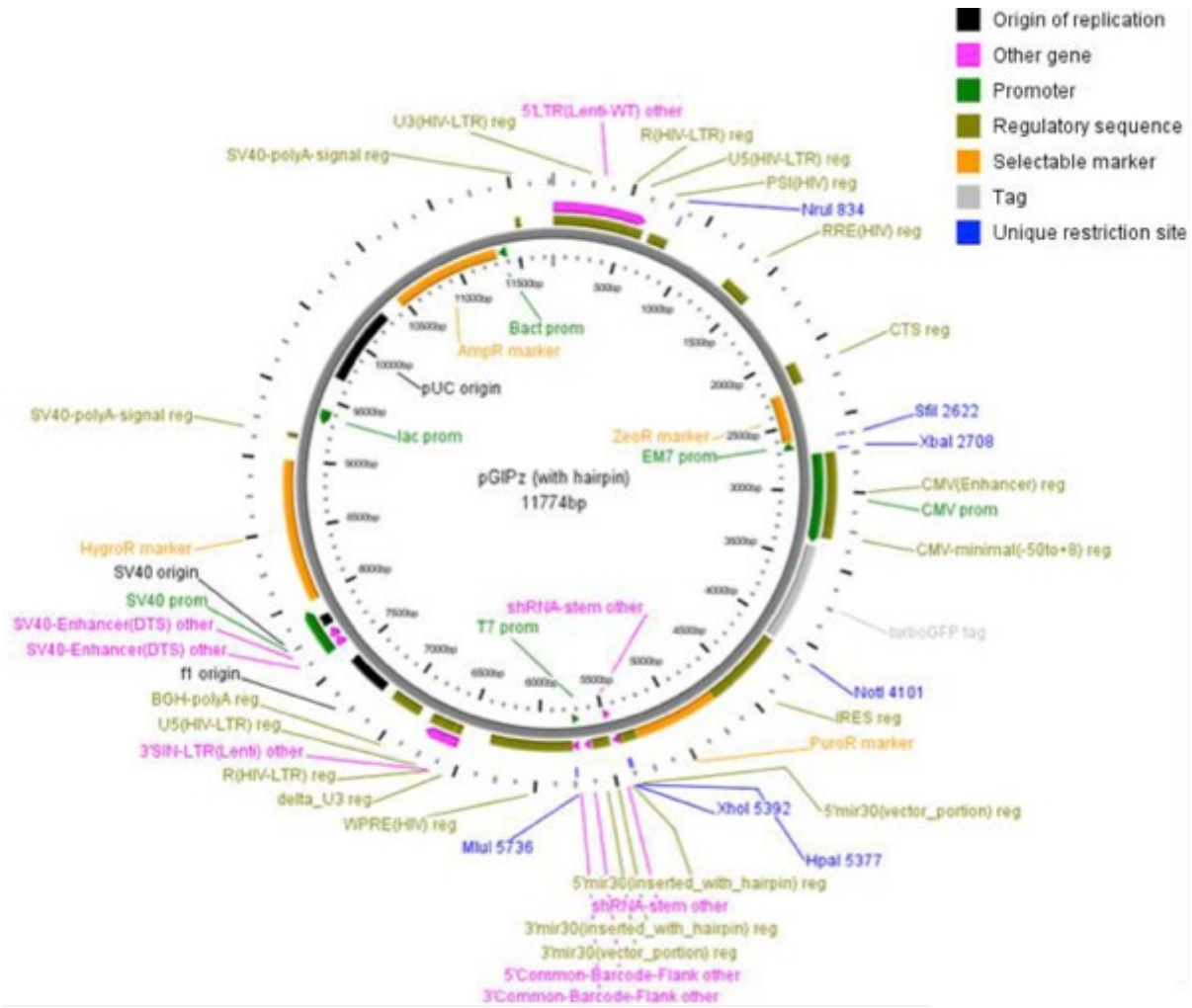

Figure 2-1. The pGIPz vector used for lentiviral mediated knockdown of *CYLD* in CCS primary cells. pGIPz vectors (Open Biosystems) have a Turbo GFP marker to track shRNAmir expression and puromycin resistance to allow selection. shRNA (shRNAmir) expression is under the control of the cytomegalovirus immediate-early (CMV) promoter.

CCS primary cells or normal skin primary cells were seeded at a density of 0.7 x 10^6 in two collagen coated T25 flasks; one to be transduced with shRNA targeting *CYLD* and the other with a non-*CYLD* targeting shRNA control. When 50 – 70% confluent, cells were transduced with 3 ml media containing lentiviral particles and 4 µg/ml polybrene for 24 hours then flasks were topped up with 4 ml complete KSFM or Epilife without decanting the lentiviral particles. At 48 hours, the lentiviral particles were replaced with fresh complete KSFM/Epilife. From 72 hours, puromycin (3 µg/ml) selection was used to obtain successfully transduced cells expressing GFP. Cells

were harvested with trypsin when confluent as previously described, and pellets stored at -80°C for downstream protein extraction.

2.3 Protein extraction

Tissue curls were cut at 30 µm on a cryostat from snap frozen CCS tumour or normal skin. Tissue was lysed in 150 µl Novagen's PhosphoSafe™ Extraction Reagent (EMD Millipore) or 8M Urea lysis buffer (8M Urea, 50 mM Tris pH 8, 300 mM NaCl, 50 mM Na2HPO4, 0.5% NP-40) and homogenised in Precellys® CK Mix 2 ml bead tubes. Samples were centrifuged in the bead tubes at 4°C 15,000 x g for 5 minutes to reduce bubbles then transferred to Eppendorf tubes. After centrifuging again at 4°C for 15 minutes at 15,000 x g, samples were sonicated 3 times for 15 seconds at 30% amplitude. Samples were centrifuged a final time at 4°C for 20 minutes at 15,000 x g then the supernatant containing protein was transferred to a new Eppendorf tube and the pellet discarded.

Protein was extracted from spheroid and 2D cell pellets by sonication for 3 x 15 seconds at 30% amplitude in 40 – 100 µl 8M Urea lysis buffer. Concentration was measured with the Pierce™ BCA protein assay kit as previously described.

2.4 Immunoblotting

Samples were prepared with 1X NuPAGE™ lithium dodecyl sulphate (LDS) loading buffer and dithioreitol (DTT) sample reducing agent (Invitrogen) at a concentration of 10 µg protein in 20 µl. Samples were heated at 70°C for 10 minutes, loaded on NuPAGE Tris-Acetate or Bis-Tris precast gels in the appropriate running buffer (NuPAGE Tris-Acetate, MES or MOPS sodium dodecyl sulphate (SDS) running buffer, Invitrogen) and separated with the NuPAGE gel electrophoresis system before transfer onto PVDF membranes with the Bio-Rad Transblot Turbo semi-dry transfer system. PVDF membranes were blocked in 1X Tris buffered saline with Tween 20 detergent (TBST) (20 mM Tris pH 7.6, 120 mM NaCl, 0.1% Tween 20) with 5% fat-free milk or 3% BSA for 1 hour, incubated in primary antibody overnight at 4°C and secondary antibody conjugated to horseradish peroxidase (HRP) (Cell signalling) or a fluorescent dye for 1 hour at room temperature (see Table 2-8 for antibodies). Washes between incubations were performed in 1X TBST for 3 x 10 minutes. HRP enzyme activity was detected with enhanced chemiluminescent (ECL)

substrate. Fluorescence was detected with the LICOR Odyssey® CLx imaging system.

Table 2-8. Antibodies used for immunoblotting. CST, Cell Signaling Technology; Thermo, ThermoFisher Scientific; Phospho, phosphorylated.

Antibody	Supplier	Cat. No.	Dilution
RelA	CST	4764	1:1000
Phospho RelA serine 536	CST	3031S	1:1000
RelB	CST	4954	1:1000
c-Rel	CST	67489	1:1000
p100/p52	CST	3017	1:1000
Phospho p100 serine 866	Abcam	Ab194919	1:500
Phospho p100 serines 866/870	CST	4810	1:1000
p105/p50	05-361	Millipore	1:1000
CYLD	CST	12797	1:1000
CYLD	CST	8462	1:1000
CYLD	Abcam	Ab137524	1:1000
IκBα	CST	9242	1:1000
Phospho IκBα serines 32/36	CST	9246	1:1000
EDAR	Protein Tech	18032-1-AP	1:1000
TNFRSF18 (syn. GITR)	CST	10419S	1:1000
KREMEN2	Abcam	Ab156007	1:1000
WNT10B	Abcam	Ab70816	1:500
Cleaved CASPASE 3	CST	9661	1:1000
GAPDH (mouse)	CST	97166	1:1000
GAPDH (rabbit)	CST	2118	1:1000
Secondary antibodies			
Goat anti-rabbit HRP linked	CST	7074	1:5000

Horse anti-mouse HRP linked	CST	7076	1:5000
IRDye® 680RD donkey anti-mouse	LI-COR	925-68072	1:5000
Alexa Fluor® 790 donkey anti-rabbit	Thermo	A11374	1:5000

2.5 Immunofluorescence

Tissue sections from snap frozen skin tumours were fixed in ice cold methanol for 10 minutes, washed in 1X PBS for 3 x 10 minutes, washed in 30% sucrose/PBS for 30 minutes then blocked in 0.3% Triton X-100/0.5% BSA/PBS for 1 hour at room temperature. Immunofluorescent labelling with primary antibodies against CYLD, CK14, CK17, CK18, CK77, DNMT3A, β-catenin and Ki67 was performed overnight at 4°C (see Table 2-9 for antibody details). The following day, sections were washed in 0.1% Triton X-100/0.2% BSA/PBS for 3 x 10 minutes. DAPI (4′,6-diamidino-2-phenylindole) nuclear stain (final concentration 0.1 µg/ml) and secondary fluorescent antibodies were applied for 1 hour at room temperature in the dark. After washing 3 x 10 minutes in 0.1% Triton X-100/0.2% BSA/PBS, coverslips were mounted with ProLong Gold Antifade (Thermofisher Scientific) and images were taken with a fluorescent microscope (Zeiss Axioimager Z2, with Apotome 2 – Carl Zeiss).

Table 2-9. Antibodies used for immunofluorescence. CST, Cell Signaling Technology; BDT, BD Transduction; Jackson, Jackson ImmunoResearch. The CYLD antibody was gifted by Prof. Ramin Massoumi, the CK77 antibody was gifted by Dr Lutz Langbein.

Antibody	Supplier	Cat. No.	Dilution
Primary antibodies			
CYLD	Gifted		1:500
CK14	Abcam	Ab7800	1:800
CK17	Abcam	Ab19067	1:100
CK18	Abcam	Ab668	1:200
CK77	Gifted		1:200
DNMT3A	CST	3598	1:50

β-catenin	BDT	610153	1:50
Ki67	CST	9449	1:400
Secondary antibodies			
Alexa Fluor® 488 goat anti-rabbit	Jackson	111-545-144	1:200
Alexa Fluor® 594 goat anti-mouse	Jackson	115-585-146	1:400
Alexa Fluor® 594 donkey anti-guinea pig	Jackson	706-585-148	1:400

2.6 Fluorescence activated cell sorting

Tissue was cut into 1 mm^3 pieces and digested by incubation in 1.5 mg/ml collagenase (Sigma C1889) for 2 hours at 37°C with gentle agitation by pipetting every 20 minutes. 2000U/µl DNase I (Sigma 10104159001) was added after one hour. After resuspension in flow buffer (1X PBS, 5mM EDTA, 2% FBS) and filtering at 40µm, cells were centrifuged at 900 x g for 5 minutes and the supernatant aspirated. Blood cells were removed by resuspending the pellet in 1X Red blood cell lysis buffer (Abcam ab204733) and incubating at room temperature for 10 minutes. Remaining cells were centrifuged at 900 x g for 5 minutes, resuspended in 2 ml flow buffer and counted. 500 µl was taken from each sample for the RNA-seq input fraction and kept on ice. The remaining cell suspension was centrifuged at 900 x g for 5 minutes and the flow buffer aspirated leaving 50 – 100 µl covering the pellet. Cells were resuspended and stained with CD45 antibody conjugated to fluorescein isothiocyanate (FITC) (Thermo Fisher 11-9459-42) at 5µl/10^5 - 10^8 cells in the dark at 4°C for 30 minutes. During this incubation, the input fractions were centrifuged at 20,000 x g for 3 minutes, resuspended in 350 µl ice cold RLT buffer from Qiagen's RNeasy Micro Kit (74004) with added 1% 2-Mercaptoethanol and frozen on dry ice. CD45 stained cells were topped up with cold flow buffer to 5 ml and centrifuged at 900 x g for 5 minutes, resuspended in flow buffer at a maximum of 1 x 10^7/ml and transferred to a FACS tube. DAPI was added at a final concentration of 3 µM immediately prior to taking the samples to the flow cytometer. Cells were sorted with the BD FACSAria™ II flow cytometer by the Newcastle University Flow Cytometry

Core Facility into 200µl neat FBS. Sorted cells were pelleted at 4°C for 3 minutes at 20,000 x g, resuspended in 350µl RLT buffer with 1% 2-Mercaptoethanol and frozen on dry ice. Samples were stored at -80°C in RLT buffer for downstream RNA extraction with the RNeasy Micro Kit (Qiagen 74004) following the manufacturer's protocol.

2.7 Polymerase Chain Reaction (PCR)

cDNA from bulk CCS tumour tissue and normal control skin was previously generated by Dr Naomi Sinclair. CYLD primers were designed with primer-BLAST in exon 9 (forward 5' CTCAGACCCTGGAAATAGAA 3') and exon 12 (reverse 5' GGCATCCAGGGTCATTACAA 3') using the *CYLD* transcript variant 1 sequence (ENST00000311559) obtained from the University of California Santa Cruz (UCSC) genome browser(Kent et al., 2002, Ye et al., 2012b). A 25 µl reaction was set up as shown in Table 2-10 for each cDNA sample and the PCR was run with the thermal cycling condition in Table 2-11. PCR products were separated by electrophoresis on 2 or 3% agarose gels for 1 hour at 100v.

Table 2-10. Reaction components for CYLD PCR with CCS tumour cDNA.

Component	Volume
MyTaq Red Mix (2X) (Bioline)	12.5 µl
Forward and reverse primer mix (20 µM each)	2 µl
cDNA template	1 µl
Nuclease free water	9.5 µl
Total	25 µl

Table 2-11. CYLD PCR thermal cycling conditions.

Step	Temperature	Time	Cycles
Initial denaturation	95°C	1 minutes	1
Denaturation	95°C	30 seconds	40
Annealing	60°C	30 seconds	
Extension	72°C	45 seconds	

2.8 Whole-genome sequencing (WGS) and whole-exome sequencing (WES)

This text is taken directly from the method section of Davies et al., 2019, on which I was second author(Davies et al., 2019). WGS and WES sample preparation was carried out by Dr Neil Rajan. WGS and WGS bioinformatic analyses were performed by Dr Helen Davies and Dr Serena Nik-Zainal at the Welcome Trust Sangar Institute and University of Cambridge.

DNA was extracted from 12 cases along with corresponding normal tissue and subjected to paired-end WGS on an Illumina HiSeq X Ten(Alexandrov et al., 2013, Nik-Zainal et al., 2016). DNA for WES was extracted from blood and cryosections of snap frozen tissue, and in five cases from formalin-fixed paraffin-embedded tissue (PD37330h, PD40536c, PD40540a, PD40545a, and PD40545c). Forty-two WES library samples were prepared using the Illumina Nextera DNA Exome Kit, prior to being sequenced on a S2 flow cell on an Illumina Novaseq machine. Three WES samples were enriched using the SureSelect Human All ExonV6 + UTR and 100 base paired-end sequencing performed on an Illumina Hiseq 2500 genome analyzers. For WES sequence depth was on average 255-fold. Resulting BAM files were aligned to the reference human genome (GRCh37) using Burrows-Wheeler Aligner, BWA-0.7.16a (r1181). Mutation calling was performed using CaVEMan (Cancer Variants through Expectation Maximization: http://cancerit.github.io/CaVEMan/) for calling somatic substitutions(Nik-Zainal et al., 2016). Indels in the tumor and normal genomes were called using a modified Pindel version 2.0 (http://cancerit.github.io/cgpPindel/) on the NCBI37 genome build. Structural variants were discovered using a bespoke algorithm, BRASS (BReakpoint AnalySiS; https://github.com/cancerit/BRASS) through discordantly mapping paired-end reads followed by de novo local assembly using Velvet to determine exact coordinates and features of breakpoint junction sequence. All mutations were annotated according to ENSEMBL version 75.

Allele-specific copy number analysis of tumors analyzed by WGS was performed using ASCAT (v2.1.1)(Nik-Zainal et al., 2016, Raine et al., 2016). ASCAT takes nonneoplastic cellular infiltration and overall tumor ploidy into consideration, to generate integer-based allele-specific copy number profiles for the tumor cells. Copy number values and estimates of aberrant tumor cell fraction provided by ASCAT

were input into the CaVEMan substitution algorithm for WGS. In addition, ASCAT segmentation profiles were used to establish the presence of LOH across CYLD and relevant mutated cancer driver genes.

Somatic mutations present in known cancer genes (Cancer gene census https://cancer.sanger.ac.uk/census) were reviewed to identify those which were likely to be driver mutations. Mutations were deemed to be potential driver mutations if they were consistent with the type of mutations found in a particular cancer gene, that is, inactivating mutations in tumor suppressor genes (including nonsense, frameshift, essential splice site mutations, and recurrent missense) and recurrent mutations in dominant oncogenes. Recurrent mutations were determined by reference to reported mutation frequency in the Catalogue of Somatic Mutations in Cancer (COSMIC) database (https://cancer.sanger.ac.uk/cosmic).

2.9 Targeted deep sequencing

This text is taken directly from the method section of Davies et al., 2019. Targeted Deep Sequencing was carried out by Dr Neil Rajan and sequencing data was provided to me for analysis.

The Truseq Myeloid panel (Illumina) was used to sequence *DNMT3A* and *BCOR* in 18 samples in accordance with the manufacturer's protocol. A 20 pM library of the PhiX genome was added to achieve a 5% PhiX spikein. This library was loaded onto a Miseq flow cell (600 cycles V3) for sequencing (Illumina, San Diego, CA, USA). Data were analyzed using BWA (v.0.7.15) to align reads to the reference sequence and Samtools used as a variant caller. Variant calls that passed strict filtering thresholds ("Filter" = PASS and "Qual" = 100) were included for the deep sequencing on sections in additional levels and in new samples.

2.10 Methylation assay and analysis

This text is taken directly from the method section of Davies et al., 2019. Dr Edward Schwalbe (Newcastle University and Northumbria University) carried out the methylation array bioinformatics analysis. I carried out the DNA and RNA extraction following the Allprep DNA/RNA/miRNA Universal Kit (Qiagen) following the

manufacturer's instructions, and analysed sequencing data for DNMT3A mutation status.

We assessed genome-wide DNA methylation in eight tumor samples with the Illumina Methylation EPIC microarray (Illumina, San Diego, CA, USA). DNA methylation assays were performed as per the standard manufacturer's protocol by MWG (Aros, Denmark). Briefly, these are eight CCS tumors in which detailed analysis was performed as follows. DNA and RNA were extracted from the same cells, and mutation status of DNMT3A and methylation profiling were performed. Methylation array processing, functional normalization(Fortin et al., 2014), and quality control checks were implemented using the R package minfi(Aryee et al., 2014). Differentially methylated probes were identified using minfi. Differentially methylated regions spanning multiple probes were identified using bumphunter(Jaffe et al., 2012); these regions were visualized using Gviz(Hahne and Ivanek, 2016). When these methylation profiles were assessed, the 500 most variably methylated probes were subject to unsupervised hierarchical clustering. The study of the 500 most variable probes is an accepted approach to help distinguish methylation profiles of tumors(Schwalbe et al., 2017). A Euclidean distance matrix was constructed and hierarchical clustering was subsequently performed using the "complete" agglomeration method. The 500 probes with the highest standard deviation were selected for visualization. This analysis demonstrated that the majority of DNMT3A2-mutant tumors clustered separately from DNMT3A2 wild-type tumors (Chapter 3, Figure 3-9). We then studied these two groups and assessed all genes related to probes that were significantly differentially methylated between these two clusters with a p value of <0.05. Network analysis of these genes using Ingenuity Pathway Analysis(Kramer et al., 2014) revealed networks of genes related by function that were ranked by p value (Chapter 3, Appendix A).

2.11 Transcriptomic analyses

Two RNA-sequencing datasets were used in this study. The first was provided to me for the analysis of alternative splicing of *DNMT3A*, *BCOR* and *CYLD* with the Integrated Genomics Viewer (IGV) v2.3. RNA was extracted from 16 snap frozen CCS tumor samples and 4 perilesional control skin samples by Dr Naomi Sinclair. Stranded preparation was performed by Eurofins Genomics Group (formerly known

as AROS Applied Biotechnology A/S) using the TruSeq Stranded mRNA Library Prep Kit (Illumina). cDNA libraries were sequenced using an Illumina Hiseq 2500 as 100 bp paired end reads. Bioinformatics analysis was performed by Mr Robert Stones (Newcastle University). Sequencing data was quality checked with FastQC and reads were aligned to the human reference genome (GRCh38) with TopHat2, a program that identifies exon-exon splice junctions during alignment(Andrews, 2010, Kim et al., 2013a). Differential gene expression was analysed with Cufflinks and CuffDiff software tools(Trapnell et al., 2012).

To generate the second RNA-Seq dataset, RNA was extracted from FACS sorted samples (n = 4 normal, n = 5 tumour) with the RNeasy Micro Kit (Qiagen 74004) and bulk tissue (n = 3 normal skin, n = 10 CCS tumour) with the Allprep DNA/RNA/miRNA Universal Kit (Qiagen 80224) following the manufacturers' protocols. For eight of the bulk CCS tumour samples (PD37330a, c, e, k, PD40539d, e, and PD40542d), DNA was also extracted for *DNMT3A* genotyping and the methylation array described above. TapeStation (Agilent) RNA quality control and stranded preparation with the NEB Nextera Low Input RNA Library Prep Kit was performed by Dr Jonathon Coxhead (Newcastle University). Libraries were single end sequenced using an Illumina NextSeq 550 system at the Newcastle University Genomics Core Facility. Bioinformatic analysis was performed by Dr Simon Cockell (Newcastle University). The quality of sequencing data was checked with FastQC and reads were aligned using the splice-aware aligner program STAR(Andrews, 2010, Dobin et al., 2012). The aligned sequencing reads for each sample were mapped to genomic features and counted using the Python package HTSeq(Anders et al., 2015). Count data was filtered to remove genes with a total read count <15, normalised by trimmed mean of M values (TMM) method in the Bioconductor package edgeR and then transformed by voom in the R package limma(Law et al., 2014, Robinson and Oshlack, 2010, Robinson et al., 2010, Ritchie et al., 2015). Differential gene expression analysis was carried out using the package DeSeq2(Love et al., 2014).

Heatmaps, volcano and PCA plots were generated using the package ggplot2(Wickham, 2016). Functional enrichment analysis of differentially expressed genes was performed with the webserver g:Profiler(Raudvere et al., 2019). Reads per kilobase of transcript, per million mapped reads (RPKM) values were input for deconvolution with the CIBERSORTx LM22 leukocyte gene signature

matrix(Newman et al., 2015, Steen et al., 2020). CIBERSORTx was run for 100 permutations with B-mode batch correction to allow comparison of the microarray derived LM22 matrix with RNA-Seq input data. Quantile normalisation was disabled as recommended for RNA-Seq data.

Chapter 3. Epigenetic modifiers *DNMT3A* and *BCOR* are recurrently mutated in CYLD cutaneous syndrome

3.1 Results

3.1.1 CYLD is strongly expressed in eccrine glands in CCS patient skin

CYLD, a ubiquitin hydrolase, negatively regulates multiple signalling pathways that are relevant in skin and hair development, including NF-κB and Wnt. CYLD cutaneous syndrome (CCS) is a rare inherited genetic skin condition, where loss of functional CYLD is associated with the formation of hair follicle tumours.

There is a longstanding debate in the literature regarding the cell of origin of these tumours, with eccrine differentiation described as well as both eccrine and hair follicle marker expression (Penneys and Kaiser, 1993, Massoumi et al., 2006b, Sellheyer, 2015). Massoumi et al. (2006) have demonstrated that CYLD protein is expressed in the Huxley cells of the inner root sheath of the adult anagen hair follicle in adults with germline *CYLD* mutations. Careful characterisation of the localisation of CYLD expression in eccrine glands in these patients is however lacking and is of interest given the debate regarding the cell of origin of cylindromas and spiradenomas.

To address this, I investigated CYLD protein expression in normal and perilesional skin from four patients with CYLD cutaneous syndrome with immunofluorescence (Figure 3-1). Cryosections were immunostained for CYLD and hair follicle/eccrine gland cytokeratin (CK) markers to aid determination of CYLD localisation in skin appendages. CK14 and 17 are expressed in the outer root sheath and companion layer of the hair follicle (Moll et al., 2008), myoepithelial cells of the eccrine gland secretory portion and luminal cells of the eccrine ductal portion(Langbein et al., 2005), CK18 labels eccrine secretory gland cells and CK77 is expressed by luminal cells of the eccrine ductal portion (Langbein et al., 2005).

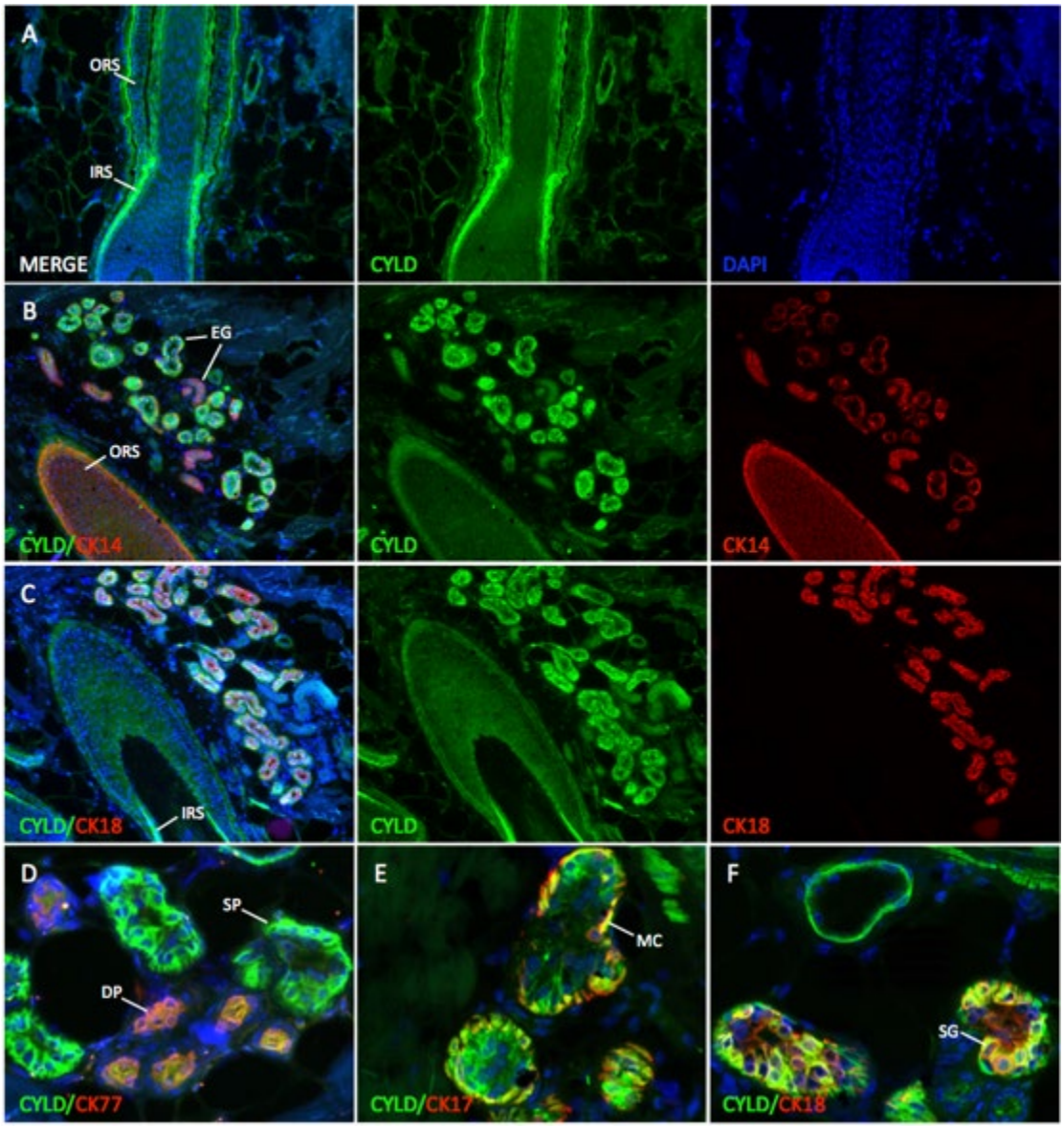

Figure 3-1. CYLD expression in eccrine glands in CYLD cutaneous syndrome (CCS). Cryosections were fixed in 100% methanol, washed in 30% w/v sucrose and blocked in 0.3% Triton X-100/0.5% BSA in 1XPBS then stained with CYLD or double labelled with CYLD and CK14, CK17, CK18 or CK77/K1b antibodies overnight followed by Alexa Fluor® secondary antibodies and DAPI. A) CYLD expression restricted to the inner root sheath (IRS) in a hair follicle from a CCS patient. B) CYLD is strongly expressed in the secretory portion of eccrine glands and co-localises with CK14 in myoepithelial cells. CK14 also labels the outer root sheath of a hair follicle and luminal cells of the eccrine ductal portion. C) CYLD is positive in the inner root sheath of a hair follicle and co-localises strongly with CK18 in eccrine secretory gland cells. D) CYLD is strongly positive in the secretory portion but relatively low or absent in the ductal portion highlighted by CK77. E) CYLD co-localises with CK17 in myoepithelial cells (yellow). F) CYLD co-localises with CK18 in secretory gland cells (yellow). EG, Eccrine glands; ORS, Outer root sheath; IRS, Inner root sheath; DP, Ductal portion; SP, Secretory portion; MC, myoepithelial cells; SG, secretory gland cells.

CYLD expression in hair follicles in skin from patients with CYLD cutaneous syndrome was restricted predominantly to the inner root sheath (IRS) as previously

described (Figure 3-1A & C). In eccrine glands, CYLD was strongly expressed in the secretory portion (Figure 3-1B – F) and weak or absent in the ductal portion highlighted by single positive CK14 (Figure 3-1B) and CK77 (Figure 3-1D). CYLD strongly co-localised with eccrine markers CK17 (myoepithelial cells, yellow Figure 3-1E) and CK18 (secretory gland cells, yellow Figure 3-1C & F).

Reduced CYLD protein expression in cylindroma tissue adjacent to strong expression in hair follicle inner root sheath keratinocytes has been demonstrated by Massoumi et al. (2006). Here, I assessed CYLD protein expression in cylindroma tissue adjacent to eccrine glands and its localisation in relation to HF and eccrine cytokeratin markers within CCS tumours (Figure 3-2).

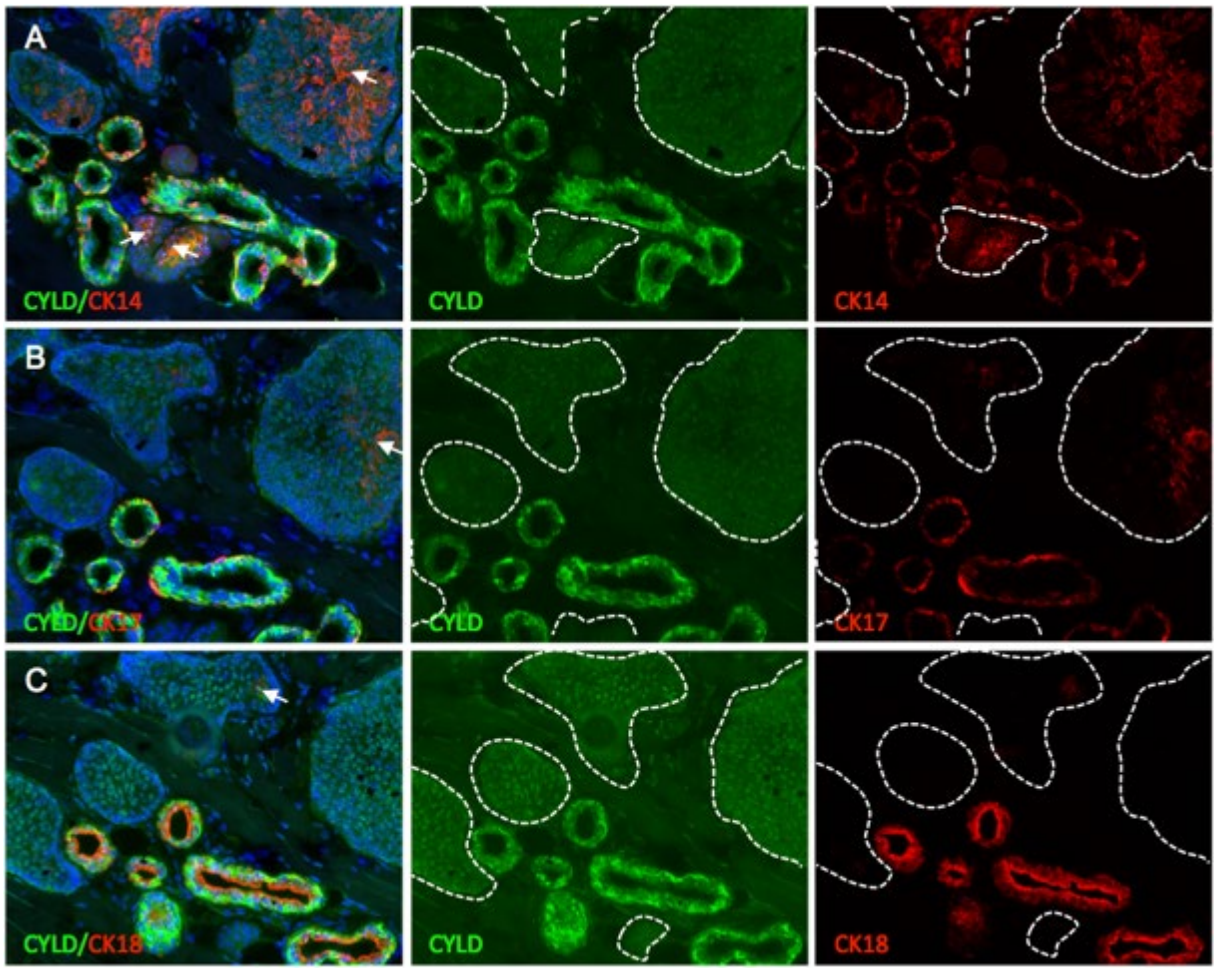

Figure 3-2. CYLD expression in cylindroma tumour tissue and adjacent eccrine glands in CYLD cutaneous syndrome. Fresh frozen tumour sections from patients with germline mutations in *CYLD* were analysed for CYLD and cytokeratin expression. CYLD expression is low but not completely lost in cylindroma tumour tissue adjacent to strongly CYLD positive eccrine glands (white dashed lines enclose cylindroma tissue). CYLD localisation in cylindroma tissue is predominantly nuclear and perinuclear in the large inner cells of tumour

islands. A subset of tumour keratinocytes co-express weak nuclear CYLD and cytoplasmic CK14 (A), CK17 (B) or CK18 (C) (white arrows).

In agreement with previously published single label immunostaining(Dubois et al., 2017), CK14 and 17 were widely expressed in cylindroma tissue while CK18 was sparsely expressed. In contrast to the strong expression of CYLD in eccrine gland secretory portions adjacent to cylindromas, CYLD was weakly detected in the nucleus and perinuclear region of the large inner cells of cylindroma tumour islands (white dashed lines). Co-localisation of weak nuclear CYLD and cytoplasmic hair follicle and eccrine cytokeratin markers in tumour tissue (white arrows) confirmed these cells as keratinocytes.

These results suggest that while CYLD expression is dramatically reduced in cylindroma tissue relative to expression in adjacent skin appendages, CYLD protein is not entirely lost in CCS tumour keratinocytes and may exist at low levels in a non-functional or partially functional truncated form with nuclear localisation.

3.1.2 Biallelic loss of CYLD drives CCS tumours

Three types of tumour with distinct histophenotypes can occur in CCS; cylindromas, spiradenomas and trichoepitheliomas. CCS tumours studied using array-based comparative genomic hybridization (CGH) demonstrate no mutations other than loss of heterozygosity (LOH) of *CYLD*, where the wild-type parental allele is lost and the germline mutation becomes homozygous (Rajan et al., 2011b). Given how histologically diverse these tumours are, additional somatic mutations such as those in *ALPK1* recently demonstrated in sporadic spiradenomas by whole exome sequencing (WES) might be expected in inherited CCS tumours (Rashid et al., 2019).

To delineate the genomic landscape of CCS, in collaboration with Dr Helen Davies at the University of Cambridge who performed the whole genome sequencing (WGS) and WES bioinformatics analyses, we studied DNA from 11 fresh frozen tumours from two directly-related patients (patients 1 and 2) using WGS and 31 tumours from 13 patients (including patients 1 and 2) using WES (Table 3-1).

Paired-end WGS was carried out on DNA from 11 fresh frozen tumours and paired normal skin samples on an Illumina Hi Seq X Ten, generating 374,496,607 unique

reads per sample with an average fold-coverage of 35.5 for all samples. WES samples were DNA extracted from blood and cryosections of snap frozen tumours apart from 5 samples extracted from formalin-fixed paraffin embedded (FFPE) tissue (PD37330h, PD40536c, PD40540a, PD40545a and PD40545c). WES libraries were prepared with the Illumina Nextera DNA Exome Kit and sequenced on an Illumina Novaseq machine, apart from three samples enriched with the SureSelect Human All ExonV6+UTR and sequenced on an Illumina Hiseq 2500 genome analyser. The average sequencing depth for WES was 255-fold.

Table 3-1. Sample information for tumours from CCS patients analysed with next generation sequencing. NGS, next generation sequencing; WGS, whole genome sequencing; WES, whole exome sequencing; TDS, targeted deep sequencing; RNASeq, RNA sequencing; EPIC, EPIC methylation array.

Sample	Patient No	Sex	Age	*CYLD* Genotype	Source	NGS	Array
PD36119a	1	F	80	*c.2460delC*	Skin	WES	
PD36119c	1	F	80	*c.2460delC*	Skin	WES, RNAseq	
PD37330a	1	F	80	*c.2460delC*	Skin	WGS, TDS, RNAseq	EPIC
PD37330c	1	F	80	*c.2460delC*	Skin	WGS, TDS, RNAseq	EPIC
PD37330e	1	F	80	*c.2460delC*	Skin	WGS, TDS, RNAseq	EPIC
PD37330f	1	F	80	*c.2460delC*	Skin	WGS, RNAseq	
PD37330g	1	F	80	*c.2460delC*	Skin	WGS, TDS	
PD37330h	1	F	80	*c.2460delC*	Lung	WES	
PD37330i	1	F	80	*c.2460delC*	Skin	WES, TDS	
PD37330j	1	F	80	*c.2460delC*	Skin	WES, TDS	
PD37330k	1	F	80	*c.2460delC*	Skin	TDS, RNAseq	EPIC
PD37330l	1	F	80	*c.2460delC*	Skin	RNAseq	
PD37331a	2	F	64	*c.2460delC*	Skin	WGS, RNAseq	
PD37331c	2	F	64	*c.2460delC*	Skin	WGS	
PD37331f	2	F	64	*c.2460delC*	Lung	WGS	
PD37331g	2	F	64	*c.2460delC*	Lung	WGS	
PD37331h	2	F	64	*c.2460delC*	Lung	WGS	
PD37331i	2	F	64	*c.2460delC*	Skin	WGS, RNAseq	
PD37331j	2	F	64	*c.2460delC*	Skin	WES	
PD37331k	2	F	64	*c.2460delC*	Skin	WES, TDS	
PD37331l	2	F	64	*c.2460delC*	Skin	WES	
PD37331m	2	F	64	*c.2460delC*	Skin	TDS	
PD37331n	2	F	64	*c.2460delC*	Skin	RNAseq	
PD37331o	2	F	64	*c.2460delC*	Skin	RNAseq	
PD40536a	3	F	48	*c.2460delC*	Skin	WES	

PD40536c	3	F	48	*c.2460delC*	Skin	WES	
PD40536d	3	F	48	*c.2460delC*	Skin	WES, TDS	
PD40536e	3	F	48	*c.2460delC*	Skin	RNAseq	
PD40537a	4	M	84	*c.2469+1G>A*	Skin	WES, TDS	
PD40537c	4	M	84	*c.2469+1G>A*	Skin	WES, TDS	
PD40538a	5	M	51	*c.2469+1G>A*	Skin	WES	
PD40538c	5	M	51	*c.2469+1G>A*	Skin	WES	
PD40538d	5	M	51	*c.2469+1G>A*	Skin	RNAseq	
PD40538e	5	M	51	*c.2469+1G>A*	Skin	RNAseq	
PD40538f	5	M	51	*c.2469+1G>A*	Skin	RNAseq	
PD40539a	6	F	87	*c.2469+1G>A*	Skin	WES	
PD40539c	6	F	87	*c.2469+1G>A*	Skin	WES	
PD40539d	6	F	87	*c.2469+1G>A*	Skin	TDS, RNAseq	EPIC
PD40539e	6	F	87	*c.2469+1G>A*	Skin	TDS, RNAseq	EPIC
PD40540a	7	M	77	*c.2460delC*	Skin	WES	
PD40540c	7	M	77	*c.2460delC*	Skin	WES, TDS	
PD40540d	7	M	77	*c.2460delC*	Skin	WES	
PD40540e	7	M	77	*c.2460delC*	Skin	RNAseq	
PD40541a	8	F	81	*c.2460delC*	Skin	WES, TDS, RNAseq	
PD40542a	9	F	75	*c.2460delC*	Skin	WES	
PD40542c	9	F	75	*c.2460delC*	Skin	WES	
PD40542d	9	F	75	*c.2460delC*	Skin	TDS, RNAseq	EPIC
PD40542e	9	F	75	*c.2460delC*	Skin	TDS	
PD40543a	10	F	43	*c.2460delC*	Skin	WES	
PD40543c	10	F	43	*c.2460delC*	Skin	RNAseq	
PD40544c	11	F	57	*c.1112C>A*	Skin	WES	
PD40544d	11	F	57	*c.1112C>A*	Skin	WES	
PD40545a	12	M	72	*c.2467C>T*	Skin	WES	
PD40545c	12	M	72	*c.2467C>T*	Skin	WES	
PD40546a	13	F	30	*c.1112C>A*	Skin	WES	
PD40546c	13	F	30	*c.1112C>A*	Skin	WES	
PD40546d	13	F	30	*c.1112C>A*	Skin	WES	
PD40547a	14	F	53	*c.2460delC*	Skin	RNAseq	
PD40548a	15	F	54	*5.5Mb deletion*	Skin	RNAseq	
PD40548c	15	F	54	*5.5Mb deletion*	Skin	RNAseq	
PD40548d	15	F	54	*5.5Mb deletion*	Skin	RNAseq	
PD40548e	15	F	54	*5.5Mb deletion*	Skin	RNAseq	

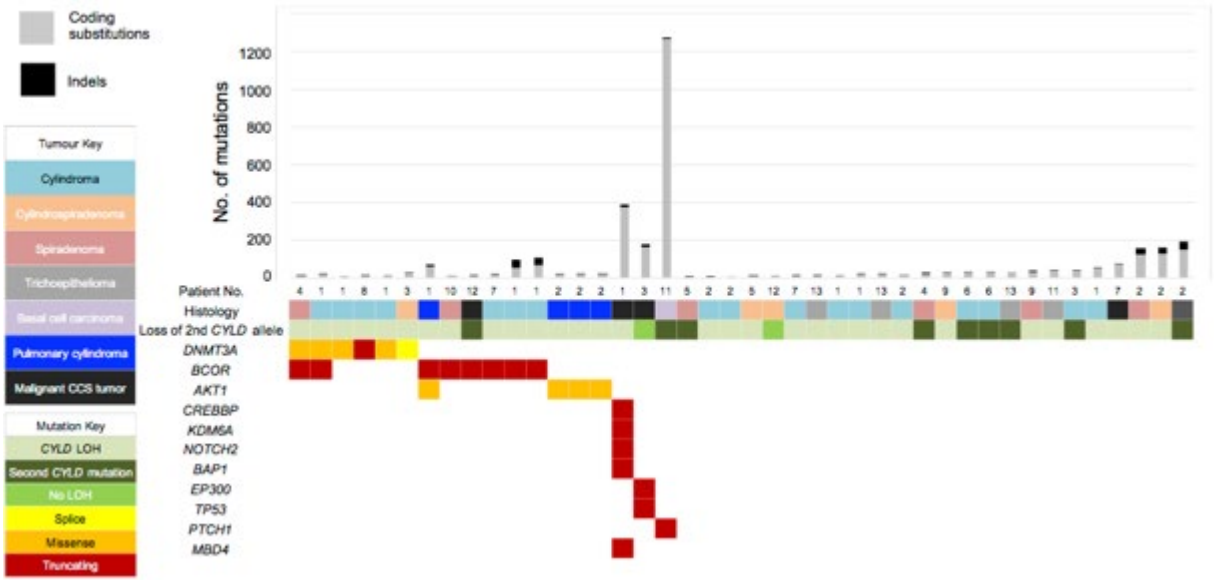

Figure 3-3. The mutational landscape of CYLD cutaneous syndrome. 42 tumours were analysed from 13 patients with CYLD cutaneous syndrome by whole genome sequencing (WGS, n = 11) or whole exome sequencing (WES, n = 31). In addition to biallelic mutation of *CYLD*, epigenetic modifiers *DNMT3A* and *BCOR* were recurrently mutated in benign CCS tumours. The mutational burden of each sample is shown by bar graph, followed by a matrix indicating the tumour histology, how the second CYLD allele was lost in each tumour and which genes in addition to CYLD had putative driver mutations. Each column represents one individual tumour sample. Samples were prepared for sequencing by Dr Neil Rajan and bioinformatic analysis was performed by Dr Helen Davies. Adapted from Davies et al. 2019.

WGS found an average of 1,381 substitutions per tumour sample (equating to 0.44 mutations per MB), 72 small insertions and deletions (indels) and one rearrangement. Biallelic mutations in *CYLD* were found in all but two CCS tumours, confirming *CYLD* loss as the primary driver mutation in CCS. Loss of the wild-type *CYLD* allele by LOH at 16q was confirmed in 31/42 tumours, while a second somatic mutation in *CYLD* was detected in 9/42 tumours (Table 3-2). WGS did not detect any structural variants including the *MYB-NFIB* gene fusion that has previously been reported in sporadic cylindromas(Fehr et al., 2011).

Table 3-2. Somatic mutations in the wild-type *CYLD* allele in familial CCS tumours.

Next generation sequencing (NGS) of 42 tumours by whole genome sequencing (WGS) and whole exome sequencing (WES) revealed 9 tumours with germline mutation of *CYLD* lost the wild-type second *CYLD* allele due to a new somatic mutation. Bioinformatic analysis was performed by Dr Helen Davies.

Sample	NGS	Germline *CYLD*	Loss of 2nd *CYLD* allele
PD37331j	WES	c.2460delC	c.2299A>T p.K767*
PD40536a	WES	c.2460delC	c.2368_2369AT>TA p.I79*
PD40537c	WES	c.2469+1G>A	c.1876G>T p.E626*
PD40538a	WES	c.2469 +1G>A	c.2806C>T p.R936*

PD40539a	WES	c.2469 +1G>A	c.2806C>T p.R936*
PD40539c	WES	c.2469 +1G>A	c.2711C>T p.P904L
PD40544c	WES	c.1112C>A	c.2616T>G p.Y872*
PD40545a	WES	c.2467C>T	c.2038A>T p.K680*
PD40546c	WES	c.1112C>A	c.2350+5G>A p.?

Recurrent mutations in *AKT1* (p.E17K) were found in 4/4 benign pulmonary cylindroma samples from patients 1 and 2 (Figure 3-3 and Table 3-1). Pulmonary cylindromas are a secondary complication that can occur in CCS patients (Brown et al., 2018). The oncogenic *AKT1*$^{-E17K}$ mutation has been found in a range of solid tumours, including breast cancer (Hyman et al., 2017). As drugs have been developed to target *AKT1* in tumours, this finding is highly clinically relevant for CCS patients with lung cylindromas (Smyth et al., 2020).

Although extremely rare, malignant transformation of benign CCS tumours may occur (Kazakov et al., 2009). Five malignant CCS tumours were analysed by WES for putative driver mutations in addition to *CYLD* LOH; basal cell adenocarcinoma-low grade (BCAC-LG), poorly differentiated adenocarcinoma removed from the breast of a 47 year old female CCS patient, basal cell carcinoma (BCC), malignant spiradenocarcinoma that presented at age 80 in patient 1 and atypical spiradenocarcinoma.

The malignant spiradenocarcinoma (PD36119a) had a relatively high number of coding substitutions (375) compared with benign CCS tumours. A previously unknown germline mutation in Methyl-CpG binding domain 4, DNA glycosylase (*MBD4*) (p.Q170fs*45) was discovered in patients 1, 2 and 10, with loss of the wild-type *MBD4* allele by LOH detected in the malignant tumour only. This tumour also had potential driver mutations in two epigenetic modifiers (CREB binding protein (*CREBBP*) and Lysine demethylase 6A (*KDM6A*)) and two tumour suppressors (Notch receptor 2 (*NOTCH2*) and BRCA1 associated protein 1 (*BAP1*)).

The poorly differentiated adenocarcinoma (PD40536c) was the only malignant tumour analysed that did not have biallelic loss of *CYLD*. This tumour had nonsense mutations in the tumour suppressor Tumour protein P53 (*TP53*) and the epigenetic modifier E1A binding protein (*EP300*). No potential driver mutations were detected in the atypical spiradenocarcinoma (PD40540a). The BCC (PD40544c) had a frameshift

mutation in the tumour suppressor Patched 1 (*PTCH1*) and had the highest number of coding substitutions (1287). The BCAC-LG (PD40545a) had a frameshift mutation in the epigenetic modifier BCL6 Corepressor (*BCOR*), which was also frequently mutated in benign CCS tumours.

In summary, this data adds to our knowledge of somatic driver mutations in rare occurrences of malignant transformation of benign CCS tumours and secondary pulmonary cylindromas. The remainder of this chapter will focus on the recurrence of somatic mutations in the epigenetic modifiers DNA methyltransferase 3 alpha (*DNMT3A*) and *BCOR* in benign cylindromas and spiradenomas.

Table 3-3. CCS tumour putative driver mutations discovered by whole genome sequencing or whole exome sequencing. Loss of *CYLD* was confirmed in all tumours apart from malignant CCS tumour PD40536c and one benign cylindroma (PD40545c). Potential driver mutations in tumour suppressor genes or dominant oncogenes were identified using the Cancer gene census (https://cancer.sanger.ac.uk/census). Bioinformatic analysis was performed by Dr Helen Davies. VAF, Variant allele frequency; ess_splice, essential splice site.

Sample	Gene	cDNA	Protein	Effect	VAF
Pulmonary cylindromas					
PD37330h	*AKT1*	c.49G>A	p.E17K	missense	0.22
PD37331f	*AKT1*	c.49G>A	p.E17K	missense	0.55
PD37331g	*AKT1*	c.49G>A	p.E17K	missense	0.44
PD37331h	*AKT1*	c.49G>A	p.E17K	missense	0.31
Malignant CCS tumours					
PD36119a	*BAP1*	c.2036_2055del20	p.I679fs*31	frameshift	0.72
PD36119a	*CREBBP*	c.4337G>A	p.R1446H	missense	0.31
PD36119a	*CREBBP*	c.3307C>T	p.R1103*	nonsense	0.39
PD36119a	*KDM6A*	c.1972C>T	p.R658*	nonsense	0.65
PD36119a	*NOTCH2*	c.6909_6910insC	p.I2304fs*9	frameshift	0.37
PD40536c	*EP300*	c.584C>A	p.S195*	nonsense	0.09
PD40536c	*EP300*	c.2855C>G	p.S952*	nonsense	0.08
PD40536c	*TP53*	c.614_615insGTA	p.E204_Y205ins*	nonsense	0.31
PD40544c	*PTCH1*	c.843_863del21insG	p.L282fs*30	frameshift	0.32
PD40545a	*BCOR*	c.1572_1573insTGGCAAAAGC	p.M525fs*35	frameshift	0.35
Benign CCS tumours					
PD37330a^{+}	*BCOR*	c.2606_2607insAGA	p.Y869delins*	nonsense	0.31
PD37330a^{+}	*DNMT3A*	c.1517AC>GG	p.H506dup	missense	0.37
PD37330c^{+}	*DNMT3A*	c.1531G>A	p.G511R	missense	0.42
PD37330g^{+}	*DNMT3A*	c.2339T>C	p.I780T	missense	0.34
PD37330h	*BCOR*	c.1722_1723insC	p.N575fs*36	frameshift	0.09
PD37330i^{+}	*BCOR*	c.1061_1062insAA	p.Y354fs*1	frameshift	0.38
PD37330j^{+}	*BCOR*	c.2221_2225delGA	p.E741fs*45	frameshift	0.31

		GAAinsTTTC			
PD40536d+	*DNMT3A*	c.1123-2A>C	p.?	ess_splice	0.10
PD40537a+	*BCOR*	c.1059delC	p.Y354fs*24	frameshift	0.07
PD40537a+	*DNMT3A*	c.2644C>T	p.R882C	missense	0.26
PD40540c+	*BCOR*	c.3621_3622insA	p.Q1208fs*8	frameshift	0.08
PD40541a+	*DNMT3A*	c.2638delA	p.M880fs*1	frameshift	0.18
PD40543a	*BCOR*	c.2428C>T	p.R810*	nonsense	0.05

+additional material from these samples was analysed by targeted deep sequencing (TDS)

3.1.3 DNMT3A and BCOR are mutated in CCS tumors

In addition to biallelic mutations in *CYLD*, 11 benign cylindromas and spiradenomas had mutations in the epigenetic modifiers *DNMT3A* (n=6, variant allele frequency range 0.10-0.42) and *BCOR* (n=7, variant allele frequency range 0.05-0.38) (Figure 3-3 and Table 3-3). Both genes were mutated in one cylindroma (PD37330a) and one spiradenoma (PD40537a). To explore the possibility that clones with different mutations in *DNMT3A* or *BCOR* may occur within an individual CCS tumour, targeted deep sequencing (TDS; average coverage of >500x) of *DNMT3A* and *BCOR* was performed on DNA from additional tissue sections from nine of the tumours studied above (labelled+ in Table 3-3). Dr Neil Rajan performed the sample preparation and TDS.

Applying a strict filtering threshold to variant calls (“Filter” = PASS and “Qual” = 100), TDS confirmed the presence of more than one mutation in *DNMT3A* or *BCOR* or mutations in both genes within the same tumour in six samples (Figure 3-4). This multi-level sampling approach confirmed that one spiradenoma (PD40537a) had two unique mutations in *DNMT3A* in addition to a mutation in BCOR.

A

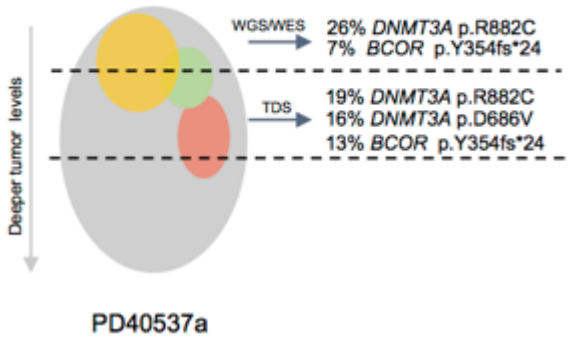

B

Sample	*DNMT3A* mutation	VAF	*BCOR* mutation	VAF
PD37330a	p.H506dup	0.34	p.Y869delins*	0.40
PD37330c	p.G511R	0.41		
	p.T671M	0.29		
PD37330g	p.I780T	0.24	p.K839fs	0.14
PD37330i			p.Y354fs*1	0.43
			p.A1428V	0.10
PD40536d	c.1123-2A>C	0.10		
	p.R729W	0.07		
PD40537a	p.D686V	0.16	p.Y354fs*24	0.13
	p.R882C	0.19		

Figure 3-4. Targeted deep sequencing (TDS) reveals intra-tumoural heterogeneity of *DNMT3A* and *BCOR* mutations. A) Sampling of different levels within a single spiradenoma (PD40537a, represented by grey sphere) reveals intra-tumoural clones with unique *DNMT3A* mutations (yellow and red spheres) and a mutation in *BCOR* (green sphere). B) Six out of nine CCS tumours analysed by TDS had mutations in both *DNMT3A* and *BCOR* or more than one mutation in *DNMT3A* or *BCOR*. Sampling was performed by Dr Neil Rajan and bioinformatic analysis of WGS/WES data was performed by Dr Helen Davies. Adapted from Davies et al. 2019.

To investigate *DNMT3A* mutational heterogeneity within CCS tumour histophenotypes, TDS was performed on DNA extracted from micro-dissected tissue from five CCS tumours that contained both cylindroma and spiradenoma (Figure 3-5A). Dr Neil Rajan performed the micro-dissection, DNA extraction and TDS procedure. The strict thresholds (“Filter” = PASS and “Qual” = 100) applied to previous TDS variant calls were relaxed for these five samples and all non-synonymous variants were included if aligned read data (confirmed using Integrated Genomics Viewer (IGV; v2.3)) supported the calls (Figure 3-5B).

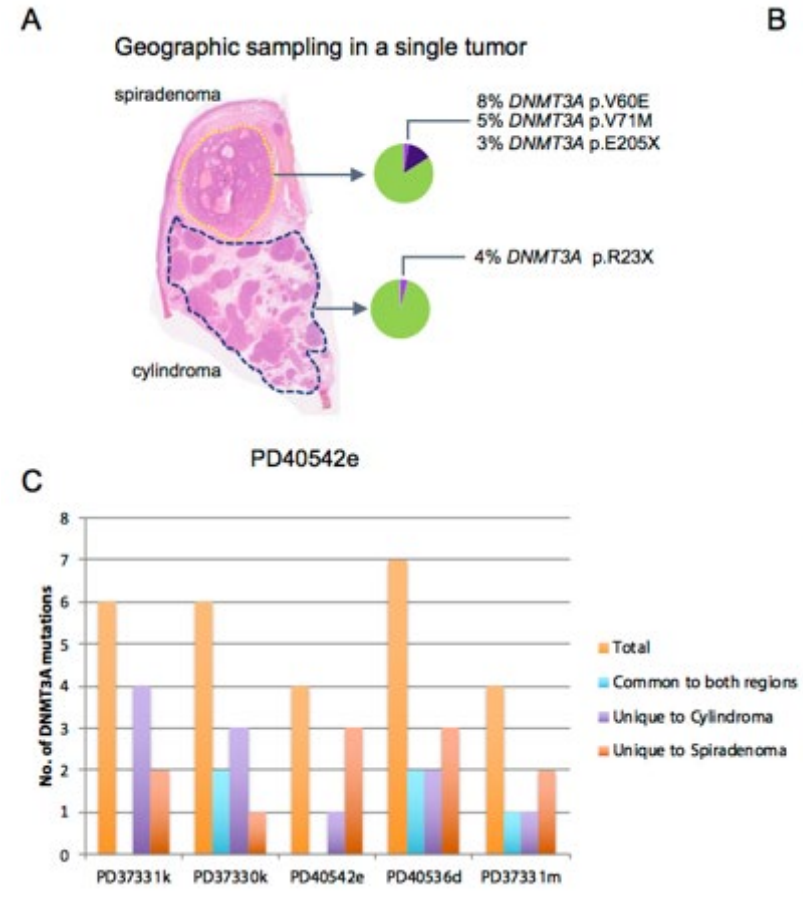

B

Sample	Mutation	Cylindroma VAF	Spiradenoma VAF
PD37331k	p.A70V	5%	0%
	p.G83R	5%	0%
	p.I539V	0%	2%
	p.R635G	0%	4%
	p.I655T	7%	0%
	p.I661fs	11%	0%
PD37330k	p.E61V	0%	5%
	p.S62G	3%	3%
	p.S73P	3%	1%
	p.D92fs	3%	0%
	p.D686V	8%	0%
	pR729Q	43%	26%
PD40542e	p.R23X	4%	0%
	p.V60E	0%	8%
	p.V71M	0%	5%
	p.E205X	0%	3%
PD40536d	p.K74E	2%	6%
	c.1123-2A>C	5%	21%
	p.V622A	0%	3%
	p.I633fs	0%	4%
	p.E667V	8%	0%
	p.G673A	7%	0%
	p.R729W	2%	7%
PD37331m	p.K67E	5%	0%
	p.K299R	1%	2%
	p.K651R	0%	7%
	p.C666R	0%	7%

Figure 3-5. Heterogeneity of *DNMT3A* mutations in distinct CCS histophenotypes. Five tumours containing regions of spiradenoma and cylindroma were micro-dissected to allow TDS of *DNMT3A* in both histophenotypes. A) TDS of a single tumour (PD40542e) revealed that regions of cylindroma and spiradenoma had unique mutant *DNMT3A* clones of different sizes. B) Table of *DNMT3A* mutations detected by TDS in five micro-dissected CCS tumours. Red colour scale indicates increasing variant allele frequency (VAF). C) Bar chart showing number of *DNMT3A* mutations per sample and how many were common or unique to micro-dissected cylindroma or spiradenoma regions. Adapted from Davies et al. 2019.

Three tumours contained a shared *DNMT3A* mutation in both spiradenoma and cylindroma regions as well as unique mutations confined to one histophenotype (Figure 3-5C). In two tumours, both regions had a unique DNMT3A mutation only. These data further support that multiple *DNMT3A* mutant clones exist within spiradenomas and cylindromas, but a correlation between *DNMT3A* mutational heterogeneity and histophenotype was not discernible.

To investigate the protein domain location of somatic *DNMT3A* and *BCOR* mutations discovered in CCS tumours using WGS, WES and TDS (passing the strict variant call

threshold of ("Filter" = PASS, "Qual" = 100, VAF > 0.05)), mutations were plotted on lollipop diagrams (Figure 3-6).

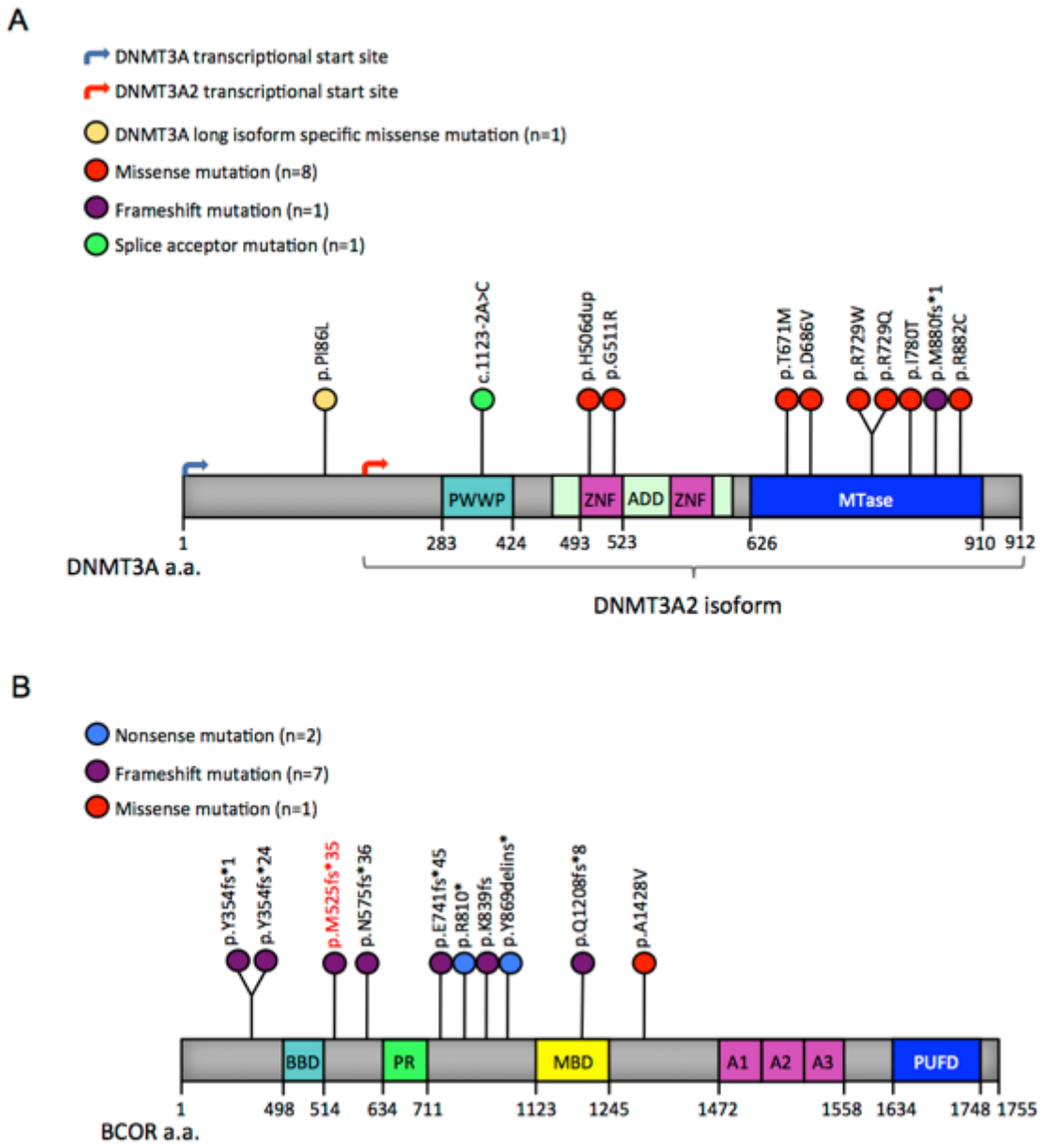

Figure 3-6. *DNMT3A* and *BCOR* mutations discovered in CCS tumours by WGS, WES and TDS. A) Lollipop diagram of somatic mutations in *DNMT3A* in CCS tumours. B) Lollipop diagram of somatic mutations in *BCOR* in CCS tumours. Red font highlights a mutation from a malignant sample (PD40545a, Basal cell adenocarcinoma-low grade). All other mutations were found in benign CCS tumours. PWWP, Proline-tryptophan-tryptophan-proline; ZNF, Zinc finger; ADD, ATRX-DNMT3-DNMT3L; MTase, Methyltransferase; BBD, BCL6 binding domain; PR, Proline rich; MBD, MLLT3 binding domain; A1 – 3, Ankyrin repeat; PUFD, Polycomb-group RING finger Ub-like fold discriminator.

Mutations in *DNMT3A* were predominantly missense and occurred within the C-terminal catalytic methyltransferase domain. Two mutations occurred in the GATA-

type zinc finger within the ATRX-DNMT3-DNMT3L (ADD) domain, which binds to unmethylated H3K4 and mediates protein-protein interactions with epigenetic regulators and transcription factors (Chen and Chan, 2014). One splice site mutation (intron 9) was found in the proline-tryptophan-tryptophan-proline (PWWP) domain, which targets DNMT3A to chromatin and binds to trimethylated lysine 36 of histone H3 (H3K36me3) and H3K36me2(Ge et al., 2004, Hahn et al., 2011, Weinberg et al., 2019). One mutation occurred in the long isoform of DNMT3A only (p.P186L), as the shorter isoform (known as DNMT3A2) lacks the initial N-terminal 223 amino acids of DNMT3A (Chen et al., 2002).

Mutations in *BCOR* were predominantly frameshift and occurred in the N-terminal half of the protein containing the BCL6 binding domain (BBD). Eight of the ten mutations result in a premature termination codon (PTC) causing C-terminal truncation and one truncating mutation occurred within the MLLT3 binding domain (MBD) that is present in the BCOR isoform encoded by transcript variant ENST00000378444.9(Srinivasan et al., 2003). No mutations were detected in the C-terminal region containing the polycomb-group RING finger (PCGF) Ub-like fold discriminator (PUFD) domain that binds to PCGF1 or PCGF3(Junco et al., 2013).

The occurrence of mutations within DNMT3A functional domains and the loss of the BCOR PUFD domain due to truncation supports that these mutations will have functional consequences that could potentially drive CCS tumour growth.

3.1.4 Mutated DNMT3A2 dysregulates methylation

The short isoform of DNMT3A, known as DNMT3A2, is more highly expressed in a range of cancers relative to normal tissues(Xu et al., 2020a). To investigate *DNMT3A* isoform expression in CCS tumours, bulk RNA sequencing data (generated by Dr Naomi Sinclair) from 15 CCS tumours and four perilesional controls was analysed for evidence of transcription from the alternative promoter of *DNMT3A2* (Figure 3-7A). CCS tumours had more reads specific to *DNMT3A2* than *DNMT3A*, suggesting dominant expression of the short isoform. In perilesional control skin, isoform specific reads for *DNMT3A* were highest. Differences in alternative splicing of *BCOR* were not apparent between CCS tumours and matched perilesional controls, and expression levels were similar (Figure 3-7B).

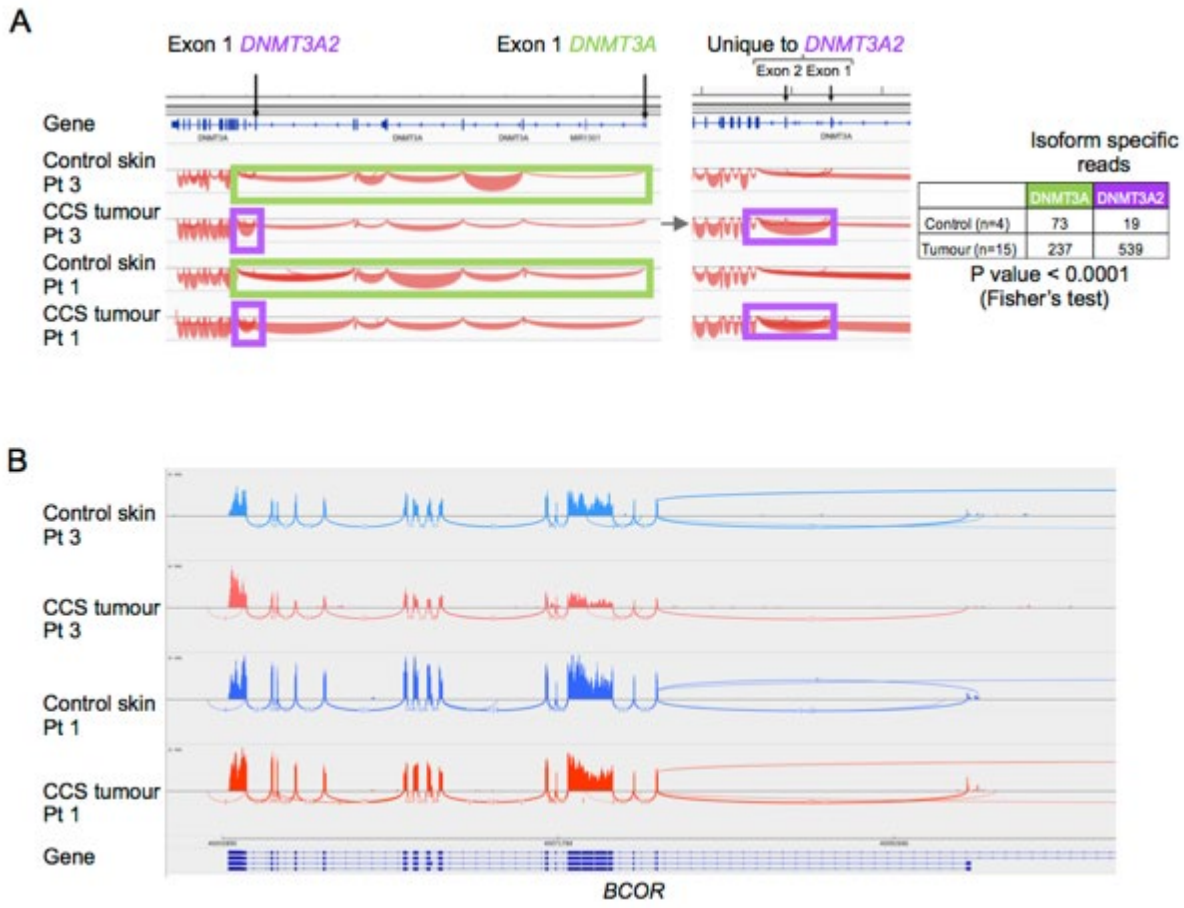

Figure 3-7. RNA sequencing reveals increased expression of *DNMT3A2* in CCS tumours. Bulk RNA sequencing data from 15 CCS tumours and 4 perilesional skin controls was provided by Dr Naomi Sinclair for analysis of *DNMT3A* and *BCOR* expression. A) Splice junctions were visualised in IGV v2.3 and isoform specific reads were compared for *DNMT3A* and the short isoform *DNMT3A2*. B) Expression of *BCOR* was similar between CCS tumour samples and matched perilesional skin.

To investigate protein expression of DNMT3A, immunostaining of cryosections from 8 CCS tumours was performed with an antibody that recognises the long isoform of DNMT3A only. Cylindromas displayed heterogeneity of DNMT3A expression, with DNMT3A positive and negative islands or 'cylinders' observed in the same tumour (Figure 3-8A). As skin tumour keratinocytes from epidermis specific *DNMT3A* knock out mice had a significant upregulation of Wnt/β-catenin signalling pathway genes and the Wnt/β-catenin pathway is known to be dysregulated in CCS tumours, sections were double stained for DNMT3A and β-catenin(Rinaldi et al., 2017). β-catenin expression was mostly cytoplasmic in tumours, with some nuclear staining in the smaller, peripheral cells enclosing tumour islands. In contrast, DNMT3A staining was nuclear and occurred mainly within the larger central cells within tumour islands. DNMT3A expression was relatively weak in perilesional epidermis and hair follicles.

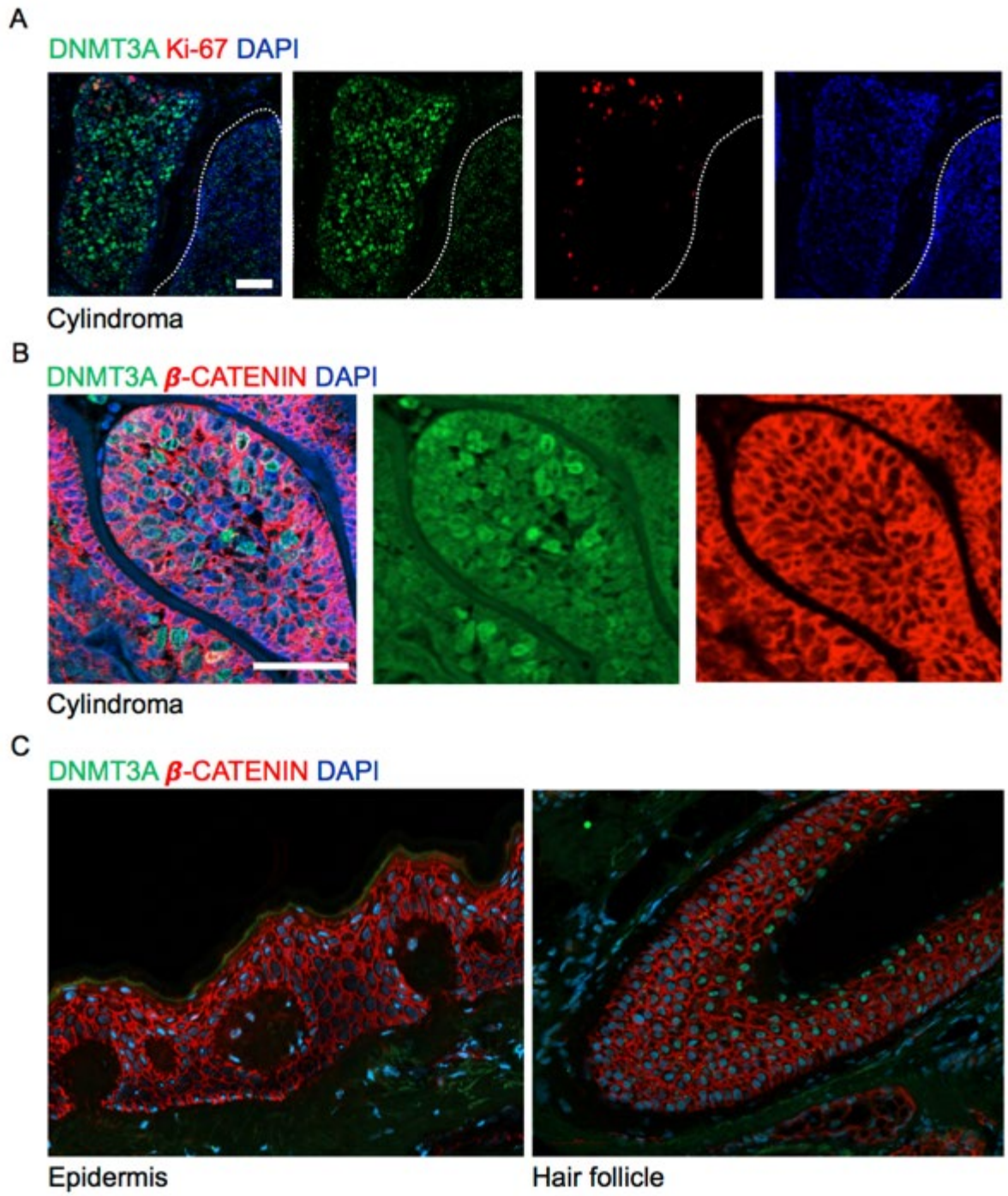

Figure 3-8. DNMT3A protein expression in CCS tumours. A) Cylindroma tumour islands display heterogeneous expression of DNMT3A and the proliferation marker Ki67. B) Nuclear DNMT3A expression in cylindromas tumours in the central cells of tumour islands, or 'cylinders. Nuclear β-catenin is expressed in the peripheral cells of cylinders. C) Weak DNMT3A expression in epidermis and hair follicles with membranous β-catenin. The *DNMT3A* mutational status of these cells is unknown. White scale bar = 50 μm.

To assess the functional impact of *DNMT3A* mutations in CCS tumours, the methylome and transcriptome of eight CCS tumour samples was assessed. Two samples were cylindroma and spiradenoma regions micro-dissected from the same

tumour section (PD37330K), the remaining six were sections from individual CCS tumours (see Table 3-1, EPIC column). DNA and RNA were extracted in tandem and samples were genotyped for DNMT3A mutational status by TDS (Figure 3-9A). Genome-wide methylation was profiled by Eurofins Genomics Group (AROS, Denmark) using the Illumina Methylation EPIC microarray. Dr Neil Rajan performed the TDS procedure and Dr Edward Schwalbe carried out the methylation array bioinformatic analysis.

Differentially methylated probes and regions spanning multiple probes were determined using the R packages minfi(Aryee et al., 2014) and bumphunter(Jaffe et al., 2012) respectively. The top 500 most differentially methylated probes were subjected to unsupervised hierarchical clustering using the complete agglomeration method, revealing two clusters (Figure 3-9B). One cluster comprised of three samples with either no *DNMT3A/2* mutations with VAF ≥0.05, a mutation in the long *DNMT3A* isoform only (p.P186L) or a mutation in *DNMT3A2* with low VAF (0.05). The other cluster contained 5 samples with *DNMT3A2* isoform specific mutation VAF ranging from 0.06 – 0.43.

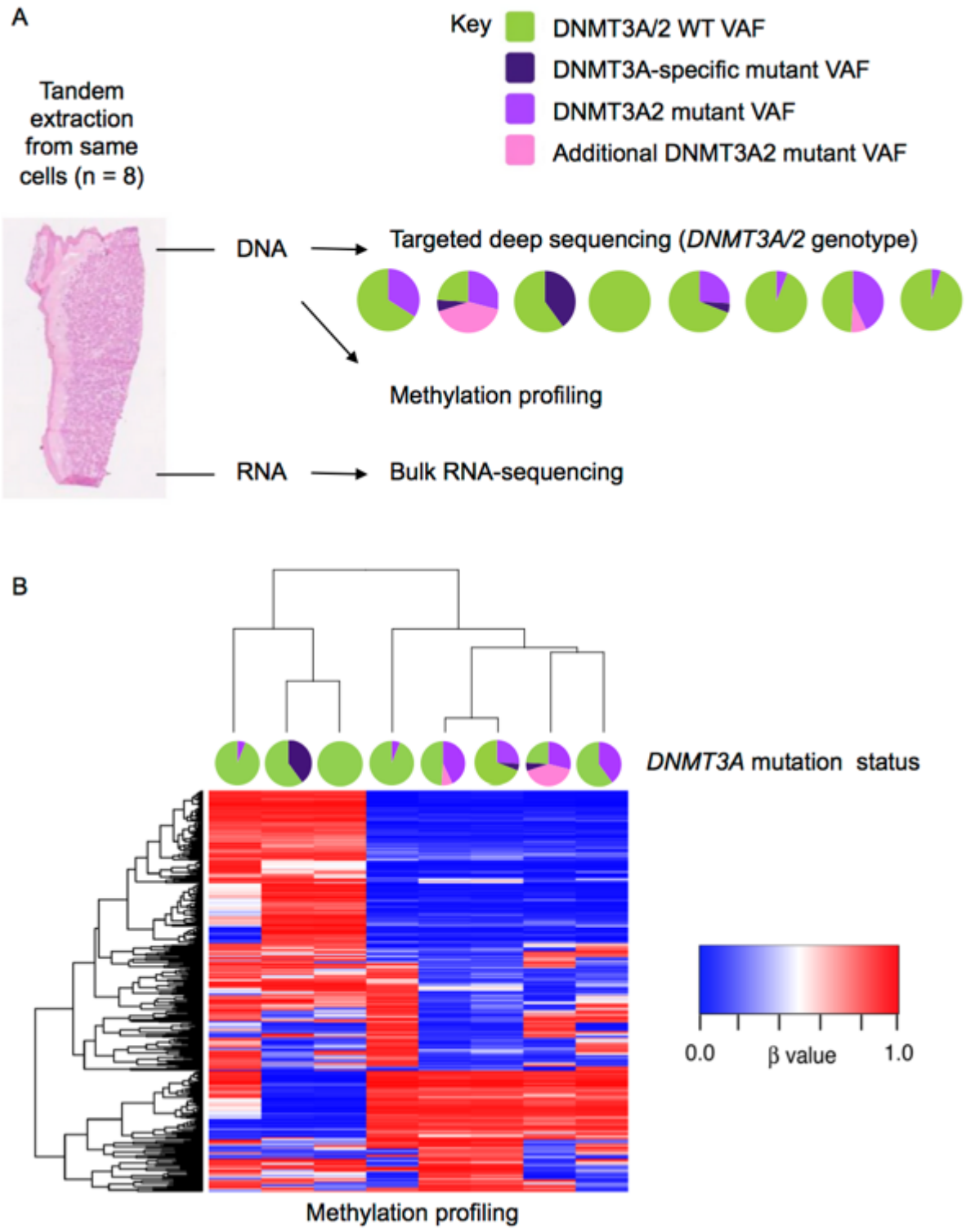

Figure 3-9. Mutated *DNMT3A2* dysregulates methylation. A) DNA and RNA were extracted in tandem from 8 CCS tumour samples. Samples were genotyped for *DNMT3A*/2 by TDS and analysed by Methylation EPIC Microarray and RNA-Sequencing (RNA-Seq). Pie charts indicate *DNMT3A/2* genotypes. B) Unsupervised hierarchical clustering of the top 500 most variably methylated EPIC microarray probes reveals the majority of tumours with isoform specific *DNMT3A2* mutation cluster separately from *DNMT3A2* wild-type tumours. Low β-values (blue) indicate hypomethylation, high β-values (red) indicate hypermethylation. Adapted from Davies et al. 2019.

Network analysis of all genes within regions differentially hypomethylated in the *DNMT3A2*-mutant tumours with Ingenuity Pathway Analysis(Kramer et al., 2014) found the most significant network to be functionally related to β-catenin ($P < 1 \times 10^{-45}$, Fisher's Exact Test) (Figure 3-10 and Appendix A).

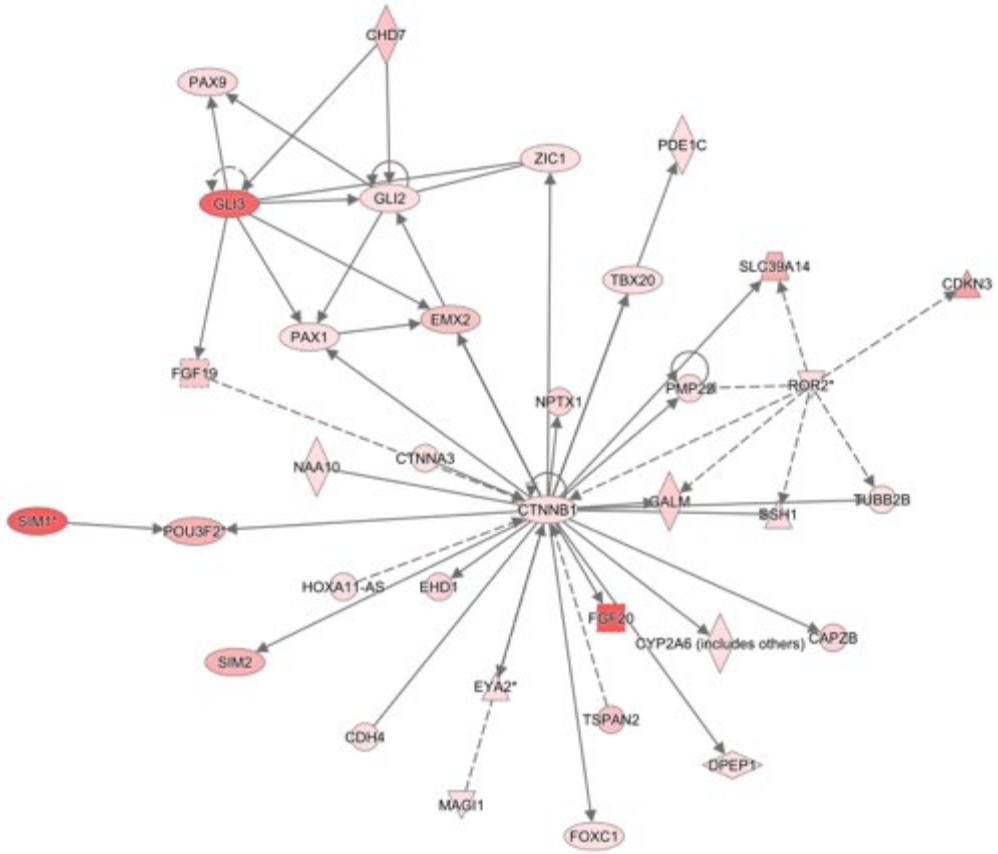

Figure 3-10. Genes functionally related to β-catenin (*CTNNB1*) are differentially methylated in CCS tumours with *DNMT3A2* mutations. Ingenuity Pathway analysis of differentially hypomethylated genes in 5 CCS tumours with *DNMT3A2* mutant VAF >0.05 relative to 3 CCS tumours with *DNMT3A2* VAF ≤0.05 found the top ranked network to be functionally related to β-catenin. Darker pink in the network diagram indicates increased hypomethylation, solid lines indicate direct interactions between genes, dashed lines indicate indirect interactions. Adapted from Davies et al. 2019.

In parallel, single-end RNA-sequencing was performed on the same 8 *DNMT3A/2* genotyped CCS samples. In R (R Core Team, 2019), when normalised and transformed RNA-seq read counts were submitted for principal component analysis (PCA), the same 5 samples with *DNMT3A2* mutant VAF >0.05 clustered separately from the 3 samples with wild type *DNMT3A2* or *DNMT3A2* mutant VAF ≤0.05 (Figure 3-11).

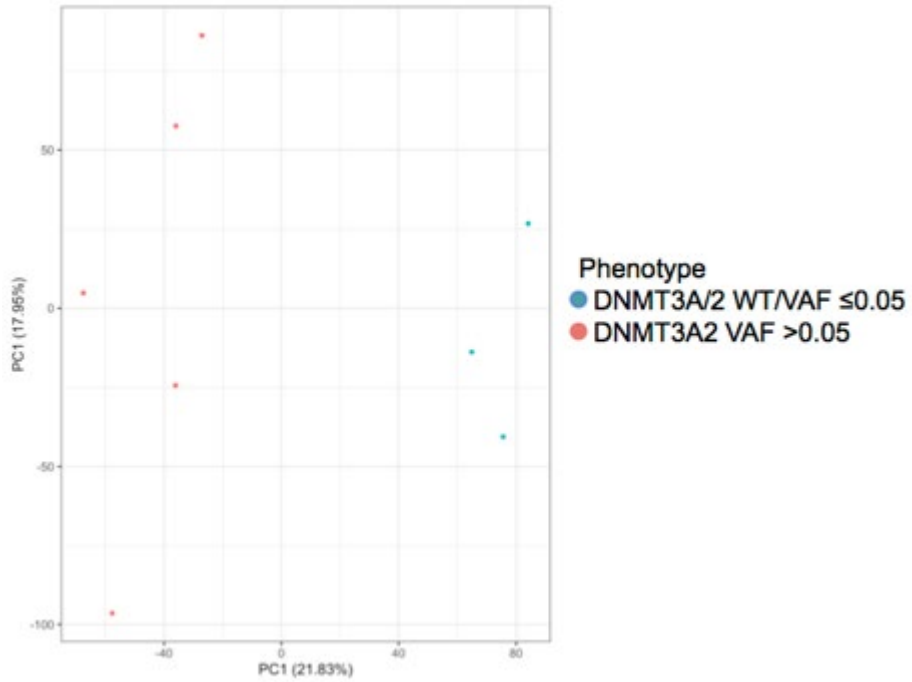

Figure 3-11. Principle component analysis (PCA) of RNA-Seq read counts from *DNMT3A/2* genotyped CCS tumours. RNA-Seq read counts were normalised by the trimmed mean of *M*-values (TMM) method(Robinson and Oshlack, 2010) in edgeR(Robinson et al., 2010), transformed by variance modelling at the observational level (voom)(Law et al., 2014) in limma(Ritchie et al., 2015) then submitted to ggplot2(Wickham, 2016) for PCA. cDNA was sequenced from 8 CCS tumour samples genotyped for DNMT3A/2 by TDS.

A comparison of gene expression between the two clusters using the R package DeSeq2(Love et al., 2014) did not find significant differential expression of Wnt/β-catenin pathway related genes. Applying a threshold of *P*-value (adjusted for multiple testing via Benjimini-Hochberg False Discovery Rate) <0.05 and $\log_2$fold-change (FC) > 2, 47 genes were significantly differentially expressed between the two clusters (Table 3-4 and Figure 3-12.). This highlighted a switch between high expression of human leukocyte antigen class II (HLA-II) genes in *DNMT3A2* wild-type or low mutant VAF tumours to HLA Class I (HLA-I) genes in *DNMT3A2*-mutant tumours. As RNA-Seq was performed on bulk samples containing a mixture of immune cells and tumour cells, it remains to be established that the CCS tumour cells (and not solely the antigen presenting cells) express HLA-I or II molecules and whether this correlates with *DNMT3A2* genotype. Additionally, an important caveat of this small dataset is that samples may be clustering by patient rather than *DNMT3A2* mutational status. These findings implicating differential methylation of β-catenin related genes in *DNMT3A2*-mutant CCS tumour and increased expression of HLA-I genes are therefore preliminary and present interesting avenues for validation in

future studies with a larger cohort of *DNMT3A*/2 genotyped CCS tumour samples and in vitro models of CCS.

Table 3-4. *DNMT3A2*-mutant CCS tumours overexpress HLA class I genes. Differential gene expression analysis of RNA-seq data found 47 genes were significantly differentially expressed (FC2, adjusted *P*-value < 0.05) between CCS tumours with wild type *DNMT3A/2* or *DNMT3A2* mutant VAF ≤0.05 and CCS tumours with *DNMT3A2* mutant VAF >0.05. Positive fold-change indicates expression is higher in CCS tumours with *DNMT3A2* mutant VAF >0.05, negative fold-change indicates expression is lower in CCS tumours with *DNMT3A2* mutant VAF >0.05.

No.	logFC	Gene	Description
1	7.4	*HLA-B*	Major histocompatibility complex, class I, B
2	6.4	*HLA-F*	Major histocompatibility complex, class I, F
3	5.8	*PPP1R11*	Protein phosphatase 1 regulatory inhibitor subunit 11
4	5.7	*GPR12*	G protein-coupled receptor 12
5	5.1	*HLA-A*	Major histocompatibility complex, class I, A
6	5.0	*KRT17P3*	Keratin 17 pseudogene 3
7	4.9	*AL450405.1*	Ribosomal protein L29 (RPL29) pseudogene
8	4.3	*GTF2H2*	General transcription factor IIH subunit 2
9	4.3	*MRPL45*	Mitochondrial ribosomal protein L45
10	4.3	*COX20P1*	COX20, cytochrome c oxidase assembly factor pseudogene1
11	4.1	*HLA-F-AS1*	HLA-F antisense RNA 1
12	3.9	*RPS2P46*	Ribosomal protein S2 pseudogene 46
13	3.8	*CSDC2*	Cold shock domain containing C2
14	3.7	*AL512625.3*	Novel transcript
15	3.7	*HLA-K*	Major histocompatibility complex, class I, K (pseudogene)
16	3.4	*LAIR1*	Leukocyte associated immunoglobulin like receptor 1
17	3.1	*LINC02332*	Long intergenic non-protein coding RNA 2332
18	3.1	*HMGB1P10*	High mobility group box 1 pseudogene 10
19	3.1	*RPS2P5*	Ribosomal protein S2 pseudogene 5
20	2.2	*OSBPL6*	Oxysterol binding protein like 6
21	-2.3	*WDFY4*	WDFY family member 4
22	-2.6	*CD1E*	CD1e molecule
23	-2.9	*HTR2A*	5-hydroxytryptamine receptor 2A
24	-3.2	*AL132780.4*	TEC
25	-3.2	*RCN1P2*	Reticulocalbin 1 pseudogene 2
26	-3.3	*AC005186.1*	Novel transcript
27	-3.7	*TRGV9*	T cell receptor gamma variable 9
28	-3.7	*NTRK3-AS1*	NTRK3 antisense RNA 1
29	-4.0	*LINC00920*	Long intergenic non-protein coding RNA 920
30	-4.0	*NEFL*	Neurofilament light
31	-4.2	*SIRPAP1*	Signal regulatory protein alpha pseudogene 1
32	-4.3	*RAD17*	RAD17 checkpoint clamp loader component
33	-4.5	*EEF1GP1*	Eukaryotic translation elongation factor 1 gamma pseudogene 1
34	-4.5	*KCNH2*	Potassium voltage-gated channel subfamily H member 2
35	-4.6	*BNC1*	Basonuclin 1

36	-4.8	*CRISP3*	Cysteine rich secretory protein 3
37	-4.9	*GSDMA*	Gasdermin A
38	-5.1	*MXRA5Y*	Matrix remodelling associated 5 Y-linked (pseudogene)
39	-5.1	*WDR81*	WD repeat domain 81
40	-5.2	*AGPAT1*	1-acylglycerol-3-phosphate O-acyltransferase 1
41	-5.5	*TGM3*	Transglutaminase 3
42	-5.6	*HLA-DRB1*	Major histocompatibility complex, class II, DR beta 1
43	-5.7	*FP565260.3*	Homo sapiens ICOS ligand (LOC102723996), mRNA.
44	-5.9	*HLA-DQA1*	Major histocompatibility complex, class II, DQ alpha 1
45	-6.2	*AC093700.1*	Proteasome (prosome, macropain) activator subunit 2 (PA28 beta) (PSME2) pseudogene
46	-6.3	*LINC01266*	Long intergenic non-protein coding RNA 1266
47	-12.1	*HLA-DQB1*	Major histocompatibility complex, class II, DQ beta 1

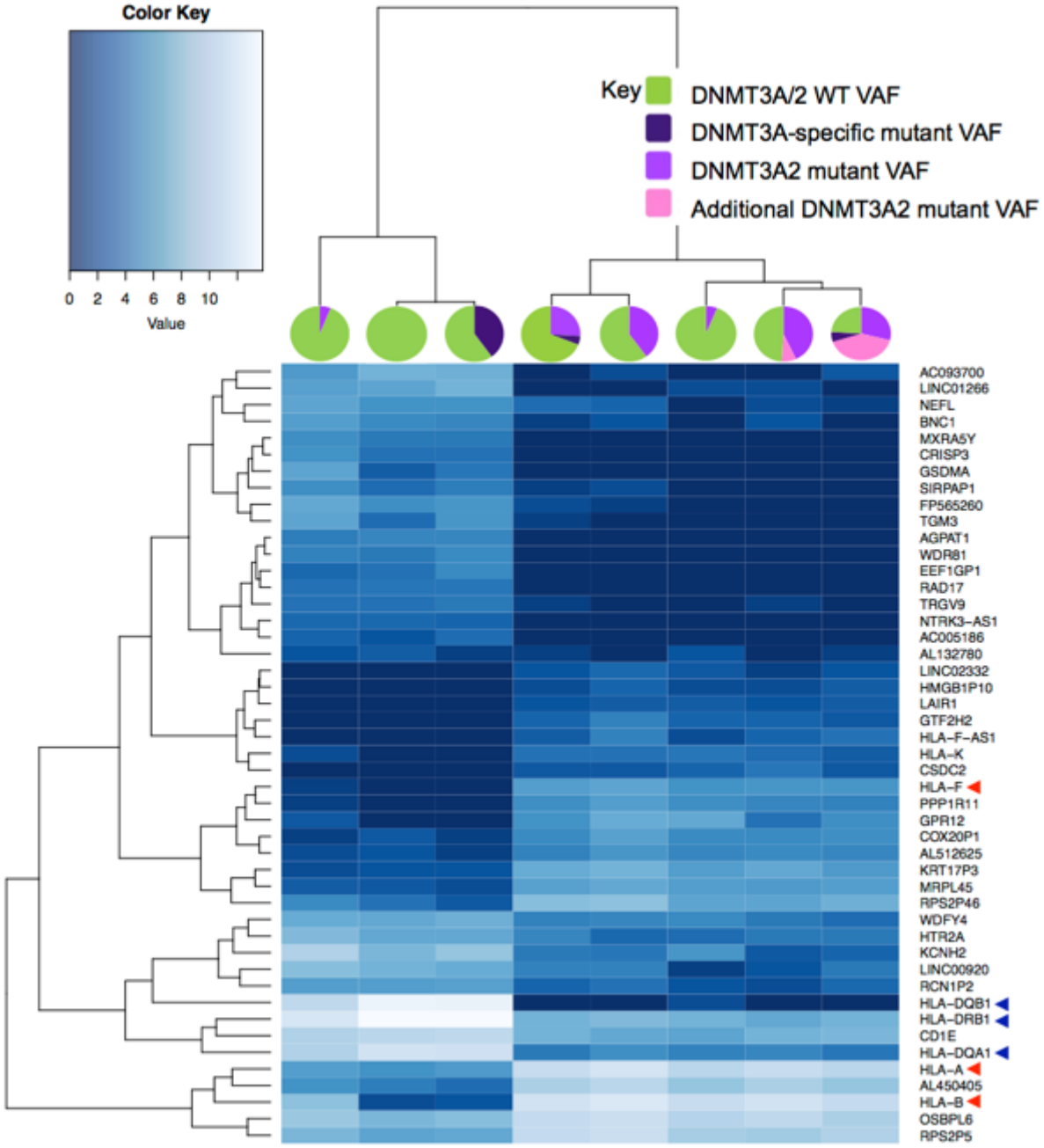

Figure 3-12. *DNMT3A2*-mutant CCS tumours differentially express HLA class I genes. Heatmap of $\log_2$ transformed RNA-Seq read counts for 47 genes significantly differentially expressed (FC2, adjusted *P*-value < 0.05) between CCS tumours with wild type *DNMT3A/2* or *DNMT3A2* mutant VAF ≤0.05 and CCS tumours with *DNMT3A2* mutant VAF >0.05. Pie charts indicate *DNMT3A/2* genotype, dark blue on the heatmap indicates low expression, light blue indicates high expression. Genes encoding HLA class I molecules were highly expressed in *DNMT3A2*-mutant tumours (red arrows). Genes encoding HLA class II molecules were upregulated in tumours with wild type *DNMT3A2* or *DNMT3A2* mutant VAF ≤0.05 (blue arrows).

3.2 Discussion

Despite having distinct histophenotypes, benign cutaneous tumours that arise in CYLD cutaneous syndrome occur due to driver mutations in a single gene (*CYLD*). This study highlights that in addition to biallelic loss of *CYLD*, the epigenetic regulators *DNMT3A* and *BCOR* are recurrently mutated in CCS tumours. Cylindromas and spiradenomas demonstrate both inter-tumoural and intra-tumoural heterogeneity of somatic *DNMT3A* and *BCOR* mutations. These findings imply that mutations *DNMT3A* and *BCOR* confer a selective advantage to CCS tumour keratinocytes, as multiple mutant clones of varying sizes exist within tumours. Furthermore, preliminary methylomic data implies that genes functionally related to β-catenin are hypomethylated in CCS tumours with isoform specific mutations in *DNMT3A2*. Thus, *DNMT3A* and *BCOR* are suggested as new driver mutations in CYLD cutaneous syndrome.

BCOR interacts with the transcription factor BCL6 and is a core subunit of the non-canonical polycomb repressive complex 1.1 (PRC1.1)(Huynh et al., 2000, Gearhart et al., 2006). PRC1.1 epigenetically regulates transcriptional repression through histone modification. BCOR binds to the core PRC1.1 component PCGF1 via its PUFD domain. The core complex recognises unmethylated CpG islands through the subunit lysine demethylase 2B (KDM2B) and adds a ubiquitin moiety to histone H2A at lysine 119 (H2AK119Ub) with the catalytic subunit ring finger protein (RING)1A or RING1B (Astolfi et al., 2019). The H2AK119Ub histone mark represses gene expression and its removal by deubiquitination contributes to gene activation(Vissers et al., 2008). BCL6, a sequence specific transcriptional repressor(Deweindt et al., 1995), binds to the BCOR N-terminus and directs the PRC1.1 to repress target genes including *TP53* and *Cyclin D2* in B cells (Gearhart et al., 2006). BCOR-PRC1.1 is critical for the maintenance of pluripotency in human embryonic stem cells due to its repression of differentiation genes(Wang et al., 2018).

We found somatic *BCOR* mutations in 9/42 CCS tumours (21.4%) analysed by WGS, WES and TDS. The majority of *BCOR* mutations were frameshift or nonsense resulting in a PTC (Figure 3-6). These mutations are predicted to cause loss of function due to truncation before the PUFD domain necessary for direct interaction with PRC1.1 and/or reduction due to nonsense mediated decay (NMD). Germline

heterozygous loss of function mutations in *BCOR* cause the X-linked autosomal dominant developmental disorder oculofaciocardiodental syndrome (OFCD) in females and are lethal in hemizygous males (Ng et al., 2004), highlighting *BCORs* involvement in the development of the eye, heart and craniofacial structures during embryogenesis. In cancer, somatic loss of function mutations in *BCOR* occur in myeloid neoplasms (~10% acute myeloid leukemias (AML) and myelodysplasias), lymphoid neoplasms (<10% pro-lymphatic T leukemias and chronic lymphocytic leukemias rising to 20 – 30% diffuse splenic lymphoma of the red pulp and extra-nodal NK/T-cells lymphoma, nasal type), central nervous system tumours (retinoblastomas, high-grade glial tumours and medulloblastomas) and a range of carcinomas including adenoid cystic carcinoma and lung tumours(Astolfi et al., 2019).

BCOR loss of function analysis using a mouse conditional *Bcor* allele ($Bcor^{Fl}$) was associated with upregulation of *HoxA5*, *HoxA7*, *HoxA9* and *HoxB4* genes in cultured *Bcor*-mutant ($Bcor^{-/Y}$) bone marrow cells from $Bcor^{Fl/Y}$ mice(Cao et al., 2016). The mutant allele was generated in vitro with CRE-recombinase induced deletion of the floxed *Bcor* exons 9 and 10, resulting in a PTC prior to the PUFD domain. ChIP-quantitative PCR found a significant reduction of H2AK119Ub at the promoters of *HoxA5*, *HoxA7* and *HoxA9* while global levels of H2AK119Ub remained unchanged in *Bcor*-mutant cells. Gene expression analysis in myelodysplastic syndrome (MDS) patient samples with and without somatic *BCOR* mutations confirmed overexpression of *HOXA9* in *BCOR*-mutated MDS. When the same *Bcor* conditional allele was used in vivo with tamoxifen-induced knockout specifically in haematopoietic stem cells (HSCs), loss of function resulted in increased expression of PRC1.1 target genes including *HoxA7* and *HoxA9* and locus specific reduction in H2AK119Ub was significantly associated with increased gene expression(Kelly et al., 2019).

The conditional $BCOR^{Fl}$ knockout allele has now been used to characterise BCOR-PRC1.1 loss of function in OFCD affected tissues during murine development(Hamline et al., 2020) and in vivo studies mimicking somatic *BCOR* loss of function mutations in non-haematological malignancies are newly emerging. Modelling of somatic *BCOR* loss of function in paediatric Sonic Hedgehog (SHH)-medulloblastoma with conditional knockout using $Bcor^{Fl}$ in granule neuron progenitors (GNPs) again implicating decreased PRC1.1 mediated H2AK119Ub at the promoter of an aberrantly upregulated driver gene (*Igf2*)(Kutscher et al., 2020).

Known BCL6-dependent roles in GNP differentiation were unaffected and C-terminally truncated BCOR was detected by immunoblot, suggesting C-terminally truncated Bcor can still bind to and act with BCL6 in GNP *Bcor*-mutant cells. Similar to in vivo studies of somatic *BCOR* mutations in AML and MDS, *Bcor* truncation alone was not sufficient for malignant transformation. In SHH-medulloblastoma this required heterozygous mutation of the oncogene *Ptch1* and in myeloid cells *Bcor* truncation cooperated with mutant *Kras* or *Tet2* to drive aggressive tumourigenesis(Tara et al., 2018, Kelly et al., 2019).

Although CCS tumours in this study were heterozygous for C-terminally truncating somatic *BCOR* mutations, it is likely that BCOR-PRC1.1 function is reduced or lost in *BCOR*-mutant CCS tumour clones. As *BCOR* is located on the X chromosome, *BCOR*-mutant clones in CCS tumours from male patients solely express the mutant allele. Data from 14 female AML patients with heterozygous somatic *BCOR* mutations suggests mutations affect the functional allele, as the mutant allele was exclusively expressed, and the wild type allele silenced by X-chromosome inactivation. Furthermore, reduced levels of *BCOR* mRNA, absence of full length BCOR and low levels of truncated BCOR were demonstrated in AML patient samples with heterozygous *BCOR* loss of function mutations similar to those found in CCS tumours and OFCD(Grossmann et al., 2011).

Due to the similarity of somatic mutations in CCS to those in AML, MDS and medulloblastoma, it is hypothesised that C-terminal truncation of BCOR results in the upregulation of BCOR-PRC1.1 target genes due to a reduction of H2AK119Ub at promoters. As BCOR can be replaced in the PRC1.1 by BCORL, which binds to the transcriptional repressor C-terminal binding protein 1 (CTBP1) rather than BCL6, and other PRC1 family complexes can monoubiquitinate H2AK119, global H2AK119Ub levels may be unaltered(Yamamoto et al., 2014, Tamburri et al., 2020). While the identity of aberrantly upregulated BCOR-PRC1.1 target genes in CCS tumour $CYLD^{-/-}/BCOR^{+/-}$ cells are yet to be defined, it is likely that loss of *BCOR* in its PRC1.1 role is cooperating with biallelic loss of the tumour suppressor *CYLD* in CYLD cutaneous syndrome.

DNMT3A and DNMT3B were originally described as the canonical de novo methyltransferase enzymes that establish patterns of methylation at cytosine

residues after genome-wide demethylation occurs during early embryonic development(Okano et al., 1998, Okano et al., 1999). A third canonical maintenance methyltransferase, DNMT1, copies established methylation patterns from the hemimethylated parental DNA strand to the unmethylated daughter strand after replication(Bestor et al., 1988, Leonhardt et al., 1992). DNMT3 enzymes are now thought to be essential for both establishing de novo methylation and maintaining DNA methylation patterns, as inactivation of Dnmt3a and Dntm3b in embryonic stem (ES) cells results in progressive loss of global methylation (Chen et al., 2003).

All three canonical DNMTs use S-adenosylmethionine as a donor to add a methyl group to the C5 position of the cytosine ring to form 5-methylcytosine (5-mC). A related non-canonical family member, DNMT3L, does not possess the catalytic methyl transferase domain but acts as a cofactor with Dnmt3a and Dnmt3b in vitro to stimulate DNA methylation(Suetake et al., 2004). Murine Dnmt3L binds to the C-terminal catalytic domain of Dnmt3a (the tetramer interface) and through a Dnmt3a-Dnmt3a interaction (the dimer interface), forms a heterotetrameric protein complex (Dnmt3L-Dnmt3a-Dnmt3a-Dnmt3L). Dnmt3L recognises and binds to unmethylated lysine 4 of histone H3 (H3K4me0), recruiting Dnmt3a to chromatin where it targets unmethylated cytosine predominantly at CpG dinucleotides(Jia et al., 2007, Ooi et al., 2007). In the absence of DNMT3L, DNMT3A forms a homotetrameric complex in vitro(Holz-Schietinger et al., 2011).

While DNMT-mediated methylation at promoters has been widely associated with transcriptional silencing due to inhibition of transcription factor binding, emerging data suggest that a subset of transcription factors preferentially bind to methylated DNA(Yin et al., 2017). Two recent studies suggest that DNMT3A is preferentially recruited to methylate H3K36me2-enriched intergenic DNA (non-coding regions of euchromatin) and DNMT3B is targeted to methylate H3K36me3-rich gene bodies via their PWWP domains(Weinberg et al., 2019, Xu et al., 2020b).

We found 11 somatic *DNMT3A* mutations in 8/42 CCS tumours (19.1%) analysed by WGS, WES and TDS(Figure 3-3, Table 3-3 & Figure 3-4). Three tumours (7.1%) had mutations in both *DNMT3A* and *BCOR*. A potential synergy between *DNMT3A* and *BCOR* mutation has been noted in haematological malignancies, for example 40% of AML with normal karyotype (NK-AML) cases with mutated *BCOR* also had somatic

mutations in *DNMT3A(Grossmann et al., 2011)*. Further functional investigation will be necessary in CCS tumours to ascertain whether *DNMT3A* and *BCOR* mutations have a synergistic effect. Single cell DNA sequencing (scDNA-seq) of bone marrow mononuclear cells from 123 AML patient samples found 45 samples (37%) had *DNMT3A* mutations and 4 had *BCOR* mutations, 2 of which co-occurred with *DNMT3A (Morita et al., 2020)*. In 3 samples, biallelic loss of *DNMT3A* was confirmed due to two different mutations on different alleles in the same cells. This finding is consistent with the reported role of *DNMT3A* as a tumour suppressor(Yang et al., 2015) and raises the possibility that some of the intra-tumoural heterogeneity reported in this study may be due to different *DNMT3A* mutations co-occurring at the cellular level on different alleles.

Ten of the *DNMT3A* mutations we discovered occurred within functional protein domains, suggesting methylation patterns will be altered in CCS tumour *DNMT3A*-mutant clones (Figure 3-6). Germline heterozygous *DNMT3A* mutations cause the overgrowth disorder Tatton-Brown-Rahman syndrome (TBRS)(Tatton-Brown et al., 2014). Loss of function due to truncation is not necessary to drive pathology, as the majority of mutations (65.5%) in a cohort of 55 TBRS patients were missense and occurred in all three functional domains(Tatton-Brown et al., 2018). Two heterozygous germline missense mutations in the PWWP domain of *DNMT3A* (p.W330R and p.D333N) have been exposed that cause microcephalic dwarfism due to gain of function (hypermethylation), the opposite phenotype to TBRS(Heyn et al., 2019). W330R affects the ability of the DNMT3A PWWP domain to bind to H3K36me2/3 in vitro and a substitution at position 333 has previously been shown to have the same affect(Dhayalan et al., 2010). In vitro characterisation of three TBRS DNMT3A PWWP missense mutations also demonstrates impaired binding to H3K36me3/2 yet results in hypomethylation of intergenic DNA(Weinberg et al., 2019). The PWWP splice site mutation we detected in one CCS tumour (c.1123-2A>G) has been reported in a patient with secondary AML arising after therapy for lymphoma and colon cancer(Fried et al., 2012). This mutation introduced a PTC at amino acid 432, therefore predicting loss of function (hypomethylation) due to absence of the ADD and MTase domains.

Somatic driver mutations in *DNMT3A* are detected in ~25% of de novo acute myeloid leukemia (AML) cases and occur at varying frequencies in other haematological

malignancies across all functional domains(Yang et al., 2015). Heterozygous missense mutations at R882 are frequently detected and account for ~60% of somatic *DNMT3A* mutations in AML. We report one frameshift mutation and 6 missense mutations in the DNMT3A MTase domain, including a substitution at the R882 mutational hotspot from arginine to cysteine (R882C). R882C is the second most common R882 substitution in NK-AML, with RH882H occurring most frequently. Heterozygous R878H mutation in murine ES cells (R882H in humans) causes hypomethylation and prevents wild-type Dnmt3a and Dnmt3b from methylating DNA (Kim et al., 2013b). Russler-Germin et al (2014) confirmed this dominant-negative effect was mediated by mutant DNMT3A^{R882H} inhibiting wild-type DNMT3A from forming active homotetramers by instead forming stable, inactive DNMT3A$^{WT\text{-}R882H}$ heterotetramers in primary NK-AML cells in vitro. We also found two *DNMT3A* missense mutations at R729 in CCS tumours (p.R729W and p.R729Q). R729W is one of three identified AML mutations located along the tetramer interface that disrupt homotetramerization and result in reduced processive methylation(Holz-Schietinger et al., 2012). The nature and location of these heterozygous missense mutations are therefore likely to be pathogenic in CCS and may result in dominant negative effects. This assertion is further supported by conditional knock in of R878H, which is sufficient to cause AML in mice(Dai et al., 2017).

We report that the short isoform *DNMT3A2* is the predominant isoform in CCS tumours (Figure 3-7A). DNMT3A2 lacks 223 aa of the N-terminal regulatory domain of DNMT3A and has a different subcellular localisation pattern(Chen et al., 2002). Dnmt3a localises to nuclear foci corresponding to heterochromatin while Dnmt3a2 has a diffuse nuclear localisation pattern consistent with euchromatin. Dnmt3a and Dnmt3a2 are differentially expressed during murine development, with strong expression of Dnmt3a2 reported in embryonic stem (ES) cells and germ cells suggesting that this isoform is primarily responsible for de novo methylation. Conversely, Dnmt3a2 expression in somatic cells is restricted to testis, spleen and thymus while Dnmt3a is ubiquitously expressed at low levels in all somatic tissues apart from small intestines(Chen et al., 2002). Although DNMT3A2 is widely expressed in human cancers, reports of DNMT3A2 isoform specific functions in solid tumours are scarce(Xu et al., 2020a). In gastric cancer, overexpression of DNMT3A2 directs metastasis via hypermethylation (repression) of *E-cadherin* and regulation of

metastasis-related genes(Cui et al., 2018). CCS tumours with wild-type *DNMT3A* therefore have aberrant expression of the cancer-related *DNMT3A2* isoform that is usually restricted in normal tissues.

The preliminary results of the methylation array hint that hypomethylation of β-catenin pathway related genes may confer an advantage to *DNMT3A2*-mutant clones in CCS tumours (Figure 3-9, Figure 3-10). *Dnmt3a* has a role in somatic HSC differentiation, as conditional homozygous knockout in vivo favours expansion of stem cell populations over differentiated cells(Challen et al., 2011). Mechanistically, the block of differentiation in Dnmt3a/Dnmt3b knock out HSCs is contributed to by hypomethylation of the *Ctnnb1* (β-catenin) promoter resulting in upregulation of β-catenin and β-catenin target genes(Challen et al., 2014). Inhibition of differentiation by β-catenin similarly occurs in mouse embryonic stem cells (ESCs) via the β-catenin target gene *Stat3*, with activation of β-catenin alone sufficient to recapitulate the effects of Wnts on ESC differentiation block(Hao et al., 2006). Overrepresentation of upregulated Wnt signalling pathway genes in tumour cells from chemically induced squamous cell carcinomas has also been described in a keratinocyte conditional Dnmt3a knock out mouse model(Rinaldi et al., 2017). Functional analysis of β-catenin signalling pathway related genes in CCS tumour keratinocytes with *DNMT3A2* mutation and their differential methylation may therefore reveal insights into clonal expansion of these cells.

Another layer of complexity is added by Rinaldi et al's initial study of the roles of DNMT3A and DNMT3B during adult human epidermal stem cell (EpSC) differentiation(Rinaldi et al., 2016). In EpScs, DNMT3A associates with active enhancers in intergenic DNA during differentiation to positively regulate gene expression by maintaining high levels of Tet2-mediation DNA hydroxymethylation in conjunction with the transcription factor p63. Thus, in human epidermal progenitors and differentiated keratinocytes, loss of DNMT3A can lead to both aberrant upregulation of genes due to hypomethylation at promotors and aberrant downregulation of genes due to loss of 5-hydroxymethylcytosine (5-hmC) at enhancers. shRNA knockdown of *DNMT3A* in human EpSCs initially drives differentiation due to reduced expression of genes involved in stem cell identity and maintenance (fos proto-oncogene, AP-1 transcription factor subunit (*FOS*), integrin subunit alpha 6 (*ITGA6*), tumour protein 63 (*TP63*) and keratin 5 (*KRT5*)) then

conversely, when cells have committed, reduces the expression of terminal differentiation genes such as *involucrin*, *loricrin*, *filaggrin* and *cornifin*.

A limitation of our study is the lack of functional analysis of *DNMT3A2* and *BCOR* mutations in CCS tumour models in vitro. Attempts were made to grow clones from primary cells derived from CCS tumours in order to perform *DNMT3A* and *BCOR* genotyping, colony forming assays and a methylation array however extracted DNA did not reach the minimum input requirement for genotyping for the majority of samples. As primary CCS tumour cells did not grow well clonally in vitro, a better approach for future studies will be to study the epigenomics of CCS tumours at the single-cell level with emerging multi-omics methods. For example, TARGET-seq allows targeted biallelic detection of multiple mutations in a single cell at high sensitivity in parallel with unbiased whole-transcriptome profiling(Rodriguez-Meira et al., 2019). This method would generate data on genotype-phenotype correlations at the single cell level for *CYLD*, *BCOR* and *DNMT3A* mutations in CCS tumour cells. Methods have also been established to analyse the methylome and transcriptome (scM&T-seq, scMT-seq) or the genome, methylome and transcriptome (scTRIO-seq) of single cells in parallel. Although this technology does not yet allow detection of single nucleotide variants, single cell multi-omic methods are under intense development(Lo and Zhou, 2018, Lee et al., 2020). Advances in the near future may therefore allow characterisation of *DNMT3A* genotype, methylation and gene expression in CCS tumour single cells. If in vitro methods can be optimised so that *BCOR* genotyped CCS cells are generated in sufficient quantity, combined use of ChIP-Seq and RNA-Seq may also be applied to assess genome-wide H2AK119Ub and gene expression in order to identify functionally relevant BCOR-PRC1.1 target genes.

In summary, this work identifies the epigenetic modifiers *DNMT3A* and *BCOR* as recurrently mutated in CYLD cutaneous syndrome. *BCOR* mutations in CCS tumours predict loss of the transcriptionally repressive H2AK119Ub mark at BCOR-PRC1.1 target genes. Somatic *DNMT3A* missense mutations mimic those in AML, however effects are likely to be tissue specific. Future studies using cutting edge single cell multi-omic methods will help to determine the functional consequences of *DNMT3A* and *BCOR* mutations in CCS tumours and guide targeted therapies in preclinical models of CYLD cutaneous syndrome.

Chapter 4. NF-κB Signalling in CYLD Defective Tumours

4.1 Results

The deubiquitinase CYLD has been established as a negative regulator of canonical NF-κB signalling(Kovalenko et al., 2003, Trompouki et al., 2003, Brummelkamp et al., 2003). This key player in the canonical NF-κB signalling pathway is mutated in CYLD cutaneous syndrome, yet characterisation of NF-κB signalling in human CCS tumour keratinocytes with homozygous *CYLD* mutations is lacking. This chapter aims to investigate the dysregulation of NF-κB transcription factors and target genes in CCS tumour tissue and 3D cell culture models relative to normal skin. Particular focus is given to non-canonical NF-κB signalling via the heterodimer p52:RelB, as a role for CYLD in this pathway has not been defined.

4.1.1 NF-κB signalling is dysregulated in CCS tumours

In preliminary work I highlighted that both canonical and non-canonical NF-κB pathways are dysregulated in CCS tumours relative to normal control skin (unpublished MRes data). To explore this further, additional bulk snap frozen skin tumour samples from genotyped CCS patients were assayed by immunoblot for NF-κB subunit protein levels (Figure 4-1A). In keeping with the role of CYLD as a negative regulator of canonical NF-κB signalling, an increase in RelA and p50 in tumours lacking full length CYLD protein was demonstrated. In the non-canonical NF-κB pathway both p100 and p52 were increased in tumours compared to normal skin, while RelB levels were reduced in some CCS tumours.

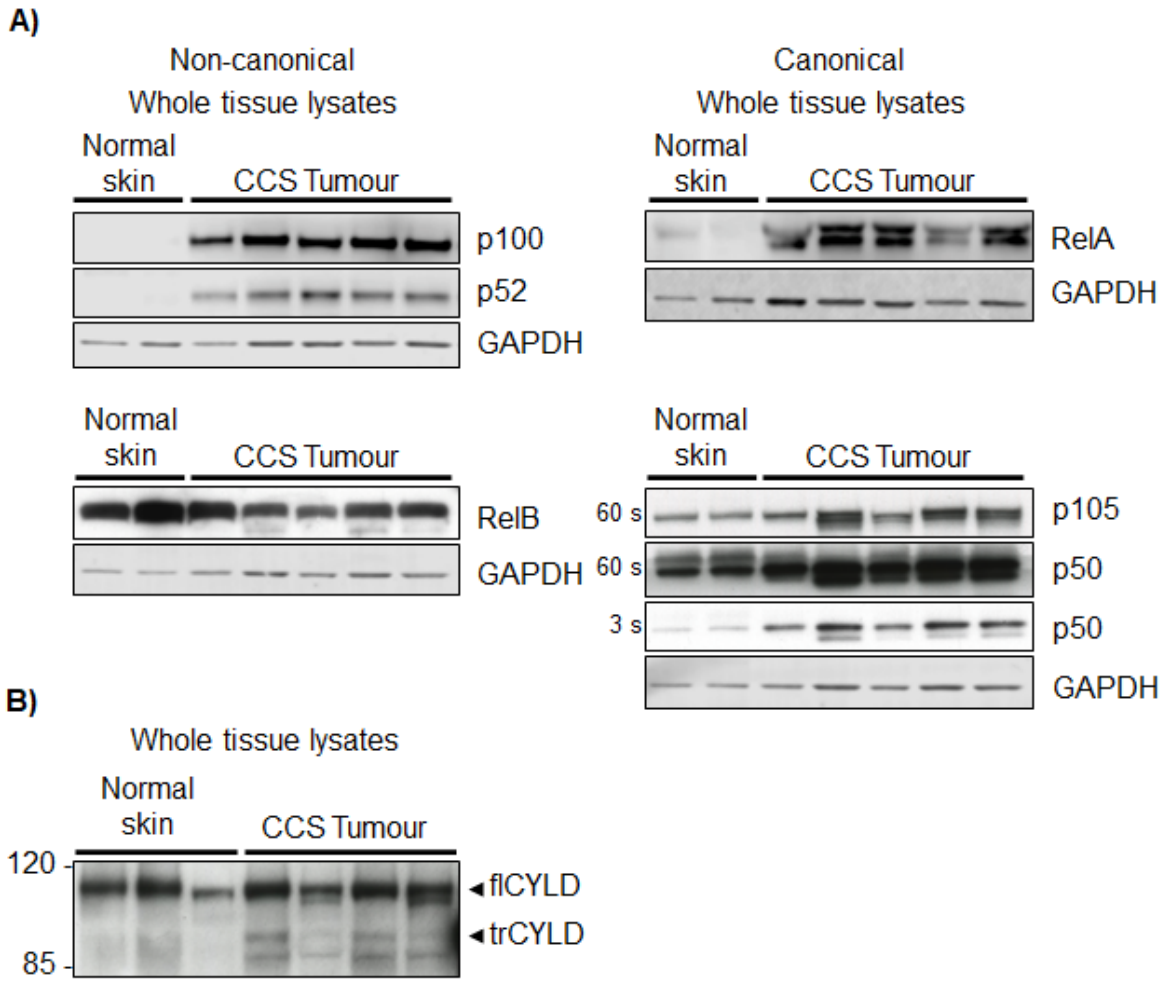

Figure 4-1. NF-κB signalling is dysregulated in CCS tumours. Protein was extracted in 8M urea lysis buffer from snap frozen normal skin and CCS patient tumour samples. Protein levels of A) non-canonical and canonical NF-κB subunits and B) CYLD were assessed by immunoblotting. flCYLD, full length CYLD; trCYLD, (putative) truncated CYLD. s, seconds of X-ray film exposure time.Full length CYLD protein was consistently detected at high levels in whole tumour lysates as well as normal skin (Figure 4-1B). This is posited to be due to the expression of CYLD in immune cells that infiltrate CCS tumours. Cylindroma and spiradenoma tissue contains a mixture of tumour keratinocytes and tumour infiltrating leukocytes (TILs). The TILs are heterozygous for the *CYLD* mutation and can therefore still express the full-length CYLD protein via the wild-type allele. To study CCS keratinocytes without the confounding impact of TILs, models were therefore developed to isolate and study the tumour keratinocytes in order to delineate the effects of CYLD loss in tumour cells.

4.1.2 Expression of non-canonical NF-κB subunits RelB and p100 is increased in 3D primary spheroid cultures derived from CCS tumours

To investigate NF-κB signalling specifically in CCS tumour cells at the protein level, a 3D spheroid culture model was developed for downstream analysis by immunoblotting (Figure 4-2). This model was built on previous work started in the Rajan lab by Dr Naomi Sinclair, who demonstrated the expression of hair cytokeratins (CK14 and CK17) and tropomyosin receptor kinase B (TRKB) by patient-derived CCS tumour spheroids with immunofluorescence (PhD thesis, unpublished data). TRKB is known to be overexpressed by CCS tumours yet is not expressed by CCS tumour derived primary cells grown in 2D adherent monolayer cultures(Rajan et al., 2011b).

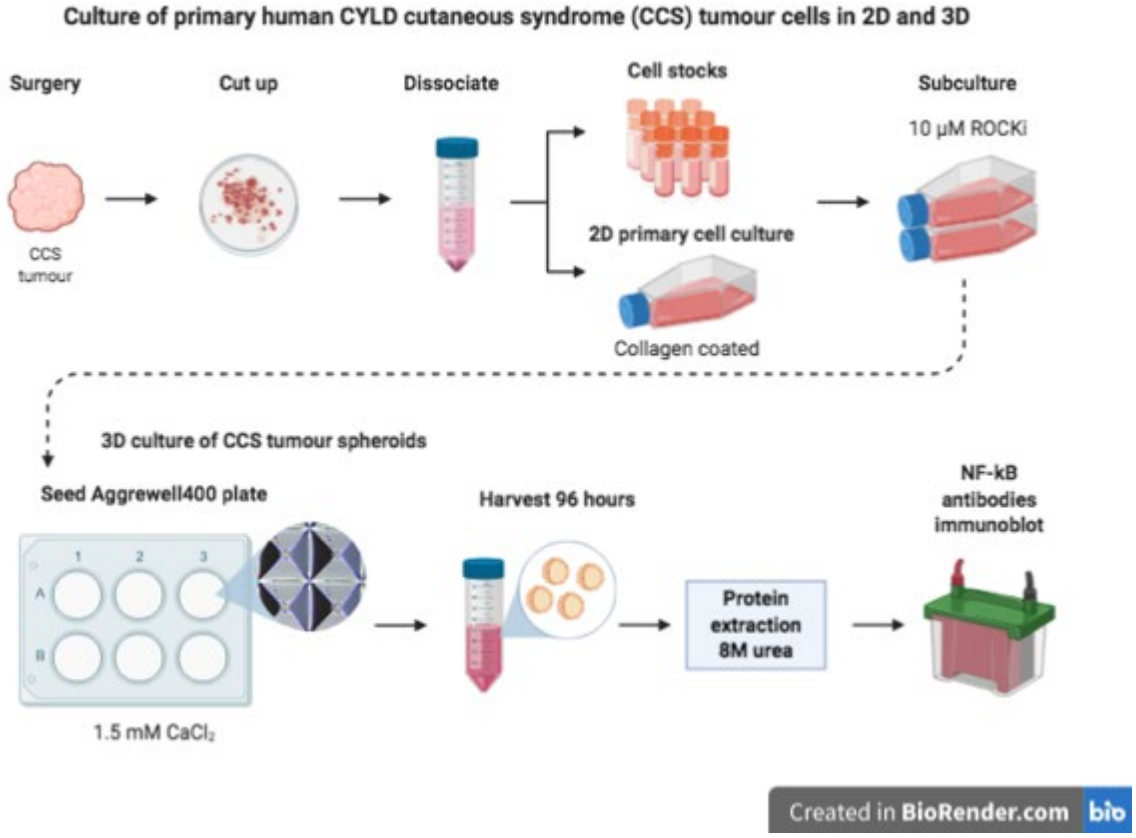

Figure 4-2. 2D and 3D culture of primary human keratinocytes derived from CCS tumours. Fresh CCS tumours were dissociated in 2.5% trypsin and 1 mg/ml collagenase at 37°C. 2D cultured cells were seeded on collagen coated T75 flasks and subcultured in keratinocyte-serum free media (KSFM) supplemented with 10 μM Y-27632 (ROCKi). Two confluent T75 flasks were pooled to seed an Aggrewell400™ plate containing 7000 microwells per well. Within 24 hours, one 3D spheroid aggregate formed per microwell. Spheroids were harvested at 96 hours and protein extracted by sonication in 8M urea lysis buffer for immunoblot analysis of NF-κB signalling.

To obtain CCS primary cells, fresh CCS tumours attained after surgery were cut into ~1 mm^3 pieces and incubated in 2.5% trypsin for 40 minutes at 37°C then 70 minutes

in 1 mg/ml collagenase/DMEM at 37°C. Dissociated tumour cells were filtering through 40 μm filters and single cell suspensions were either seeded directly onto a collagen coated T75 flask in keratinocyte serum free media (KSFM) or cryopreserved in 10% DMSO/FBS.

As human primary keratinocytes have a limited lifespan, 10 μM Y-27632 was added to media during subculture. The rho-kinase inhibitor (ROCKi) Y-27632 allows primary keratinocytes to be grown for longer periods in culture by inhibiting terminal differentiation. The karyotype of primary cells grown with 10 μM Y-27632 remains normal and cells retain the ability to differentiate when Y-27632 is removed(Strudwick et al., 2015).

To generate spheroids, Aggrewell400™ 6 well plates were seeded from 2 pooled confluent T75 flasks. Each well of an Aggrewell400™ plate contains 7000 microwells in which cells form one spheroid aggregate. Spheroids were seeded in culture medium supplemented with 1.5 mM $CaCl_2$, as a physiological calcium concentration is necessary for keratinocyte stem cells in 3D culture to form cell junctions during aggregation(Wallace L., 2013). Primary spheroids were grown in Aggrewell400™ plates for 96 hours then harvested for protein extraction. Protein was extracted from cell pellets by sonication in 8M urea lysis buffer.

Immortalised keratinocyte cell lines, such as HaCaTs, often acquire mutations over time that can confer phenotypic differences to the original cell type(Lehman et al., 1993). To provide a control with the primary human phenotype more analogous to *in vivo* instead of cell lines, a protocol was optimised to obtain keratinocytes from fresh normal human skin. This process involved collecting donated skin on the day of surgery, incubating the tissue in 1U/ml Dispase II/DMEM overnight at 4°C then using fine tweezers to separate the epidermis from the dermis. Epidermal keratinocytes were dissociated in 0.05% trypsin for 30 minutes at 37°C then plated onto a collagen coated T25 flask in media that selects for keratinocytes (EpiLife™ medium). Cells were subcultured with 10 μM Y-27632 into T75s then frozen in 10% DMSO/FBS at passage 3 or used directly to generate spheroids (Figure 4-3A). Different dissociation protocols were necessary due to the different tissue architecture of CCS tumours and normal skin. The Dispase II protease was sufficient for gentle dissociation of normal

skin while collagenase was needed to break down CCS tumours that excessively produce collagen VII(Bruckner-Tuderman et al., 1991).

To confirm the advantage of the 3D spheroid primary cell model over the 2D adherent primary cell model, the levels of RelB and p105/p50 were assessed in both models by immunoblot (Figure 4-3B). As fibroblast contamination is a characteristic problem of 2D primary cell culture, levels of full length CYLD were also assessed to establish whether the 3D culture model is less likely to contain contaminating cells expressing wild type *CYLD*.

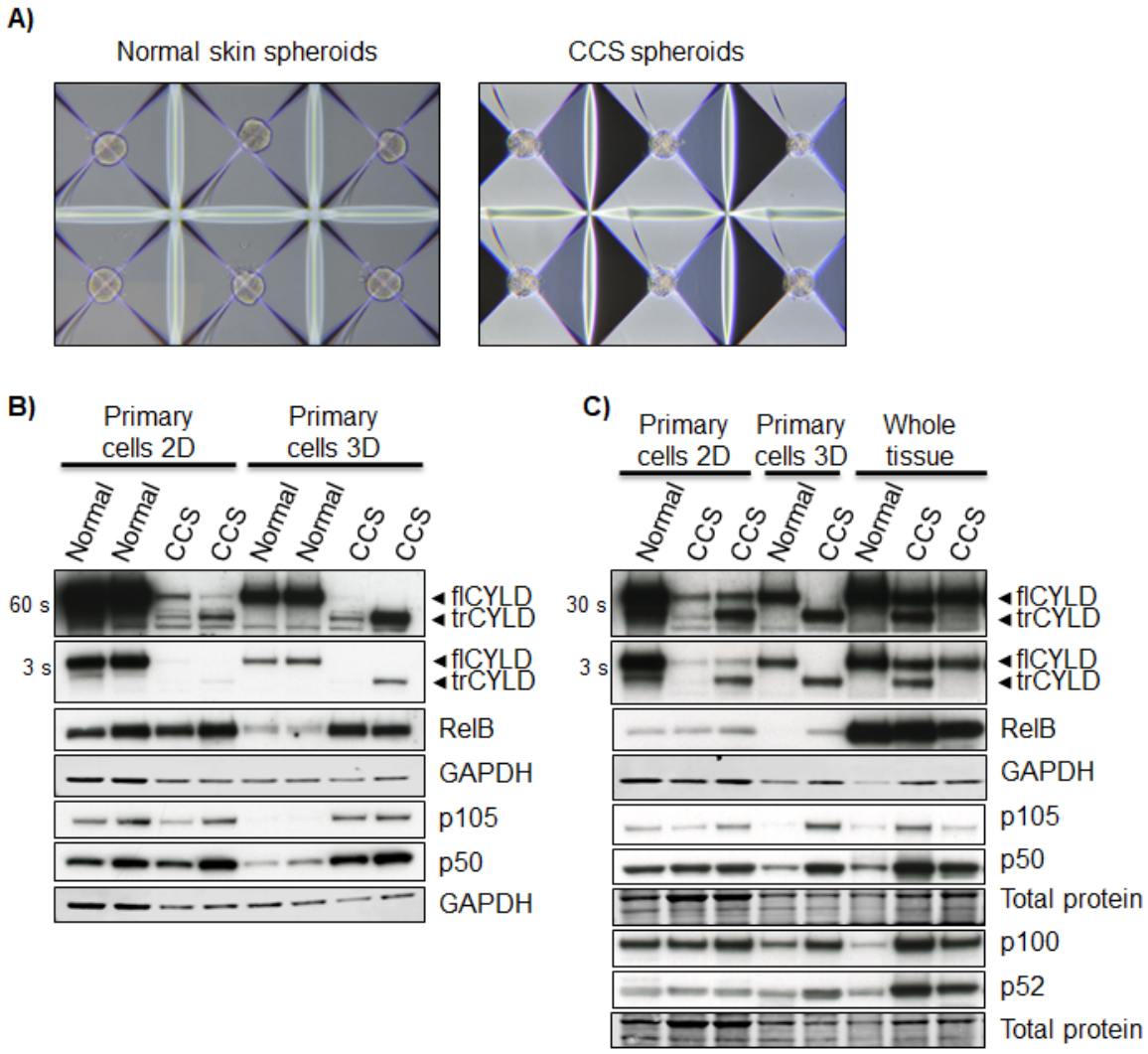

Figure 4-3. CCS primary tumour spheroids provide a purified population of *CYLD* defective cells. Primary cells derived from normal control skin or CCS tumours were cultured in keratinocyte media supplemented with 1.5 mM $CaCl_2$ in Aggrewell™400 plates (3D spheroids) or media without 1.5 mM $CaCl_2$ in monolayer cultures (2D). A) Brightfield images of normal and CCS tumour 3D primary spheroids within 6 microwells of Aggrewell™400 plates. B). Protein was extracted from 2D and 3D cell pellets by sonication in 8M urea and levels of the indicated proteins were assessed by immunoblot. C) Protein levels

in cell lysates and whole tissue lysates from normal skin and CCS patient tumours were assessed by immunoblot as indicated. Loading was evaluated by GAPDH or REVERT Total Protein Stain. GAPDH is shown once below immunoblots from the same gel. flCYLD, full length CYLD; trCYLD, truncated CYLD; s, seconds of X-ray film exposure time.

Based on levels of flCYLD, the 3D CCS spheroids resulted in purer populations of CYLD defective keratinocytes ($CYLD^{-/-}$) relative to 2D CCS lysates. flCYLD in CCS lysates was presumed to originate from fibroblasts heterozygous for the *CYLD* mutation ($CYLD^{+/-}$) that can survive in the culture medium and are able to express flCYLD from the wild-type allele.

Levels of RelB and p50 were strongly increased in 3D CCS spheroid lysates relative to normal controls (Figure 4-3B). Levels of RelB and p105/p50 appeared unaltered between normal and CCS 2D samples, however the GAPDH loading controls suggest that the normal 2D lysates were overloaded.

After the 2D normal lysates were diluted and re-measured by BCA assay, further immunoblots were carried out (Figure 4-3C). Lysates from whole tissue were also included to allow comparison of *in vitro* models to *in vivo*. Achieving equal loading across 2D, 3D and whole tissue (measured by both GAPDH and REVERT Total Protein Stain) proved difficult, potentially due to tissue sample contaminants such as lipids that affect accurate protein measurement. According to GAPDH, loading between 2D lysates on the CYLD and RelB blots was even. Confirming results in Figure 4-3B, levels of RelB, p105/p50 or p100/p52 remained unaltered between normal and CCS 2D lysates. The spheroid model better recapitulated tumour lysates for increased p50 and p100/p52. Comparison of RelB across models suggests that the spheroid model may offer additional insights that would otherwise be masked by NF-κB signalling from TILs or fibroblast contamination.

In view of these results, the 3D spheroid model was deemed to be superior to 2D primary cell culture and levels of all NF-κB subunits were analysed in primary spheroid lysates (Figure 4-4).

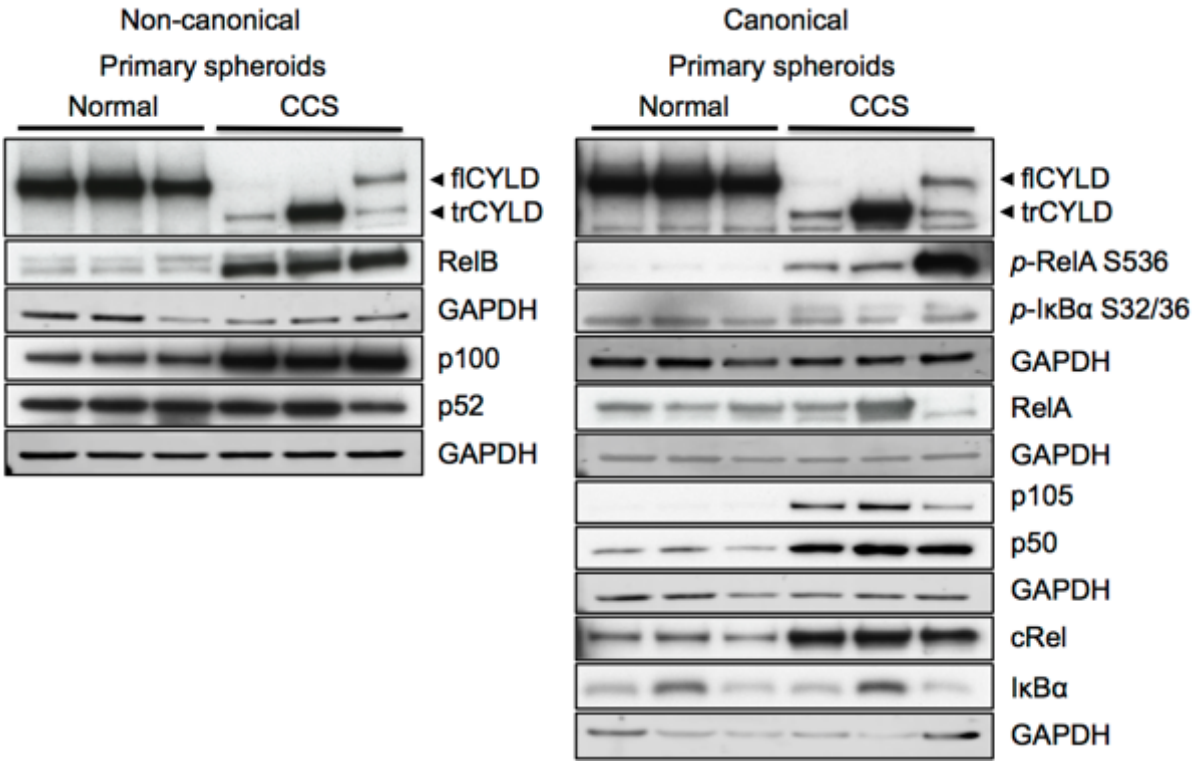

Figure 4-4. CCS primary tumour spheroids display increased levels of non-canonical and canonical NF-κB subunits. CCS tumour and normal skin primary spheroids were generated in Aggrewell^{TM}400 plates and protein was extracted by sonication in 8M urea. Levels of the indicated proteins were assessed by immunoblot. CCS spheroids in lanes 4 and 6 were derived from tumours with a 1bp deletion in *CYLD* (c.2460delC), Lane 5 spheroids were derived from a tumour with a splice site mutation (c.2469+1A>G). GAPDH is shown once below immunoblots from the same gel. flCYLD, full length CYLD; trCYLD, truncated CYLD.

Confirming results in whole tissue lysates (Figure 4-1A), CCS spheroids from 3 patients showed increased levels of expression of both canonical and non-canonical subunits (Figure 4-4B). c-Rel and p105/p50 were clearly increased in CCS spheroids while levels of RelA phosphorylated at serine 536 suggest the canonical signalling pathway is active in tumour keratinocytes. A double band for *p*-IκBα (Ser32/36) was detected in CCS spheroids while a single band was detected in normal skin spheroids. As the antibody used should detect one band for IκBα phosphorylated at serines 32 and 36, and total IκBα levels were variable between samples, it is probable that the smaller, homogenously expressed band in the *p*-IκBα immunoblot is a non-specific band and the higher molecular weight band is phosphorylated IκBα. In the non-canonical pathway, CCS spheroids displayed a strong increase in both RelB and p100. flCYLD was detected in one CCS spheroid lysate, confirming fibroblast contamination is possible in the 3D culture model.

In the whole tumour and spheroid CYLD immunoblots, a smaller band around 90 kDa was detected (Figure 4-1B, Figure 4-3B-C and Figure 4-4). This band resolves at the predicted size of the truncated CYLD product resulting from the c.2460delC *CYLD* mutation, which results in a PTC in exon 18 (p.C820*). The splice site mutation c.2469+1A>G occurs at the splice donor site of exon 18 with unknown consequences at the protein level. All lysates derived from tumours from the patient with this mutation invariably produce a strong band ~90 kDa detected by the CYLD antibody (see Figure 4-3B lane 8, Figure 4-3C lanes 3, 5 and 7 and Figure 4-4 lane 2). The identity of this band, designated 'trCYLD', will be addressed in chapter 5.

In summary, these results suggest that both the canonical and non-canonical NF-κB signalling pathways are upregulated in CCS tumour keratinocytes. I chose to focus particularly on dysregulation of the non-canonical NF-κB pathway, as the role of CYLD in this pathway is understudied.

4.1.3 FACS purified CCS tumour keratinocytes express signature cytokeratins

Tumours consist of different cell types, including endothelial cells, tumour-associated fibroblasts and infiltrating immune cells, which together make up the Tumour Microenvironment(Hanahan and Weinberg, 2011). Identifying the quantity and type of immune cells within the tumour microenvironment can help to predict responsiveness to immunotherapies such as immune-checkpoint blockade(Binnewies et al., 2018). As highlighted by whole CCS tumour western blots (Figure 4-1 and Figure 4-3), analysing whole tumours can be problematic due to signals from TILs that can obscure or confuse the detection of signalling in the tumour cells. To address this and investigate both the CCS tumour cells and TILs as separate purified populations, a flow activated cell sorting (FACS) based CD45 depletion method was used to isolate cells from fresh tumours (n = 5) or normal skin (n = 4) for downstream analysis by RNA-seq (Figure 4-5). RNA-seq allows transcriptome-wide analysis of differential gene expression between samples. This is important because characterising differences in gene expression between the tumours cells and normal skin keratinocytes will help to elucidate which cellular pathways, molecular functions and biological processes are affected by *CYLD* mutation. Similarly, looking at differences in gene expression between the TILs and normal skin immune cells may

give insights into the CCS tumour immune microenvironment that may inform future therapeutic strategies.

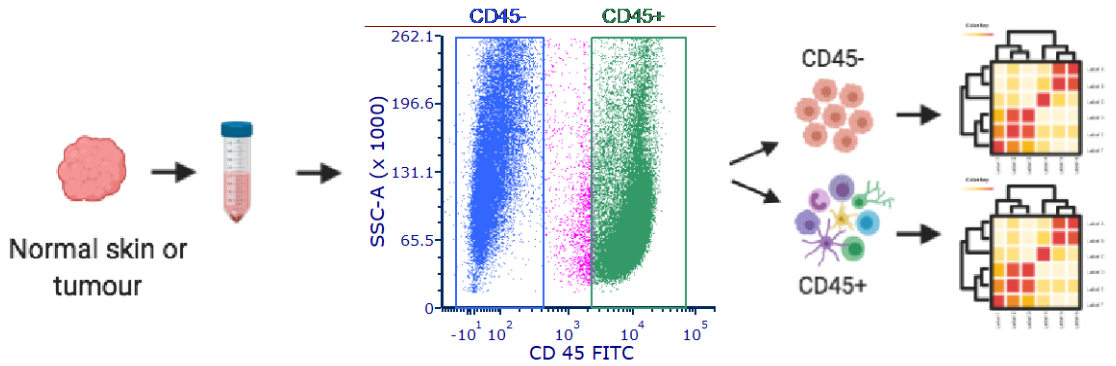

Figure 4-5. FACS separation of CCS tumour keratinocytes and tumour infiltrating leukocytes (TILs) by CD45 depletion. Fresh CCS patient tumours or normal skin were dissociated into single cell suspensions and stained with CD45-FITC conjugated antibody. Cell suspensions were separated by FACS into CD45+ CCS tumour/normal skin immune cells and CD45- CCS tumour/normal skin keratinocytes.

Immediately after surgery, normal skin or CCS tumours were dissociated into single cells and stained with CD45 antibody conjugated to a fluorescent dye (FITC). CD45 was used to label the immune cells prior to FACS because CD45 protein is expressed on all nucleated cells of hematopoietic lineage(Trowbridge and Thomas, 1994, Hermiston et al., 2003). Mixed populations of cells were separated by flow cytometry into populations of $CD45^+$ leukocytes and $CD45^-$ tumour cells, which are predominantly keratinocytes, but may include endothelial cells and fibroblasts. Hereafter, I refer to the CD45- cells in relation to their dominant fraction of keratinocytes. Both $CD45^+$ leukocyte and $CD45^-$ keratinocyte populations were collected after FACS for RNA extraction. An input fraction of disassociated cells was also taken prior to staining, resulting in the derivation of three fractions from each sample (input, $CD45^+$ and $CD45^-$) that were subject to RNA-seq (Table 4-1). After TapeStation quality control for RNA integrity, 40 samples were selected for RNA sequencing including snap frozen whole tissue from 10 CCS tumours and 3 unrelated normal skin samples.

Table 4-1. RNA-seq sample information. Sorted fractions with ultra-low RNA concentrations were excluded from quality control analysis to preserve sample volume. RIN; RNA integrity number.

Sample No.	Description	Fraction	RNA (ng/µl)	RIN
1	Normal skin	Input	63	8.9
2	Normal skin	CD45 positive	3.35	
3	Normal skin	CD45 negative	2.9	
4	Normal skin	Input	24.3	8.2
5	Normal skin	CD45 positive	2.63	
6	Normal skin	CD45 negative	7.16	
7	Cylindroma	Input	146	8.4
8	Cylindroma	CD45 positive	46	9.5
9	Cylindroma	CD45 negative	32.8	9.1
10	Cylindroma	Input	63	9
11	Cylindroma	CD45 positive	35.2	9.1
12	Cylindroma	CD45 negative	4.2	
13	Spiradenoma	Bulk tissue	80	9.1
14	Cylindrospiradenoma	Bulk tissue	27	9.6
15	Cylindroma	Bulk tissue	88.8	9.4
16	Cylindroma	Input	42.6	9
17	Cylindroma	CD45 positive	15.7	7.3
18	Cylindroma	CD45 negative	5.94	
19	Normal skin	Input	56.2	8.9
20	Normal skin	CD45 positive	16.2	8.7
21	Normal skin	CD45 negative	14.7	8.7
22	Normal skin	Input	41.1	8.9
23	Normal skin	CD45 positive	10.4	
24	Normal skin	CD45 negative	9.48	
25	Cylindroma	Input	104	8.8
26	Cylindroma	CD45 positive	71.4	9.2
27	Cylindroma	CD45 negative	52.8	9.3
28	Cylindroma	Input	83.4	8.9
29	Cylindroma	CD45 positive	32.2	8.7
30	Cylindroma	CD45 negative	31.8	8.9
31	Normal skin	Bulk tissue	65.8	6
32	Normal skin	Bulk tissue	65.4	5.3
33	Normal skin	Bulk tissue	104	9.1
34	Cylindroma matched to FACS #25	Bulk tissue	98.2	8.5
35	Cylindroma matched to FACS #28	Bulk tissue	154	8.4
36	Cylindroma	Bulk tissue	65.2	9.7
37	Cylindrospiradenoma	Bulk tissue	38	9.3
38	Cylindroma matched to FACS #7	Bulk tissue	90.6	9.3
39	Spiradenoma	Bulk tissue	36.2	9.7
40	Cylindroma	Bulk tissue	17.6	9.3

Single-end sequencing on an Illumina Novaseq 6000 produced an average of 24,400,000 75-bp reads per sample. In R(R Core Team, 2019), count data was filtered according to standard criteria (genes with a total count < 15 were removed). This removed 25,794 genes from consideration, leaving 32,882 of the original 58,676 for statistical tests. Normalised and transformed count data explored by principal component analysis (PCA) showed that samples clustered by group and phenotype (Figure 4-6).

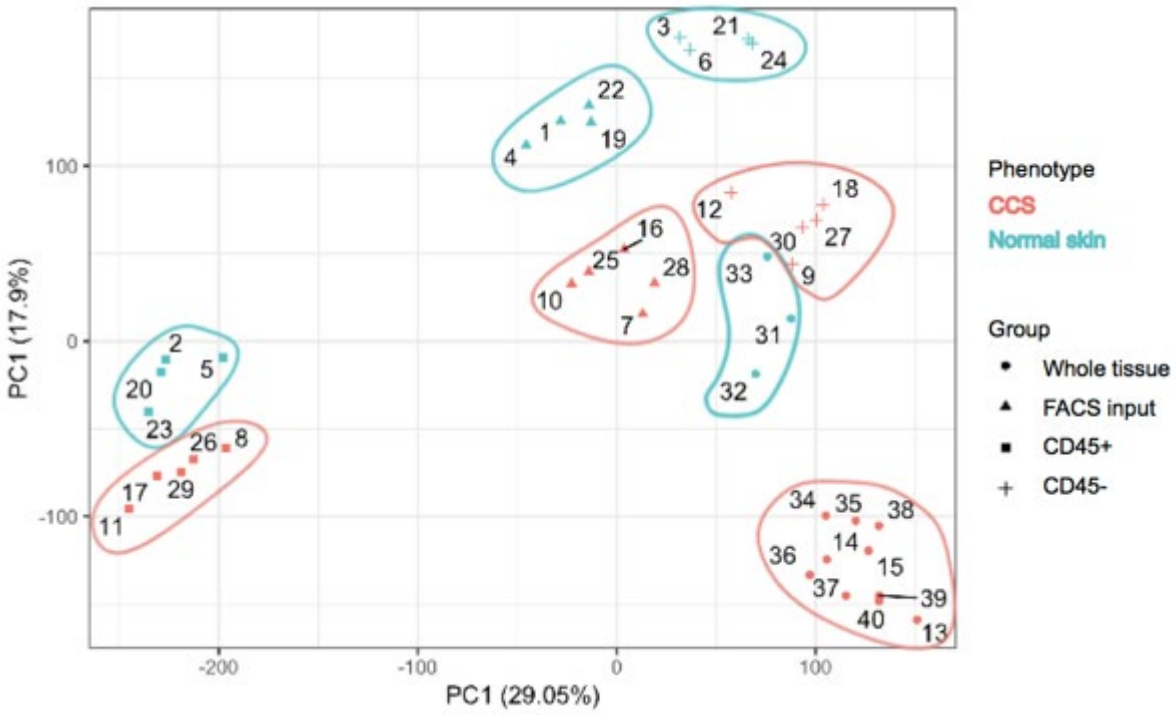

Figure 4-6. Principle component analysis (PCA) of RNA-seq read counts from CCS tumours and normal skin. RNA-seq read counts were normalised by the trimmed mean of *M*-values (TMM)(Robinson and Oshlack, 2010) method in edgeR(Robinson et al., 2010), transformed by variance modelling at the observational level (voom)(Law et al., 2014) in limma(Ritchie et al., 2015) then submitted to ggplot2(Wickham, 2016) for PCA. cDNA was sequenced from whole tissue, unsorted cells dissociated from whole tissue (FACS input) and CD45 positive or negative cells isolated from dissociated tissue by FACS.

Due to sample processing there was an impact on the transcriptome, as demonstrated by separate clustering of the dissociated FACS input group (triangles on PCA) from the whole tissue group (circles). The $CD45^-$ CCS tumour keratinocytes cluster separately from the $CD45^-$ normal skin keratinocytes (plus symbols) and the CD45+ immune cells from CCS tumours clustered separately from normal skin immune cells (squares). To explore this further, genes were analysed for differential expression between CCS and normal skin samples in all groups using cut-offs of

log_2fold change (FC) > 1 and *P*-value (adjusted for multiple testing via Benjimini-Hochberg False Discovery Rate) < 0.05. Results were visualised with volcano plots to assess the robustness of the FACS based CD45 depletion method, as differences between the whole tissue and input groups give an idea of how gene expression was affected during dissociation (Figure 4-7).

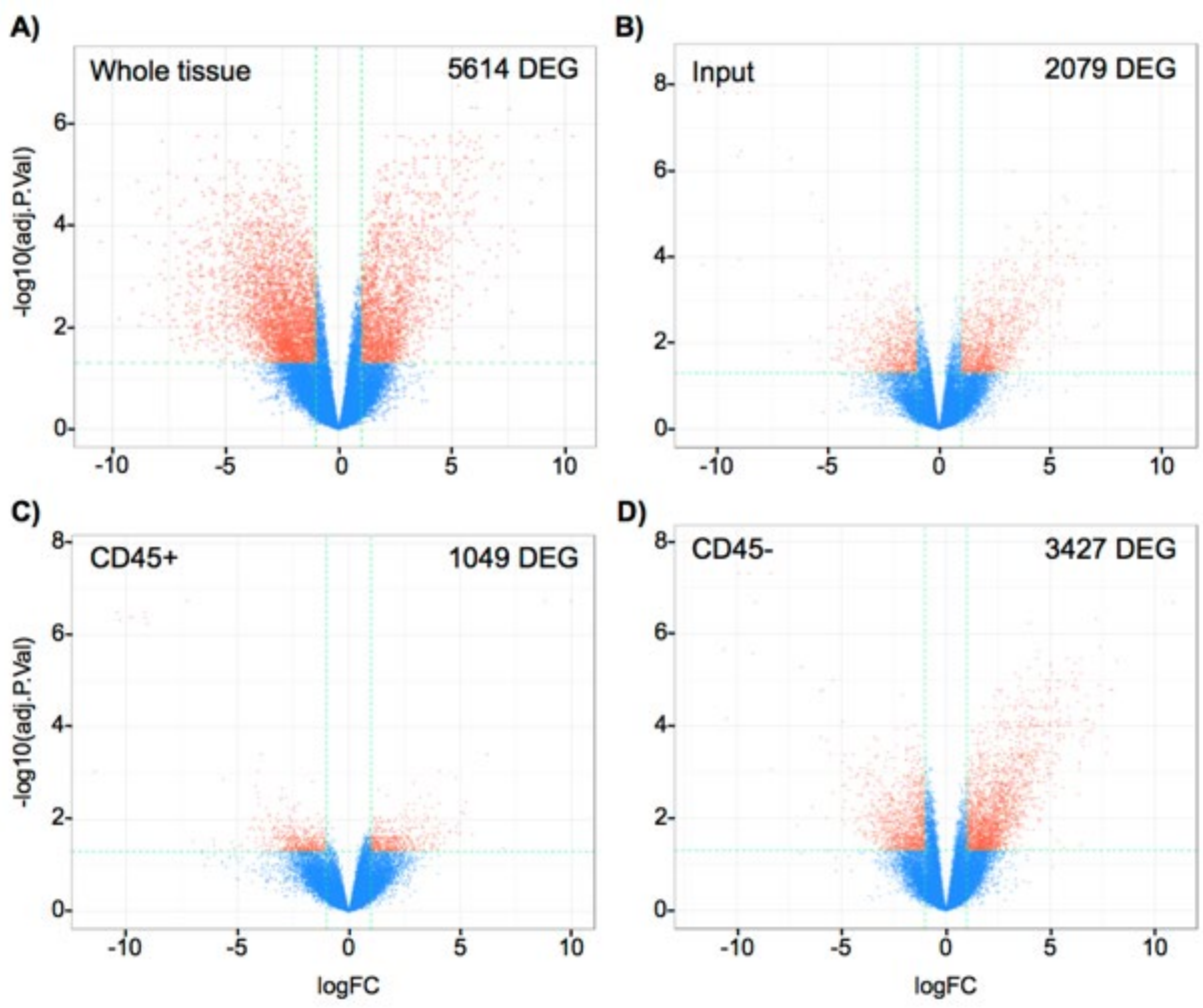

Figure 4-7. Volcano plots showing differential gene expression between CCS and normal skin samples. Gene expression was analysed by DESeq2(Love et al., 2014) with a threshold of log_2FC > 1 in either direction and adjusted *P*-value < 0.05. Orange data points are significantly differentially expressed genes; blue data points are not significant. Positive fold-change indicates expression is higher in CCS samples and lower in normal skin, negative fold-change indicates expression is lower in CCS samples. A) Whole tissue samples. B) Unsorted cells dissociated from whole tissue (Input). C) CD45 positive leukocytes isolated by FACS. D) CD45 negative tumour cells isolated by FACS. DEG; differentially expressed genes.

Comparison of differentially expressed genes (DEGs) between whole tissue and input groups confirmed that some in vivo information is lost through the process of generating the cell suspension, a key example being that significant upregulation of

NTRK3 (FC 3.4) and *NTRK2* (FC 3.3) in CCS whole tumour tissue was lost from the Input and $CD45^-$ sorted keratinocyte fractions. These genes encode TRKC and TRKB respectively, which are overexpressed in CCS tumours in vivo(Rajan et al., 2011b). The top 20 upregulated and downregulated DEGs (ranked by FC) from the RNA sequencing of $CD45^+$ and $CD45^-$ cells are shown in Table 4-2. Genes on the sex chromosomes were excluding from the top 20 DEG lists as these were overrepresented due to the genders of the normal skin donors (male) and CCS patients (female).

Table 4-2. The top 20 upregulated and downregulated DEGs (ranked by log_2FC) from CD45+ leukocytes and CD45- keratinocytes enriched by FACS.

No.	logFC	Gene	Description
CD45+ leukocyte DEGs			
1	6.9	IGLV3-19	Immunoglobulin lambda variable 3-19
2	5.6	SOX11	SRY-box 11
3	5.3	VPREB3	V-set pre-B cell surrogate light chain 3
4	5.2	FCRL1	Fc receptor like 1
5	5.0	ODAM	Odontogenic, ameloblast associated
6	5.0	GABRP	Gamma-aminobutyric acid type A receptor pi subunit
7	5.0	TCL1A	T cell leukemia/lymphoma 1A
8	5.0	CLCA4	Chloride channel accessory 4
9	4.8	IGHM	Immunoglobulin heavy constant mu
10	4.8	B4GALNT3	Beta-1,4-N-acetyl-galactosaminyltransferase 3
11	-4.5	TMEM233	Transmembrane protein 233
12	-4.6	TRIM63	Tripartite motif containing 63
13	-4.9	PRR26	Proline rich 26
14	-5.1	AL157895.1	Antisense, uncharacterised
15	-5.2	TPSG1	Tryptase gamma 1
16	-5.8	CMA1	Chymase 1
17	-6.0	TPSB2	Tryptase beta 2 (gene/pseudogene)
18	-6.1	CALB2	Calbindin 2
19	-6.6	HLA-C	Major histocompatibility complex, class I, C
20	-7.0	ADCYAP1	Adenylate cyclase activating polypeptide 1
CD45- keratinocyte DEGs			
1	8.2	EDAR	Ectodysplasin A receptor
2	8.0	SOX14	SRY-box 14
3	7.9	SERPINA11	Serpin family A member 11
4	7.7	CLCA4	Chloride channel accessory 4
5	7.7	DLX2	Distal-less homeobox 2
6	7.5	CLEC4F	C-type lectin domain family 4 member F
7	7.4	ODAM	Odontogenic, ameloblast associated
8	7.4	AC022509.1	Novel transcript, antisense to SSPN

9	7.3	KCNJ5	Potassium voltage-gated channel subfamily J member 5
10	7.1	NPPC	Natriuretic peptide C
11	-5.0	CIDEA	Cell death-inducing DFFA-like effector a
12	-5.0	HSPB3	Heat shock protein family B (small) member 3
13	-5.0	BMP3	Bone morphogenetic protein 3
14	-5.4	KRTDAP	Keratinocyte differentiation associated protein
15	-5.4	SPRR1A	Small proline rich protein 1A
16	-5.5	SPRR1B	Small proline rich protein 1B
17	-5.7	AC079467.1	Processed transcript
18	-6.0	PNLIPRP3	Pancreatic lipase related protein 3
19	-6.4	ADAMDEC1	ADAM like decysin 1
20	-7.1	HLA-C	Major histocompatibility complex, class I, C

Next, the $CD45^-$ normal and CCS tumour keratinocytes were compared to see if there were significant changes in the expression of cytokeratin genes and how this compared with published cytokeratin profiles from CCS cutaneous and pulmonary cylindromas (Brown et al., 2018). The sorted CCS tumour CD45- keratinocytes had a similar cytokeratin profile to those previously reported in CCS tumours, including significant overexpression of *KRT8*, *KRTCAP3* and *KRT13* and downregulation of *KRT1*, *KRT6A* and *KRT2* (Figure 4-8), confirming these cells are indeed CCS tumour keratinocytes. In keeping with the skin appendage origin of CCS tumours, the keratin with the highest positive fold-change (FC4.3, *KRT74*, syn. *K6IRS4*) is normally expressed specifically in the Huxley cells of the hair follicle(Rogers et al., 2003), the compartment of the inner root sheath where CYLD is strongly expressed in normal hair follicles(Massoumi et al., 2006b).

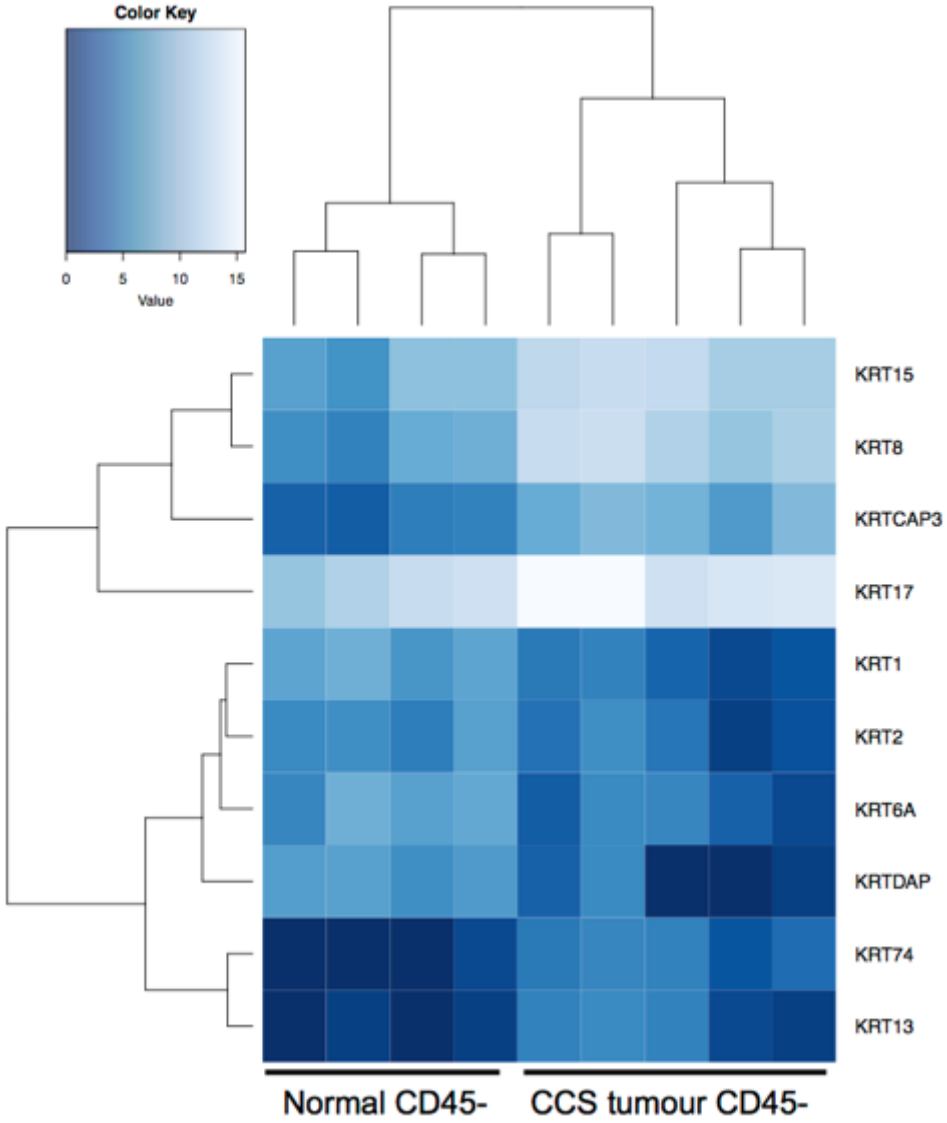

Figure 4-8. CD45$^-$ CCS tumour keratinocytes have a different cytokeratin profile to CD45$^-$ normal skin keratinocytes. CD45$^-$ keratinocytes isolated from CCS tumours and normal skin by FACS differentially express 10 protein coding keratin genes ($log_2FC>2$, adjusted *P*-value < 0.05). Dark blue indicates low expression, light blue indicates high expression. The gene encoding keratin 74 (*KRT74*), a hair follicle specific keratin, was ranked first by positive fold-change.

4.1.4 NF-κB transcription factor binding sites are significantly over-represented in genes up-regulated by CCS tumour keratinocytes

As the RNA-seq differential gene expression analysis resulted in large gene lists, functional enrichment was used to identify groups of genes that were over-represented in each dataset more than would be expected by chance. It was hypothesised that both canonical and non-canonical NF-κB target genes would be enriched in the CD45- CCS tumour keratinocytes relative to CD45- normal skin

keratinocytes. All groups were subjected to functional enrichment analysis to allow comparison of NF-κB target gene or pathway enrichment between the TILs and tumour keratinocytes. The functional enrichment analysis was first performed on the top 500 positive DEGs (ranked by fold change) in each group using g:Profiler g:GOSt (version e99_eg46_p14_f929183) with g:SCS multiple testing correction method applying significance threshold of 0.05(Raudvere et al., 2019). g:GOSt maps input gene lists to functional information sources including Gene Ontology (GO), the Human Protein Atlas (HPA) and CORUM: the comprehensive resource of mammalian protein complexes. The top 20 significantly enriched terms from each information source are given in Appendix B. Here, as we are interested in whether NF-κB target gene expression is increased in CCS tumour keratinocytes and wish to identify potential NF-κB target genes dysregulated in CYLD cutaneous syndrome, I focus on the significant regulatory motif matches from TRANSFAC® (http://genexplain.com/transfac/), the database of eukaryotic transcription factors and their binding sites(Knuppel et al., 1994) (Figure 4-9).

g:GOSt retrieves putative transcription factor binding sites (TFBSs) from the TRANSFAC database using a prediction pipeline. The program Match^{TM} uses the position weight matrix (PWM) library in TRANSFAC to find TFBSs +/-1kb from transcription start sites (TSS) (Kel et al., 2003). TRANSFACS PWMs are derived from experimental data and reflect the base preference in each position of the TFBS. TSS are provided by annotating principal splice isoforms (APPRIS) through Ensembl biomart. If a gene has multiple TSS, g:GOSt selects the one with the most transcription factor matches. Matches are split into two groups that are not mutually exclusive; match class 0 TFBSs have at least 1 match per gene and match class 1 TFBSs have at least 2 matches per gene.

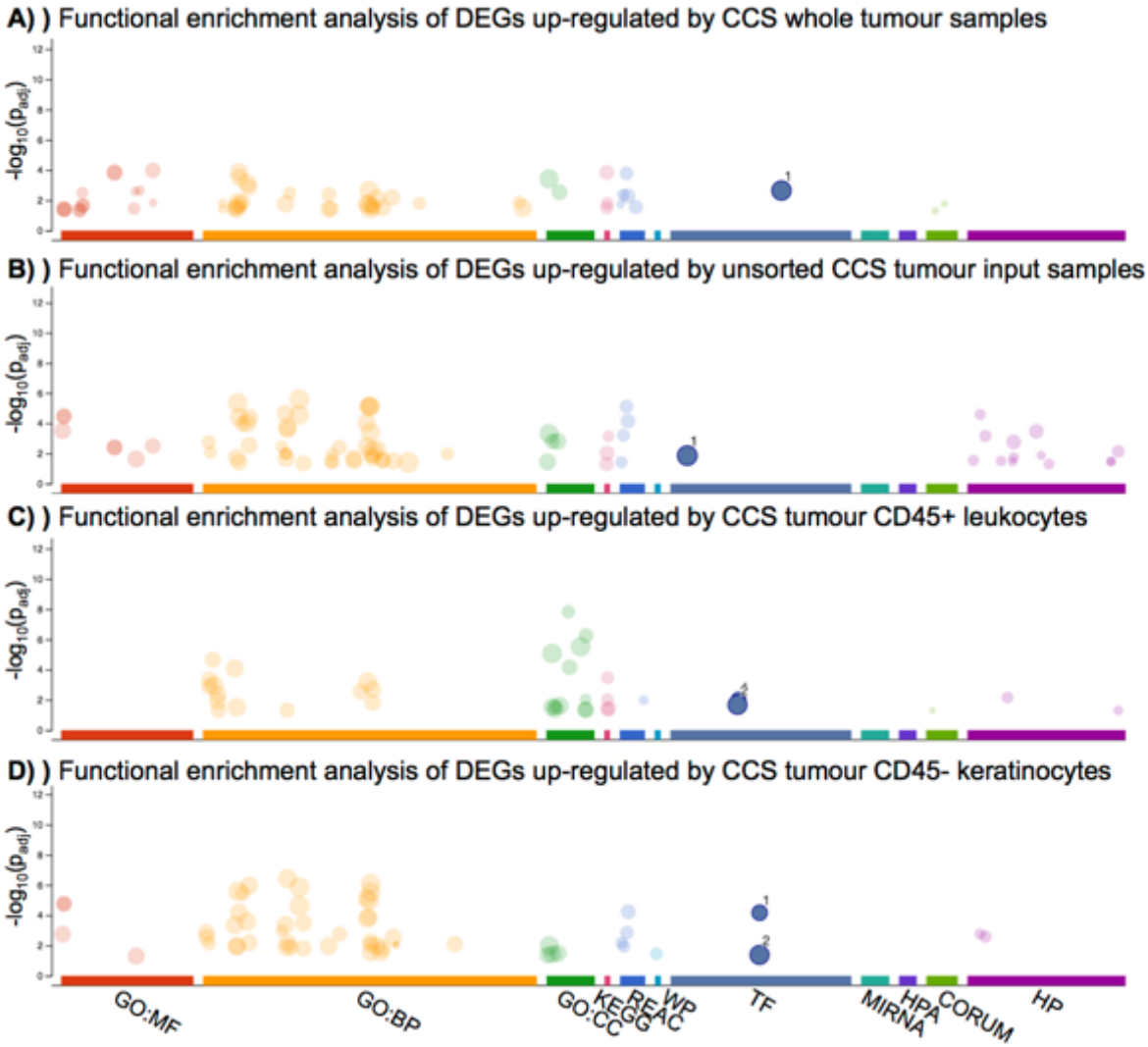

Sample group	ID	Term Name	Term ID	p_{adj}
Whole tissue	1	Factor: RelB:p50; motif: RGAAANTCCCYNNHGC	TF:M03882_0	0.0023
Input	1	Factor: c-Rel; motif: NGGGAATYTCCN	TF:M03545_0	0.0137
CD45+ leukocytes	1	Factor: IRF; motif: RAAANTGAAAN	TF:M00972_1	0.0095
	2	Factor: IRF-4; motif: NYGAAASYGAAACYN	TF:M11686_0	0.0214
CD45- keratinocytes	1	Factor: NF-kappaB; motif: NGGGGAMTTTCCNN	TF:M00194_1	0.0001
	2	Factor: NF-kappaB; motif: NGGGACTTTCCA	TF:M00208_0	0.0416

Figure 4-9. TRANSFAC® transcription factor (TF) motif matches in g:Profiler. Differential gene expression between CCS tumours and normal skin was analysed by DESeq2(Love et al., 2014) for four RNA-seq sample groups. The top 500 DEGs (ranked by positive fold change) for each group were input to g:Profiler for functional enrichment analysis. Positive fold-change indicates expression is higher in CCS tumours and lower in normal skin. A) Significant transcription factor motif matches in the whole tissue gene list. B) Significant transcription factor motif matches in the gene list from unsorted cells dissociated from whole tissue (input). C) Significant transcription factor matches in the gene list from CD45+ leukocytes isolated from dissociated tissue by FACs and D) Significant transcription factor matches in the gene list from CD45- keratinocytes isolated from dissociated tissue by FACS. GO:MF; Gene Ontology Molecular Function, GO:BP; Gene Ontology Biological Process, GO:CC; Gene Ontology Cellular Component, KEGG; Kyoto Encyclopaedia of Genes and Genomes, REAC; Reactome, WP; WikiPathways, MIRNA; miRTarBase, HPA; Human Protein Atlas, HP; Human Phenotype Ontology.

In whole tissue (Figure 4-9A), Input (Figure 4-9B) and $CD45^-$ keratinocytes (Figure 4-9D), a significant NF-κB motif match was found in the regulatory regions of genes upregulated in CCS tumours. A significant NF-κB motif match was not found in genes upregulated by CCS tumour $CD45^+$ TILs (Figure 4-9C). Rather, binding sites for the transcription factors interferon regulatory factor 1 (IRF1) and IRF4 were significantly over-represented. When the same g:Profiler analysis was performed with the top 500 negative DEGs in each group (Appendix C), a significant NF-κB motif match was not found in any dataset. Overall, the TRANSFAC® results of the functional enrichment analysis provide evidence that a significant number of the genes up-regulated by CCS tumour keratinocytes are potential NF-κB target genes.

Next, the $CD45^+$ TILs were examined to assess the impact of CCS tumour keratinocytes on the tumour microenvironment (TME).

4.1.5 CD45 positive tumour-infiltrating leukocytes (TILs) down-regulate chemokine activity and extracellular matrix organisation

Cell to cell communication is facilitated by secreted ligands such as cytokines, chemokines and growth factors. Cells also secrete proteases that regulate extracellular matrix organisation, and some of these, such as MMP2, can also function as ligands(Godefroy et al., 2014). Aberrant secretion of these proteins due to dysregulated NF-κB signalling in both tumour cells and infiltrating immune cells can sustain tumour-promoting inflammation, create an immunosuppressive TME, activate oncogenic cell signalling pathways and cause remodelling of the extracellular matrix to facilitate tumour growth(Capece et al., 2018). In CCS, the crosstalk between infiltrating immune cells and tumour cells has not been characterised. To investigate paracrine signalling between CCS tumour cells and the immune cells in the TME, a list of 437 known human ligands was obtained from the International Union of Basic and Clinical Pharmacology (IUPHAR) / British Pharmacological Society (BPS) Guide to PHARMACOLOGY(Armstrong et al., 2020) database (https://www.guidetopharmacology.org/) and the Database of Ligand-Receptor Partners (https://dip.doe-mbi.ucla.edu/dip/DLRP.cgi). Expression of the 437 ligands was then evaluated in the four RNA-seq groups (Figure 4-10).

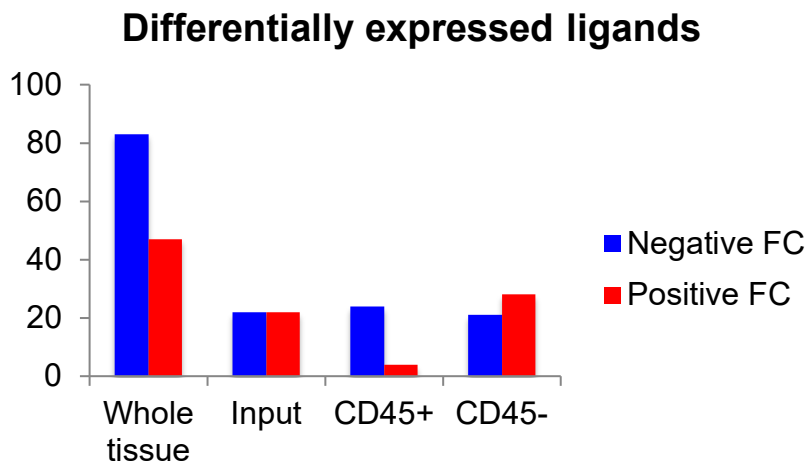

Figure 4-10. Ligands differentially expressed by normal skin and CCS tumours.437 human ligands were checked for significant differential expression (log_2FC>2, adjusted *P*-value < 0.05) in RNA-seq datasets before (whole tissue and input) and after FACS ($CD45^+$ and $CD45^-$). FC; fold-change.

Only four ligands were overexpressed by CCS TILs, three of which have been reported in NF-κB target gene databases(Table 4-3). The acute phase protein SAA1 is a major chemoattractant expressed during inflammation that can activate canonical NF-κB signalling via TLR2 and 4, and is an NF-κB target gene downstream of proinflammatory cytokines(O'Reilly et al., 2014). *IFNG* is expressed by a range of immune cell types, including macrophages, T cells, natural killer (NK) cells, NK T cells, B cells and antigen presenting cells. It is critical for host defence against pathogens and also protects against tumour development(Schroder et al., 2004). Interestingly, three of the ligands (SFRP1, NGF and IFNG) upregulated by CCS TILs cause termination of hair growth by inducing catagen, the regression stage of the hair cycle(Hawkshaw et al., 2018, Peters et al., 2004, Ito et al., 2005, Peters et al., 2006).

Table 4-3. Ligands differentially expressed between normal skin and CCS tumour CD45+ immune cells. Applying a threshold of $log_2FC>2$, adjusted *P*-value < 0.05, 29 ligands out of 437 were significantly differentially expressed by CD45+ immune cells enriched by FACS. Positive fold-change indicates expression is higher in CCS tumour CD45+ immune cells and lower in normal skin CD45+ immune cells, negative fold-change indicates expression is lower in CCS tumour CD45+ immune cells relative to normal skin CD45+ immune cells.

No.	logFC	Gene	Description
1	3.9	*SFRP1*	Secreted frizzled related protein 1
2	3.2	*SAA1*	Serum amyloid A1 *
3	2.9	*NGF*	Nerve growth factor*
4	2.6	*IFNG*	Interferon gamma *
5	-2.0	*CXCL2*	C-X-C motif chemokine ligand 2 *
6	-2.0	*TIMP1*	TIMP metallopeptidase inhibitor 1
7	-2.1	*FBN1*	Fibrillin 1
8	-2.2	*VTN*	Vitronectin
9	-2.3	*GDF15*	Growth differentiation factor 15
10	-2.5	*EREG*	Epiregulin *
11	-2.5	*PDGFA*	Platelet derived growth factor subunit A *
12	-2.5	*CXCL3*	C-X-C motif chemokine ligand 3*
13	-2.5	*MMP2*	Matrix metallopeptidase 2 *
14	-2.6	*CXCL1*	C-X-C motif chemokine ligand 1 *
15	-2.6	*CXCL12*	C-X-C motif chemokine ligand 12 *
16	-2.6	*IL36RN*	Interleukin 36 receptor antagonist
17	-2.6	*VEGFA*	Vascular endothelial growth factor A *
18	-2.8	*UTS2*	Urotensin 2
19	-2.8	*CCL17*	C-C motif chemokine ligand 17 *
20	-2.9	*CCL19*	C-C motif chemokine ligand 19 *
21	-2.9	*COL1A1*	Collagen type I alpha 1 chain *
22	-3.1	*COL3A1*	Collagen type III alpha 1 chain
23	-3.2	*CCL22*	C-C motif chemokine ligand 22*
24	-3.4	*SFRP2*	Secreted frizzled related protein 2
25	-3.6	*RSPO1*	R-spondin 1
26	-3.6	*CALCA*	Calcitonin related polypeptide alpha
27	-3.7	*IL12B*	Interleukin 12B *
28	-4.0	*ANGPTL1*	Angiopoietin like 1
29	-4.3	*CXCL5*	C-X-C motif chemokine ligand 5*

*In NF-κB target gene databases ((Yang et al., 2016) or https://www.bu.edu/nf-kb/gene-resources/target-genes/)

The majority (83.4%) of significantly differentially expressed ligands in the $CD45^+$ dataset were downregulated by CCS TILs, including the gene encoding the neutrophil chemoattractant CXCL5(Zhou et al., 2013). Though SFRP2 usually functions as a Wnt antagonist, it has been shown in cultured human hair follicle dermal papilla cells to increase Wnt signalling and enhance trichogenicity(Kwack et

al., 2016). Rspo1 also has a positive effect on Wnt signalling and is upregulated in murine dermal papilla cells before anagen, the growth phase of the hair cycle(Li et al., 2016). CCS TILs may therefore downregulate ligands that enhance hair growth and upregulate ligands that suppress hair growth. A number of ligands involved in extracellular matrix organisation were also downregulated in CCS TILs (*TIMP1*, *FBN1*, *MMP2*, *COL1A1*, *COL3A1*). Similarly, a comparison of the functional enrichment analysis results for the top 500 positive and negative DEGs in the $CD45^+$ group reveals there is a highly significant overrepresentation of genes involved in extracellular matrix organisation that are down-regulated by CCS tumour $CD45^+$ TILs (Figure 4-11). The top 20 significantly enriched terms from each g:Profiler information source are given in Appendix B and C.

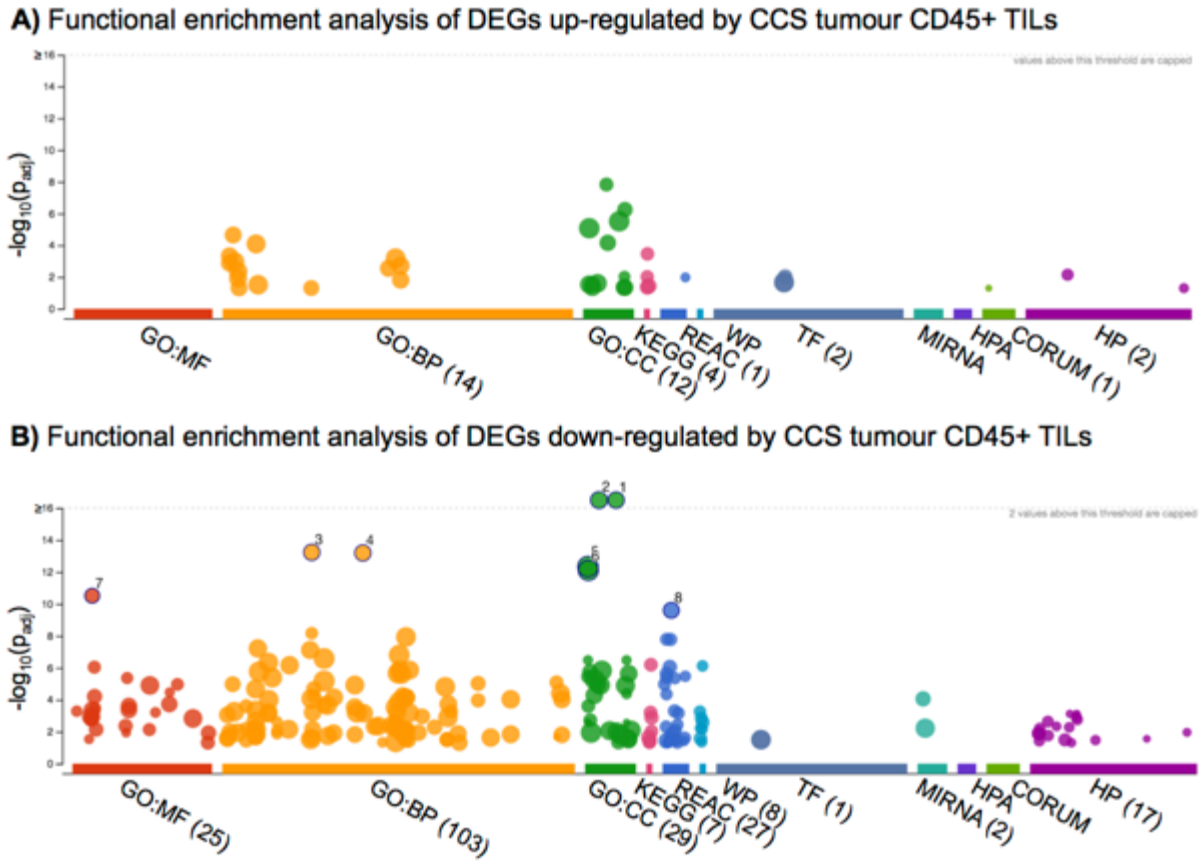

ID	Source	Term Name	Term ID	p_{adj}
1	GO:CC	Collagen-containing extracellular matrix	GO:0062023	3.05E-21
2	GO:CC	Extracellular matrix	GO:0031012	9.66E-21
3	GO:BP	Extracellular matrix organization	GO:0030198	5.87E-14
4	GO:BP	Extracellular structure organization	GO:0043062	6.45E-14
5	GO:CC	Extracellular region	GO:0005576	4.60E-13
6	GO:CC	Extracellular space	GO:0005615	8.02E-13
7	GO:MF	Extracellular matrix structural constituent	GO:0005201	3.08E-11
8	REAC	Extracellular matrix organization	REAC:R-HSA-1474244	2.52E-10

Figure 4-11. g:Profiler functional enrichment analysis of genes differentially expressed between normal skin and CCS tumour CD45+ leukocytes. A) Zero GO:MF terms were significantly overrepresented in DEGs upregulated by CCS tumour CD45+ TILs. B) CCS tumour CD45+ TILs down-regulate genes involved extracellular matrix organisation. The 8 most significantly overrepresented terms across all databases are shown. GO:MF; Gene Ontology Molecular Function, GO:BP; Gene Ontology Biological Process, GO:CC; Gene Ontology Cellular Component, KEGG; Kyoto Encyclopaedia of Genes and Genomes, REAC; Reactome, WP; WikiPathways, MIRNA; miRTarBase, HPA; Human Protein Atlas, HP; Human Phenotype Ontology.

No Gene Ontology Molecular Function (GO:MF) terms were significantly overrepresented by the genes up-regulated by CCS tumour CD45^{+} TILs (Figure 4-11A), while 25 GO:MF terms were significantly overrepresented by genes down-regulated by CCS tumour CD45^{+} TILs (Fig. Figure 4-11B and Table 4-4). In addition

to genes involved in extracellular matrix structure and binding, this included down-regulation of groups of genes related to chemokine and cytokine activity.

Table 4-4. g:Profiler functional enrichment analysis of genes downregulated by CCS tumour CD45$^+$ TILs. Input of the top 500 differentially expressed genes ranked by negative fold change yields 25 significantly overrepresented Gene Ontology Molecular Function terms.

No.	Source	Term Name	Term ID	P_{adj}
1	GO:MF	Extracellular matrix structural constituent	GO:0005201	3.08E-11
2	GO:MF	Collagen binding	GO:0005518	9.10E-07
3	GO:MF	Extracellular matrix structural constituent conferring tensile strength	GO:0030020	4.37E-06
4	GO:MF	Extracellular matrix binding	GO:0050840	1.09E-05
5	GO:MF	Identical protein binding	GO:0042802	1.27E-05
6	GO:MF	Platelet-derived growth factor binding	GO:0048407	3.43E-05
7	GO:MF	Glycosaminoglycan binding	GO:0005539	6.23E-05
8	GO:MF	Receptor ligand activity	GO:0048018	1.88E-04
9	GO:MF	Signaling receptor activator activity	GO:0030546	2.42E-04
10	GO:MF	Chemokine activity	GO:0008009	3.39E-04
11	GO:MF	Structural molecule activity	GO:0005198	4.24E-04
12	GO:MF	Receptor regulator activity	GO:0030545	4.35E-04
13	GO:MF	Fibronectin binding	GO:0001968	5.20E-04
14	GO:MF	CXCR chemokine receptor binding	GO:0045236	6.20E-04
15	GO:MF	Signaling receptor binding	GO:0005102	1.11E-03
16	GO:MF	Cytokine receptor binding	GO:0005126	1.45E-03
17	GO:MF	Molecular function regulator	GO:0098772	1.47E-03
18	GO:MF	Cytokine activity	GO:0005125	1.67E-03
19	GO:MF	Growth factor binding	GO:0019838	4.38E-03
20	GO:MF	Heparin binding	GO:0008201	7.17E-03
21	GO:MF	Chemokine receptor binding	GO:0042379	7.33E-03
22	GO:MF	Interleukin-1 binding	GO:0019966	1.15E-02
23	GO:MF	Sulfur compound binding	GO:1901681	1.19E-02
24	GO:MF	Complement receptor activity	GO:0004875	2.92E-02
25	GO:MF	Immune receptor activity	GO:0140375	4.81E-02

These results suggest that paracrine and functional cell signalling within immune cells is more active in normal healthy skin than in the CCS TME. CCS tumour cells expressing and secreting immunomodulatory molecules due to dysregulation of pathways including NF-κB are therefore likely to be establishing an immunosuppressive TME and preventing the normal regulation of extracellular matrix organisation. Other non-immune stromal cells such as fibroblasts within the TME may also contribute to an immunosuppressive TME phenotype(Giraldo et al., 2019).

4.1.6 Deconvolution of CD45 positive RNA-seq data imputes that CCS tumours contain a higher proportion of T cell infiltrate than normal skin

Knowledge of the immune cell subsets within the CCS TME is lacking and is of clinical significance given the emergence of immunotherapies and prediction of response based on immune cell composition. To better understand the TME in CCS, deconvolution was performed on the bulk $CD45^+$ RNA-seq data to estimate the immune cell populations that might be in the tumour. To infer CCS tumour immune cell composition, the $CD45^+$ TIL gene expression data were analysed with CIBERSORTx. CIBERSORTx (http://cibersortx.standford.edu/) is an *in silico* deconvolution method that uses a machine learning approach (support vector regression) to estimate the composition of immune cell infiltrate from bulk tumour transcriptomes(Newman et al., 2015, Chen et al., 2018, Steen et al., 2020). CIBERSORTx applies a signature matrix of marker gene expression for 22 mature leukocyte subsets (LM22) to gene expression data from bulk tumours to estimate the relative fractions of each immune cell type (Figure 4-12).

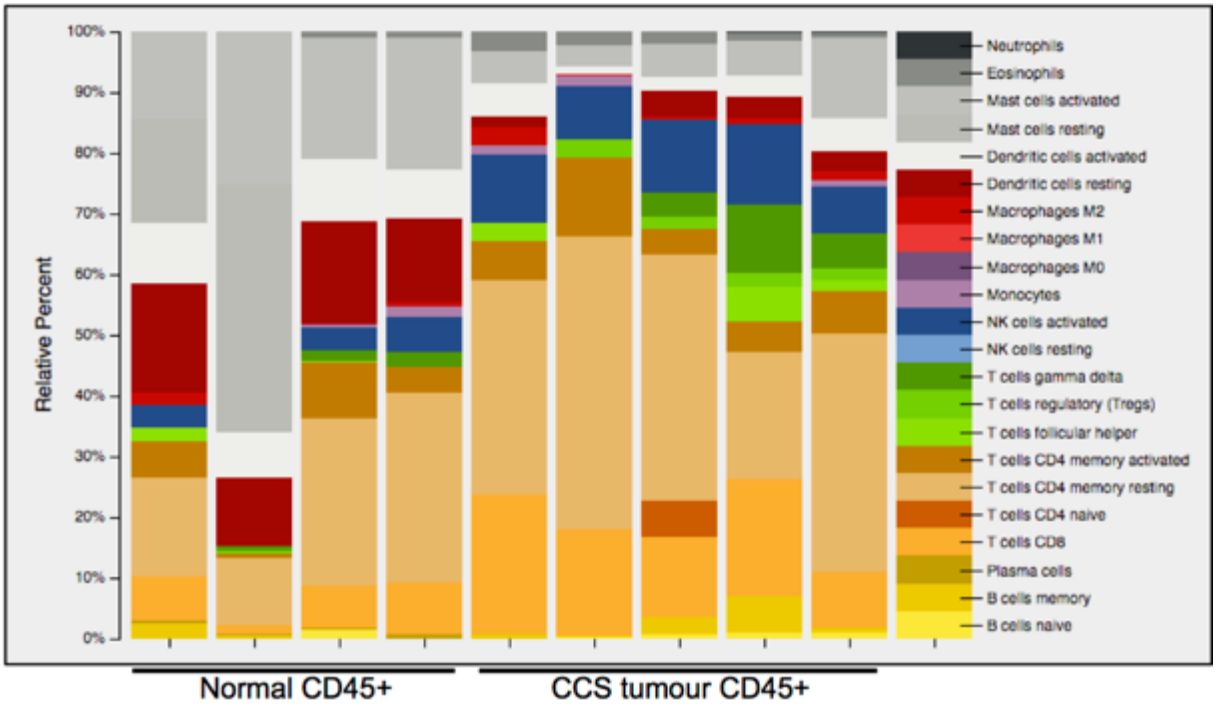

Figure 4-12. CIBERSORTx profiling of immune cell type abundance in CD45+ cell populations isolated from normal skin and CCS tumours by FACS. Normalised RNA-seq read counts (reads per kilobase million (RPKM)) were input for deconvolution with the LM22 signature matrix (CIBERSORTx generated *P*-values < 0.01).

CIBERSORTx estimates of immune cell type abundances indicate that the CCS CD45+ TILs contained a higher proportion of CD8 T cells and activated natural killer (NK) cells than CD45+ immune cells isolated from normal skin. Most CCS samples contained a higher relative proportion of CD4 memory resting T cells and 3 out of 5 tumours had more gamma delta T cells. T follicular helper cells (T_{FH}) were present in 4 out of 5 tumours. Tumour infiltrating T_{FH} cells are associated with increased survival in colorectal and breast cancer, and their presence alongside CD3, CD8, CD4 T helper 1 and memory T cells are indicative of 'hot' tumours that respond well to immunotherapy(Galon and Bruni, 2019). The infiltration of T_{FH} cells with cytotoxic CD8 and NK cells suggests that CCS patients could benefit from immune checkpoint inhibition immunotherapies. As the majority of tumours also had a higher proportion of regulatory T cells (Tregs), combination immunotherapy to inhibit the immunosuppressive role of Tregs such as targeting the GITR/GITRL (syn. TNFSFR18/TNFSF18) axis could strengthen the response(Knee et al., 2016).

Resting mast cells were inferred to be absent from CCS tumour TILs and activated mast cell abundance was deduced to be lower in tumour samples. Mast cells are

resident immune cells in skin that are found in high numbers in the upper papillary dermis(Brown and Krishnamurthy, 2021). In addition to regulating the immune response to allergens and pathogens, they have a prominent role in wound repair. Upon activation, mast cells release preformed mediators stored in internal granules such as TNFα, histamine and proteases. They can also synthesise and secrete a range of chemokines and growth factors including keratinocyte growth factor (KGF), fibroblast growth factor 2 (FGF2), epidermal growth factor (EGF), nerve growth factor (NGF) and vascular endothelial growth factor (VEGF)(Wilgus and Wulff, 2014). Mast cells within and at the periphery of skin cancers and other tumours have been reported as both pro-tumourigenic and anti-tumourigenic(Varricchi et al., 2017, Komi and Redegeld, 2020). Mast cell degranulation in the TME is proinflammatory and attracts both adaptive and innate immune cells to attack the tumour. Conversely, secreted proteins including VEGF, MMP9, TGF-β1 and IL-10 can promote angiogenesis, facilitate invasiveness due to degradation of the extracellular matrix and cause immunosuppression(Oldford and Marshall, 2015). In a melanoma mouse model, depletion of tumour infiltrating mast cells with sunitimib or imatinib resulted in complete response to anti-PD1 therapy(Somasundaram et al., 2021). As activated mast cells are inferred to be present in CCS tumours, albeit at lower levels relative to normal skin, their depletion in combination with checkpoint inhibition could potentially enhance response to treatment.

Deconvolution of the bulk CD45+ immune RNA-seq data inferred that CCS tumours do not contain more professional antigen-presenting cell (APC) infiltrate (dendritic cells, B cells and macrophages) than normal skin. Only M2 type macrophages were estimated to be present in CCS tumours, which are immune suppressing rather than activating(Tormoen et al., 2018). Professional APCs activate CD4 T cells by presenting exogenous antigens on MHC class II molecules and activate CD8 T cells by presenting endogenous antigens on MHC class I molecules(de Charette et al., 2016). APCs also ‘cross-present’ exogenous antigens (including tumour cell antigens) to prime naive CD8 T cells through the MHC I pathway, resulting in cytotoxic CD8 T cell activation. Dendritic cells (DCs), particularly conventional type 1 DC (cDC1) subsets, are the main professional APC that carry out cross-presentation in vivo(Sánchez-Paulete et al., 2017). DCs, which are prevalent in environment facing tissues such as skin and mucosal surfaces(Ronchese et al., 2020), were

relatively less abundant in CCS tumours than normal skin. Strategies to increase cDC1 subset number and function could be considered to further increase antitumour CD8 T cell infiltrate and augment the success of checkpoint inhibition therapy(Gajewski and Cron, 2020).

Overall, CIBERSORTx predicts that several T cell subsets are increased in CCS tumours relative to normal skin, while sentinel cells of myeloid lineage (mast cells and dendritic cells) are decreased. Future work should explore the localisation and densities of immune subsets in CCS tumour sections with immunohistochemistry and the expression of T cell checkpoints such as PD1 and CTLA4 to help guide potential treatment options.

4.1.7 A subset of genes differentially expressed in CD45 negative keratinocytes contain a non-canonical NF-κB binding site motif

The g:Profiler functional enrichment analysis of genes differentially expressed between FACS sorted $CD45^-$ normal skin and CCS tumour keratinocytes confirmed an increase in the expression of genes with NF-κB transcription factor binding sites in CCS tumour cells (Figure 4-9). As the role of CYLD in the p52:RelB mediated non-canonical NF-κB signalling pathway is understudied, identification of potential non-canonical target genes upregulated by CCS tumour cells is of particular interest. To predict which of the potential NF-κB target genes up-regulated in CCS tumour keratinocytes might be non-canonical target genes, the TRANSFAC PWM library and Match tool were used to identify genes with a p52:RelB TFBS motif. The heterodimer p52:RelB was searched in the TRANSFAC® database to obtain the TRANSFAC Matrix accession number M01239, which corresponds to the 'Term ID' in g:Profiler. g:Convert in g:Profiler was then used to retrieve the match class 0 and match class 1 lists of all human genes associated to this Term ID. When, merged, this resulted in a list of 799 genes with at least one p52:RelB TFBS match (motif GGGGNTTTCC) +/- 1kb from the TSS. Next, a comparison was made to see how many of the genes differentially expressed ($log_2FC>2$, adjusted *P*-value < 0.05) between $CD45^-$ normal and tumour keratinocytes have at least one p52:RelB TFBS motif.

Out of 1767 differentially expressed genes, 49 were found to have the p52:RelB motif +/-1kb from the TSS. These genes may not exclusively have the p52:RelB motif, for example the most highly overexpressed potential non-canonical target gene *EDAR*

also matched the RelA:p50 TFBSs under Term IDs M01244 and M08891. Nonetheless, they all have the potential to be non-canonical targets. Full gene descriptions and fold-changes for these potential non-canonical target genes are given in Table 4-5. To visualise the range of expression of DEGs containing the p52:RelB binding site motif, RNA-seq read counts were log_2 transformed and plotted on a heatmap (Figure 4-13). Normal skin and CCS tumour $CD45^-$ samples clustered separately as expected, and the difference in expression of *EDAR* (Red arrow), *SOX14* and *ITIH* between groups was particularly striking.

Table 4-5. Potential non-canonical NF-κB target genes differentially expressed between CD45- normal skin and CCS tumour keratinocytes. Applying a threshold of $log_2FC>2$ and adjusted *P*-value < 0.05, 49 differentially expressed genes contain a p52:RelB binding site +/-1kb from the transcription start site. Positive FC indicates expression is higher in CCS tumour CD45- keratinocytes relative to CD45- keratinocytes from normal skin.

No.	logFC	Gene	Description
1	8.2	*EDAR*	Ectodysplasin A receptor
2	8.0	*SOX14*	SRY-box 14
3	5.4	*KREMEN2*	Kringle containing transmembrane protein 2
4	5.2	*CD164L2*	CD164 molecule like 2
5	5.2	*PLA2G4D*	Phospholipase A2 group IVD
6	5.0	*LCP1*	Lymphocyte cytosolic protein 1
7	5.0	*SOX21*	SRY-box 21
8	4.1	*COL22A1*	Collagen type XXII alpha 1 chain
9	4.0	*FAM71E1*	Family with sequence similarity 71 member E1
10	3.9	*RHOV*	Ras homolog family member V
11	3.8	*FAM83F*	Family with sequence similarity 83 member F
12	3.5	*KY*	Kyphoscoliosis peptidase
13	3.5	*FAAH2*	Fatty acid amide hydrolase 2
14	3.4	*FFAR2*	Free fatty acid receptor 2
15	3.2	*TSTD1*	Thiosulfate sulfurtransferase like domain containing 1
16	3.2	*DDR1*	Discoidin domain receptor tyrosine kinase 1
17	3.2	*DUSP2*	Dual specificity phosphatase 2
18	3.1	*ANO9*	Anoctamin 9
19	3.1	*ANK3*	Ankyrin 3
20	2.9	*KCNB2*	Potassium voltage-gated channel subfamily B member 2
21	2.9	*VAX2*	Ventral anterior homeobox 2
22	2.9	*ELF3*	E74 like ETS transcription factor 3
23	2.6	*LHFPL4*	LHFPL tetraspan subfamily member 4
24	2.5	*THSD7B*	Thrombospondin type 1 domain containing 7B
25	2.5	*NMBR*	Neuromedin B receptor
26	2.5	*STAP2*	Signal transducing adaptor family member 2
27	2.5	*HEPACAM*	Hepatic and glial cell adhesion molecule
28	2.4	*ZNF385C*	Zinc finger protein 385C
29	2.4	*DAPP1*	Dual adaptor of phosphotyrosine and 3-phosphoinositides 1
30	2.4	*TRAF1*	TNF receptor associated factor 1
31	2.4	*SAMD5*	Sterile alpha motif domain containing 5
32	2.4	*ARHGAP4*	Rho GTPase activating protein 4
33	2.3	*BSN*	Bassoon presynaptic cytomatrix protein
34	2.3	*SGPP2*	Sphingosine-1-phosphate phosphatase 2
35	2.2	*GOLT1A*	Golgi transport 1A
36	2.2	*AGBL2*	ATP/GTP binding protein like 2
37	2.1	*GNA15*	G protein subunit alpha 15
38	2.1	*HPCA*	Hippocalcin
39	2.0	*RNF227*	Ring finger protein 227

No.	logFC	Gene	Description
40	-2.0	*CLGN*	Calmegin
41	-2.1	*HTRA1*	HtrA serine peptidase 1
42	-2.2	*CLDN5*	Claudin 5
43	-2.3	*PTGDS*	Prostaglandin D2 synthase
44	-2.3	*RRAD*	Ras related glycolysis inhibitor and calcium channel regulator
45	-2.4	*ACKR1*	Atypical chemokine receptor 1 (Duffy blood group)
46	-2.5	*RSPO1*	R-spondin 1
47	-2.9	*RIMS2*	Regulating synaptic membrane exocytosis 2
48	-3.6	*TOR4A*	Torsin family 4 member A
49	-4.0	*ITIH1*	Inter-alpha-trypsin inhibitor heavy chain 1

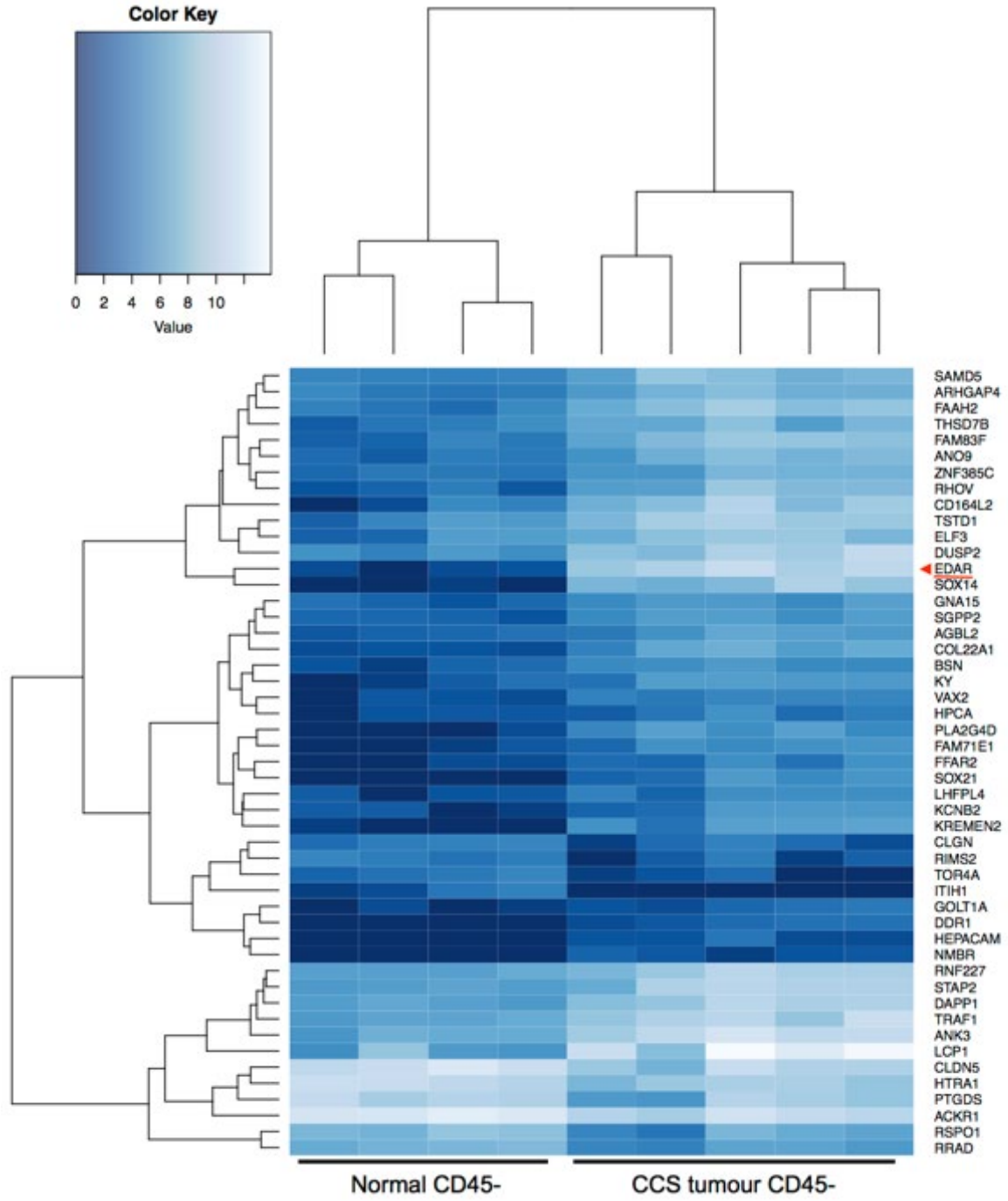

Figure 4-13. A subset of genes differentially expressed between normal skin and CCS tumour keratinocytes contain a p52:RelB binding motif. $CD45^-$ keratinocytes isolated from CCS tumours and normal skin by FACS differentially express 49 genes containing the p52:RelB motif GGGGNTTTCC. Dark blue indicates low expression, light blue indicates high expression. The gene encoding the ectodysplasin A Receptor (*EDAR*) was ranked first by positive fold-change out of 1767 genes differentially expressed ($log_2FC>2$, adjusted *P*-value < 0.05) by $CD45^-$ CCS keratinocytes (red arrow).

4.1.8 Ectodysplasin A receptor (EDAR) and candidate EDA/EDAR target genes are differentially expressed in CCS tumour keratinocytes

The gene encoding the ectodysplasin A receptor (*EDAR)* was of particular interest in the RNA-seq DEG results, as it was both the top overexpressed gene (ranked by FC) by CD45$^-$ CCS tumour keratinocytes overall (log_2FC 8.2) and a potential non-canonical NF-κB target gene (Figure 4-13, red arrow). Upon binding to its ligand ectodysplasin isoform-A1 (EDA-A1), EDAR activates canonical NF-κB and JNK signalling via the death domain adaptor protein EDARADD(Kumar et al., 2001, Headon et al., 2001a, Doffinger et al., 2001). EDA/EDAR mediated NF-κB signalling has a critical role in human hair follicle development and mutations in *EDA* (OMIM 300451), *EDAR* (OMIM 604095) and *EDARADD* (OMIM 606603) cause the disease hypohidrotic ectodermal dysplasia (HED)(Laurikkala et al., 2002, {Schmidt-Ullrich, 2006 #246), (Zhang et al., 2009)}. Symptoms include abnormal morphogenesis of hair and eccrine sweat glands, which is of relevance given the skin appendage origin of CCS tumours.

To explore EDA/EDAR signalling in CCS tumours, candidate EDA/EDAR signal transduction target genes were obtained from literature(Cui et al., 2002, Cui et al., 2006, Esibizione et al., 2008, Lefebvre et al., 2012) and differential expression in the CD45$^-$ keratinocytes was assessed (Figure 4-14). Sixteen candidate EDA/EDAR signalling target genes were differentially expressed by CCS tumour keratinocytes. Of these, three were chosen for validation by immunoblot in section 4.1.9 as potential markers of EDA/EDAR pathway activation; Kringle containing transmembrane protein 2 (*KREMEN2*), Wnt family member 10B (*WNT10B*) and TNF superfamily receptor family 18 (*TNFRSF18*, syn. *GITR*). The Wnt antagonist *Kremen2* is a known Eda target in murine embryonic skin during hair follicle development(Cui et al., 2006). In addition to its roles in murine hair follicle induction(Zhang et al., 2009) and regeneration(Li et al., 2013), Wnt10B is of interest given its links with Edar to collagen accumulation in mouse prostate(Wegner et al., 2019), as cylindroma tumours are known to overexpress collagen VII(Pfaltz et al., 1989, Bruckner-Tuderman et al., 1991). Tnfsfr18 has the same discrete localisation pattern in murine developing epidermis and hair follicles as Edar(Wang et al., 2005) and overexpression may be of therapeutic relevance, as a number of cancer immunotherapy molecules are currently in trial targeting the TNFRSF18/TNFSF18 (syn. GITR/GITRL) axis(Knee et al., 2016). TNFRSF18 and its ligand TNFSF18 were also shown to activate non-canonical NF-κB signalling via NIK and TRAF2 by the two

groups that discovered this receptor in humans (Gurney et al., 1999, Kwon et al., 1999).

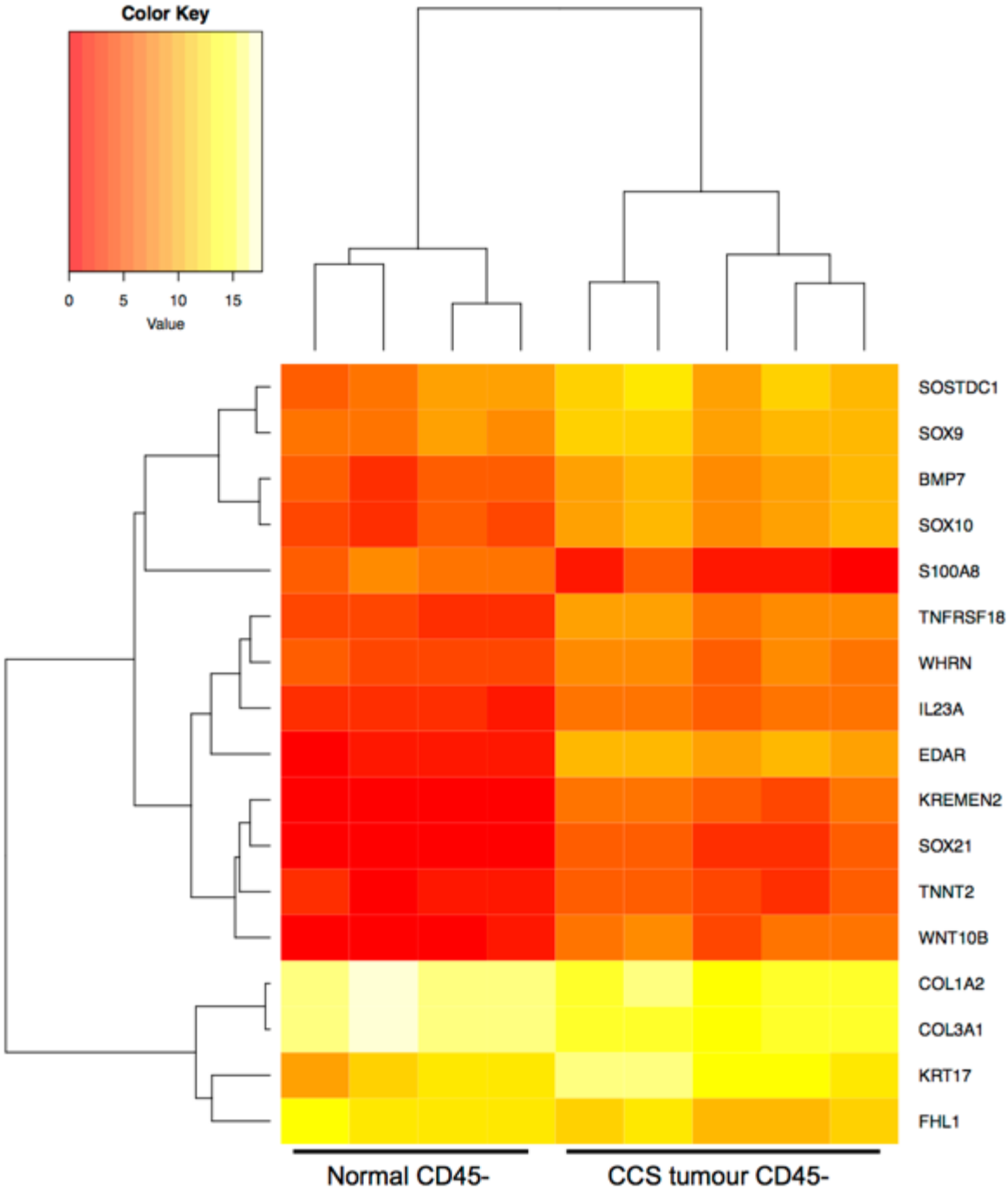

Figure 4-14. *EDAR* and candidate EDA/EDAR target genes differentially expressed by CD45- CCS tumour keratinocytes. $CD45^-$ keratinocytes isolated from CCS tumours and normal skin by FACS differentially express 16 potential EDA/EDAR signaling pathway target genes ($log_2FC>2$, adjusted *P*-value < 0.05). Red indicates low expression, yellow indicates high expression.

4.1.9 CCS tumour spheroids overexpress EDAR

To confirm that EDAR protein levels reflect *EDAR* overexpression in CCS tumour keratinocytes, EDAR expression in normal and CCS tumour primary cells (both

adherent and spheroid) was assessed by immunoblot (Figure 4-15). Immunoblot confirmed that CCS primary spheroids express higher levels of EDAR than normal primary spheroids while the absence of EDAR in 2D CCS cultures reinforces the utility of using spheroids to model CCS. Ectodysplasin A1 (*EDA-A1),* the ligand for EDAR, was not significantly upregulated in any of the RNA-seq datasets.

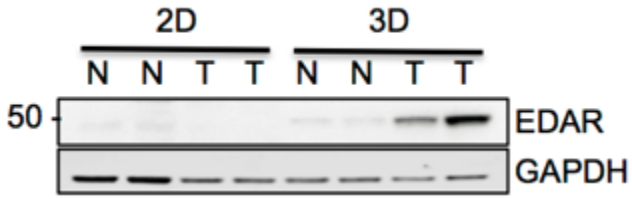

Figure 4-15. EDAR is upregulated by CCS tumour spheroids. EDAR at the predicted molecular weight of 49 kDa was detected in lysates from CCS tumour spheroids (3D) but not in lysates from adherent CCS primary cell cultures (2D). N; normal skin sample, T; CCS tumour sample.

As 2D primary cells are more convenient for the optimisation of time-points and treatment concentrations than spheroids, some initial experiments were performed with the EDA-A1 (the cognate ligand for EDAR) in 2D primary cells. To assess whether 2D CCS cells express EDAR after exposure EDA-A1, two CPCCs were stimulated with 10 ng/ml recombinant EDA-A1 and harvested at the times shown in figure 13. This concentration was chosen as a starting point because stimulation of human corneal epithelial cells with EDA-A1 in the range of 0 – 20 ng/ml up-regulated protein levels of phosphorylated extracellular signalling related kinase (p-ERK), epidermal growth factor receptor (EGFR) and p-EGFR in a dose dependent manner(Li et al., 2017). RelB and p50 were used as potential markers of EDA/EDAR signalling activation, as these subunits have been shown to accumulate in the nucleus of HaCaTs (a human keratinocyte cell line which the authors modified to stably express EDAR) after stimulation with EDA-A1 conditioned media(Sima et al., 2018).

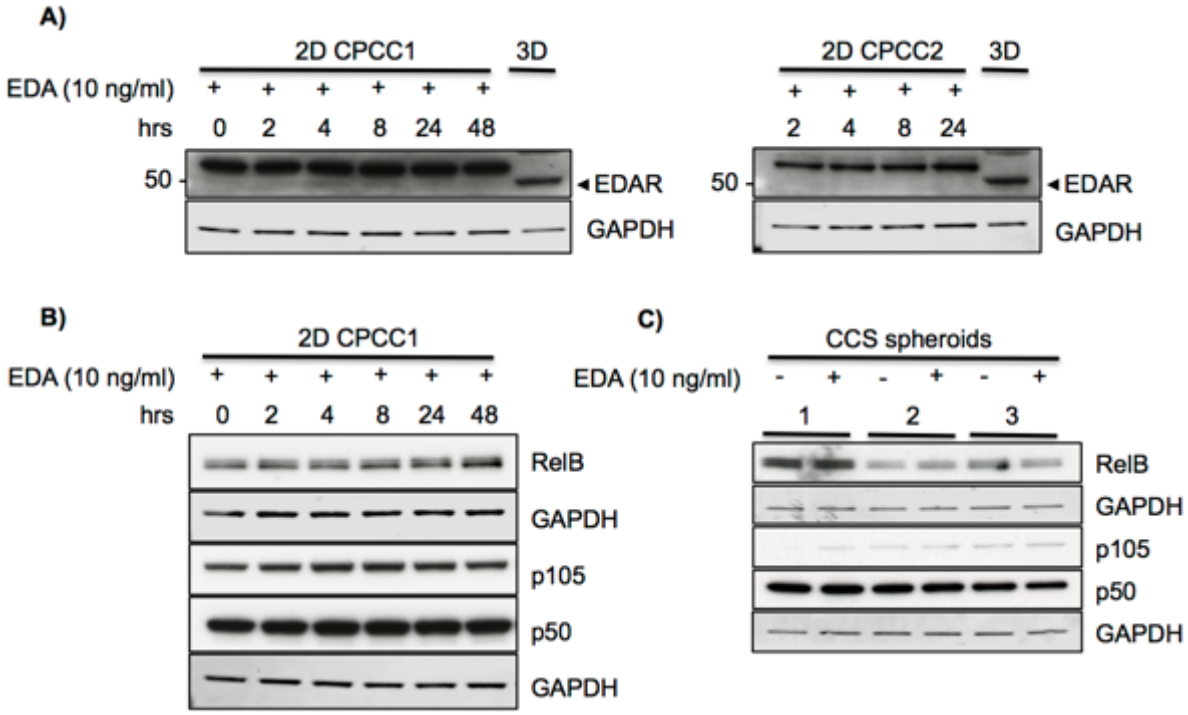

Figure 4-16. EDA-A1 stimulation of 2D and 3D CCS primary cell cultures. A) Two adherent 2D CPCCs were stimulated with 10 ng/ml EDA-A1 and harvested at the indicated time-points. A 3D spheroid lysate was included as a positive control for EDAR at 49 kDa. B) CPCC1 expression of RelB and p105/p50, putative markers of activated EDA/EDAR signalling. C) Expression of RelB and p105/p50 by 3 CCS spheroid cultures stimulated with 10 ng/ml EDA and harvested at 6 hours.

Faint bands were detected at 4 and 8 hrs for EDAR at the predicted molecular weight of 49 kDa in CPCC1 (Figure 4-16A) however this was not replicated in the second 2D culture. Apart from a very slight increase in p105 at 4-8 hours and RelB at 48 hours, the 2D CCS cells did not convincingly show an increase in EDA/EDAR signalling when stimulated with 10 ng/ml EDA-A1 (Figure 4-16B). As EDAR was faintly detected at 4 and 8 hours in CPCC1 (Figure 4-16A), 6 hours was used as a time-point for harvesting 3 CCS spheroid cultures stimulated with 10 ng/ml EDA-A1 (Figure 4-16C).

As stimulation with 10 ng/ml EDA-A1 for 6 hours did not have an effect on RelB or p50 levels in spheroids, additional optimisation was performed. Further review of the literature suggested that EDA-A1 stimulation in the range of 100 ng/ml for 24 hours might be appropriate for keratinocytes(Mou et al., 2006). As RelB and p50 are not guaranteed markers of EDA/EDAR activation in CCS spheroids, expression of the three potential EDA/EDAR target genes selected from Figure 4-14 was also assessed.

To evaluate the effects of increased EDA-A1 concentration on candidate EDA/EDAR targets, one 2D CPCC was stimulated with EDA-A1 at the concentrations indicated in Figure 4-17A for 24 hours. In agreement with Figure 4-15, EDAR at the predicted molecular weight of 49 kDa was not detected in 2D CPCC after stimulation with EDA-A1 up to 100 ng/ml. All putative markers of active EDA/EDAR signalling were negative apart from TNFRSF18, which increased in a dose dependent manner. Subsequent to these experiments, the KREMEN2 antibody was recalled by the manufacturer for failing to meet quality standards. The WNT10B antibody was also deemed to be unreliable and excluded from further experiments due to the detection of multiple non-specific bands near the predicted weight of 43 kDa and the usually observed molecular weight of 47 kDa. None of these bands varied with EDA-A1 concentration.

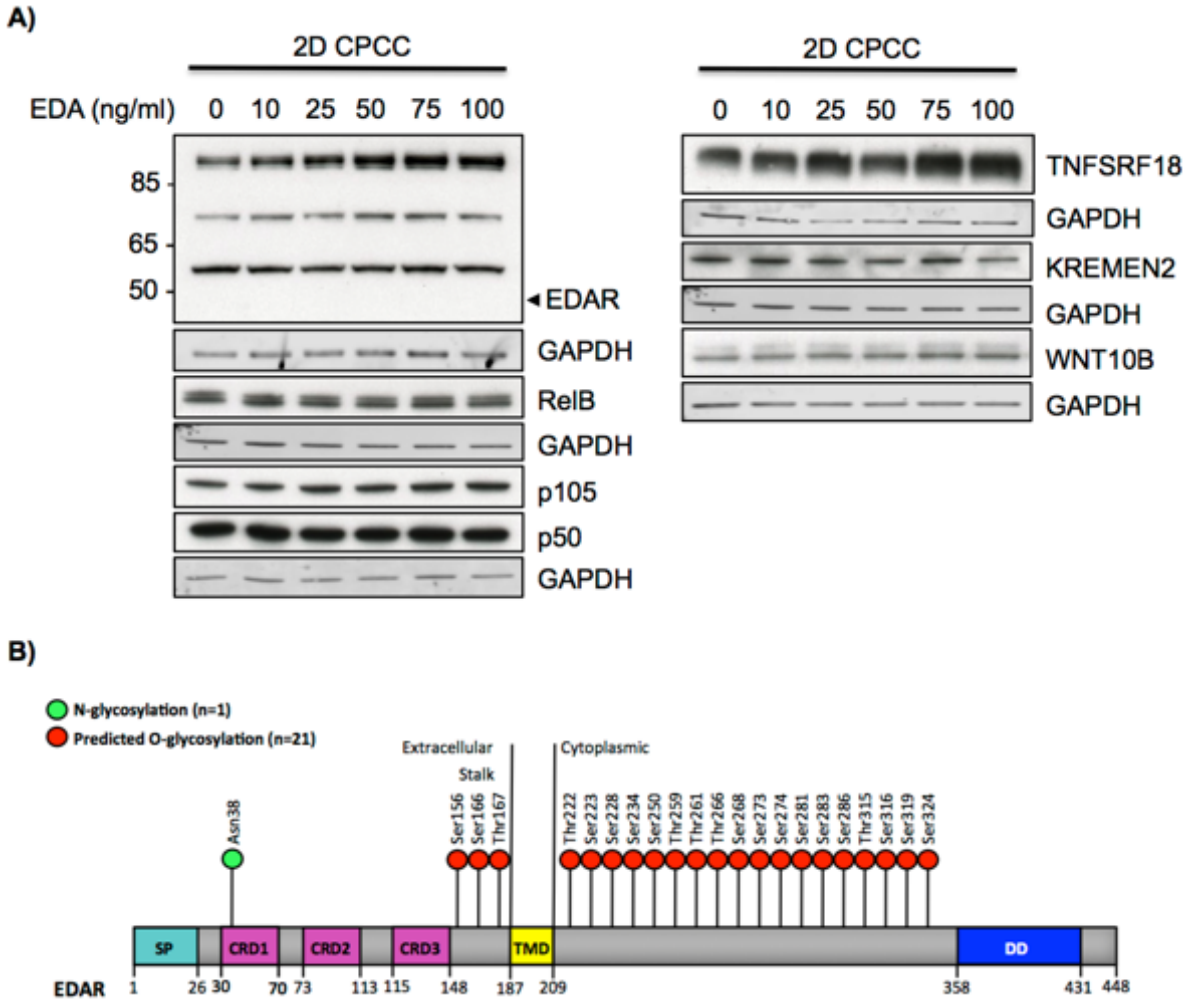

Figure 4-17. Stimulation of EDA/EDAR signalling in CCS 2D primary cells. A) TNFRSF18 increased in a dose-dependent manner to stimulation with recombinant EDA-A1 in a 2D CCS primary cell culture. B) Schematic of EDAR showing predicted O-glycosylation

sites from the NetOGlycan 4.0 Server(Steentoft et al., 2013) with positive prediction confidence scores >0.5.

In addition to bands above 50 and 65 kDa, a higher molecular weight protein was detected with the EDAR antibody ~90 kDa that increased with EDA-A1 stimulation in a dose dependent manner. EDAR has been detected by immunoblot at ~70-75 kDa, with the 20-30 kDa shift posited to be due to post-translational glycosylation(Elomaa et al., 2001). EDAR has one N-glycosylation site at asparagine 38 (www.uniprot.org) and 21 predicted O-glycosylation sites according to the NetOGlycan 4.0 Server (http://www.cbs.dtu.dk/services/NetOGlyc/), 6 of which had prediction confidence scores >0.8 (Figure 4-17B). It is therefore conceivable that EDAR may run at a higher molecular weight than predicted due to glycosylation in 2D CCS primary cells.

As levels of TNFRSF18 were highest after stimulation with 75-100 ng/ml EDA-A1, 100 ng/ml was selected for use in spheroid assays to investigate EDA/EDAR signalling. Prior to analysing protein levels of candidate markers of active EDA/EDAR signalling in spheroids after 24 hours stimulation with 100 ng/ml EDA-A1, spheroid protein lysates were probed for a marker of apoptosis (cleaved CASPASE 3) by immunoblot due to the unhealthy appearance of the normal primary spheroids in this experiment (Figure 4-18A). This deterioration was noted at 96 hours, prior to stimulation with EDA-A1. A CCD1106 lysate was included to allow comparison of levels of apoptosis in normal and CCS spheroids with levels of apoptosis in a 2D keratinocyte cell line. The cleaved CASPASE 3 immunoblot confirmed that the normal primary spheroids were undergoing increased apoptosis in the culture model relative to CCS primary spheroids. Consequently, normal spheroid protein lysates were excluded from further analysis.

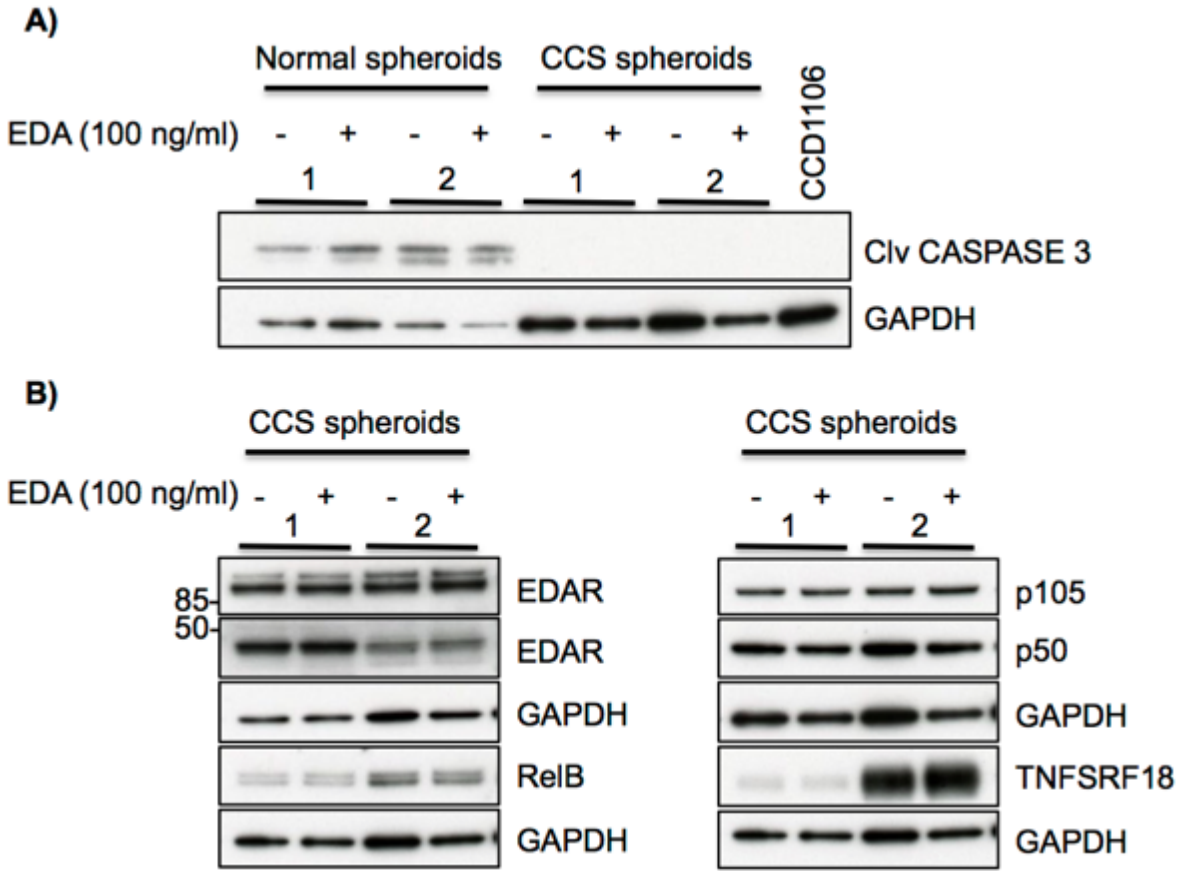

Figure 4-18. Stimulation of EDA/EDAR signalling in CCS primary spheroids. Spheroids were grown for 96 hours then stimulated with 100 ng/ml recombinant EDA-A1. Protein was extracted 24 hours after treatment. A) Normal primary spheroids exhibited increased levels of cleaved CASPASE 3 relative to CCS spheroids. B) EDA-A1 stimulation did not remarkably increase protein levels of selected candidate markers of EDA/EDAR signalling in CCS spheroids. GAPDH images are duplicated for immunoblots from the same gel.

Bands were detected for EDAR in spheroids at the predicted molecular weight and ~90 kDa. It is therefore possible that non-glycosylated and glycosylated forms of EDAR may be produced in CCS spheroids. Levels of EDAR did not change in spheroids with EDA-A1 stimulation (Figure 4-18B). When putative markers of active EDA/EDAR signalling (RelB and p105/p50) were assessed in CCS spheroids after EDA-A1 stimulation, no changes were detected. TNFRSF18 was strongly expressed in CCS spheroid 2 and did increase after EDA-A1 stimulation for 24 hours, however this was not replicated in CCS spheroid 1. While the low concentrations of protein recovered from CCS spheroid lysates precluded further investigation of the EDA/EDAR signal transduction pathway, this limited data suggests that TNFRSF18 regulation by EDA/EDAR may warrant assessment in additional CCS samples.

4.1.10 EDAR expression is reduced by IKKα inhibition in CCS spheroids

While EDA-A1 stimulation of CCS primary spheroids did not reveal new insights into downstream effects of *EDAR* overexpression, EDAR upregulation in CCS spheroids was confirmed (Figure 4-15). *EDAR* was matched in the TRANSFAC database with a p52:RelB TFBS, suggesting non-canonical NF-κB signalling may regulate *EDAR* expression in CCS keratinocytes. To investigate whether *EDAR* is a direct p52:RelB target gene in CCS tumour keratinocytes, *EDAR* and three additional upregulated genes from the 49 potential non-canonical NF-κB target gene subset (Table 4-5, Figure 4-13) were chosen for RT-qPCR validation in CCS primary spheroids. The additional genes were selected based on fold-change and relevance to skin/hair follicle development (Table 4-6).

Table 4-6. TaqMan® probe IDs. Four genes containing a p52:RelB binding motif selected for RT-qPCR validation by TaqMan® Gene Expression Assay.

Gene	TaqMan® probe ID	Ref	Role
EDAR	Hs00223468_m1	Laurikkala *et al*., 2002	Regulates hair follicle development with ligand ectodysplasin (EDA-A1)
KREMEN2	Hs00225867_m1	Cui *et al*., 2006	EDA/EDAR target gene during hair differentiation
SOX21	Hs01072517_s1	Kiso *et al*., 2009	Mediates hair shaft cuticle differentiation
COL22A1	Hs01377218_m1	Koch *et a*l., 2004	Expressed at tissue junction between anagen hair follicle and dermis

To assess the effects of non-canonical NF-κB pathway inhibition on the selected potential target genes, 3 CCS spheroid cultures were drugged at 96 hours with a small molecule inhibitor targeting IKKα (Compound Z, University of Strathclyde) for 24 hours then harvested for RNA extraction and RT-qPCR by TaqMan® Gene Expression Assay. Raw threshold cycle (Ct) values from control and treated samples were compared for two housekeeping genes (*PUM1* and *GAPDH*) previously validated for RT-qPCR with CCS tumour samples by the Rajan lab. As *PUM1* expression was reduced by Compound Z, and *GAPDH* was less affected (data not shown), gene expression was normalised to *GAPDH* for quantification with the $2^{-\Delta Ct}$ method (Figure 4-19).

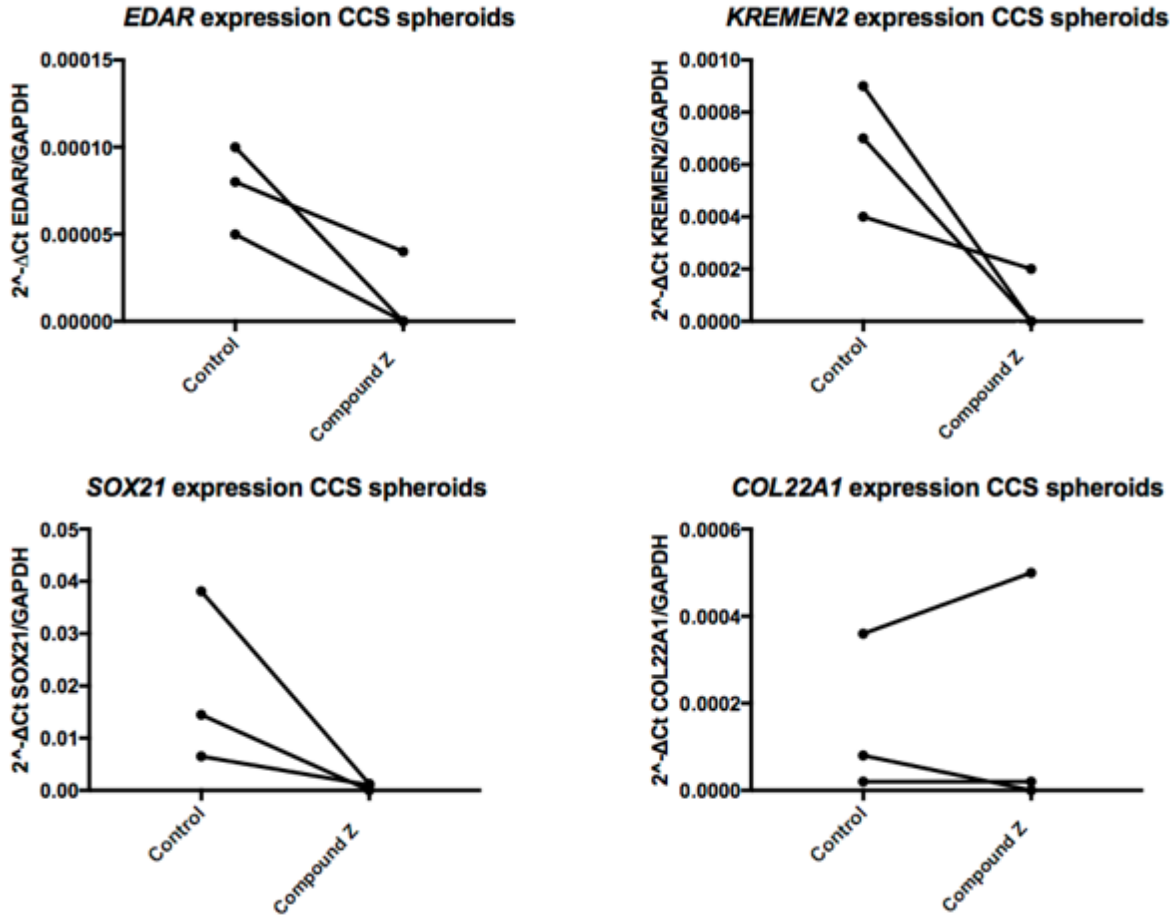

Figure 4-19. Expression of potential NF-κB non-canonical target genes in CCS spheroids. Spheroids derived from CCS tumours were grown in Aggrewell^{TM}400 plates for 96 hours then IKKα was inhibited with 3 μM Compound Z. Total RNA was extracted 24 hours after treatment and cDNA was synthesised by reverse transcription from 50 ng total RNA. Samples were pre-amplified with TaqMan®PreAmp master mix prior to qPCR by TaqMan® Gene Expression Assay. Relative gene expression normalised to *GAPDH* was measured using the $2^{-\Delta Ct}$ method. Four replicates of each reaction were performed. Plots are representative of two independent replicates.

Expression of *EDAR* was reduced or completely ablated after treatment with 3 uM Compound Z, while *KREMEN2* and *SOX21* expression was also significantly reduced (unpaired t-test of dCt values control vs treated p=0.0155 and 0.0411 respectively), suggesting that regulation of these three genes is IKKα-dependent in CCS tumour keratinocytes.

4.2 Discussion

In this chapter, I provide evidence that the non-canonical NF-κB signalling pathway is dysregulated in CYLD cutaneous syndrome by showing upregulation of RelB and p100 in addition to c-Rel, *p*-RelA (S536) and p105/p50 in CCS tumour derived primary spheroids. Using a FACS based CD45 depletion method, I show that keratinocytes isolated from tumours differentially express a subset of potential non-canonical NF-κB target genes including the ectodysplasin a receptor (*EDAR*). EDAR overexpression was confirmed in CCS tumour derived spheroids, and expression was reduced after treatment with a small molecule IKKα inhibitor. These findings suggest that *EDAR* overexpression may be IKKα-dependent in CCS tumour keratinocytes and highlight IKKα as a potential therapeutic target in CYLD cutaneous syndrome.

EDAR belongs to the tumour-necrosis factor receptor (TNFR) family of receptors that contain an intracellular death domain. Binding of EDAR to its ligand EDA-A1 results in activation of canonical NF-κB signalling via recruitment of EDARADD, which binds to a complex consisting of TRAF6, TAB2 and TAK1(Morlon et al., 2005, Kumar et al., 2001). Polyubiquitination of TRAF6 at lysine 63 (K63) promotes activation of the TRAF6/TAB2/TAK1 complex, which leads to phosphorylation of IKK and downstream degradation of IκBα. EDA/EDAR mediated NF-κB signalling is critical for the development of ectodermal derived structures as mutations in a number of pathway components cause the genetic disorder hypohidrotic ectodermal dysplasia (HED) which is characterised by hypotrichosis (sparse body hair), hypodontia (missing or malformed teeth) and hypohidrosis (lack of sweat glands).

The murine homologues of *EDA, EDAR and EDARADD* are the *tabby*, *downless* and *crinkled* genes, respectively. The *tabby*, *downless* and *crinkled* mutant mice are models for human HED, with characteristic defects in sweat glands, teeth, hair and other structures that develop from down growth of epithelial buds into the mesenchyme(Srivastava et al., 1997, Headon and Overbeek, 1999, Headon et al., 2001b). In addition to mutations in *EDA*, *EDAR* and *EDARADD*, over 90 mutations in *IKBKG* (syn. *NEMO*) have been reported to cause X-linked HED defects often with immunodeficiency (Trzeciak and Koczorowski, 2016). One heterozygous mutation in *TRAF6* has been reported to cause HED(Wisniewski and Trzeciak, 2012) and Traf6

deficient mice display the same HED phenotype as tabby/downless/crinkled mice with additional abnormalities in sebaceous glands(Naito et al., 2002). Further establishing NF-κB as downstream of EDAR in ectodermal appendages, mice ubiquitously expressing a non-degrading form of IκBα (the NF-κB super-repressor IκBαΔN which lacks the phosphorylation and ubiquitination sites) also have an identical phenotype to the tabby/downless/crinkled mice(Schmidt-Ullrich et al., 2001).

During embryonic murine hair follicle development, there is mutual regulation between Wnt/β-catenin signalling and Edar-mediated NF-κB signalling. At early stages of primary hair follicle (HF) placode formation, Wnt/B-catenin activity increases in the epithelium at pre-placodes leading to the expression of *Eda* and *Edar*. Eda/Edar NF-κB signalling is then required for the maintenance of Wnt/β-catenin signalling and expression of *Wnt10b*, *Wnt10a* and the Wnt antagonist *Dkk4* during later stages(Zhang et al., 2009). Chromatin immunoprecipitation (ChIP) showed binding of β-catenin complexes to a Tcf/Lef binding site in the promoter region of *Edar* and direct binding of RelA to *Wnt10b* and *Dkk4* NF-κB consensus sites in wild-type murine epidermal extracts. Edar also has a critical role in the maintenance of postnatal murine HF cycling(Fessing et al., 2006). Expression of *Eda*, *Edar*, *Edaradd* and *Traf6* is strongest during late anagen (the growth phase)/early catagen (the regression phase). HFs from *downless* (*dl*) mice show accelerated catagen and increased apoptosis. Consistent with this, analysis of apoptotic gene expression highlighted a significant decrease in the expression of the apoptosis inhibitor *Xiap* in HF from *dl* mouse skin. These results suggest that Eda/Edar signalling in postnatal HFs protects against apoptosis and confirm an important role for Eda/Edar/NF-κB in HF homoeostasis.

We show *EDAR* overexpression in $CD45^-$ CCS tumour keratinocytes isolated by FACS and confirm EDAR upregulation in a CCS patient derived tumour spheroid model (Figure 4-14 & Figure 4-15). Both CYLD and A20 have been implicated in the regulation of EDA/EDAR mediated NF-κB signalling. Wild-type (WT) CYLD inhibited activation of NF-κB downstream from EDAR in HEK293T cells co-transfected with *EDAR* and *CYLD* expression vectors(Trompouki et al., 2003). Co-expression of *EDAR* with a vector expressing C-terminally truncated *CYLD* (mimicking CCS) markedly reduced the ability of CYLD to inhibit NF-κB. In agreement, our results suggest that loss of CYLD due to truncation downstream from EDAR increases NF-

κB activity in CCS tumour cells. As CYLD can negatively regulate NF-κB via deubiquitination of TRAF6, NEMO and TAK1, one or more of these target substrates may underlie CYLD's negative regulation of EDA/EDAR-mediated NF-κB signalling (Kovalenko et al., 2003, Reiley et al., 2007a).

Epidermis-specific A20-knock out mice ($A20^{EKO}$) develop abnormalities in ectodermal appendages similar to those observed in transgenic mice overexpressing *Eda-A1* or *Edar* under the keratin 14 (K14) promoter in the ectoderm, excluding extra teeth and nipples(Lippens et al., 2011). Mice overexpressing *Eda-A1* have abnormal hair, sebaceous glands and teeth, longer nails, initiate new HFs continuously from E14 until birth and display prolonged anagen during HF cycling(Mustonen et al., 2003). In embryonic (E14) $Eda^{-/-}$ (*Tabby* mouse) skin explants, Eda-A1 treatment induced *A20* expression and A20 blocked EDAR mediated NF-κB activation in HEK293T cells, suggesting a negative feedback loop(Lippens et al., 2011). EDAR overexpression has been reported in the autoimmune disorder Sjögren's syndrome (SS), which is characterised by symptoms of dry eyes and dry mouth due to defective meibomian and salivary glands(Sisto et al., 2016). Polymorphisms in *A20* are associated with this and other inflammatory diseases such as psoriasis. Sisto et al (2016) confirmed that both *EDA* and *EDAR* are upregulated in SS derived salivary gland epithelial cells (SGECs). Silencing of *A20* in healthy SGECs increased the protein expression of EDA and EDAR and activated canonical NF-κB signalling. SS SGECs transfected with the super-repressor IκBαΔN displayed a reduction in canonical NF-κB signalling however NF-κB was not responsible for the expression of *EDA* and *EDAR*, as mRNA levels remained equivalent to healthy SGECs. This study further supports that A20 is a response gene involved in a negative feedback loop with activated EDA/EDAR/NF-κB, in agreement with the $A20^{EKO}$ mouse model. Lippens et al (2011) found A20 mediated inhibition of EDA/EDAR signalling to be independent of its deubiquitinase function, as a DUB mutant form of A20 could still inhibit NF-κB activation. This could indicate that in CCS tumour cells, A20 is able to carry out some level of DUB-independent negative regulation of EDAR-induced NF-κB signalling but without CYLD, TRAF6 polyubiquitination and NF-κB hyperactivation can persist.

In addition to aberrant activation of NF-κB, EDAR overexpression may enhance Wnt/β-catenin signalling. EDAR is overexpressed in colorectal cancer (CRC) and promotes tumourigenesis by increasing β-catenin levels, leading to upregulation of

Wnt/B-catenin target genes involved in cell cycle checkpoint regulation(Wang et al., 2020). EDAR knockdown with shRNA in CRC cell lines increased apoptosis and inhibited proliferation due to cell cycle arrest in G1 phase. Xenograft mice with EDAR knockdown in transplanted tumours had decreased tumour burden and tumour tissue displayed reduced levels of β-catenin and its target gene c-Myc. Treatment with a β-catenin agonist in CRC cells with EDAR knockdown reverted cell cycle signalling to the non-silenced proliferative phenotype, suggesting EDAR enhances tumour proliferation via β-catenin. The exact mechanism for EDAR modulation of β-catenin levels in CRC is not understood.

It is possible that there is crosstalk between EDAR-induced NF-κB signalling and Wnt signalling in CCS. CCS tumours are known to have increased levels of nuclear β-catenin relative to perilesional skin and upregulation of Wnt/β-catenin pathway-related genes(Tauriello et al., 2010, Rajan et al., 2011a). In addition to NF-κB, CYLD is a negative regulator of the canonical Wnt signalling pathway where it removes K63-linked ubiquitin chains from Dishevelled segment polarity protein 1 (DVL1). Loss of CYLD in CCS tumours is therefore thought to promote tumourigenesis through hyperactivation of both NF-κB and Wnt signalling(Brummelkamp et al., 2003, Kovalenko et al., 2003, Trompouki et al., 2003, Massoumi et al., 2006a, Tauriello et al., 2010). Like the mutual regulation between Wnt and NF-κB during murine HF induction, it is possible that EDAR signalling in CCS enhances Wnt by activating transcription of a Wnt agonist such as *WNT10B*, which in turn promotes β-catenin-TCF/LEF transcription of *EDAR*. Both *EDAR* and *WNT10B* were significantly upregulated in CCS CD45- keratinocytes relative to control skin (Figure 4-14). Changes in levels of WNT10B could not be validated in CCS primary cell models after stimulation with EDA-A1 due to the non-specificity of the WNT10B antibody (Figure 4-17).

Selected markers of EDA/EDAR signalling activation in 2D CCS primary cells showed a lack of response to EDA-A1 stimulation apart from TNFRSF18, which increased in a dose-dependent manner (Figure 4-17). Although lack of response could be attributed to 2D CCS primary cells not expressing EDAR, the changes to TNFRSF18 suggest that EDAR may be expressed and run at a higher molecular weight on immunoblots than predicted due to glycosylation. Ligand penetration in spheroids may be a reason to account for the failure to induce detectable changes to

candidate EDA/EDAR targets, however the lack of response in 2D cells suggests experimental conditions are likely to be responsible. Further optimisation of time-points and EDA-A1 concentration will therefore be necessary in future experiments, together with assessment of a wider panel of potential EDA/EDAR target genes. It will also be crucial to knockdown *EDAR* with shRNA in CCS primary cell cultures to assess which EDAR immunoblot bands are affected.

There is in vitro experimental evidence that overexpression of *EDAR* alone can lead to NF-κB signal activation *(Kumar et al., 2001, Sima et al., 2016)*. Introduction of an *Edar*-overexpressing locus into *Eda*$^{-/-}$ mice rescued primary hair follicle formation(Mou et al., 2006). *Edar*-overexpression was quantified as 4-fold higher in transgenic skin relative to non-transgenic skin, suggesting moderate overexpression of *Edar* can lead to ligand-independent signalling. A limitation of this PhD study is the lack of characterisation of EDA-A1 and EDAR localisation in CCS tumour tissue with immunohistochemistry. The source of soluble EDA-A1 within the tumours remains an important question to address, as in the absence of ligand, EDAR has been reported to act as a 'dependence receptor' in mouse models of melanoma (Vial et al., 2019). Dependence receptors contain a death domain and trigger apoptosis, however this is initiated solely by the absence of ligand rather than ligand binding. Transient transfection of HEK293T or A-549 cells with EDAR induced apoptosis via EDARADD and Caspase 8, and this was inhibited in a dose dependent manner with EDA-A1. This pro-apoptotic role is predicted to prevent tumour growth, raising the possibility that, in the absence of EDA-A1, EDAR could act as a conditional tumour suppressor in CCS.

In CCS spheroids, inhibition of IKKα reduced the expression of three potential non-canonical target genes (*EDAR*, *KREMEN2*, *SOX21*) (Figure 4-19). This could indicate that *EDAR* is a direct target of the non-canonical NF-κB signalling pathway in CCS tumours. The initial study identifying EDAR's role in NF-κB signalling reported that EDAR-induced NF-κB activation (measured by luciferase assay) was effectively blocked by a dominant-negative IKKα mutant and catalytic or truncated NIK mutants(Kumar et al., 2001). As IKKα also positively regulates that stability of β-catenin independently of NF-κB (Lamberti et al., 2001, {Albanese, 2003 #1238), (Carayol and Wang, 2006)} and Edar is a known direct target gene of β-catenin (zhang 2009, Wegner 2019), *EDAR* repression in CCS spheroids after Compound Z

may be due to inhibition of β-catenin-TCF/LEF mediated transcription rather than non-canonical NF-κB. IKKα has been shown to stimulate β-catenin-Tcf/Lef mediated transcription by inhibiting β-catenin degradation in both the canonical Axin/APC/GSK-3β Wnt signalling and p53/Siah-1 induced degradation pathways(Carayol and Wang, 2006). Inhibition of degradation appears to be mediated by IKKα phosphorylation at the N-terminus of β-catenin leading to prevention of β-catenin ubiquitination. NIK depletion has also been reported to reduce the occupancy of β-catenin at the promoter of Survivin in a melanoma cell line and reduce the expression of other β-catenin target genes*(Thu et al., 2012)*. The mechanism behind NIK regulation of β-catenin activity has not been resolved and may be at the level of IKKα. Analysis of *EDAR* expression with RT-qPCR after inhibition of the Wnt signalling pathway in CCS spheroids, for example with a small molecule Tankyrase inhibitor, could be used to in future to assess whether expression of *EDAR* is driven by Wnt signalling.

Genome-wide identification of Wnt and NF-κB target genes in CCS primary spheroids may be achieved in a future study with β-catenin and NF-κB subunit chromatin immunoprecipitation followed by high throughput sequencing (ChIP-seq) combined with RNA-seq analysis of the relevant Wnt/NF-κB-regulated transcriptome. Analysis of the genome wide distribution of β-catenin, RelA, RelB, p50, p52 and c-Rel will reveal genes with overlapping binding regions and confirm genes with selective binding of RelB and p52 or β-catenin in CCS. Performing this experiment with and without IKKα inhibition with Compound Z will delineate IKKα-dependent regulation of non-canonical NF-κB and Wnt signalling target genes in CYLD-deficient tumours cells. In addition to direct comparisons of overlapping ChIP-seq target genes and differentially expressed genes between treated and untreated spheroids, both types of data can be compared with Binding and Expression Target Analysis (BETA). BETA is a free software package that integrates differential gene expression data and ChIP-seq to predict whether transcription factors (TFs) are activating or repressing, infer direct target genes and identify both the TF binding motif and collaborators that may affect the TF's activator or repressor function(Wang et al., 2013). This approach will also reveal if Compound Z has off-target effects on canonical NF-κB signalling.

Inhibiting IKKα with Compound Z has potential as a targeted therapy that may repress both non-canonical NF-κB and oncogenic Wnt signalling in CCS tumour

cells. Targeting two dysregulated signalling pathways simultaneously may result in a broad therapeutic window between CCS tumour cells and normal skin keratinocytes. The effects of Compound Z in CCS tumour and normal skin spheroids will be explored in chapter 5.

Chapter 5. Targeting Non-canonical NF-κB Signalling in CYLD Defective Tumours

5.1 Results

CYLD cutaneous syndrome (CCS) is a disfiguring disease that can severely impact quality of life(Rajan et al., 2009). No medical treatments are currently available to prevent tumourigenesis or control tumour growth. Kinase-targeting small molecule inhibitors are a personalised medicine strategy that exploits vulnerabilities in tumour cells, such as oncogenic dependencies on aberrantly activated signalling pathways(Hoelder et al., 2012). Given the upregulation of canonical and non-canonical NF-κB signalling in CCS tumours demonstrated in chapter 4, in this chapter I use patient derived tumour spheroids as a preclinical model to predict the clinical efficacy of small molecule inhibitors targeting the cellular kinases inhibitory-κB kinase (IKK) α and IKKβ.

5.1.1 Truncated CYLD (trCYLD) may be expressed by tumour keratinocytes

The majority of CCS causative mutations are frameshift or nonsense mutations that are predicted to result in a truncated CYLD protein due to a premature termination codon (PTC)(Blake and Toro, 2009). Nonsense mediated decay (NMD) of mRNA is usually triggered during translation when a PTC occurs ≥50-55 nucleotides upstream of an exon-exon junction(Kurosaki et al., 2019). However, NMD efficiency is not 100% and varies between individuals(Sarkar et al., 2019, Nguyen et al., 2014). It is therefore possible that CCS tumour cells produce a dominant-negative, partially functional or non-functional truncated CYLD protein.

A shorter CYLD protein may also be expected due to alternative splicing of *CYLD*. A naturally occurring short isoform of CYLD, termed ‘sCYLD’, was discovered when a mouse strain with targeted deletion of *CYLD* exon 7 no longer produced full length CYLD and solely overexpressed the sCYLD isoform lacking both exons 7 and 8(Hovelmeyer et al., 2007). In humans, the equivalent isoform (Ensembl CYLD-212, Transcript ID ENST00000568704) lacks exons 10 and 11, resulting in a 771 aa CYLD protein in contrast to full length CYLD at 956 aa (Figure 5-1).

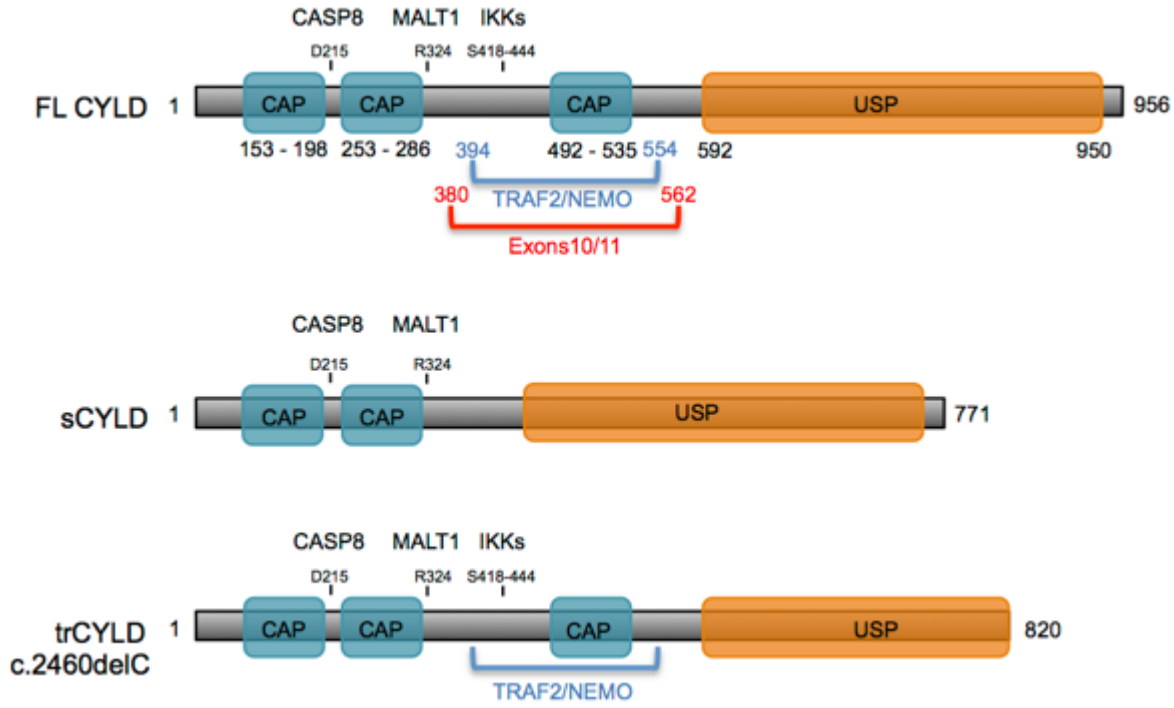

Figure 5-1. Schematic of full length CYLD, short CYLD and C-terminally truncated CYLD. Full length CYLD (FL CYLD) has three CAP-Gly domains and a catalytic ubiquitin specific protease (USP) domain. Cleavage sites by Caspase 8 (aspartic acid 215) and MALT1 (arginine 324) and a region containing serines phosphorylated by IKKs (418 – 444) are shown. The short CYLD (sCYLD) isoform encoded by transcript variant ENST00000568704.2 lacks exons 10 and 11. Consequently, this variant lacks IKK phosphorylation sites and the TRAF2 and NEMO binding domains. The truncated CYLD (trCYLD) protein predicted to result from the CCS patient mutation c.2460delC (p.C820*) lacks 136 amino acids at the C-terminus and therefore has a truncated USP domain.

When CCS tumour and CCS spheroid lysates were assessed by immunoblot for full length CYLD contamination, a smaller band around 90 kDa was consistently detected that was posited to be a shorter form of CYLD(see Chapter 4). To test the specificity of the CYLD antibody and confirm that the band of interest was indeed CYLD rather than a non-specific band, CCS 2D adherent primary cell cultures from 4 patients were transduced with pGIPZ lentiviral particles containing short hairpin RNA (shRNA) targeting CYLD (shCyl1 or shCyl2) or non-CYLD targeting controls. Successfully transduced cells expressing GFP were selected with puromycin (3 µg/ml) and analysed by immunoblot for flCYLD and trCYLD levels (Figure 5-2).

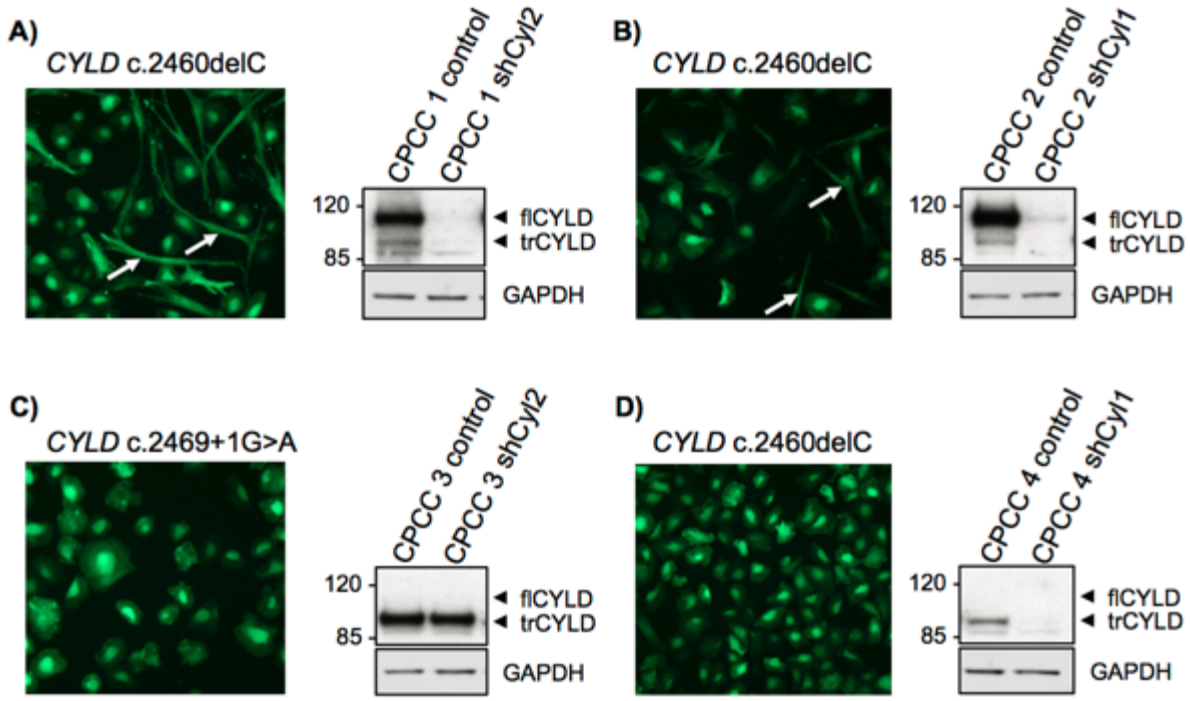

Figure 5-2. Knockdown of CYLD in 2D adherent cylindroma primary cell cultures (CPCCs) using pGIPZ lentiviral shRNA. A) fl and trCYLD levels were reduced in a CPCC culture with fibroblast contamination (white arrows) transduced with shCyl2. B) fl and trCYLD levels were reduced in a CPCC culture with fibroblast contamination transduced with shCyl1. C) shCyl2 did not affect trCYLD levels in a fibroblast free CPCC from a tumour with a splice site mutation in *CYLD*. D) trCYLD was reduced by shCyl1 in a fibroblast free CPCC. flCYLD; full length CYLD, trCYLD; truncated CYLD.

Two CCS cultures contained a mixture of fibroblasts, which are heterozygous for the CYLD mutation (*CYLD*$^{+/-}$), and tumour keratinocytes, which are homozygous for the CYLD mutation (*CYLD*$^{-/-}$) (Figure 5-2A and B). Lysates obtained from these cultures produced bands for flCYLD and trCYLD. The CCS cultures in Figure 5-2C and D did not contain fibroblast contamination and consistent with this, flCYLD was not detected by immunoblot. Both flCYLD and putative trCYLD were knocked down by shRNA targeting exons 11 and 12 (shCyl1) or exon 19 (shCyl2) of *CYLD* mRNA in CCS primary cultures derived from tumours with a PTC in exon 18 (c.2460delC) (Figure 5-2A, B & D). shCyl2 did not affect trCYLD levels in the primary cell culture with a splice site mutation in *CYLD* (Figure 5-2C), possibly due to the proximity of the guide sequence of shCyl2 to the mutated splice site (Figure 1-3). Nevertheless, successful knockdown of the ~90 kDa band in 3 CPCCs with shRNA targeting *CYLD* supports the theory that this band may be truncated CYLD or a shorter splice isoform of CYLD that has not yet been characterised in CCS tumours.

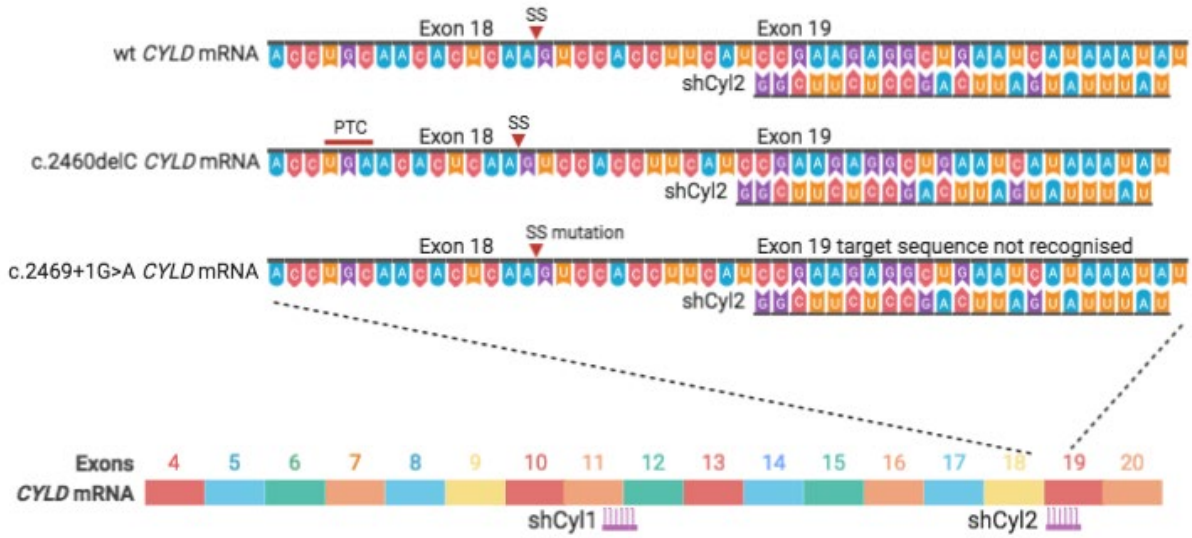

Figure 5-3. Binding sites of two short hairpin RNA (shRNA) sequences targeting *CYLD* mRNA. The shCyl1 target sequence binds across exons 11 and 12 of *CYLD*. The shCyl2 target sequence binds to exon 19 of *CYLD* mRNA. The proximity of the shCyl2 target sequence to the premature termination codon (PTC) inducing c.2460delC mutation and c.2469+1G>A splice site (SS) mutation is indicated. Created in BioRender.com.

5.1.2 sCYLD is not detected in CCS tumour transcriptomic data

To assess whether 'trCYLD' in CCS tumour keratinocytes is the naturally occurring short splice isoform 'sCYLD' lacking exons 10 and 11 (transcript variant ENST00000568704.2), bulk RNA-seq data (provided by Dr Naomi Sinclair and Dr Neil Rajan) from 16 CCS tumours and 4 control skin samples from CCS patients was analysed. Splicing at junctions of interest was visualised for each sample using the Splice Junctions Track alignment of the Integrative genomics Viewer (IGV)(Robinson et al., 2011). This approach found zero reads skipping both exons 10 and 11 in all samples. One control sample and three CCS tumour samples had low numbers of reads for a transcript variant skipping exon 11 only (Figure 1-4A).

To validate the RNA-Seq analysis, primers were designed in exons 9 (P1) and 12 (P2) of *CYLD* to allow differentiation of the full length *CYLD* transcript (amplicon 768 bp), *sCYLD* ENST00000568704.2 (amplicon 222 bp) and the transcript variant skipping exon 11 only (amplicon 602 bp) by PCR of cDNA (Figure 1-4B). PCR was performed with cDNA from 3 normal skin and 7 tumour tissue samples and amplicons were run on an agarose gel to assess the presence of alternative transcript variants

of *CYLD* (Figure 1-4C). In agreement with RNA-seq data, an amplicon at 222 bp corresponding to sCYLD was not detected in CCS tumour samples. A band was detected ~600 bp in both normal and CCS tumour samples (excluding one tumour, lane 7) that potentially corresponds to the transcript variant lacking exon 11 present at low levels in RNA-seq data. This variant would be estimated to produce a 99 kDa CYLD protein, as such it cannot be ruled out that this rare transcript is responsible for the ~90 kDa protein designated 'trCYLD' detected by immunoblot in CCS tumour lysates.

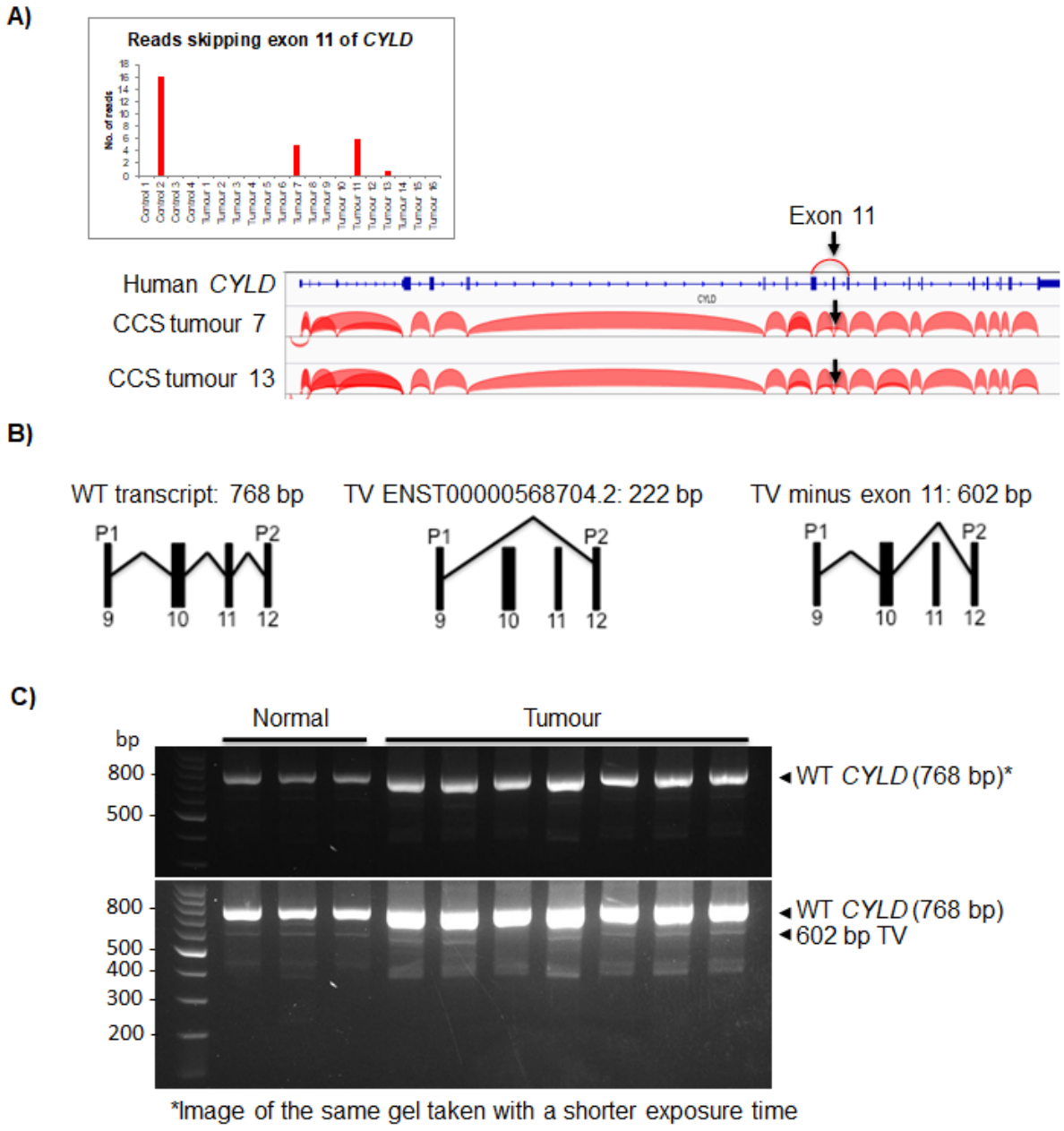

Figure 5-4. sCYLD is not detected in transcriptomic data. A) Splice Junction Track alignment of RNA-seq data in the Integrative Genome Viewer (IGV) shows a rare *CYLD*

transcript variant skipping exon 11 in a subset of CCS tumours and control skin from CCS patients. B) Primers were designed in exons 9 and 12 of *CYLD* to investigate the presence of a naturally occurring short splice isoform lacking exons 10 and 11 (sCYLD, transcript variant ENST00000568704.2) in CCS tumours. Primers 1 and 2 generate a 768 bp amplicon from the wild type (full length) *CYLD* transcript, a 222 bp amplicon from ENST00000568704.2. and a 602 bp amplicon from the rare transcript variant skipping exon 11. C) PCR of cDNA from normal control skin and CCS tumours with primers in exons 9 and 12 of CYLD produces a 768 bp band for the wild type *CYLD* transcript in all samples. A band is also present in normal skin and tumours ~600 bp that could correspond to the rare transcript variant lacking exon 11. Bands at 222 bp corresponding to ENST00000568704.2 (sCYLD) were not detected. Gel image is representative of three technical replicates.

In summary, the investigation of sCYLD in CCS samples is of relevance to NF-κB signalling given the lack of TRAF2 and NEMO binding sites in this isoform and is of interest due the detection of a shorter CYLD protein in CCS tumour samples by immunoblot. Here, I do not find evidence of *sCYLD* expression in transcriptomic data from CCS tumours or strong evidence that alternative splicing is responsible for trCYLD in CCS tumours.

5.1.3 Compound Z reduces trCYLD in CCS primary cells

Intriguingly, it was found that the IKKα inhibitor (Compound Z) used to investigate potential non-canonical target genes overexpressed by $CD45^-$ CCS keratinocytes in chapter 4 also reduced levels of trCYLD in CCS spheroids (Figure 5-5A). To confirm this result, levels of full length and truncated CYLD were assessed in 2D CCS and normal primary cells after treatment with Compound Z. The IKKβ inhibitor TPCA-1, dual IKKβ and IKKα inhibitor BMS345541 and the IKKα inhibitor Compound Y were also assessed to see if other small molecule IKK inhibitors affect levels of trCYLD in CCS primary cells. Cells were drugged in 6 well plates for 24 hours at mean IC_{50} concentrations determined by CCS spheroid dose-response assays (detailed in section 5.1.7) rounded to the nearest whole number apart from Compound Z, which was used at the mean IC_{50} (2.74 μM) rounded up and down to 2 and 3 μM, respectively (Figure 5-5B-C).

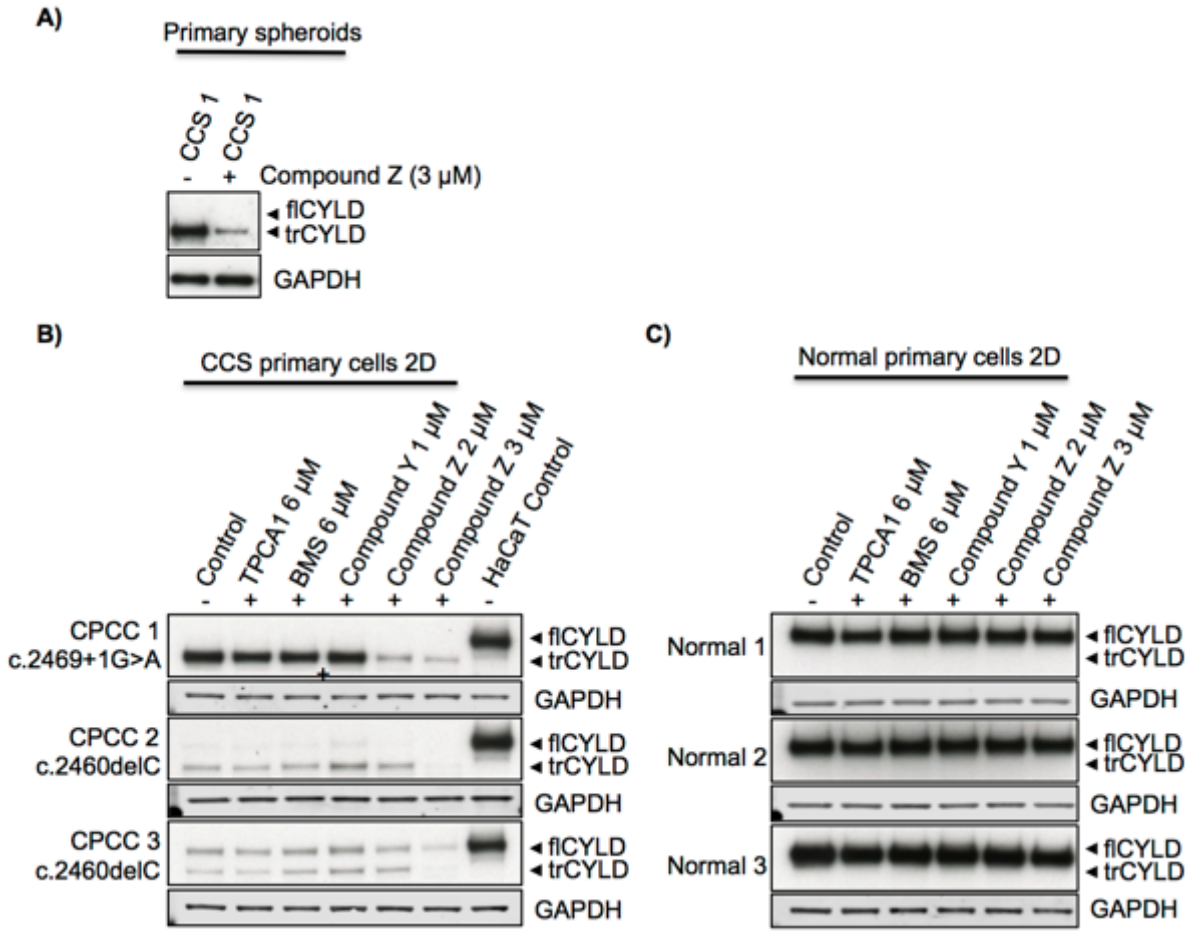

Figure 5-5. Effects of IKK inhibition on CYLD in CCS primary cells. A) Inhibition of IKKα with Compound Z reduced levels of truncated CYLD (trCYLD) in a CCS spheroid culture. B) 2D CCS primary cells were cultured in small molecule IKK inhibitors for 24 hrs; TPCA-1 targeting IKKβ, BMS345541 targeting IKKβ and IKKα, Compound Y targeting IKKα or Compound Z targeting IKKα. trCYLD reduced after Compound Z only, both in samples with a truncating *CYLD* mutation (c.2460delC) and a splice site mutation (c.2469+1G>A). A HaCaT lysate was included as a size marker for full length CYLD (flCYLD). C) Compound Z did not affect levels of flCYLD in normal primary keratinocytes. CPCC, CCS primary cell culture.

In samples with a truncating *CYLD* mutation (c.2460delC), trCYLD was reduced after treatment with 3 μM Compound Z, while 2 μM was sufficient to cause a decrease in the sample derived from a tumour with a splice site mutation (c.2469+1G>A). The previous generation of this compound (Compound Y) had no effect on trCYLD in CPCC 2 and resulted in a slight increase in trCYLD relative to controls in CPCCs 1 and 3. The effect on trCYLD therefore appears to be unique to Compound Z. None of the small molecule inhibitors tested affected levels of flCYLD in normal primary keratinocytes.

5.1.4 Compound Z may induce cleavage of trCYLD by MALT1

To investigate trCYLD protein degradation after compound Z, 2D primary cell lysates were run on a 4-12% Bis-Tris gel in MES running buffer to evaluate the appearance of lower molecular weight bands after 3 μM Compound Z. Two CYLD cleavage sites have been reported (Figure 1-6A). Caspase 8 cleaves CYLD at aspartic acid (Asp) 215 (D215) resulting in a 25 kDa N-terminal fragment and an unstable p82 fragment that is degraded by the proteasome (O'Donnell et al., 2011). Mucosa-associated lymphoid tissue 1 (MALT1) cleaves CYLD at arginine 324 (R324) resulting in a 40 kDa N-terminal fragment and a C-terminal 70 kDa fragment(Staal et al., 2011). Determining if trCYLD is cleaved by MALT1 may be of functional relevance, as consequences are cell type specific. MALT1 cleavage of CYLD in T cells has been shown to activate T cell receptor (TCR)-induced JNK signalling(Staal et al., 2011), while in microvascular endothelial cells, CYLD cleavage by MALT1 results in microtubule destabilisation and cellular permeability(Klei et al., 2016).

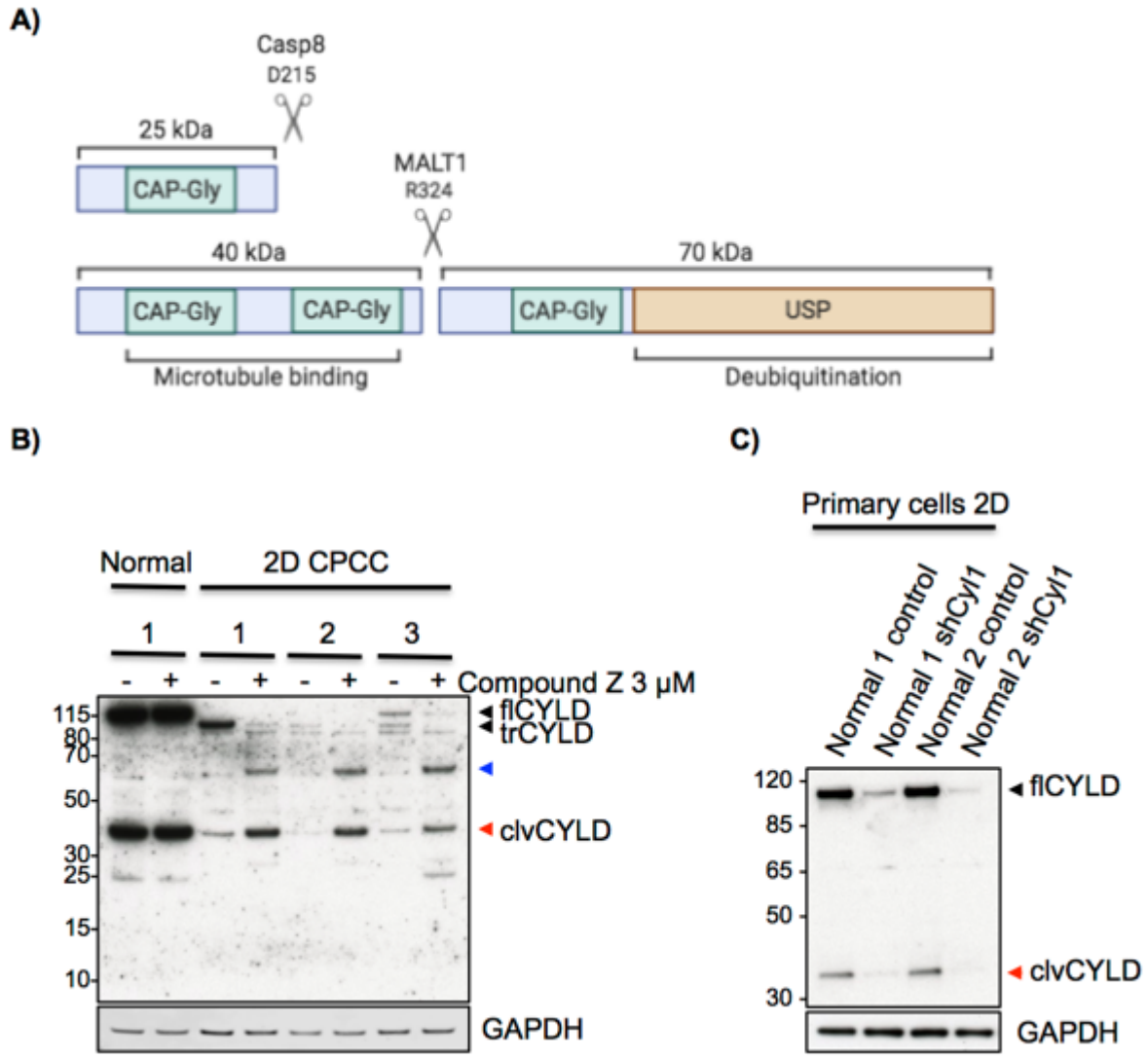

Figure 5-6. Compound Z may induce cleavage of trCYLD by MALT1. A) Schematic of CYLD showing Caspase 8 and MALT1 cleavage sites (created in BioRender.com). B) Normal keratinocytes produce a ~35-40 kDa band detected by the CYLD antibody corresponding to the N-terminal 40 kDa fragment generated by MALT1 (clvCYLD). Bands at ~60-65 (blue arrow) and 35-40 kDa (red arrow) increase in CCS 2D lysates after treatment with Compound Z for 24 hours. C) Lentiviral knockdown of CYLD in normal skin primary keratinocytes caused a reduction in full length CYLD (flCYLD) and the ~35-40 kDa band detected by the CYLD antibody (red arrow). CAP-Gly, cytoskeleton-associated protein-glycine conserved domain; USP, ubiquitin specific protease domain.

In 2D normal primary keratinocytes, a strong band was detected ~40 kDa that does not alter upon treatment with Compound Z (Figure 1-6B). In CCS primary cells, this band was weakly detected in untreated cells but increased after Compound Z, suggesting MALT1 cleavage of trCYLD. A 70 kDa fragment was not detected by the CYLD antibody, which recognises an unmapped epitope between the N-terminal half of CYLD (amino acids 1 – 400). A band appeared for all 3 CCS lysates at 60-65 kDa after Compound Z that could correspond to a truncated C-terminal fragment if the

antibody recognised a region encompassing the MALT1 cleavage site. Presumably however, this would also result in detection of a 70 kDa band in the normal cells. The identity of this band therefore remains undetermined.

Evaluation of normal skin primary cells with lentiviral knockdown of CYLD further supports that the ~40 kDa band is CYLD rather than a non-specific band, as in addition to flCYLD, bands at this weight were also reduced (Figure 1-6C).

5.1.5 Protein evidence suggests trCYLD is C-terminally truncated CYLD

The 40 kDa CYLD fragment generated by CCS primary cells after Compound Z was equal in size to the cleaved fragment in normal keratinocytes, suggesting that trCYLD is not truncated at the N-terminus. To test this assumption, immunoblots for flCYLD and trCYLD were performed with N-terminal and C-terminal CYLD antibodies (Figure 1-7).

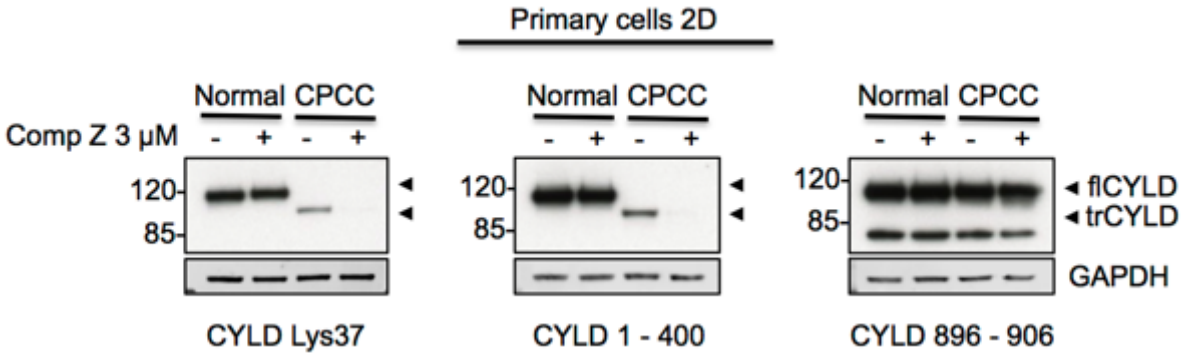

Figure 5-7. trCYLD is not truncated at the N-terminus. 2D primary cell lysates derived from one normal skin donor and one CCS tumour with a splice site mutation in *CYLD* (c.2469+1A>G) were loaded at 10 µg on 7% Tris-acetate gels. PVDF membranes were probed with one of three antibodies targeting CYLD. Full length (flCYLD) is 956 amino acids in length. trCYLD is detected by an N-terminal antibody that recognises CYLD residues surrounding lysine 37 (CST#8462 monoclonal antibody D1A10) and an antibody that recognises an epitope located within the N-terminal half of CYLD between amino acids 1 – 400 (CST#12797 monoclonal antibody D6O5O). trCYLD was not recognised by an antibody raised against the C-terminus of CYLD (Abcam #ab137524 polyclonal antibody). This antibody detected a band at the same molecular weight as flCYLD in the CCS lysates suggesting it may cross-react with other proteins. Comp Z, Compound Z.

Results suggest that trCYLD is not N-terminally truncated, as it is recognised by both the CYLD antibody used throughout (CST#12797 which recognises an unmapped epitope between amino acids 1 – 400 of CYLD) and an antibody raised against the N terminus of CYLD (CST#8462 which recognises residues surrounding CYLD lysine

37) (Figure 1-7). trCYLD was not detected by an antibody raised against the C-terminus of CYLD (Abcam #ab137524, recognises CYLD amino acids 896-906), however this polyclonal antibody was deemed unreliable. Although it recognised bands at the correct weight for flCYLD in normal lysates, it also detected strong bands at this weight in the CCS lysates shown by the monoclonal CST antibodies to be flCYLD free. A monoclonal antibody raised against the C-terminus of CYLD was not available for analysis.

To further investigate whether the ~90 kDa band designated 'trCYLD' is C-terminally truncated CYLD resulting from *CYLD* mutation, CYLD immunoblots were performed with lysates from tumours carrying *CYLD* mutations in a range of exons alongside tumours with the 2 mutations (c.2460delC and c.2469+1G>A) that consistently produce bands at ~90 kDa (Table 5-1. & Figure 1-8). The lysates marked with an asterisk were obtained from a patient with a 5.5MB germline deletion on chromosome 16q encompassing one allele of *CYLD*. Each tumour that arises in this patient contains a unique somatic mutation in the remaining *CYLD* allele. Estimated molecular weights of mutant CYLD proteins were based on the average molecular weight of an amino acid (110 Da).

Table 5-1. CCS tumour *CYLD* mutation information for Figure 1-8. Estimated molecular weights of mutant CYLD are based on the average amino acid molecular weight (110 Da). The protein consequences of the splice site mutations are classed as unknown and estimates of size are based on the number of amino acids preceding the mutation. Aa, amino acid.

Tumour	Nucleotide change	Mutation type	Aa change	Exon	No. of aa	Est. kDa
1	c.1112C>A	Nonsense	p.S371X	9	371	40.8
2	c.1112C>A*	Nonsense	p.S371X	9	371	40.8
3	c.2158G>A*	Missense	p.E720K	16	720	79.2
4	c.2460delC	Nonsense	p.C820X	18	820	90.2
5	c.2469+1G>A	Splice	p.?	Donor site pre-exon 19	823	90.5
6	c.2687-2A>G	Splice	p.?	Acceptor site pre-exon 20	895	98.5
7	c.2806C>T	Nonsense	p.R936X	20	935	102.9

*Somatic mutations with germline 5.5MB *CYLD* deletion.

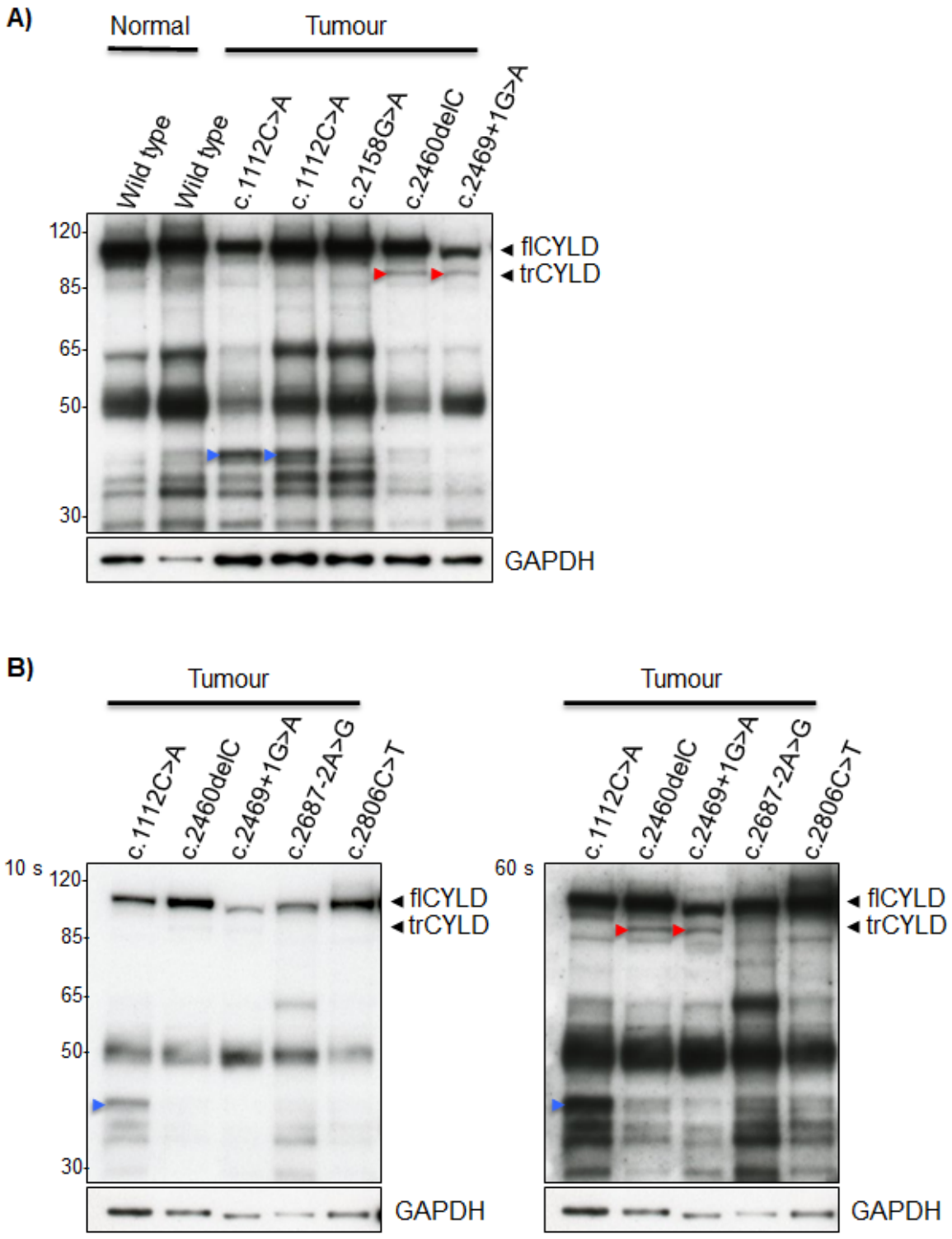

Figure 5-8. trCYLD detection in CCS whole tumour lysates from patients with a range of *CYLD* mutations. Seven whole CCS tumour lysates from 6 patients were analysed for evidence of truncated CYLD corresponding to *CYLD* mutation (see **Table 5-1** for predicted molecular weights of CYLD mutants). Two normal skin whole tissue lysates were included as controls for full length CYLD (flCYLD). FlCYLD was detected in all tumour samples, indicating the presence of immune cells in the lysates. The non-specific bands in these and the normal skin lysates may therefore originate from the tumour/normal skin infiltrating leukocytes or CCS tumour/normal skin keratinocytes. A) trCYLD at ~90 kDa was detected solely in the tumour with c.2460delC predicted to result in a truncated protein of ~90 kDa and

the tumour with c.2469+1G>A (red arrows). Bands at ~45 kDa were detected in tumours with c.1112C>A predicted to result in a truncated protein ~40 kDa (blue arrows). B) trCYLD was not detected in tumours with mutations occurring before or after exon 18. s, seconds of X-ray film exposure time.

The protein designated 'trCYLD' was only detected in the two samples with mutations in or near exon 18 with a predicted molecular weight of ~90 kDa (red arrows, Figure 1-8A-B), suggesting that this band is C-terminally truncated CYLD resulting from the c.2460delC or c.2469+1G>A mutations and arguing against this band being a shorter splice isoform of CYLD. A candidate band ~40 kDa was detected in the lysates with the c.1112C>A mutation in exon 9 predicted to result in a truncated protein (blue arrows, Figure 1-8A-B). A unique band ~80 kDa was not detected in the tumour lysate with the c.2158G>A mutation in exon 16, however this is a missense mutation that may not result in a truncated protein (Figure 1-8A). Similarly, a candidate band ~99 kDa was not identified in the c.2687-2A>G lysate. This splice site mutation however has unknown consequences and could therefore result in a truncated protein larger than predicted that cannot be distinguished from full length CYLD by immunoblot or may not result in a truncated protein. The size of c.2806C>T truncated CYLD (935 aa, ~103 kDa) is likely to be too close to full length CYLD (956 aa, 107 kDa) to allow detection by immunoblot (Figure 1-8B).

In summary, analysis of trCYLD expression in whole tissue lysates from CCS tumours with different mutations in *CYLD* did not reveal a ~90 kDa band in all tumours. Candidate bands were detected in 4 out of 7 tumours that could correspond to truncated CYLD caused by CCS mutations. Overall, the evidence presented suggests that 'trCYLD' is C-terminally truncated CYLD rather than an alternative splice isoform that would be homogenous in all tumours.

5.1.6 p100 processing is altered in CCS tumour keratinocytes

Given the antagonistic effect of Compound Z on trCYLD and the activation of non-canonical NF-κB signalling in CCS tumour cells (see Chapter 4), the specificity of Compound Z for targeting the non-canonical NF-κB pathway in CCS tumour keratinocytes was assessed. 2D CCS primary cells were drugged with 3 μM Compound Z for 24 hours and evaluated for markers of on-target engagement with IKKα (*p*-p100 S866/870 and p52) and off-target engagement with IKKβ (IκBα) (Figure 5-9). Levels of *p*-RelA S536 were also evaluated, however as this serine is

phosphorylated by multiple kinases including IKKβ and IKKα, this marker was not categorised as an indicator of on or off target engagement(Christian et al., 2016).

The phosphorylation of p100 at serines 866 and 870 is dependent on both IKKα and NIK (Liang et al., 2006), therefore levels of *p*-p100 S866/870 should decrease after IKKα inhibition. As phosphorylation at S866 and S870 is indispensable for the processing of p100 into p52, levels of p52 should also decrease after IKKα inhibition. After 24 hours treatment with Compound Z, a lower molecular weight band was detected for total p100 in CCS primary cells (Figure 5-9A). This finding supports the assertion that p100 processing is altered in CYLD defective tumour keratinocytes and shows that Compound Z affects p100 processing in 2D CCS primary cells differently to normal primary keratinocytes.

Under these conditions, no changes were observed in the levels of p52 in 2D normal or CCS primary cells. Similarly, a reduction in p100 phosphorylated and S866 was not detected at the predicted molecular weight. Rather, Compound Z caused a large increase in a non-specific band ~200 kDa in CCS primary cells and this result was replicated with an antibody that detects p100 phosphorylated at S866 and S870.

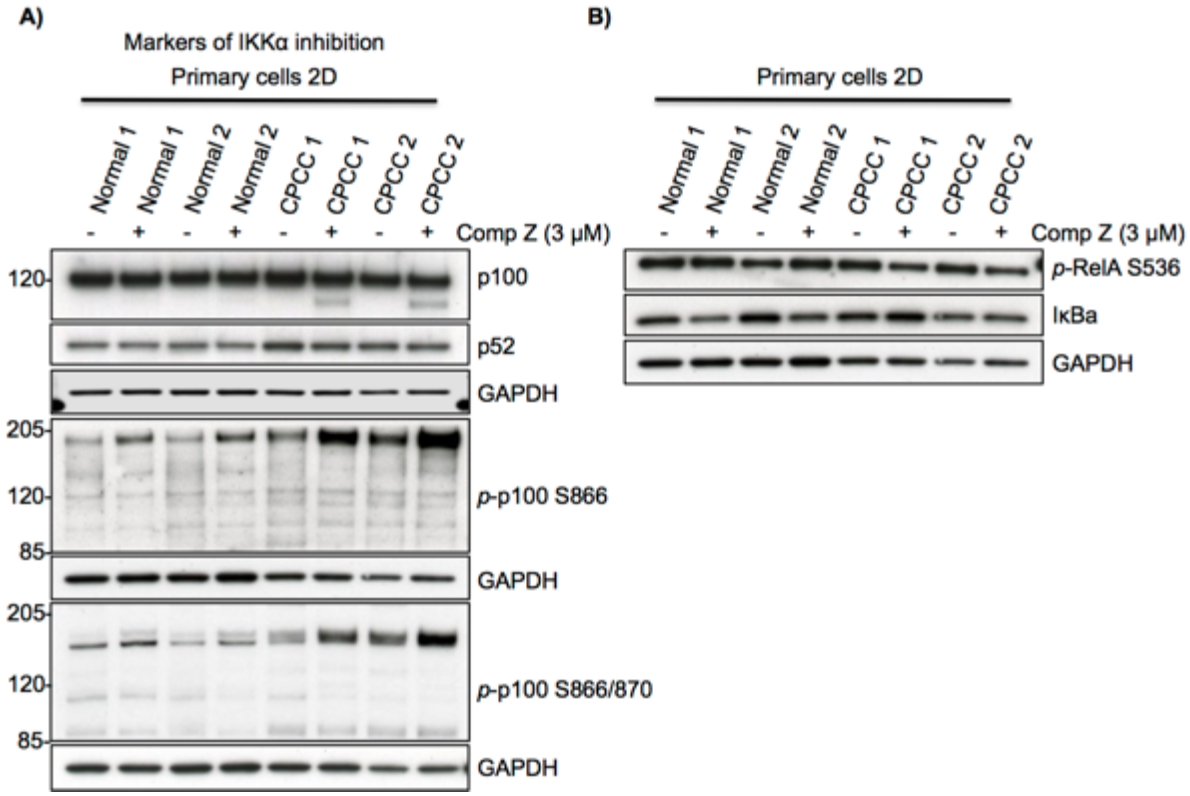

Figure 5-9. Effects of Compound Z IKKα inhibition in 2D primary cells. Normal and CCS tumour primary cells were cultured in Compound Z IKKα inhibitor for 24 hrs. A) p100 processing in CCS primary cells was altered by Compound Z but levels of p52 were not affected. B) IκBα levels did not increase after Compound Z, suggesting the inhibitor did not engage with IKKβ. Compound Z reduced levels of *p*-RelA S536 in CCS primary cells. GAPDH images are duplicated for immunoblots from the same gel. CPCC; CCS primary cell culture. Comp Z, Compound Z.

IκBα levels did not alter in 2D CCS primary cells after treatment with Compound Z, suggesting Compound Z did not engage IKKβ (Figure 5-9B). IκBα should not be affected by treatment with Compound Z because IKKα is dispensable for activation of the IKK complex and the degradation of IκBα (Hu et al., 1999). An increase in IκBα would therefore indicate off target engagement with IKKβ due to inhibition of phosphorylation of IκBα at serines 32 and 36 and subsequent lack of degradation (DiDonato et al., 1996, Zandi et al., 1997). A reduction in IκBα was observed in normal primary keratinocytes after Compound Z, suggesting an increase in canonical NF-κB signalling. Levels of *p*-RelA S536 decreased in CCS primary cells after Compound Z but whether this was due to inhibition of phosphorylation by IKKα or off target prevention of IKKβ from phosphorylating S536 was not determined (Figure 5-9B).

As the 2D primary cell model does not recapitulate CCS tumours as well as the 3D spheroid model, the same analysis was carried out with normal skin and CCS primary spheroid cultures grown in 3 μM Compound Z for 24 hours (Figure 5-10).

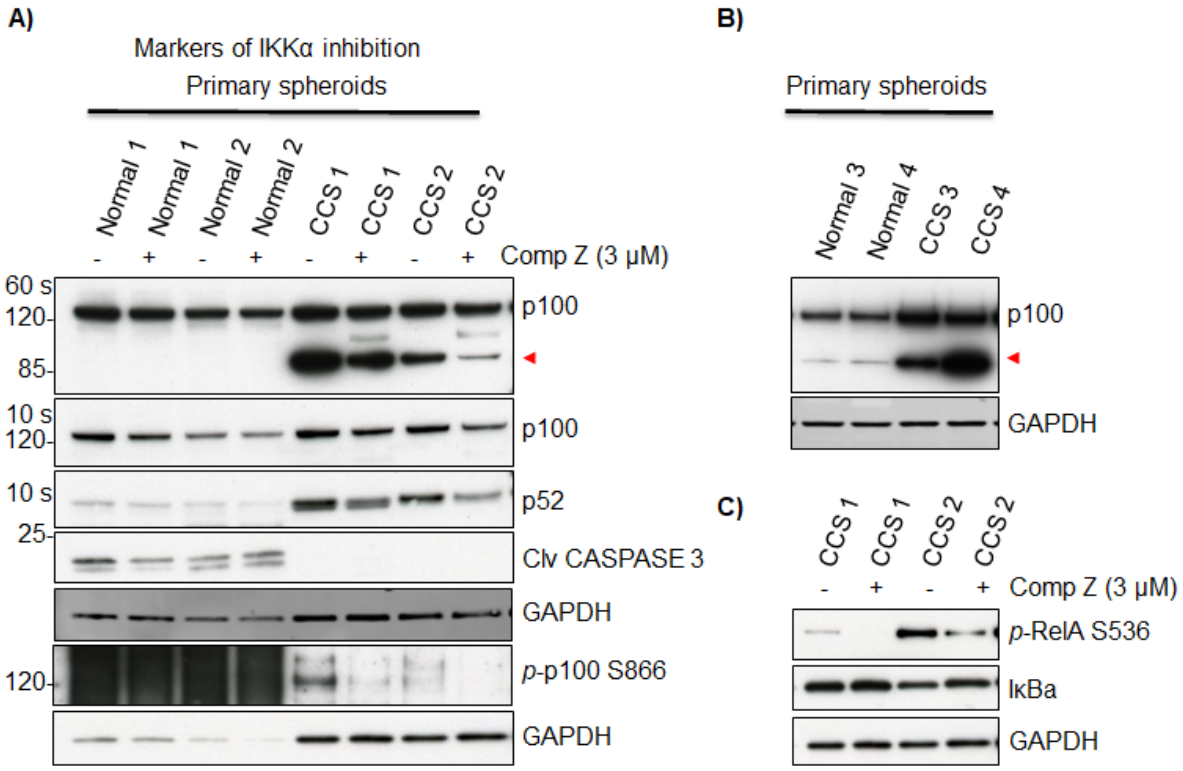

Figure 5-10. Effects of Compound Z IKKα inhibition in 3D primary spheroids. Normal and CCS tumour spheroids were cultured in Compound Z IKKα inhibitor for 24 hrs. A) p100 processing in CCS spheroids was altered by Compound Z and levels of *p*-p100 S866 and p52 decreased. Cleaved CASPASE 3 levels show that the normal primary spheroids were undergoing increased levels of apoptosis in the culture model. B) Additional untreated spheroid lysates showing expression of a band ~85 kDa detected by the p100 antibody (red arrows). C) IκBα levels increased after Compound Z, suggesting some off-target engagement with IKKβ. Compound Z reduced levels of *p*-RelA S536 in CCS spheroids. GAPDH images are duplicated for immunoblots from the same gel. CPCC; CCS primary cell culture. Comp Z, Compound Z; s, seconds of X-ray film exposure time.

Levels of p52 and phosphorylated p100 (S866) were reduced in CCS tumour spheroids after Compound Z, suggesting on target engagement of the inhibitor with IKKα (Figure 5-10A). As seen in 2D CCS primary cells (Figure 5-9A), a shorter band was detected for p100 after Compound Z. A strong band was also detected with the p100 antibody in CCS spheroids at ~85 kDa that reduced considerably with Compound Z (red arrow, Figure 5-10A). This band has previously been detected in untreated CCS spheroids and (at a much lower level) in normal skin spheroids that were not undergoing apoptosis (red arrow, Figure 5-10B).

The cleaved CASPASE 3 and GAPDH results in Figure 5-10A show that the normal primary spheroid lysates were undergoing apoptosis and are not therefore representative of healthy keratinocytes. As a result, these lysates were excluded from further analysis. In agreement with 2D CCS lysates, levels of RelA phosphorylated at S536 were reduced by Compound Z in CCS spheroids (Figure 5-10C). IκBα did increase slightly in CCS spheroids after Compound Z, suggesting limited off target engagement with IKKβ.

Overall, these results suggest that p100 processing is altered in CCS tumours and, based on the reduction in levels of *p*-p100 (S866) and p52, Compound Z is effectively targeting the non-canonical NF-κB signalling pathway.

5.1.7 Targeting IKKα in CCS primary spheroids reduces cell viability

To investigate the therapeutic potential of inhibiting IKKα in CCS tumours, primary spheroids were used as a preclinical model. Dose-response assays were carried out to determine the effective concentrations of different NF-κB inhibitors and examine how well each drug decreased the growth of CCS tumours grown in vitro. Initially, two novel IKKα inhibitors that preceded the development of Compound Z were evaluated (Compound X and Compound Y, provided by Prof. Simon Mackay, Strathclyde University). Inhibitors targeting canonical NF-κB signalling via IKKβ (TPCA-1, Tocris) or both IKKα and IKKβ (BMS345541, Tocris) were also tested to ascertain which pathway is more important to the tumour cells for survival. Primary cells were seeded in Corning® 96 well spheroid microplates at 30,000 cells per well in media supplemented with 1.5 mM $CaCl_2$. Spheroids were drugged on day 8 at a range of concentrations then cell viability was assessed at 72 hours with the CellTiter-Glo® Luminescent Cell Viability Assay. Luminescent output was used to generate dose-response curves and IC_{50}s for each inhibitor (Figure 5-11).

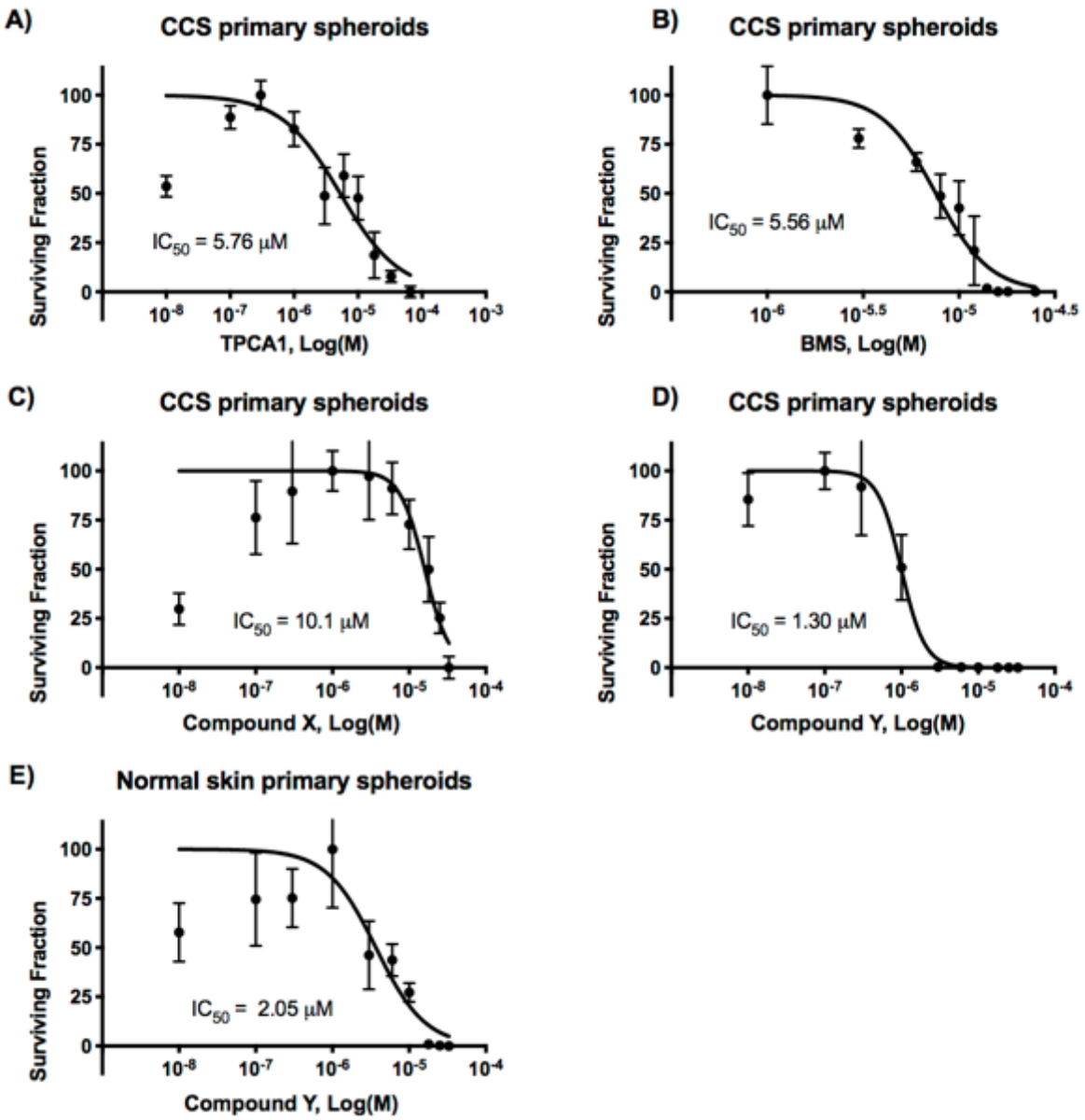

Figure 5-11. CCS primary spheroid dose-response to small molecule IKK inhibitors. Primary cells derived from CCS tumours or normal skin were seeded in 96 well plates at 30,000 per well in media supplimented with 1.5 mM $CaCl_2$. Spheroids were grown for one week then drugged with either A) TPCA-1 targeting IKKβ. B) BMS345541 targeting IKKβ and IKKα. C). Compound X targeting IKKα or D) & E) Compound Y targeting IKKα over a range of concentrations. IC_{50}s are the mean of three independent replicates; plots are representative of three independent replicates; error bars are standard deviation of the mean of three replicates.

In CCS spheroid cell cultures, the IKKα inhibitor Compound Y was the most efficient drug tested (Figure 5-11D). IC_{50}s calculated for Compound Y were considerably lower (range 827 nM – 2.08 μM) compared to the IKKα inhibitor Compound X (range 7.19 – 15.9 μM). Accordingly, Compound Y was assessed in primary spheroids grown from normal skin for comparison with CCS primary spheroid response to IKKα

inhibition (Figure 5-11E). Compound Y was also effective at low concentrations in normal primary spheroid cultures (mean IC_{50} 2.05 μM normal spheroids vs 1.30 μM CCS spheroids). Targeting IKKα with Compound Y in CCS tumours may not therefore be viable due to adverse effects on perilesional skin and the method of application, such as transdermal delivery or topical application, would have to take this toxicity into account.

When the next generation of Compound Y became available (Compound Z), dose-response assays were repeated with normal and CCS primary spheroids (Figure 5-12). The 96 well drug assay protocol was shortened to a total of 5 days due to the deterioration of normal primary spheroids observed in Aggrewell plate assays.

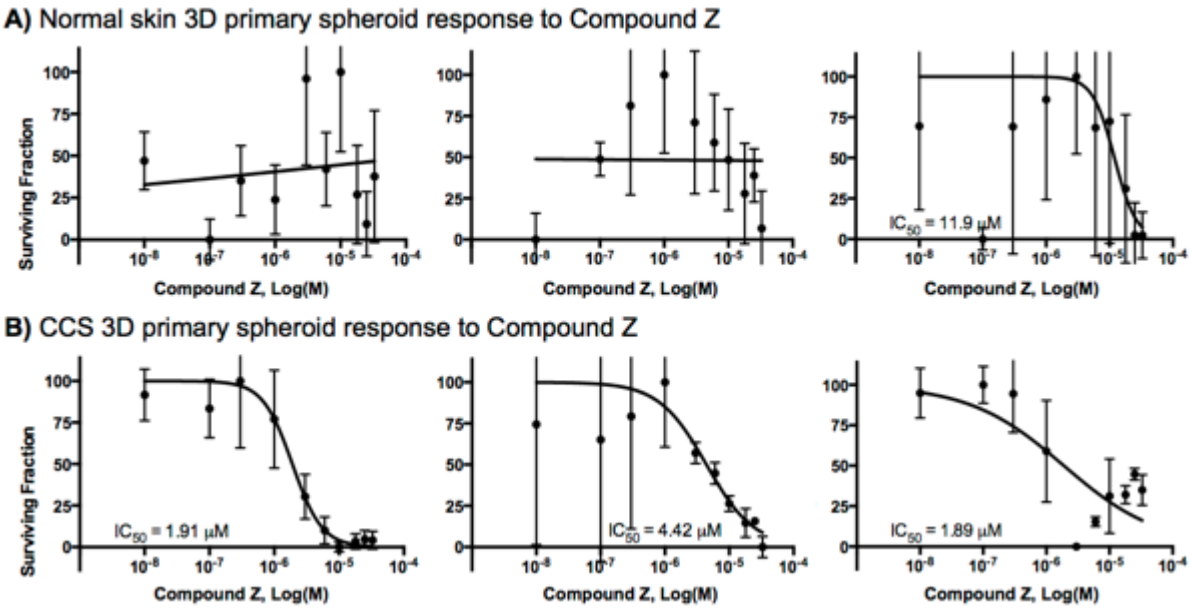

Figure 5-12. CCS and normal skin primary spheroid dose-response to Compound Z targeting IKKα. Primary cells derived from tumours from 3 CCS patients or normal skin from 3 donors were seeded in 96 well plates at 30,000 per well in media supplimented with 1.5 mM $CaCl_2$. Spheroids were drugged at day 3 for 48 hours with Compound Z at a range of concentrations. A) Normal keratinocytes tolerate higher concentrations of Compound Z than CCS spheroids. B) Compound Z affects CCS spheroid viability at the indicated concentrations. Error bars are standard deviation of the mean of three replicates.

With this IKKα inhibitor, a broader therapeutic window was achieved. Compound Z reached a mean IC_{50} of 2.74 µM in CCS spheroids, while in normal spheroids a dose-response curve could only be fitted to results for one plate (IC_{50} 11.9 µM). Dose-response results for all small molecule inhibitors tested are summarised in Figure 5-13.

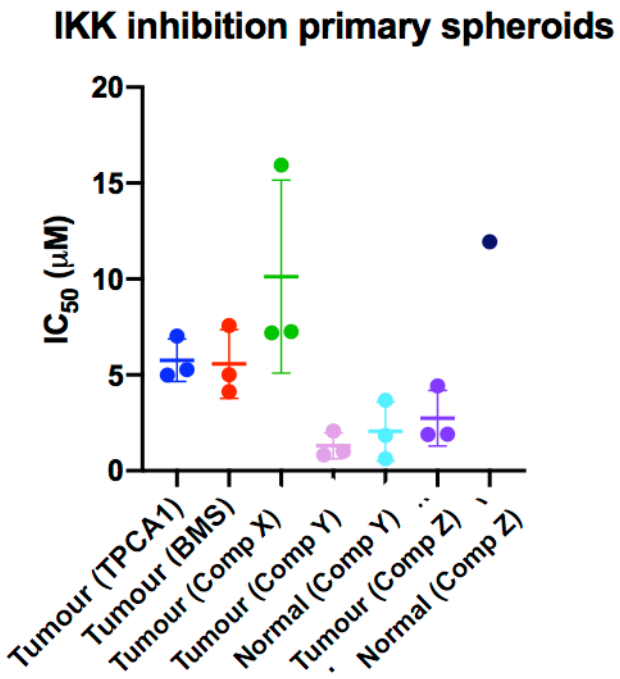

Figure 5-13. IKK inhibition in CCS spheroids. CCS tumour spheroids and normal primary keratinocyte spheroids were cultured in small molecule inhibitors targeting IKK over a range of concentrations, and IC_{50}s were calculated. Each data plot represents one independent replicate, three independent replicates were performed with normal spheroids for Compound Z but an IC_{50} could only be calculated from one of the dose response plots. Lines are at mean values with standard deviation. BMS; BMS345541. Comp, Compound.

While these assays will need to be repeated after additional optimization of the spheroid 96 well plate protocol to reduce the size of the error bars, these preliminary results suggest that IKKα inhibition with Compound Z can reduce CCS primary cell viability at concentrations that are tolerated by normal skin keratinocytes.

5.2 Discussion

In this chapter I demonstrate with lentiviral shRNA knockdown of *CYLD* that CCS tumour cells produce a shorter CYLD protein designated ‘trCYLD’. Inhibition of IKKα with the Compound Z reduced trCYLD protein levels in primary cells derived from CCS tumours and induced trCYLD cleavage at R324 by MALT1. Compound Z reduced markers of IKKα inhibition (p100 phosphorylated at serine 866 and p52 protein levels) in CCS tumour primary spheroids and highlighted that processing of p100 is altered in CCS tumour keratinocytes. Finally, dose-response results in CCS spheroids suggest inhibition of IKKα with Compound Z may have therapeutic potential for the treatment of CYLD cutaneous syndrome.

It is possible that truncated CYLD (trCYLD) in CCS tumour keratinocytes has a dominant-negative effect that contributes to tumourigenesis. It is striking that all *Cyld*-knockout mouse models are viable while transgenic mice with impaired Cyld DUB activity due to C-terminal truncation ($Cyld^{\Delta 932}$) or deletion of exon 9 ($Cyld^{E\Delta 9/\Delta 9}$) die shortly after birth due to impaired lung maturation(Massoumi et al., 2006a, Reiley et al., 2006, Zhang et al., 2006, Trompouki et al., 2009, Eguether et al., 2014). The knockout phenotype varies depending on the genetic background of the mice, as those generated in a C57BL/6 background have no overt phenotype and have a normal lifespan (Massoumi et al., 2006a, Zhang et al., 2006) while those generated in a mixed genetic background (C57BL/6xDBA/2) exhibit developmental defects including ciliopathies, male infertility and osteoporosis(Reiley et al., 2006, Jin et al., 2007, Reiley et al., 2007b, Wright et al., 2007, Yang et al., 2014, Yang and Zhou, 2016, Jin et al., 2008). The knock in mouse model with Cyld truncation at amino acid 932 ($Cyld^{\Delta 932}$), which mimics the *CYLD* hotspot mutation c.2806C>T, p.R936* in humans, dies perinatally due to lung defects(Eguether et al., 2014). Comparison of primary mouse embryonic fibroblasts from $Cyld^{WT}$ and $Cyld^{\Delta 932}$ littermate embryos found that truncation of Cyld reduced the formation of motile cilia on cells in the trachea. The number of multiciliated cells in the trachea of *Cyld* knockout ($Cyld^{KO}$) embryos was not different from $Cyld^{WT}$, suggesting that C-terminally truncated Cyld has a dominant-negative effect on cilia formation(Eguether et al., 2014). The discrepancy between viable *Cyld* knockout and lethal knock in phenotypes could suggest that truncated, catalytically dead CYLD can still bind to target substrates and prevent compensatory mechanisms in a dominant-negative manner.

Neither $Cyld^{KO}$ mice or mice with conditional knock in of *Cyld* mutations in keratinocytes under the K14 promoter ($Cyld^{\Delta 932}$ or $Cyld^{E\Delta 9/\Delta 9}$) spontaneously develop skin tumours. It is noteworthy however that the knockout mice have a normal skin and hair phenotype, while the conditional K14-driven $Cyld^{E\Delta 9/\Delta 9}$ knock in has hair, dental and sebaceous gland defects(Massoumi et al., 2006a, Jin et al., 2016). While similar defects were not reported in the $Cyld^{\Delta 932}$ K14-driven mouse model, evaluation of K63 ubiquitination of CYLD targets in cell lines expressing this truncation report an increase in substrate polyubiquitination relative to background, consistent with a dominant-negative effect(Trompouki et al., 2003, Miliani de Marval et al., 2011).

In addition to its role as a deubiquitinase (DUB) in cell signalling pathways, CYLD has roles mediated by its N-terminal protein domains that are usually not affected by CCS mutations. CYLD binds directly to tubulin and microtubules via its first two CAP-Gly domains to regulate microtubule functions (Gao et al., 2008). CYLD also directly binds to histone deacetylase 6 (HDAC6) via its first CAP-Gly domain, an enzyme that deacetylates α-tubulin and associates with microtubules(Wickstrom et al., 2010). Biological processes regulated by CYLD targeted to microtubules include cell cycle progression, cell migration and ciliogenesis(Yang and Zhou, 2016). Some of these roles are known to require both the DUB and microtubule-targeting activities of CYLD, for example N-terminal interaction with HDAC6 causes CYLD to localize to the perinuclear region and delay the G1/S transition of the cell cycle by deubiquitination of BCL3(Wickstrom et al., 2010). It is therefore possible that catalytically dead trCYLD can still carry out the N-terminal portion of a role such as inhibition of HDAC6 and perinuclear translocation but is then unable to complete its DUB function.

I provide evidence that truncated CYLD (trCYLD) is produced by CCS tumours with a C-terminal truncating or splice site mutation and that trCYLD protein levels can be reduced by inhibition of IKKα (Figure 5-2, Figure 5-5, Figure 1-7 and Figure 1-8). Direct phosphorylation of CYLD by IKKα and IKKβ at a cluster of serines (particularly residues 418 and 422) and IKKε (S418) is reported to transiently reduce CYLD's ability to deubiquitinate targets and result in canonical NF-κB signalling activation(Reiley et al., 2005, Hutti et al., 2009). The effect of Compound Z IKKα blockade on CYLD protein stability described in this study appears to be limited to trCYLD in CCS tumour cells, since no effect on flCYLD was observed in normal primary keratinocytes (Figure 5-5C). In addition to cleavage by Caspase 8 and MALT1, CYLD protein degradation is mediated by ubiquitination. The E3 ubiquitin ligase β-TRCP from the SCF (Skp-Cullin1-F-box protein) complex ($SCF^{\beta\text{-}TRCP}$) regulates the ubiquitination and degradation of CYLD(Wu et al., 2014). Recognition of CYLD by $SCF^{\beta\text{-}TRCP}$ requires IKK phosphorylation of serines 432 and 436 and shRNA knockdown of IKKα or IKKβ in HEK293T cells resulted in CYLD accumulation, indicating a potential role for both kinases in promoting the degradation of CYLD. The opposite effect was seen on trCYLD levels after IKKα

blockade in CCS cells, suggesting $SCF^{\beta\text{-}TRCP}$-mediated polyubiquitination is not responsible for trCYLD degradation.

More recently, MIB2 has been shown to add K48-linked polyubiquitin chains to CYLD at lysine 338 and 530, resulting in CYLD proteasomal degradation(Uematsu et al., 2019). Knockdown of $SCF^{\beta\text{-}TRCP}$ did not affect MIB2-mediated CYLD degradation, suggesting these are independent mechanisms. In CCS primary cells, a 40 kDa CYLD fragment was detected by immunoblot after treatment with Compound Z, indicating cleavage by MALT1 contributes to IKKα-blockade induced trCYLD degradation (Figure 1-6). It is possible that in CCS tumour cells, direct IKKα phosphorylation of trCYLD prevents MALT1 proteolytic cleavage and/or ubiquitination by MIB2. A similar role for IKKα has been described in preventing β-catenin ubiquitin-dependent degradation in the Wnt signalling pathway(Lamberti et al., 2001, Carayol and Wang, 2006).

It is also possible that inhibition of IKKα repressed trCYLD at the transcriptional level, as CYLD is an established canonical NF-κB target gene(Jono et al., 2004). IKKα can contribute to canonical NF-κB mediated transcription by phosphorylation of both nuclear receptor corepressor 2 (NCOR2 syn. SMRT) and chromatin bound RelA at serine 536. This leads to replacement of repressive p50:p50 homodimers with the RelA:p50 heterodimer at NF-κB responsive elements, allowing transcription to occur(Hoberg et al., 2006). The reduction in levels of *p*-RelA(S536) in spheroids after treatment with Compound Z could therefore be due to inhibition of phosphorylation by IKKα rather than off-target engagement of the inhibitor with IKK-β or other kinases that phosphorylate RelA at serine 536(Figure 5-10C).

Compound Z appears to be on target with IKKα in the non-canonical pathway based on the reduction of p52 and *p*-p100 (S866) in CCS spheroids after treatment (Figure 5-10A). A lower molecular weight band was detected with the p100 antibody in CCS 2D primary cells and spheroids after treatment with Compound Z, and it was considered that this shorter form of p100 might be generated by the same paracaspase (MALT1) that cleaves CYLD upon IKKα inhibition (Figure 5-9, Figure 5-10). MALT1 must have arginine (R) at position P1 (the cleavage site) and has selectivity for serine (S) at P2 (upstream of P1) but can recognise alanine (A) or proline (P)(Wiesmann et al., 2012). Upstream of P2, P3 contributes weakly to

substrate recognition and P4 accepts hydrophobic residues. In the p100 amino acid sequence (900 amino acids in length), the most C-terminal SR residues are at positions 427 and 428. If MALT1 were to cleave p100 at this site (R428), the resulting protein would be similar in size to p52. There are two candidate MALT1 recognition sequences in p100 at amino acids 608 - 611 ($VRAR_{611}$) and 661-664 ($VNAR_{664}$) with alanine at P2 and a hydrophobic valine (V) residue at P4. The known cellular MALT1 substrates have either serine (CYLD, A20, RelB, BCL10, NIK, Roquin-2) or proline at P2 (HOIL-1, Roquin-1, Regnase-1)(Jeltsch et al., 2014), suggesting that although alanine is possible at P2 it is not preferred. Dual treatment of CCS primary spheroids with Compound Z and the MALT1 inhibitor z-VRPR-fmk may resolve whether MALT1 cleavage is responsible for the generation of shorter p100 after inhibition of IKKα.

Importantly, the effective concentration of Compound Z in CCS spheroids relative to normal skin spheroids suggests that targeting IKKα with Compound Z has therapeutic potential for CCS (Figure 5-12).

On the basis of these findings and those detailed in chapter 4, I propose a model in which both EDAR-mediated canonical NF-κB signalling and non-canonical NF-κB signalling are upregulated in CCS tumour keratinocytes. In addition, truncated and catalytically dead CYLD may be able to bind to target substrates and prevent compensation by DUBS with functional redundancy, such as A20 in the canonical NF-κB pathway. The Wnt-β-catenin signalling pathway is also hyperactive in CCS tumour cells and is relevant to the model because trCYLD may interact with Dishevelled and IKKα has a role in protecting β-catenin from proteasomal degradation. After Compound Z inhibition of IKKα, trCYLD protein is reduced by MALT1 cleavage with potential consequences on K63 polyubiquitin levels of target substrates. In the canonical NF-κB signalling pathway, gene transcription can persist, as IKKβ alone is sufficient for IκBα degradation. A subset of genes regulated by nuclear IKKα phosphorylation of RelA at S536 may no longer be transcribed. In the non-canonical NF-κB pathway, inhibition of IKKα prevents p100 processing and the p52:RelB dimer cannot enter the nucleus. In the Wnt signalling pathway, β-catenin may undergo increased proteasomal degradation due to loss of IKKα-mediated prevention of N-terminal ubiquitination. As *EDAR* is a known β-catenin target gene and also contains a p52:RelB consensus site, inhibition of non-canonical NF-κB signalling or Wnt-β-catenin signalling may contribute to a reduction in *EDAR*

expression and a consequent reduction in EDAR-mediated canonical NF-κB signalling. Compound Z may therefore reduce CCS tumour cell viability through dual inhibition of aberrantly activated non-canonical NF-κB signalling and IKKα-dependent Wnt-β-catenin signalling.

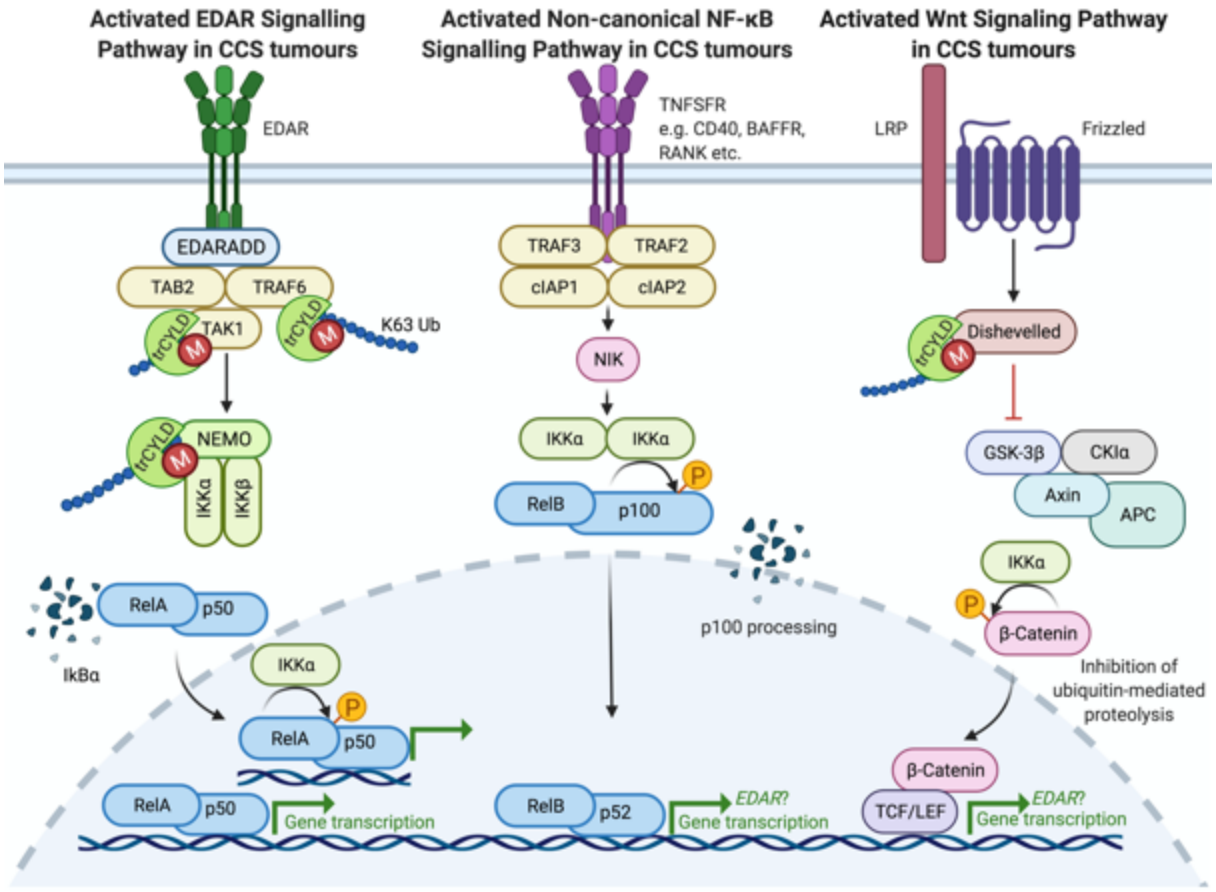
Activated EDAR Signalling Pathway in CCS tumours
Activated Non-canonical NF-κB Signalling Pathway in CCS tumours
Activated Wnt Signaling Pathway in CCS tumours
EDAR
TNFSFR
e.g. CD40, BAFFR, RANK etc.
LRP
Frizzled
EDARADD
TAB2
TRAF6
TAK1
trCYLD
M
K63 Ub
TRAF3
TRAF2
cIAP1
cIAP2
NIK
Dishevelled
GSK-3β
CKIα
Axin
APC
NEMO
IKKα
IKKβ
RelB
p100
P
RelA
p50
IkBα
p100 processing
β-Catenin
Inhibition of ubiquitin-mediated proteolysis
p52
TCF/LEF
EDAR?
Gene transcription

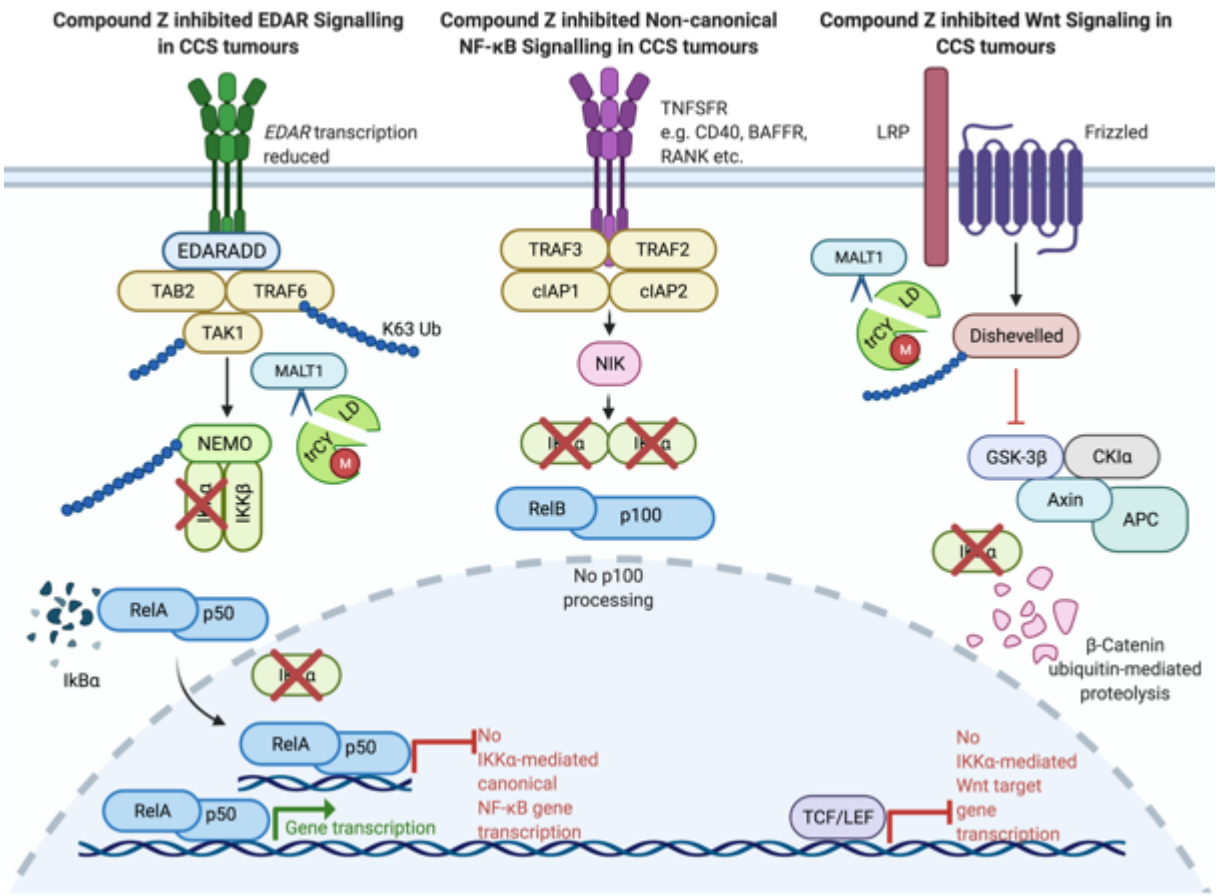
Compound Z inhibited EDAR Signalling in CCS tumours
Compound Z inhibited Non-canonical NF-κB Signalling in CCS tumours
Compound Z inhibited Wnt Signaling in CCS tumours
EDAR transcription reduced
TNFSFR
e.g. CD40, BAFFR, RANK etc.
LRP
Frizzled
EDARADD
TAB2
TRAF6
TAK1
K63 Ub
MALT1
LD
trCYLD
M
TRAF3
TRAF2
cIAP1
cIAP2
NIK
Dishevelled
GSK-3β
CKIα
Axin
APC
NEMO
IKKβ
RelB
p100
No p100 processing
RelA
p50
IkBα
β-Catenin ubiquitin-mediated proteolysis
No IKKα-mediated canonical NF-κB gene transcription
No IKKα-mediated Wnt target gene transcription
TCF/LEF
Gene transcription

Figure 5-14. Model of Compound Z inhibition of IKKα in CCS tumour cells. EDAR-mediated canonical NF-κB signalling, non-canonical NF-κB signalling and Wnt/β-catenin signalling is upregulated in CCS tumours. Truncated CYLD (trCYLD) is catalytically dead but may interact with target substrates, preventing other deubiquitinases with functional redundancy from removing lysine 63 (K63) linked polyubiquitin chains. IKKα has a kinase-dependent role in all three pathways. Inhibition of IKKα with Compound Z reduces trCYLD protein levels through an unknown mechanism. The MALT1 paracaspase may be responsible for trCYLD degradation after Compound Z. As IKKα is dispensable for canonical NF-κB activation, downstream targets of EDAR signalling may continue to be transcribed. Transcription of a subset of genes that require nuclear IKKα phosphorylation of RelA at serine 536 may be lost. Inhibition of IKKα in the non-canonical NF-κB pathway prevents p100 processing and results in loss of all downstream target genes. Inhibition of IKKα-mediated protection of β-catenin proteasomal degradation or non-canonical NF-κB signalling may prevent transcription of *EDAR*, which may reduce the strength the canonical NF-κB signal. Created with BioRender.com.

As IKKα has diverse functions including an NF-κB independent role in keratinocyte differentiation, further studies will be needed to identify the mechanism behind IKKα-dependent regulation of trCYLD protein stability and establish whether trCYLD reduction affects K63 ubiquitin levels of known CYLD target substrates (Li et al., 1999, Takeda et al., 1999, Hu et al., 2001). Knockdown of IKKα in CCS tumour primary cells using lentivirus may recapitulate the effect of Compound Z. If trCYLD is not reduced by IKKα knockdown, and treatment with Compound Z reduces trCYLD in IKKα knockdown cells, this will show there is something in addition to IKKα involved. A caveat of this experiment would be that catalytically dead IKKα is different from completely absent IKKα. A NIK inhibitor (e.g. NIK SMI1) could be used on CCS primary cells and results compared with Compound Z. If the reduction of trCYLD is indeed via IKKα the effects should be similar. A MALT1 inhibitor such as z-VRPR-fmk could also be used with Compound Z to see if trCYLD reduction is rescued. Due to the rare nature of CCS, it will be difficult to obtain primary cells from fresh tumours with a range of mutations to assess trCYLD expression and reduction after Compound Z. The Rajan lab has developed HEK293 cells overexpressing CCS patient *CYLD* mutations, and these may be used in future to assess whether Compound Z reduces all of the modelled mutated CYLD proteins or a specific subset.

The preliminary spheroid dose-response data presented in this chapter suggests that the IKKα inhibitor Compound Z is a good candidate for further testing in preclinical and in vivo models of CCS. Providing lentiviral knockdown of IKKα does not reduce CCS cell viability, carrying out Compound Z dose response assays with IKKα knockdown cells could determine whether reduction in CCS spheroid viability is an

on-target effect. Compound Z has ideal attributes for topical application, and if absorbed, is rapidly metabolised (unpublished data, Simon Mackay). A patient derived xenograft (PDX) mouse has recently been established from cylindromas and this could provide an excellent model for further investigation of IKKα inhibition in CCS tumours(Andersson et al., 2019).

Chapter 6. Concluding Remarks and Future Directions

In this project, comprehensive genomic technologies were used to characterise the genetic landscape of CCS tumours. This approach revealed that in addition to loss of the wild-type CYLD allele, somatic mutations in two epigenetic modifier genes frequently occur and clonally expand in CCS tumours. Upregulated potential NF-κB target genes were identified in CCS tumour cells using a CD45 cell depletion method to separate the mixed populations of tumour keratinocytes and tumour infiltrating leukocytes (TILs). Using this technique, I identified *EDAR* as highly overexpressed in CCS keratinocytes in an IKKα-dependent manner. A patient derived CCS tumour spheroid model was developed in which to validate tumour specific changes in NF-κB target gene expression and explore the therapeutic potential of novel small molecule IKKα inhibitors. This model was used to confirm that the non-canonical NF-κB signalling pathway is dysregulated in CCS tumours and that targeting IKKα is a promising therapeutic strategy in CYLD cutaneous syndrome.

These findings are of clinical significance for CCS, as no current medical treatments are available other than surgery to remove tumours. The TRAC study has demonstrated safety of topical tropomyosin kinase inhibition, however dose escalation studies are needed to determine clinical efficacy. In relation to IKK, a small pilot study using topical salicylic acid to target the canonical NF-κB kinase IKKβ in CCS tumours was not taken forward due to insufficient response(Oosterkamp et al., 2006). Small molecule inhibitors of IKKβ have not been approved in clinic due to systemic toxicity(Ramadass et al., 2020). My work suggests that targeting IKKα with Compound Z as a topical agent may be effective in CCS tumours at concentrations that are not toxic to normal keratinocytes. It is hypothesized that in addition to targeting IKKα in the non-canonical NF-κB and Wnt signaling pathways, Compound Z may target multiple dysregulated pathways in CCS tumours by decreasing levels of trCYLD.

This study has contributed to gaps in the knowledge of CCS tumour biology, as no potential driver mutations have been comprehensibly defined in inherited CCS tumours other than in *CYLD*. Preclinical models of CCS for screening drug candidates are lacking, as mice with conditional knock-in of *CYLD* mutations under keratin promoters to date have not developed the CCS phenotype(Miliani de Marval

et al., 2011, Jin et al., 2016, Alameda et al., 2019). I have built on a CCS tumour primary spheroid model generated in the Rajan laboratory. This model now includes normal skin primary spheroids as controls and can be used to validate gene and protein expression in CCS tumours relative to normal skin as well as response to small molecule inhibitors. Future work to refine this model will increase its utility. This study has added to our understanding of NF-κB subunit and target gene expression in human CCS tumour samples. The FACS CD45 depletion method optimised here could be expanded to enrich specific immune populations and used to investigate the tumour immune microenvironment of other tumour types. The RNA-seq dataset generated in this study is unique and complements CCS tumour RNA-seq data derived from bulk tumour cDNA.

The findings reported here raise some intriguing questions; Is non-canonical NF-κB signalling altered in CCS tumours due to loss of functional CYLD in a direct role or due to crosstalk from the canonical NF-κB signalling pathway? Is IKKα-mediated *EDAR* upregulation via non-canonical NF-κB or Wnt signalling? Is p100 cleaved in CCS spheroids after Compound Z? Is a shorter form of p100 excessively produced in CCS spheroids? How does IKKα inhibition induce MALT1 cleavage of trCYLD? Is trCYLD preventing compensation by other DUBs? While the answers to these questions are important for future research, the in vitro evidence presented here makes a strong case for directly taking Compound Z forward for in vivo assessment in a patient-derived xenograft model of CCS.

Appendices

Appendix A. Ingenuity pathway analysis of hypomethylated probes.

The top 5 significant networks are shown.

Network	p value*	Molecules in Network	Top Diseases and Functions
1	$1x10^{-45}$	CAPZB, CDH4, CDKN3, CHD7, CTNNA3, CTNNB1, CYP2A6 (includes others), DPEP1, EHD1, EMX2, EYA2, FGF19, FGF20, FOXC1, GALM, GLI2, GLI3, HOXA11-AS, MAGI1, NAA10, NPTX1, PAX1, PAX9, PDE1C, PMP22, POU3F2, ROR2, SIM1, SIM2, SLC39A14, SSH1, TBX20, TSPAN2, TUBB2B, ZIC1	[Embryonic Development, Nervous System Development and Function, Organ Development]
2	$1x10^{-37}$	ADAMTS4, CRELD2, FOXA2, FOXH1, GFRA1, Hedgehog, HNF1B, IFITM5, LAMA3, LRP5, MAFB, MAN1A1, MNX1, MUC6, NKX6-1, NR2F2, NR5A2, ONECUT1, OSTM1, P38 MAPK, PDIA6, PDX1, RBP1, S100A11, SARM1, SATB2, SLC2A2, SORCS3, SOX8, SP7, SSBP3, TMSB4, TP53AIP1, TRIO, UST	[Digestive System Development and Function, Embryonic Development, Endocrine System Development and Function]
3	$1x10^{-35}$	ANXA9, ARHGDIB, ATP2A3, BBX, Calmodulin, CDH5, CDX1, CDX2, COL12A1, CPNE5, CTSE, DCN, EGLN, estrogen receptor, ETS1, FMO1, FOXK1, HHEX, HOTTIP, HOXA13, IRS1, LTF, MAP7, OPCML, P-TEFb, PDGFD, PDGFRL, PPFIA4, PRSS56, PTPRN2, SASH1, SHROOM3, SPEG, TGFB3, WNT5A	[Cancer, Skeletal and Muscular Disorders, Tissue Morphology]
4	$1x10^{-31}$	AURKC, BAHCC1, BANP, BCL11A, BRD7, C1q, CD93, CDK14, EXOC5, FAM49A, FGF5, Fgfr, HBG2, Hdac, Histone h3, Histone h4, HOXA3, ING1, KCNH2, KDM3A, MAD1L1, MECOM, MEGF10, MEIS2, MGMT, Notch, OSR1, PBX1, RNF207, SHANK2, SPATS2L, TACC2, TBX3, TMPRSS2, ZNF767P	[Cell Cycle, Hematological Disease, Hereditary Disorder]
5	$1x10^{-31}$	AATK, ADCY, ADCY1, ATXN1, BACE1, CACNA2D3, CADM1, Calcineurin protein(s), CD2, CIDEA, CLASP2, DNER, GNAO1, GNG7, GRIA1, Ifn gamma, INPP5A, LGI1, Nfat (family), NR3C1, NR3C2, PLC, PRKAA, PRKAR1B, PTGDR, RCAN2, RELT, RRAGC, RTN4, SLAMF1, SLC25A33, TNFRSF12A, TNNT3, TUBA3E, ZFYVE28	[Behavior, Cell-To-Cell Signaling and Interaction, Nervous System Development and Function]

**p*-value is calculated using Fisher's Exact Test

Appendix B. g:Profiler functional enrichment analysis (g:GOSt) results (positive fold-change).

Significant terms identified by g:GOSt from the top 500 differentially expressed genes (ranked by positive fold-change) between normal skin and CCS tumours. The top 20 significant terms are shown for information sources with >20 significant terms. GO:MF; Gene Ontology Molecular Function, GO:BP; Gene Ontology Biological Process, GO:CC; Gene Ontology Cellular Component, KEGG; Kyoto Encyclopaedia of Genes and Genomes, REAC; Reactome, WP; WikiPathways, MIRNA; miRTarBase, HPA; Human Protein Atlas, HP; Human Phenotype Ontology.

Whole tissue g:GOSt results (positive fold-change)

source	term_name	term_id	adj_p_value
GO:MF	receptor ligand activity	GO:0048018	1.04E-04
GO:MF	signaling receptor activator activity	GO:0030546	1.31E-04
GO:MF	receptor regulator activity	GO:0030545	1.63E-04
GO:MF	CXCR chemokine receptor binding	GO:0045236	2.27E-03
GO:MF	neurotrophin binding	GO:0043121	2.55E-03
GO:MF	chemokine activity	GO:0008009	3.22E-03
GO:MF	CXCR3 chemokine receptor binding	GO:0048248	1.45E-02
GO:MF	heparin binding	GO:0008201	2.14E-02
GO:MF	glycosaminoglycan binding	GO:0005539	2.34E-02
GO:MF	chemokine receptor binding	GO:0042379	3.47E-02
GO:MF	DNA-binding transcription activator activity, RNA polymerase II-specific	GO:0001228	3.61E-02
GO:MF	DNA-binding transcription activator activity	GO:0001216	3.94E-02
GO:MF	G protein-coupled receptor binding	GO:0001664	4.13E-02
GO:MF	cytokine activity	GO:0005125	4.40E-02
GO:MF	potassium channel activity	GO:0005267	4.76E-02
GO:BP	nervous system development	GO:0007399	1.35E-04
GO:BP	central nervous system development	GO:0007417	3.05E-04
GO:BP	anatomical structure morphogenesis	GO:0009653	7.11E-04
GO:BP	animal organ morphogenesis	GO:0009887	1.34E-03
GO:BP	system development	GO:0048731	2.19E-03
GO:CC	extracellular region	GO:0005576	3.80E-04
GO:CC	extracellular matrix	GO:0031012	2.92E-03
KEGG	Cytokine-cytokine receptor interaction	KEGG:04060	1.43E-04
KEGG	ECM-receptor interaction	KEGG:04512	1.59E-02
KEGG	Viral protein interaction with cytokine and cytokine receptor	KEGG:04061	3.10E-02
REAC	Degradation of the extracellular matrix	REAC:R-HSA-1474228	1.66E-04
REAC	Chemokine receptors bind chemokines	REAC:R-HSA-380108	4.33E-03
REAC	Extracellular matrix organization	REAC:R-HSA-1474244	5.07E-03

REAC	Activation of TRKA receptors	REAC:R-HSA-187015	1.82E-02
REAC	Peptide ligand-binding receptors	REAC:R-HSA-375276	2.73E-02
TF	Factor: RelB:p50; motif: RGAAANTCCCYNNHGC; match class: 0	TF:M03882_0	2.26E-03
CORUM	NGF-p75 complex	CORUM:5424	1.67E-02
CORUM	SORT1-NGFR-NGFB complex	CORUM:1795	4.98E-02

Input g:GOSt results (positive fold-change)

source	term_name	term_id	adj_p_value
GO:MF	DNA-binding transcription activator activity, RNA polymerase II-specific	GO:0001228	3.25E-05
GO:MF	DNA-binding transcription activator activity	GO:0001216	3.68E-05
GO:MF	DNA-binding transcription factor activity, RNA polymerase II-specific	GO:0000981	3.09E-04
GO:MF	receptor ligand activity	GO:0048018	3.15E-03
GO:MF	signaling receptor activator activity	GO:0030546	3.80E-03
GO:MF	receptor regulator activity	GO:0030545	4.15E-03
GO:MF	sequence-specific DNA binding	GO:0043565	2.27E-02
GO:BP	multicellular organismal process	GO:0032501	2.56E-06
GO:BP	multicellular organism development	GO:0007275	4.39E-06
GO:BP	generation of neurons	GO:0048699	6.87E-06
GO:BP	anatomical structure development	GO:0048856	7.21E-06
GO:BP	system development	GO:0048731	8.60E-06
GO:BP	neurogenesis	GO:0022008	2.24E-05
GO:BP	developmental process	GO:0032502	2.81E-05
GO:BP	nervous system development	GO:0007399	3.92E-05
GO:BP	tissue development	GO:0009888	4.19E-05
GO:BP	cell development	GO:0048468	8.95E-05
GO:BP	anatomical structure morphogenesis	GO:0009653	9.76E-05
GO:BP	epidermis development	GO:0008544	1.10E-04
GO:BP	cell differentiation	GO:0030154	1.75E-04
GO:BP	neuron differentiation	GO:0030182	2.59E-04
GO:BP	cellular developmental process	GO:0048869	4.04E-04
GO:BP	morphogenesis of a branching structure	GO:0001763	1.75E-03
GO:BP	animal organ morphogenesis	GO:0009887	2.90E-03
GO:BP	animal organ development	GO:0048513	3.41E-03
GO:BP	nerve development	GO:0021675	3.42E-03
GO:BP	skin development	GO:0043588	3.94E-03
GO:CC	extracellular region	GO:0005576	4.87E-04
GO:CC	cell junction	GO:0030054	1.53E-03
GO:CC	cell-cell junction	GO:0005911	1.55E-03
GO:CC	nuclear chromatin	GO:0000790	3.52E-02
KEGG	Nicotine addiction	KEGG:05033	7.40E-04
KEGG	PI3K-Akt signaling pathway	KEGG:04151	9.43E-03
KEGG	Ras signaling pathway	KEGG:04014	4.94E-02

REAC	Degradation of the extracellular matrix	REAC:R-HSA-1474228	7.77E-06
REAC	Extracellular matrix organization	REAC:R-HSA-1474244	7.14E-05
REAC	Collagen formation	REAC:R-HSA-1474290	6.15E-04
REAC	Assembly of collagen fibrils and other multimeric structures	REAC:R-HSA-2022090	3.76E-02
TF	Factor: c-Rel; motif: NGGGAATYTCCN; match class: 0	TF:M03545_0	1.37E-02
HP	Selective tooth agenesis	HP:0001592	2.62E-05
HP	Reduced number of teeth	HP:0009804	3.43E-04
HP	Sparse body hair	HP:0002231	6.94E-04
HP	Abnormal number of teeth	HP:0006483	1.70E-03
HP	Sparse or absent eyelashes	HP:0200102	7.18E-03
HP	Palate fistula	HP:0010294	1.32E-02
HP	Agenesis of incisor	HP:0006485	1.80E-02
HP	Conical tooth	HP:0000698	2.83E-02
HP	Malnutrition	HP:0004395	3.06E-02
HP	Peg-shaped maxillary lateral incisors	HP:0006342	3.36E-02
HP	Bilateral cleft lip	HP:0100336	3.36E-02
HP	Unilateral cleft palate	HP:0100334	3.36E-02
HP	Abnormal number of permanent teeth	HP:0011044	4.93E-02

FACS enriched CD45+ leukocyte g:GOSt results (positive fold-change)

source	term_name	term_id	adj_p_value
GO:BP	adaptive immune response	GO:0002250	2.24E-05
GO:BP	immune response	GO:0006955	8.22E-05
GO:BP	cytokine production	GO:0001816	4.66E-04
GO:BP	regulation of response to stimulus	GO:0048583	6.65E-04
GO:BP	immune system process	GO:0002376	1.11E-03
GO:BP	regulation of cytokine production	GO:0001817	1.30E-03
GO:BP	regulation of immune response	GO:0050776	1.92E-03
GO:BP	lymphocyte activation	GO:0046649	2.79E-03
GO:BP	regulation of immune system process	GO:0002682	4.32E-03
GO:BP	positive regulation of immune system process	GO:0002684	1.22E-02
GO:BP	positive regulation of immune response	GO:0050778	1.51E-02
GO:BP	cell surface receptor signaling pathway	GO:0007166	3.02E-02
GO:BP	immune response-regulating signaling pathway	GO:0002764	4.75E-02
GO:BP	lymphocyte differentiation	GO:0030098	4.86E-02
GO:CC	T cell receptor complex	GO:0042101	1.49E-08
GO:CC	plasma membrane signaling receptor complex	GO:0098802	5.66E-07
GO:CC	cell periphery	GO:0071944	3.06E-06
GO:CC	plasma membrane	GO:0005886	8.36E-06
GO:CC	receptor complex	GO:0043235	6.99E-05
GO:CC	protein complex involved in cell adhesion	GO:0098636	9.54E-03
GO:CC	intrinsic component of plasma membrane	GO:0031226	2.42E-02

GO:CC	external side of plasma membrane	GO:0009897	2.73E-02
GO:CC	integral component of plasma membrane	GO:0005887	2.95E-02
GO:CC	cell surface	GO:0009986	4.38E-02
GO:CC	side of membrane	GO:0098552	4.43E-02
GO:CC	plasma membrane protein complex	GO:0098797	4.48E-02
KEGG	Hematopoietic cell lineage	KEGG:04640	3.45E-04
KEGG	ECM-receptor interaction	KEGG:04512	9.60E-03
KEGG	Human papillomavirus infection	KEGG:05165	3.63E-02
KEGG	Focal adhesion	KEGG:04510	4.29E-02
REAC	Type I hemidesmosome assembly	REAC:R-HSA-446107	1.04E-02
TF	Factor: IRF; motif: RAAANTGAAAN; match class: 1	TF:M00972_1	9.46E-03
TF	Factor: IRF-4; motif: NYGAAASYGAAACYN; match class: 0	TF:M11686_0	2.14E-02
CORUM	CD8A-LCK complex	CORUM:1067	4.98E-02
HP	Decrease in T cell count	HP:0005403	7.08E-03
HP	Oral mucosal blisters	HP:0200097	4.97E-02

FACS enriched CD45- keratinocyte g:GOSt results (positive fold-change)

source	term_name	term_id	adj_p_value
GO:MF	DNA-binding transcription activator activity, RNA polymerase II-specific	GO:0001228	1.63E-05
GO:MF	DNA-binding transcription activator activity	GO:0001216	1.86E-05
GO:MF	DNA-binding transcription factor activity, RNA polymerase II-specific	GO:0000981	1.77E-03
GO:MF	sequence-specific DNA binding	GO:0043565	4.94E-02
GO:BP	cell differentiation	GO:0030154	3.78E-07
GO:BP	anatomical structure development	GO:0048856	8.31E-07
GO:BP	tissue development	GO:0009888	1.08E-06
GO:BP	developmental process	GO:0032502	1.42E-06
GO:BP	multicellular organism development	GO:0007275	2.62E-06
GO:BP	cellular developmental process	GO:0048869	2.93E-06
GO:BP	epidermis development	GO:0008544	3.42E-06
GO:BP	cell development	GO:0048468	7.41E-06
GO:BP	system development	GO:0048731	1.06E-05
GO:BP	multicellular organismal process	GO:0032501	2.38E-05
GO:BP	nervous system development	GO:0007399	6.52E-05
GO:BP	generation of neurons	GO:0048699	1.30E-04
GO:BP	animal organ development	GO:0048513	1.62E-04
GO:BP	anatomical structure morphogenesis	GO:0009653	2.64E-04
GO:BP	cellular component morphogenesis	GO:0032989	3.20E-04
GO:BP	neurogenesis	GO:0022008	4.27E-04
GO:BP	movement of cell or subcellular component	GO:0006928	4.41E-04
GO:BP	nerve development	GO:0021675	1.04E-03
GO:BP	cell morphogenesis	GO:0000902	1.34E-03
GO:BP	skin development	GO:0043588	1.73E-03

GO:CC	extracellular region	GO:0005576	1.02E-02
GO:CC	cell junction	GO:0030054	3.31E-02
GO:CC	integral component of plasma membrane	GO:0005887	3.71E-02
GO:CC	nuclear chromatin	GO:0000790	4.20E-02
REAC	Extracellular matrix organization	REAC:R-HSA-1474244	5.79E-05
REAC	Degradation of the extracellular matrix	REAC:R-HSA-1474228	1.38E-03
REAC	Assembly of collagen fibrils and other multimeric structures	REAC:R-HSA-2022090	6.55E-03
REAC	Collagen formation	REAC:R-HSA-1474290	1.14E-02
WP	Hair Follicle Development: Cytodifferentiation (Part 3 of 3)	WP:WP2840	3.51E-02
TF	Factor: NF-kappaB; motif: NGGGGAMTTTCCNN; match class: 1	TF:M00194_1	6.75E-05
TF	Factor: NF-kappaB; motif: NGGGACTTTCCA; match class: 0	TF:M00208_0	4.16E-02
HP	Selective tooth agenesis	HP:0001592	1.71E-03
HP	Sparse body hair	HP:0002231	2.57E-03

Appendix C. g:Profiler functional enrichment analysis (g:GOSt) results (negative fold-change).

Significant terms identified by g:GOSt from the top 500 differentially expressed genes (ranked by negative fold-change) between normal skin and CCS tumours. The top 20 significant terms are shown for information sources with >20 significant terms. GO:MF; Gene Ontology Molecular Function, GO:BP; Gene Ontology Biological Process, GO:CC; Gene Ontology Cellular Component, KEGG; Kyoto Encyclopaedia of Genes and Genomes, REAC; Reactome, WP; WikiPathways, MIRNA; miRTarBase, HPA; Human Protein Atlas, HP; Human Phenotype Ontology.

Whole tissue g:GOSt results (negative fold-change)

source	term_name	term_id	adj_p_value
GO:MF	structural constituent of skin epidermis	GO:0030280	1.19E-04
GO:MF	oxidoreductase activity, acting on the CH-OH group of donors, NAD or NADP as acceptor	GO:0016616	2.05E-04
GO:MF	oxidoreductase activity, acting on CH-OH group of donors	GO:0016614	4.81E-04
GO:MF	calcium ion binding	GO:0005509	6.62E-04
GO:MF	carboxylic ester hydrolase activity	GO:0052689	6.88E-04
GO:MF	triglyceride lipase activity	GO:0004806	1.90E-03
GO:MF	organic acid binding	GO:0043177	1.72E-02
GO:MF	oxidoreductase activity	GO:0016491	1.88E-02
GO:BP	epidermis development	GO:0008544	3.22E-31
GO:BP	keratinocyte differentiation	GO:0030216	1.22E-30
GO:BP	keratinization	GO:0031424	1.61E-29
GO:BP	epidermal cell differentiation	GO:0009913	1.76E-29
GO:BP	skin development	GO:0043588	1.22E-28
GO:BP	cornification	GO:0070268	1.72E-26
GO:BP	epithelial cell differentiation	GO:0030855	2.07E-20
GO:BP	tissue development	GO:0009888	8.38E-17
GO:BP	epithelium development	GO:0060429	2.28E-16
GO:BP	lipid metabolic process	GO:0006629	6.36E-12
GO:BP	cellular lipid metabolic process	GO:0044255	1.93E-07
GO:BP	cell differentiation	GO:0030154	4.65E-07
GO:BP	lipid catabolic process	GO:0016042	6.54E-07
GO:BP	animal organ development	GO:0048513	1.14E-06
GO:BP	cellular developmental process	GO:0048869	3.31E-06
GO:BP	peptide cross-linking	GO:0018149	5.35E-06
GO:BP	multicellular organismal process	GO:0032501	7.54E-06

GO:BP	fatty acid metabolic process	GO:0006631	1.05E-05
GO:BP	anatomical structure development	GO:0048856	3.05E-05
GO:BP	monocarboxylic acid metabolic process	GO:0032787	3.36E-05
GO:CC	cornified envelope	GO:0001533	6.52E-17
GO:CC	extracellular region	GO:0005576	5.17E-11
GO:CC	intermediate filament	GO:0005882	9.40E-06
GO:CC	intermediate filament cytoskeleton	GO:0045111	2.57E-05
GO:CC	extracellular space	GO:0005615	2.76E-05
GO:CC	extracellular matrix	GO:0031012	8.24E-05
GO:CC	collagen-containing extracellular matrix	GO:0062023	1.30E-04
GO:CC	vesicle	GO:0031982	4.58E-03
GO:CC	keratin filament	GO:0045095	1.03E-02
GO:CC	lipid droplet	GO:0005811	1.41E-02
GO:CC	extracellular vesicle	GO:1903561	1.75E-02
GO:CC	extracellular organelle	GO:0043230	1.89E-02
GO:CC	extracellular exosome	GO:0070062	2.23E-02
GO:CC	hemoglobin complex	GO:0005833	3.54E-02
GO:CC	chitosome	GO:0045009	4.87E-02
GO:CC	pigment granule membrane	GO:0090741	4.87E-02
GO:CC	melanosome membrane	GO:0033162	4.87E-02
KEGG	PPAR signaling pathway	KEGG:03320	1.50E-08
KEGG	Neuroactive ligand-receptor interaction	KEGG:04080	2.50E-05
KEGG	Chemical carcinogenesis	KEGG:05204	2.69E-05
KEGG	Metabolism of xenobiotics by cytochrome P450	KEGG:00980	8.19E-05
KEGG	Retinol metabolism	KEGG:00830	2.49E-04
KEGG	Linoleic acid metabolism	KEGG:00591	3.31E-04
KEGG	Drug metabolism - cytochrome P450	KEGG:00982	3.78E-04
KEGG	Steroid hormone biosynthesis	KEGG:00140	8.73E-04
KEGG	Tyrosine metabolism	KEGG:00350	1.54E-03
KEGG	Metabolic pathways	KEGG:01100	1.55E-02
REAC	Formation of the cornified envelope	REAC:R-HSA-6809371	1.31E-33
REAC	Keratinization	REAC:R-HSA-6805567	1.24E-25
REAC	Metabolism of lipids	REAC:R-HSA-556833	1.58E-08
REAC	Developmental Biology	REAC:R-HSA-1266738	2.53E-07
REAC	Melanin biosynthesis	REAC:R-HSA-5662702	8.25E-04
REAC	Metabolism	REAC:R-HSA-1430728	1.02E-03
REAC	Metal sequestration by antimicrobial proteins	REAC:R-HSA-6799990	2.43E-03
REAC	Fatty acid metabolism	REAC:R-HSA-8978868	1.29E-02
REAC	Adrenoceptors	REAC:R-HSA-390696	1.92E-02
REAC	Wax biosynthesis	REAC:R-HSA-9640463	2.68E-02

WP	PPAR signaling pathway	WP:WP3942	7.30E-06
WP	Differentiation of white and brown adipocyte	WP:WP2895	3.06E-03
WP	Transcription factor regulation in adipogenesis	WP:WP3599	2.02E-02
WP	Adipogenesis	WP:WP236	3.79E-02
WP	Fatty Acid Omega Oxidation	WP:WP206	4.99E-02
WP	Major receptors targeted by epinephrine and norepinephrine	WP:WP4589	4.99E-02
TF	Factor: C/EBPgamma; motif: YTBATTTCARAAW; match class: 1	TF:M00622_1	6.33E-06
TF	Factor: HSF2; motif: NGAANNWTCK; match class: 1	TF:M00147_1	9.14E-04
TF	Factor: CLOCK; motif: NNCAYGYGYN; match class: 0	TF:M11046_0	3.02E-03
TF	Factor: Oct3; motif: NATGCAANNN; match class: 0	TF:M01307_0	7.47E-03
TF	Factor: HSF2; motif: NGAANNWTCK; match class: 0	TF:M00147_0	8.03E-03
TF	Factor: FOXM1; motif: TRTTTATNN; match class: 1	TF:M08883_1	2.10E-02
TF	Factor: GR; motif: RGRACATTNTGTYC; match class: 0	TF:M04750_0	2.34E-02
TF	Factor: HSF1; motif: TCYAGAANNTTC; match class: 0	TF:M07259_0	2.52E-02
TF	Factor: C/EBPgamma; motif: YTBATTTCARAAW; match class: 0	TF:M00622_0	2.63E-02
TF	Factor: LBX2; motif: CTNRANSTAATTA; match class: 1	TF:M04383_1	2.67E-02
TF	Factor: GR; motif: RGNACANMNTGTNCY; match class: 0	TF:M09941_0	3.00E-02
TF	Factor: AP-3; motif: TKGAAAKN; match class: 0	TF:M04609_0	3.31E-02
TF	Factor: HOXA9; motif: DTGATTTATKGY; match class: 0	TF:M07450_0	3.66E-02
TF	Factor: POU6F1; motif: NTAATGAKATGNNN; match class: 0	TF:M11958_0	3.68E-02
TF	Factor: Oct-2; motif: NYATGCAAATN; match class: 1	TF:M10034_1	3.73E-02
TF	Factor: AR; motif: NGNACANNNTGTTCYNN; match class: 0	TF:M09589_0	4.34E-02
TF	Factor: SMAD3; motif: CAGACAS; match class: 0	TF:M07429_0	4.46E-02
HPA	hair; cells in cuticle	HPA:020020	3.85E-11
HPA	hair; cells in internal root sheath	HPA:020040	3.85E-11
HPA	hair	HPA:020000	6.01E-11
HPA	hair; cells in cortex/medulla	HPA:020010	6.01E-11
HPA	hair; cells in external root sheath	HPA:020030	6.01E-11
HPA	hair; cells in cuticle[Supported,Not detected]	HPA:020020_10	8.62E-09
HPA	hair; cells in internal root sheath[Supported,Not detected]	HPA:020040_10	8.62E-09
HPA	hair; cells in cortex/medulla[Supported,Not detected]	HPA:020010_10	1.33E-08
HPA	hair; cells in external root sheath[Supported,Not detected]	HPA:020030_10	1.33E-08
HPA	skin; sebaceous cells	HPA:042010	2.49E-04

HPA	skin; sweat ducts	HPA:042030	2.49E-04
HPA	skin	HPA:042000	2.49E-04
HPA	skin; secretory cells	HPA:042020	2.49E-04
HPA	skin; secretory cells[Supported,Not detected]	HPA:042020_10	1.22E-03
HPA	skin; sebaceous cells[Supported,Not detected]	HPA:042010_10	1.22E-03
HPA	skin; sweat ducts[Supported,Not detected]	HPA:042030_10	1.22E-03
HPA	hair; cells in internal root sheath[Uncertain,Medium]	HPA:020040_02	1.20E-02
HPA	hair; cells in internal root sheath[Uncertain,Low]	HPA:020040_01	1.20E-02
HPA	hair; cells in internal root sheath[Uncertain,High]	HPA:020040_03	1.20E-02
HPA	hair; cells in internal root sheath[Supported,Low]	HPA:020040_11	1.20E-02
CORUM	Calprotectin heterotetramer	CORUM:6826	1.67E-02
CORUM	iNOS-S100A8/A9 complex	CORUM:6827	4.98E-02
HP	Epidermal thickening	HP:0011368	3.55E-06
HP	Thickened skin	HP:0001072	1.29E-05
HP	Erythroderma	HP:0001019	2.11E-04
HP	Hyperkeratosis	HP:0000962	2.96E-04
HP	Congenital ichthyosiform erythroderma	HP:0007431	3.75E-04
HP	Abnormality of epidermal morphology	HP:0011124	1.10E-03
HP	Hypotrichosis	HP:0001006	7.61E-03
HP	Pruritus	HP:0000989	1.83E-02
HP	Heinz body anemia	HP:0005511	2.88E-02
HP	Ichthyosis	HP:0008064	3.19E-02
HP	Erythema	HP:0010783	4.07E-02
HP	Palmoplantar keratoderma	HP:0000982	4.76E-02

Input g:GOSt results (negative fold-change)

source	term_name	term_id	adj_p_value
GO:MF	extracellular matrix structural constituent conferring tensile strength	GO:0030020	1.71E-05
GO:MF	platelet-derived growth factor binding	GO:0048407	5.91E-04
GO:MF	extracellular matrix structural constituent	GO:0005201	8.14E-04
GO:MF	organic acid binding	GO:0043177	3.68E-02
GO:MF	protein homodimerization activity	GO:0042803	4.93E-02
GO:MF	alpha-adrenergic receptor activity	GO:0004936	4.99E-02
GO:MF	calcium ion binding	GO:0005509	4.99E-02
GO:BP	extracellular matrix organization	GO:0030198	1.02E-06
GO:BP	extracellular structure organization	GO:0043062	1.08E-06
GO:BP	tissue development	GO:0009888	4.73E-05
GO:BP	anatomical structure development	GO:0048856	9.39E-05
GO:BP	multicellular organismal process	GO:0032501	1.04E-04

GO:BP	developmental process	GO:0032502	6.93E-04
GO:BP	system development	GO:0048731	1.88E-03
GO:BP	cornification	GO:0070268	2.55E-03
GO:BP	cell adhesion	GO:0007155	2.67E-03
GO:BP	skin development	GO:0043588	2.68E-03
GO:BP	anatomical structure morphogenesis	GO:0009653	2.77E-03
GO:BP	regulation of amine transport	GO:0051952	2.96E-03
GO:BP	biological adhesion	GO:0022610	3.09E-03
GO:BP	multicellular organism development	GO:0007275	3.10E-03
GO:BP	drug transport	GO:0015893	3.76E-03
GO:BP	blood circulation	GO:0008015	3.78E-03
GO:BP	regulation of system process	GO:0044057	4.45E-03
GO:BP	circulatory system process	GO:0003013	5.35E-03
GO:BP	amine transport	GO:0015837	6.07E-03
GO:BP	peptide cross-linking	GO:0018149	6.75E-03
GO:CC	extracellular region	GO:0005576	2.46E-10
GO:CC	extracellular matrix	GO:0031012	1.14E-06
GO:CC	extracellular space	GO:0005615	2.71E-06
GO:CC	collagen trimer	GO:0005581	6.80E-06
GO:CC	collagen-containing extracellular matrix	GO:0062023	9.89E-06
GO:CC	cornified envelope	GO:0001533	4.04E-03
GO:CC	banded collagen fibril	GO:0098643	1.44E-02
GO:CC	fibrillar collagen trimer	GO:0005583	1.44E-02
GO:CC	contractile fiber	GO:0043292	4.11E-02
GO:CC	intrinsic component of plasma membrane	GO:0031226	4.21E-02
GO:CC	integral component of plasma membrane	GO:0005887	4.92E-02
KEGG	Protein digestion and absorption	KEGG:04974	5.46E-07
KEGG	Malaria	KEGG:05144	5.25E-04
KEGG	Neuroactive ligand-receptor interaction	KEGG:04080	1.45E-03
KEGG	Steroid hormone biosynthesis	KEGG:00140	1.91E-02
REAC	Collagen degradation	REAC:R-HSA-1442490	1.05E-06
REAC	Collagen biosynthesis and modifying enzymes	REAC:R-HSA-1650814	1.83E-06
REAC	Extracellular matrix organization	REAC:R-HSA-1474244	2.54E-05
REAC	Collagen chain trimerization	REAC:R-HSA-8948216	4.95E-05
REAC	Collagen formation	REAC:R-HSA-1474290	4.99E-05
REAC	Degradation of the extracellular matrix	REAC:R-HSA-1474228	1.95E-04
REAC	Assembly of collagen fibrils and other multimeric structures	REAC:R-HSA-2022090	7.90E-04
REAC	Integrin cell surface interactions	REAC:R-HSA-216083	1.84E-03
REAC	Formation of the cornified envelope	REAC:R-HSA-6809371	2.58E-03

REAC	Erythrocytes take up oxygen and release carbon dioxide	REAC:R-HSA-1247673	6.39E-03
REAC	Muscle contraction	REAC:R-HSA-397014	1.88E-02
REAC	Cardiac conduction	REAC:R-HSA-5576891	3.07E-02
REAC	O2/CO2 exchange in erythrocytes	REAC:R-HSA-1480926	3.41E-02
REAC	Erythrocytes take up carbon dioxide and release oxygen	REAC:R-HSA-1237044	3.41E-02
REAC	ECM proteoglycans	REAC:R-HSA-3000178	3.77E-02
WP	miRNA targets in ECM and membrane receptors	WP:WP2911	4.77E-03
TF	Factor: FOXP1; motif: TNTGTTTMY; match class: 0	TF:M09933_0	1.39E-02
HP	Y-linked inheritance	HP:0001450	7.07E-03
HP	Heinz body anemia	HP:0005511	2.59E-02
HP	Abnormal sclera morphology	HP:0000591	4.12E-02
HP	Blue sclerae	HP:0000592	4.25E-02
HP	Hyperkeratosis	HP:0000962	4.88E-02

FACS enriched CD45+ leukocyte g:GOSt results (negative fold-change)

source	term_name	term_id	adj_p_value
GO:MF	extracellular matrix structural constituent	GO:0005201	3.08E-11
GO:MF	collagen binding	GO:0005518	9.10E-07
GO:MF	extracellular matrix structural constituent conferring tensile strength	GO:0030020	4.37E-06
GO:MF	extracellular matrix binding	GO:0050840	1.09E-05
GO:MF	identical protein binding	GO:0042802	1.27E-05
GO:MF	platelet-derived growth factor binding	GO:0048407	3.43E-05
GO:MF	glycosaminoglycan binding	GO:0005539	6.23E-05
GO:MF	receptor ligand activity	GO:0048018	1.88E-04
GO:MF	signaling receptor activator activity	GO:0030546	2.42E-04
GO:MF	chemokine activity	GO:0008009	3.39E-04
GO:MF	structural molecule activity	GO:0005198	4.24E-04
GO:MF	receptor regulator activity	GO:0030545	4.35E-04
GO:MF	fibronectin binding	GO:0001968	5.20E-04
GO:MF	CXCR chemokine receptor binding	GO:0045236	6.20E-04
GO:MF	signaling receptor binding	GO:0005102	1.11E-03
GO:MF	cytokine receptor binding	GO:0005126	1.45E-03
GO:MF	molecular function regulator	GO:0098772	1.47E-03
GO:MF	cytokine activity	GO:0005125	1.67E-03
GO:MF	growth factor binding	GO:0019838	4.38E-03
GO:MF	heparin binding	GO:0008201	7.17E-03
GO:BP	extracellular matrix organization	GO:0030198	5.87E-14
GO:BP	extracellular structure organization	GO:0043062	6.45E-14
GO:BP	collagen fibril organization	GO:0030199	6.87E-09

GO:BP	regulation of multicellular organismal process	GO:0051239	1.18E-08
GO:BP	cell adhesion	GO:0007155	6.15E-08
GO:BP	biological adhesion	GO:0022610	7.66E-08
GO:BP	anatomical structure development	GO:0048856	1.57E-07
GO:BP	developmental process	GO:0032502	2.66E-07
GO:BP	response to external stimulus	GO:0009605	4.60E-07
GO:BP	cell migration	GO:0016477	6.91E-07
GO:BP	cell motility	GO:0048870	1.38E-06
GO:BP	localization of cell	GO:0051674	1.38E-06
GO:BP	multicellular organism development	GO:0007275	1.73E-06
GO:BP	system development	GO:0048731	2.23E-06
GO:BP	regulation of developmental process	GO:0050793	2.47E-06
GO:BP	response to organic substance	GO:0010033	4.10E-06
GO:BP	multicellular organismal process	GO:0032501	6.69E-06
GO:BP	neutrophil migration	GO:1990266	8.15E-06
GO:BP	myeloid leukocyte migration	GO:0097529	9.46E-06
GO:BP	response to molecule of bacterial origin	GO:0002237	1.06E-05
GO:CC	collagen-containing extracellular matrix	GO:0062023	3.05E-21
GO:CC	extracellular matrix	GO:0031012	9.66E-21
GO:CC	extracellular region	GO:0005576	4.60E-13
GO:CC	extracellular space	GO:0005615	8.02E-13
GO:CC	banded collagen fibril	GO:0098643	3.33E-07
GO:CC	fibrillar collagen trimer	GO:0005583	3.33E-07
GO:CC	vesicle	GO:0031982	1.49E-06
GO:CC	endoplasmic reticulum lumen	GO:0005788	1.76E-06
GO:CC	secretory vesicle	GO:0099503	2.34E-06
GO:CC	collagen trimer	GO:0005581	3.57E-06
GO:CC	endomembrane system	GO:0012505	5.29E-06
GO:CC	secretory granule	GO:0030141	1.12E-05
GO:CC	cytoplasmic vesicle	GO:0031410	1.22E-05
GO:CC	intracellular vesicle	GO:0097708	1.29E-05
GO:CC	complex of collagen trimers	GO:0098644	4.17E-05
GO:CC	cell surface	GO:0009986	5.21E-05
GO:CC	basement membrane	GO:0005604	2.50E-04
GO:CC	Golgi lumen	GO:0005796	1.88E-03
GO:CC	collagen type V trimer	GO:0005588	2.69E-03
GO:CC	collagen type VI trimer	GO:0005589	2.69E-03
KEGG	Amoebiasis	KEGG:05146	6.39E-07
KEGG	Protein digestion and absorption	KEGG:04974	6.23E-04
KEGG	Fluid shear stress and atherosclerosis	KEGG:05418	1.30E-03

KEGG	Rheumatoid arthritis	KEGG:05323	9.37E-03
KEGG	Cytokine-cytokine receptor interaction	KEGG:04060	2.29E-02
KEGG	Cell adhesion molecules (CAMs)	KEGG:04514	3.82E-02
KEGG	ECM-receptor interaction	KEGG:04512	4.66E-02
REAC	Extracellular matrix organization	REAC:R-HSA-1474244	2.52E-10
REAC	Collagen degradation	REAC:R-HSA-1442490	1.65E-08
REAC	ECM proteoglycans	REAC:R-HSA-3000178	1.68E-08
REAC	Degradation of the extracellular matrix	REAC:R-HSA-1474228	8.74E-07
REAC	Collagen formation	REAC:R-HSA-1474290	2.24E-06
REAC	Syndecan interactions	REAC:R-HSA-3000170	3.38E-06
REAC	Collagen biosynthesis and modifying enzymes	REAC:R-HSA-1650814	4.09E-06
REAC	Interleukin-10 signaling	REAC:R-HSA-6783783	4.42E-06
REAC	Assembly of collagen fibrils and other multimeric structures	REAC:R-HSA-2022090	1.07E-05
REAC	Collagen chain trimerization	REAC:R-HSA-8948216	4.47E-05
REAC	Integrin cell surface interactions	REAC:R-HSA-216083	5.06E-04
REAC	Non-integrin membrane-ECM interactions	REAC:R-HSA-3000171	6.88E-04
REAC	NCAM1 interactions	REAC:R-HSA-419037	3.61E-03
REAC	Chemokine receptors bind chemokines	REAC:R-HSA-380108	4.91E-03
REAC	Interleukin-4 and Interleukin-13 signaling	REAC:R-HSA-6785807	8.81E-03
REAC	GPCR ligand binding	REAC:R-HSA-500792	1.62E-02
REAC	Signaling by PDGF	REAC:R-HSA-186797	2.45E-02
REAC	Glycosaminoglycan metabolism	REAC:R-HSA-1630316	2.70E-02
REAC	Diseases associated with glycosaminoglycan metabolism	REAC:R-HSA-3560782	2.83E-02
REAC	Class A/1 (Rhodopsin-like receptors)	REAC:R-HSA-373076	3.65E-02
WP	miRNA targets in ECM and membrane receptors	WP:WP2911	7.59E-07
WP	Prostaglandin Synthesis and Regulation	WP:WP98	5.45E-04
WP	Lung fibrosis	WP:WP3624	1.41E-03
WP	Human Complement System	WP:WP2806	2.59E-03
WP	IL1 and megakaryocytes in obesity	WP:WP2865	6.10E-03
WP	Photodynamic therapy-induced NF-κB survival signaling	WP:WP3617	6.63E-03
WP	Allograft Rejection	WP:WP2328	2.65E-02
WP	Complement Activation	WP:WP545	4.39E-02
TF	Factor: FOXO1; motif: GNNTTGTTTACNTT; match class: 0	TF:M00474_0	3.16E-02
MIRNA	hsa-miR-29b-3p	MIRNA:hsa-miR-29b-3p	8.78E-05
MIRNA	hsa-miR-335-5p	MIRNA:hsa-miR-335-5p	6.02E-03
HP	Hyperextensibility at wrists	HP:0005072	7.62E-04
HP	Increased laxity of fingers	HP:0006149	7.62E-04
HP	Finger joint hypermobility	HP:0006094	1.23E-03

HP	Abnormality of hand joint mobility	HP:0006256	1.76E-03
HP	Pneumothorax	HP:0002107	2.31E-03
HP	Protrusio acetabuli	HP:0003179	4.63E-03
HP	Ascending tubular aorta aneurysm	HP:0004970	5.29E-03
HP	Atrophic scars	HP:0001075	6.18E-03
HP	Genital hernia	HP:0100823	1.09E-02
HP	Bruising susceptibility	HP:0000978	1.27E-02
HP	Hyperextensible skin	HP:0000974	1.34E-02
HP	Subarachnoid hemorrhage	HP:0002138	1.74E-02
HP	Reduced muscle collagen VI	HP:0030095	2.80E-02
HP	Dermal atrophy	HP:0004334	3.23E-02
HP	Diaphragmatic weakness	HP:0009113	3.36E-02
HP	Fragile skin	HP:0001030	3.76E-02
HP	Arterial dissection	HP:0005294	4.89E-02

FACS enriched CD45- keratinocyte g:GOSt results (negative fold-change)

source	term_name	term_id	adj_p_value
GO:MF	calcium ion binding	GO:0005509	2.99E-04
GO:MF	G protein-coupled receptor binding	GO:0001664	4.14E-03
GO:MF	receptor regulator activity	GO:0030545	2.23E-02
GO:MF	postsynaptic neurotransmitter receptor activity	GO:0098960	2.43E-02
GO:MF	neurotransmitter receptor activity involved in regulation of postsynaptic membrane potential	GO:0099529	2.46E-02
GO:MF	receptor ligand activity	GO:0048018	4.48E-02
GO:MF	inhibitory extracellular ligand-gated ion channel activity	GO:0005237	4.94E-02
GO:BP	regulation of system process	GO:0044057	2.23E-04
GO:BP	cell-cell signaling	GO:0007267	4.25E-04
GO:BP	muscle contraction	GO:0006936	6.71E-04
GO:BP	muscle system process	GO:0003012	1.35E-03
GO:BP	cell-cell adhesion via plasma-membrane adhesion molecules	GO:0098742	2.94E-03
GO:BP	peptide cross-linking	GO:0018149	4.37E-03
GO:BP	tissue development	GO:0009888	6.43E-03
GO:BP	myeloid leukocyte migration	GO:0097529	8.52E-03
GO:BP	cAMP-mediated signaling	GO:0019933	8.78E-03
GO:BP	regulation of blood circulation	GO:1903522	1.11E-02
GO:BP	regulation of the force of heart contraction	GO:0002026	1.29E-02
GO:BP	granulocyte migration	GO:0097530	1.33E-02
GO:BP	regulation of membrane potential	GO:0042391	1.81E-02
GO:BP	anatomical structure development	GO:0048856	1.92E-02
GO:BP	multicellular organismal process	GO:0032501	1.95E-02

GO:BP	second-messenger-mediated signaling	GO:0019932	2.08E-02
GO:BP	blood circulation	GO:0008015	2.28E-02
GO:BP	developmental process	GO:0032502	2.35E-02
GO:BP	regulation of muscle system process	GO:0090257	2.55E-02
GO:BP	cell adhesion	GO:0007155	2.58E-02
GO:CC	extracellular matrix	GO:0031012	7.29E-07
GO:CC	cornified envelope	GO:0001533	7.59E-07
GO:CC	extracellular region	GO:0005576	2.74E-06
GO:CC	collagen-containing extracellular matrix	GO:0062023	1.48E-04
GO:CC	intrinsic component of plasma membrane	GO:0031226	1.29E-03
GO:CC	synaptic membrane	GO:0097060	3.57E-03
GO:CC	plasma membrane	GO:0005886	3.94E-03
GO:CC	integral component of plasma membrane	GO:0005887	7.16E-03
GO:CC	cell periphery	GO:0071944	7.80E-03
GO:CC	plasma membrane region	GO:0098590	8.48E-03
GO:CC	anchored component of membrane	GO:0031225	9.15E-03
GO:CC	GABA-ergic synapse	GO:0098982	1.31E-02
GO:CC	extracellular space	GO:0005615	1.96E-02
GO:CC	postsynaptic membrane	GO:0045211	3.49E-02
GO:CC	transmembrane transporter complex	GO:1902495	4.18E-02
KEGG	Neuroactive ligand-receptor interaction	KEGG:04080	1.14E-03
KEGG	Dilated cardiomyopathy (DCM)	KEGG:05414	1.65E-02
KEGG	Adrenergic signaling in cardiomyocytes	KEGG:04261	1.73E-02
KEGG	Viral protein interaction with cytokine and cytokine receptor	KEGG:04061	2.04E-02
REAC	Muscle contraction	REAC:R-HSA-397014	7.08E-04
REAC	Class A/1 (Rhodopsin-like receptors)	REAC:R-HSA-373076	3.42E-03
REAC	Peptide ligand-binding receptors	REAC:R-HSA-375276	8.72E-03
REAC	GPCR ligand binding	REAC:R-HSA-500792	3.10E-02
REAC	Platelet activation, signaling and aggregation	REAC:R-HSA-76002	3.88E-02
REAC	Cardiac conduction	REAC:R-HSA-5576891	4.23E-02
REAC	Hemostasis	REAC:R-HSA-109582	4.71E-02
TF	Factor: SMAD3; motif: CAGACAS; match class: 0	TF:M07429_0	9.17E-06
TF	Factor: RSRFC4; motif: ANKCTAWAAATAGMHYN; match class: 0	TF:M00407_0	4.18E-05
TF	Factor: CDX-2; motif: TTTATN; match class: 0	TF:M02087_0	2.50E-02
TF	Factor: RSRFC4; motif: RNKCTATTTWTAGMWN; match class: 0	TF:M00026_0	3.43E-02
CORUM	TTR-RBP complex	CORUM:6821	4.98E-02
CORUM	Calprotectin heterotetramer	CORUM:6826	4.98E-02
HP	Y-linked inheritance	HP:0001450	2.50E-03

References

AGARWAL, P., AGARWAL, C., BHARDWAJ, M., AHUJA, A. & RANI, S. 2015. Trichoepithelioma and Basal Cell Carcinoma with Squamous Differentiation: Is it Causal or Coincidental? *Indian J Dermatol,* 60**,** 394-6.

ALAMEDA, J. P., RAMIREZ, A., GARCIA-FERNANDEZ, R. A., NAVARRO, M., PAGE, A., SEGOVIA, J. C., SANCHEZ, R., SUAREZ-CABRERA, C., PARAMIO, J. M., BRAVO, A., FERNANDEZ-ACENERO, M. J. & CASANOVA, M. L. 2019. Premature aging and cancer development in transgenic mice lacking functional CYLD. *Aging (Albany NY),* 11**,** 127-159.

ALEXANDROV, L. B., NIK-ZAINAL, S., WEDGE, D. C., CAMPBELL, P. J. & STRATTON, M. R. 2013. Deciphering signatures of mutational processes operative in human cancer. *Cell Rep,* 3**,** 246-59.

ANDERS, S., PYL, P. T. & HUBER, W. 2015. HTSeq--a Python framework to work with high-throughput sequencing data. *Bioinformatics,* 31**,** 166-9.

ANDERSSON, M. K., KOLBY, L., NILSSON, J. A. & STENMAN, G. 2019. Clinical, genetic and experimental studies of the Brooke-Spiegler (CYLD) skin tumor syndrome. *J Plast Surg Hand Surg,* 53**,** 71-75.

ANDREOLI, M. T. & ITANI, K. M. 2011. Malignant eccrine spiradenoma: a meta-analysis of reported cases. *Am J Surg,* 201**,** 695-9.

ANDREWS, S. 2010. FastQC: a quality control tool for high throughput sequence data. Available online at http://www.bioinformatics.babraham.ac.uk/projects/fastqc.

ANNUNZIATA, C. M., DAVIS, R. E., DEMCHENKO, Y., BELLAMY, W., GABREA, A., ZHAN, F., LENZ, G., HANAMURA, I., WRIGHT, G., XIAO, W., DAVE, S., HURT, E. M., TAN, B., ZHAO, H., STEPHENS, O., SANTRA, M., WILLIAMS, D. R., DANG, L., BARLOGIE, B., SHAUGHNESSY, J. D., JR., KUEHL, W. M. & STAUDT, L. M. 2007. Frequent engagement of the classical and alternative NF-kappaB pathways by diverse genetic abnormalities in multiple myeloma. *Cancer Cell,* 12**,** 115-30.

ANTIGNANO, F., POSARAC, V., EWEN, C. L., JOVANOVIC, V. K., LIANG, A., WOODSIDE, S. M., KOKAJI, A. I., EAVES, A. C. & THOMAS, T. E. 2020. Isolation of human CD45+ leukocytes from tissues and human tumor xenografts in humanized mice. *The Journal of Immunology,* 204**,** 242.38-242.38.

ARAN, D., HU, Z. & BUTTE, A. J. 2017. xCell: digitally portraying the tissue cellular heterogeneity landscape. *Genome Biology,* 18**,** 220.

ARMSTRONG, J. F., FACCENDA, E., HARDING, S. D., PAWSON, A. J., SOUTHAN, C., SHARMAN, J. L., CAMPO, B., CAVANAGH, D. R., ALEXANDER, S. P. H., DAVENPORT, A. P., SPEDDING, M., DAVIES, J. A. & NC, I. 2020. The IUPHAR/BPS Guide to PHARMACOLOGY in 2020: extending immunopharmacology content and introducing the IUPHAR/MMV Guide to MALARIA PHARMACOLOGY. *Nucleic Acids Res,* 48**,** D1006-D1021.

ARYEE, M. J., JAFFE, A. E., CORRADA-BRAVO, H., LADD-ACOSTA, C., FEINBERG, A. P., HANSEN, K. D. & IRIZARRY, R. A. 2014. Minfi: a flexible and comprehensive Bioconductor package for the analysis of Infinium DNA methylation microarrays. *Bioinformatics,* 30**,** 1363-9.

ASTOLFI, A., FIORE, M., MELCHIONDA, F., INDIO, V., BERTUCCIO, S. N. & PESSION, A. 2019. BCOR involvement in cancer. *Epigenomics,* 11**,** 835-855.

ATTISANO, L. & WRANA, J. L. 2002. Signal transduction by the TGF-beta superfamily. *Science,* 296**,** 1646-7.

BANSAL, C., BATRA, M., LAL, N. & SRIVASTAVA, A. N. 2012. Solitary cylindroma with malignant transformation. *Indian J Dermatol,* 57**,** 141-3.

BARTON, D., HOGENESCH, H. & WEIH, F. 2000. Mice lacking the transcription factor RelB develop T cell-dependent skin lesions similar to human atopic dermatitis. *Eur J Immunol,* 30**,** 2323-32.

BAUD, V. & KARIN, M. 2009. Is NF-kappaB a good target for cancer therapy? Hopes and pitfalls. *Nat Rev Drug Discov,* 8**,** 33-40.

BEG, A. A. & BALTIMORE, D. 1996. An essential role for NF-kappaB in preventing TNF-alpha-induced cell death. *Science,* 274**,** 782-4.

BESTOR, T., LAUDANO, A., MATTALIANO, R. & INGRAM, V. 1988. Cloning and sequencing of a cDNA encoding DNA methyltransferase of mouse cells. The carboxyl-terminal domain of the mammalian enzymes is related to bacterial restriction methyltransferases. *J Mol Biol,* 203**,** 971-83.

BIGGS, P. J., WOOSTER, R., FORD, D., CHAPMAN, P., MANGION, J., QUIRK, Y., EASTON, D. F., BURN, J. & STRATTON, M. R. 1995. Familial cylindromatosis (turban tumour syndrome) gene localised to chromosome 16q12-q13: evidence for its role as a tumour suppressor gene. *Nat Genet,* 11**,** 441-3.

BIGNELL, G. R., WARREN, W., SEAL, S., TAKAHASHI, M., RAPLEY, E., BARFOOT, R., GREEN, H., BROWN, C., BIGGS, P. J., LAKHANI, S. R., JONES, C., HANSEN, J., BLAIR, E., HOFMANN, B., SIEBERT, R., TURNER, G., EVANS, D. G., SCHRANDER-STUMPEL, C., BEEMER, F. A., VAN DEN OUWELAND, A., HALLEY, D., DELPECH, B., CLEVELAND, M. G., LEIGH, I., LEISTI, J. & RASMUSSEN, S. 2000. Identification of the familial cylindromatosis tumour-suppressor gene. *Nat Genet,* 25**,** 160-5.

BINNEWIES, M., ROBERTS, E. W., KERSTEN, K., CHAN, V., FEARON, D. F., MERAD, M., COUSSENS, L. M., GABRILOVICH, D. I., OSTRAND-ROSENBERG, S., HEDRICK, C. C., VONDERHEIDE, R. H., PITTET, M. J., JAIN, R. K., ZOU, W., HOWCROFT, T. K., WOODHOUSE, E. C., WEINBERG, R. A. & KRUMMEL, M. F. 2018. Understanding the tumor immune microenvironment (TIME) for effective therapy. *Nature Medicine,* 24**,** 541-550.

BLAKE, P. W. & TORO, J. R. 2009. Update of cylindromatosis gene (CYLD) mutations in Brooke-Spiegler syndrome: novel insights into the role of deubiquitination in cell signaling. *Hum Mutat,* 30**,** 1025-36.

BROOKE, J. D., FITZPATRICK, J. E. & GOLITZ, L. E. 1989. Papillary mesenchymal bodies: a histologic finding useful in differentiating trichoepitheliomas from basal cell carcinomas. *J Am Acad Dermatol,* 21**,** 523-8.

BROWN, S. M., AREFI, M., STONES, R., LOO, P. S., BARNARD, S., BLOXHAM, C., STEFANOS, N., LANGTRY, J. A. A., WORTHY, S., CALONJE, E., HUSAIN, A. & RAJAN, N. 2018. Inherited pulmonary cylindromas: extending the phenotype of CYLD mutation carriers. *Br J Dermatol,* 179**,** 662-668.

BROWN, T. M. & KRISHNAMURTHY, K. 2021. Histology, Dermis. *StatPearls.* Treasure Island (FL): StatPearls Publishing

BRUCKNER-TUDERMAN, L., PFALTZ, M. & SCHNYDER, U. W. 1991. Cylindroma overexpresses collagen VII, the major anchoring fibril protein. *J Invest Dermatol,* 96**,** 729-34.

BRUMMELKAMP, T. R., NIJMAN, S. M., DIRAC, A. M. & BERNARDS, R. 2003. Loss of the cylindromatosis tumour suppressor inhibits apoptosis by activating NF-kappaB. *Nature,* 424**,** 797-801.

CAO, Q., GEARHART, M. D., GERY, S., SHOJAEE, S., YANG, H., SUN, H., LIN, D. C., BAI, J. W., MEAD, M., ZHAO, Z., CHEN, Q., CHIEN, W. W., ALKAN, S., ALPERMANN, T., HAFERLACH, T., MÜSCHEN, M., BARDWELL, V. J. & KOEFFLER, H. P. 2016. BCOR regulates myeloid cell proliferation and differentiation. *Leukemia,* 30**,** 1155-1165.

CAPECE, D., VERZELLA, D., TESSITORE, A., ALESSE, E., CAPALBO, C. & ZAZZERONI, F. 2018. Cancer secretome and inflammation: The bright and the dark sides of NF-κB. *Seminars in Cell & Developmental Biology,* 78**,** 51-61.

CARAYOL, N. & WANG, C.-Y. 2006. IKKα stabilizes cytosolic β-catenin by inhibiting both canonical and non-canonical degradation pathways. *Cellular Signalling,* 18**,** 1941-1946.

CHALLEN, G. A., SUN, D., JEONG, M., LUO, M., JELINEK, J., BERG, J. S., BOCK, C., VASANTHAKUMAR, A., GU, H., XI, Y., LIANG, S., LU, Y., DARLINGTON, G. J., MEISSNER, A., ISSA, J.-P. J., GODLEY, L. A., LI, W. & GOODELL, M. A. 2011. Dnmt3a is essential for hematopoietic stem cell differentiation. *Nature genetics,* 44**,** 23-31.

CHALLEN, G. A., SUN, D., MAYLE, A., JEONG, M., LUO, M., RODRIGUEZ, B., MALLANEY, C., CELIK, H., YANG, L., XIA, Z., CULLEN, S., BERG, J., ZHENG, Y., DARLINGTON, G. J., LI, W. & GOODELL, M. A. 2014. Dnmt3a and Dnmt3b have overlapping and distinct functions in hematopoietic stem cells. *Cell Stem Cell,* 15**,** 350-364.

CHEN, B.-F. & CHAN, W.-Y. 2014. The de novo DNA methyltransferase DNMT3A in development and cancer. *Epigenetics,* 9**,** 669-677.

CHEN, B., KHODADOUST, M. S., LIU, C. L., NEWMAN, A. M. & ALIZADEH, A. A. 2018. Profiling Tumor Infiltrating Immune Cells with CIBERSORT. *Methods in molecular biology (Clifton, N.J.),* 1711**,** 243-259.

CHEN, T., UEDA, Y., DODGE, J. E., WANG, Z. & LI, E. 2003. Establishment and Maintenance of Genomic Methylation Patterns in Mouse Embryonic Stem Cells by Dnmt3a and Dnmt3b. *Molecular and Cellular Biology,* 23**,** 5594-5605.

CHEN, T., UEDA, Y., XIE, S. & LI, E. 2002. A novel Dnmt3a isoform produced from an alternative promoter localizes to euchromatin and its expression correlates with active de novo methylation. *J Biol Chem,* 277**,** 38746-54.

CHRISTIAN, F., SMITH, E. L. & CARMODY, R. J. 2016. The Regulation of NF-kappaB Subunits by Phosphorylation. *Cells,* 5.

CLEVERS, H. 2006. Wnt/beta-catenin signaling in development and disease. *Cell,* 127**,** 469-80.

COGSWELL, P. C., GUTTRIDGE, D. C., FUNKHOUSER, W. K. & BALDWIN, A. S., JR. 2000. Selective activation of NF-kappa B subunits in human breast cancer: potential roles for NF-kappa B2/p52 and for Bcl-3. *Oncogene,* 19**,** 1123-31.

COORNAERT, B., BAENS, M., HEYNINCK, K., BEKAERT, T., HAEGMAN, M., STAAL, J., SUN, L., CHEN, Z. J., MARYNEN, P. & BEYAERT, R. 2008. T cell antigen receptor stimulation induces MALT1 paracaspase-mediated cleavage of the NF-kappaB inhibitor A20. *Nat Immunol,* 9**,** 263-71.

CUI, C. Y., DURMOWICZ, M., TANAKA, T. S., HARTUNG, A. J., TEZUKA, T., HASHIMOTO, K., KO, M. S., SRIVASTAVA, A. K. & SCHLESSINGER, D. 2002. EDA targets revealed by skin gene expression profiles of wild-type, Tabby and Tabby EDA-A1 transgenic mice. *Hum Mol Genet,* 11**,** 1763-73.

CUI, C. Y., HASHIMOTO, T., GRIVENNIKOV, S. I., PIAO, Y., NEDOSPASOV, S. A. & SCHLESSINGER, D. 2006. Ectodysplasin regulates the lymphotoxin-beta pathway for hair differentiation. *Proc Natl Acad Sci U S A,* 103**,** 9142-7.

CUI, H., HU, Y., GUO, D., ZHANG, A., GU, Y., ZHANG, S., ZHAO, C., GONG, P., SHEN, X., LI, Y., WU, H., WANG, L., ZHAO, Z. & FAN, H. 2018. DNA methyltransferase 3A isoform b contributes to repressing E-cadherin through cooperation of DNA methylation and H3K27/H3K9 methylation in EMT-related metastasis of gastric cancer. *Oncogene,* 37**,** 4358-4371.

CUI, Z., KANG, H., GRANDIS, J. R. & JOHNSON, D. E. 2021. CYLD Alterations in the Tumorigenesis and Progression of Human Papillomavirus-Associated Head and Neck Cancers. *Mol Cancer Res,* 19**,** 14-24.

DAI, Y.-J., WANG, Y.-Y., HUANG, J.-Y., XIA, L., SHI, X.-D., XU, J., LU, J., SU, X.-B., YANG, Y., ZHANG, W.-N., WANG, P.-P., WU, S.-F., HUANG, T., MI, J.-Q., HAN, Z.-G., CHEN, Z. & CHEN, S.-J. 2017. Conditional knockin of Dnmt3a R878H initiates acute myeloid leukemia with mTOR pathway involvement. *Proceedings of the National Academy of Sciences,* 114**,** 5237-5242.

DANILENKO, M., HODGSON, K., STONES, R., HUSAIN, A., ZANGARINI, M., VEAL, G. & RAJAN, N. 2019. Diverse assays from a single skin punch biopsy to assess topical drug intervention. *Br J Dermatol,* 180**,** 937-938.

DANILENKO, M., STAMP, E., STOCKEN, D. D., HUSAIN, A., ZANGARINI, M., CRANSTON, A., STONES, R., SINCLAIR, N., HODGSON, K., BOWETT, S. A., ROBLIN, D., TRAVERSA, S., PLUMMER, R., VEAL, G., LANGTRY, J. A. A., ASHWORTH, A., BURN, J. & RAJAN, N. 2018. Targeting Tropomyosin Receptor Kinase in Cutaneous CYLD Defective Tumors With Pegcantratinib: The TRAC Randomized Clinical Trial. *JAMA Dermatol,* 154**,** 913-921.

DAS, P. M. & SINGAL, R. 2004. DNA methylation and cancer. *Journal of clinical oncology,* 22**,** 4632-4642.

DAVIES, C. & TOURNIER, C. 2012. Exploring the function of the JNK (c-Jun N-terminal kinase) signalling pathway in physiological and pathological processes to design novel therapeutic strategies. *Biochem Soc Trans,* 40**,** 85-9.

DAVIES, H. R., HODGSON, K., SCHWALBE, E., COXHEAD, J., SINCLAIR, N., ZOU, X., COCKELL, S., HUSAIN, A., NIK-ZAINAL, S. & RAJAN, N. 2019. Epigenetic modifiers DNMT3A and BCOR are recurrently mutated in CYLD cutaneous syndrome. *Nature Communications,* 10**,** 4717.

DE CHARETTE, M., MARABELLE, A. & HOUOT, R. 2016. Turning tumour cells into antigen presenting cells: The next step to improve cancer immunotherapy? *European Journal of Cancer,* 68**,** 134-147.

DEWEINDT, C., ALBAGLI, O., BERNARDIN, F., DHORDAIN, P., QUIEF, S., LANTOINE, D., KERCKAERT, J. P. & LEPRINCE, D. 1995. The LAZ3/BCL6 oncogene encodes a sequence-specific transcriptional inhibitor: a novel function for the BTB/POZ domain as an autonomous repressing domain. *Cell Growth Differ,* 6**,** 1495-503.

DHAYALAN, A., RAJAVELU, A., RATHERT, P., TAMAS, R., JURKOWSKA, R. Z., RAGOZIN, S. & JELTSCH, A. 2010. The Dnmt3a PWWP domain reads histone 3 lysine 36 trimethylation and guides DNA methylation. *J Biol Chem,* 285**,** 26114-20.

DIDONATO, J., MERCURIO, F., ROSETTE, C., WU-LI, J., SUYANG, H., GHOSH, S. & KARIN, M. 1996. Mapping of the inducible IkappaB phosphorylation sites that signal its ubiquitination and degradation. *Mol Cell Biol,* 16**,** 1295-304.

DOBIN, A., DAVIS, C. A., SCHLESINGER, F., DRENKOW, J., ZALESKI, C., JHA, S., BATUT, P., CHAISSON, M. & GINGERAS, T. R. 2012. STAR: ultrafast universal RNA-seq aligner. *Bioinformatics,* 29**,** 15-21.

DOBSON-STONE, C., HALLUPP, M., SHAHHEYDARI, H., RAGAGNIN, A. M. G., CHATTERTON, Z., CAREW-JONES, F., SHEPHERD, C. E., STEFEN, H., PARIC, E., FATH, T., THOMPSON, E. M., BLUMBERGS, P., SHORT, C. L., FIELD, C. D., PANEGYRES, P. K., HECKER, J., NICHOLSON, G., SHAW, A. D., FULLERTON, J. M., LUTY, A. A., SCHOFIELD, P. R., BROOKS, W. S., RAJAN, N., BENNETT, M. F., BAHLO, M., LANDERS, J. E., PIGUET, O., HODGES, J. R., HALLIDAY, G. M., TOPP, S. D., SMITH, B. N., SHAW, C. E., MCCANN, E., FIFITA, J. A., WILLIAMS, K. L., ATKIN, J. D., BLAIR, I. P. & KWOK, J. B. 2020. CYLD is a causative gene for frontotemporal dementia - amyotrophic lateral sclerosis. *Brain,* 143**,** 783-799.

DOFFINGER, R., SMAHI, A., BESSIA, C., GEISSMANN, F., FEINBERG, J., DURANDY, A., BODEMER, C., KENWRICK, S., DUPUIS-GIROD, S., BLANCHE, S., WOOD, P., RABIA, S. H., HEADON, D. J., OVERBEEK, P. A., LE DEIST, F., HOLLAND, S. M., BELANI, K., KUMARARATNE, D. S., FISCHER, A., SHAPIRO, R., CONLEY, M. E., REIMUND, E., KALHOFF, H., ABINUN, M., MUNNICH, A., ISRAEL, A., COURTOIS, G. & CASANOVA, J. L. 2001. X-linked anhidrotic ectodermal dysplasia with immunodeficiency is caused by impaired NF-kappaB signaling. *Nat Genet,* 27**,** 277-85.

DRABER, P., KUPKA, S., REICHERT, M., DRABEROVA, H., LAFONT, E., DE MIGUEL, D., SPILGIES, L., SURINOVA, S., TARABORRELLI, L., HARTWIG, T., RIESER, E., MARTINO, L., RITTINGER, K. & WALCZAK, H. 2015. LUBAC-Recruited CYLD and A20 Regulate Gene Activation and Cell Death by Exerting Opposing Effects on Linear Ubiquitin in Signaling Complexes. *Cell Rep,* 13**,** 2258-72.

DUBOIS, A., HODGSON, K. & RAJAN, N. 2017. Understanding Inherited Cylindromas: Clinical Implications of Gene Discovery. *Dermatol Clin,* 35**,** 61-71.

EGUETHER, T., ERMOLAEVA, M. A., ZHAO, Y., BONNET, M. C., JAIN, A., PASPARAKIS, M., COURTOIS, G. & TASSIN, A. M. 2014. The deubiquitinating enzyme CYLD controls apical docking of basal bodies in ciliated epithelial cells. *Nat Commun,* 5**,** 4585.

ELLIOTT, P. R., LESKE, D., HRDINKA, M., BAGOLA, K., FIIL, B. K., MCLAUGHLIN, S. H., WAGSTAFF, J., VOLKMAR, N., CHRISTIANSON, J. C., KESSLER, B. M., FREUND, S. M., KOMANDER, D. & GYRD-HANSEN, M. 2016. SPATA2 Links CYLD to LUBAC, Activates CYLD, and Controls LUBAC Signaling. *Mol Cell,* 63**,** 990-1005.

ELOMAA, O., PULKKINEN, K., HANNELIUS, U., MIKKOLA, M., SAARIALHO-KERE, U. & KERE, J. 2001. Ectodysplasin is released by proteolytic shedding and binds to the EDAR protein. *Hum Mol Genet,* 10**,** 953-62.

ESIBIZIONE, D., CUI, C. Y. & SCHLESSINGER, D. 2008. Candidate EDA targets revealed by expression profiling of primary keratinocytes from Tabby mutant mice. *Gene,* 427**,** 42-6.

FEHR, A., KOVACS, A., LONING, T., FRIERSON, H., JR., VAN DEN OORD, J. & STENMAN, G. 2011. The MYB-NFIB gene fusion-a novel genetic link between adenoid cystic carcinoma and dermal cylindroma. *J Pathol,* 224**,** 322-7.

FESSING, M. Y., SHAROVA, T. Y., SHAROV, A. A., ATOYAN, R. & BOTCHKAREV, V. A. 2006. Involvement of the Edar signaling in the control of hair follicle involution (catagen). *Am J Pathol,* 169**,** 2075-84.

FORTIN, J. P., LABBE, A., LEMIRE, M., ZANKE, B. W., HUDSON, T. J., FERTIG, E. J., GREENWOOD, C. M. & HANSEN, K. D. 2014. Functional normalization of 450k methylation array data improves replication in large cancer studies. *Genome Biol,* 15**,** 503.

FRIED, I., BODNER, C., PICHLER, M. M., LIND, K., BEHAM-SCHMID, C., QUEHENBERGER, F., SPERR, W. R., LINKESCH, W., SILL, H. & WÖLFLER, A. 2012. Frequency, onset and clinical impact of somatic DNMT3A mutations in therapy-related and secondary acute myeloid leukemia. *Haematologica,* 97**,** 246-250.

FUJIMURA, T., KAKIZAKI, A., FURUDATE, S., KAMBAYASHI, Y. & AIBA, S. 2016. Tumor-associated macrophages in skin: How to treat their heterogeneity and plasticity. *Journal of Dermatological Science,* 83**,** 167-173.

GAJEWSKI, T. F. & CRON, K. R. 2020. cDC1 dysregulation in cancer: An opportunity for intervention. *Journal of Experimental Medicine,* 217.

GALON, J. & BRUNI, D. 2019. Approaches to treat immune hot, altered and cold tumours with combination immunotherapies. *Nat Rev Drug Discov,* 18**,** 197-218.

GAO, J., HUO, L., SUN, X., LIU, M., LI, D., DONG, J. T. & ZHOU, J. 2008. The tumor suppressor CYLD regulates microtubule dynamics and plays a role in cell migration. *J Biol Chem,* 283**,** 8802-9.

GE, Y. Z., PU, M. T., GOWHER, H., WU, H. P., DING, J. P., JELTSCH, A. & XU, G. L. 2004. Chromatin targeting of de novo DNA methyltransferases by the PWWP domain. *J Biol Chem,* 279**,** 25447-54.

GEARHART, M. D., CORCORAN, C. M., WAMSTAD, J. A. & BARDWELL, V. J. 2006. Polycomb Group and SCF Ubiquitin Ligases Are Found in a Novel BCOR Complex That Is Recruited to BCL6 Targets. *Molecular and Cellular Biology,* 26**,** 6880-6889.

GERONDAKIS, S., GRUMONT, R., GUGASYAN, R., WONG, L., ISOMURA, I., HO, W. & BANERJEE, A. 2006. Unravelling the complexities of the NF-kappaB signalling pathway using mouse knockout and transgenic models. *Oncogene,* 25**,** 6781-99.

GIRALDO, N. A., SANCHEZ-SALAS, R., PESKE, J. D., VANO, Y., BECHT, E., PETITPREZ, F., VALIDIRE, P., INGELS, A., CATHELINEAU, X., FRIDMAN, W. H. & SAUTÈS-FRIDMAN, C. 2019. The clinical role of the TME in solid cancer. *British Journal of Cancer,* 120**,** 45-53.

GODEFROY, E., GALLOIS, A., IDOYAGA, J., MERAD, M., TUNG, N., MONU, N., SAENGER, Y., FU, Y., RAVINDRAN, R., PULENDRAN, B., JOTEREAU, F., TROMBETTA, S. & BHARDWAJ, N. 2014. Activation of toll-like receptor-2 by endogenous matrix metalloproteinase-2 modulates dendritic-cell-mediated inflammatory responses. *Cell reports,* 9**,** 1856-1870.

GRINBERG-BLEYER, Y., DAINICHI, T., OH, H., HEISE, N., KLEIN, U., SCHMID, R. M., HAYDEN, M. S. & GHOSH, S. 2015. Cutting edge: NF-kappaB p65 and c-Rel control epidermal development and immune homeostasis in the skin. *J Immunol,* 194**,** 2472-6.

GROSSMANN, V., TIACCI, E., HOLMES, A. B., KOHLMANN, A., MARTELLI, M. P., KERN, W., SPANHOL-ROSSETO, A., KLEIN, H.-U., DUGAS, M., SCHINDELA, S., TRIFONOV, V., SCHNITTGER, S., HAFERLACH, C., BASSAN, R., WELLS, V. A., SPINELLI, O., CHAN, J., ROSSI, R., BALDONI,

S., DE CAROLIS, L., GOETZE, K., SERVE, H., PECENY, R., KREUZER, K.-A., ORUZIO, D., SPECCHIA, G., DI RAIMONDO, F., FABBIANO, F., SBORGIA, M., LISO, A., FARINELLI, L., RAMBALDI, A., PASQUALUCCI, L., RABADAN, R., HAFERLACH, T. & FALINI, B. 2011. Whole-exome sequencing identifies somatic mutations of BCOR in acute myeloid leukemia with normal karyotype. *Blood,* 118**,** 6153-6163.

GURNEY, A. L., MARSTERS, S. A., HUANG, R. M., PITTI, R. M., MARK, D. T., BALDWIN, D. T., GRAY, A. M., DOWD, A. D., BRUSH, A. D., HELDENS, A. D., SCHOW, A. D., GODDARD, A. D., WOOD, W. I., BAKER, K. P., GODOWSKI, P. J. & ASHKENAZI, A. 1999. Identification of a new member of the tumor necrosis factor family and its receptor, a human ortholog of mouse GITR. *Curr Biol,* 9**,** 215-8.

HAHN, M., BURCKERT, J. P., LUTTENBERGER, C. A., KLEBOW, S., HESS, M., AL-MAARRI, M., VOGT, M., REISSIG, S., HALLEK, M., WIENECKE-BALDACCHINO, A., BUCH, T., MULLER, C. P., PALLASCH, C. P., WUNDERLICH, F. T., WAISMAN, A. & HOVELMEYER, N. 2018. Aberrant splicing of the tumor suppressor CYLD promotes the development of chronic lymphocytic leukemia via sustained NF-kappaB signaling. *Leukemia,* 32**,** 72-82.

HAHN, M. A., WU, X., LI, A. X., HAHN, T. & PFEIFER, G. P. 2011. Relationship between gene body DNA methylation and intragenic H3K9me3 and H3K36me3 chromatin marks. *PLoS One,* 6**,** e18844.

HAHNE, F. & IVANEK, R. 2016. Visualizing Genomic Data Using Gviz and Bioconductor. *In:* MATHÉ, E. & DAVIS, S. (eds.) *Statistical Genomics: Methods and Protocols.* New York, NY: Springer New York.

HAILFINGER, S., NOGAI, H., PELZER, C., JAWORSKI, M., CABALZAR, K., CHARTON, J. E., GUZZARDI, M., DECAILLET, C., GRAU, M., DORKEN, B., LENZ, P., LENZ, G. & THOME, M. 2011. Malt1-dependent RelB cleavage promotes canonical NF-kappaB activation in lymphocytes and lymphoma cell lines. *Proc Natl Acad Sci U S A,* 108**,** 14596-601.

HAMLINE, M. Y., CORCORAN, C. M., WAMSTAD, J. A., MILETICH, I., FENG, J., LOHR, J. L., HEMBERGER, M., SHARPE, P. T., GEARHART, M. D. & BARDWELL, V. J. 2020. OFCD syndrome and extraembryonic defects are revealed by conditional mutation of the Polycomb-group repressive complex 1.1 (PRC1.1) gene BCOR. *Dev Biol*.

HANAHAN, D. & WEINBERG, R. A. 2011. Hallmarks of Cancer: The Next Generation. *Cell,* 144**,** 646-674.

HAO, J., LI, T. G., QI, X., ZHAO, D. F. & ZHAO, G. Q. 2006. WNT/beta-catenin pathway up-regulates Stat3 and converges on LIF to prevent differentiation of mouse embryonic stem cells. *Dev Biol,* 290**,** 81-91.

HAWKSHAW, N. J., HARDMAN, J. A., HASLAM, I. S., SHAHMALAK, A., GILHAR, A., LIM, X. & PAUS, R. 2018. Identifying novel strategies for treating human hair loss disorders: Cyclosporine A suppresses the Wnt inhibitor, SFRP1, in the dermal papilla of human scalp hair follicles. *PLoS Biol,* 16**,** e2003705.

HAYDEN, M. S. & GHOSH, S. 2004. Signaling to NF-kappaB. *Genes Dev,* 18**,** 2195-224.

HAYDEN, M. S. & GHOSH, S. 2012. NF-kappaB, the first quarter-century: remarkable progress and outstanding questions. *Genes Dev,* 26**,** 203-34.

HEADON, D. J., EMMAL, S. A., FERGUSON, B. M., TUCKER, A. S., JUSTICE, M. J., SHARPE, P. T., ZONANA, J. & OVERBEEK, P. A. 2001a. Gene defect in

ectodermal dysplasia implicates a death domain adapter in development. *Nature,* 414**,** 913-916.
HEADON, D. J., EMMAL, S. A., FERGUSON, B. M., TUCKER, A. S., JUSTICE, M. J., SHARPE, P. T., ZONANA, J. & OVERBEEK, P. A. 2001b. Gene defect in ectodermal dysplasia implicates a death domain adapter in development. *Nature,* 414**,** 913-6.
HEADON, D. J. & OVERBEEK, P. A. 1999. Involvement of a novel Tnf receptor homologue in hair follicle induction. *Nat Genet,* 22**,** 370-4.
HELLERBRAND, C., BUMES, E., BATAILLE, F., DIETMAIER, W., MASSOUMI, R. & BOSSERHOFF, A. K. 2007. Reduced expression of CYLD in human colon and hepatocellular carcinomas. *Carcinogenesis,* 28**,** 21-7.
HERMISTON, M. L., XU, Z. & WEISS, A. 2003. CD45: A Critical Regulator of Signaling Thresholds in Immune Cells. *Annual Review of Immunology,* 21**,** 107-137.
HEYN, P., LOGAN, C. V., FLUTEAU, A., CHALLIS, R. C., AUCHYNNIKAVA, T., MARTIN, C.-A., MARSH, J. A., TAGLINI, F., KILANOWSKI, F., PARRY, D. A., CORMIER-DAIRE, V., FONG, C.-T., GIBSON, K., HWA, V., IBÁÑEZ, L., ROBERTSON, S. P., SEBASTIANI, G., RAPPSILBER, J., ALLSHIRE, R. C., REIJNS, M. A. M., DAUBER, A., SPROUL, D. & JACKSON, A. P. 2019. Gain-of-function DNMT3A mutations cause microcephalic dwarfism and hypermethylation of Polycomb-regulated regions. *Nature Genetics,* 51**,** 96-105.
HIRATA, H., HINODA, Y., NAKAJIMA, K., KAWAMOTO, K., KIKUNO, N., KAWAKAMI, K., YAMAMURA, S., UENO, K., MAJID, S., SAINI, S., ISHII, N. & DAHIYA, R. 2009. Wnt antagonist gene DKK2 is epigenetically silenced and inhibits renal cancer progression through apoptotic and cell cycle pathways. *Clin Cancer Res,* 15**,** 5678-87.
HIRATA, Y., TAKAHASHI, M., MORISHITA, T., NOGUCHI, T. & MATSUZAWA, A. 2017. Post-Translational Modifications of the TAK1-TAB Complex. *Int J Mol Sci,* 18.
HOBERG, J. E., POPKO, A. E., RAMSEY, C. S. & MAYO, M. W. 2006. IkappaB kinase alpha-mediated derepression of SMRT potentiates acetylation of RelA/p65 by p300. *Mol Cell Biol,* 26**,** 457-71.
HOELDER, S., CLARKE, P. A. & WORKMAN, P. 2012. Discovery of small molecule cancer drugs: successes, challenges and opportunities. *Mol Oncol,* 6**,** 155-76.
HOLZ-SCHIETINGER, C., MATJE, D. M., HARRISON, M. F. & REICH, N. O. 2011. Oligomerization of DNMT3A controls the mechanism of de novo DNA methylation. *J Biol Chem,* 286**,** 41479-88.
HOLZ-SCHIETINGER, C., MATJE, D. M. & REICH, N. O. 2012. Mutations in DNA methyltransferase (DNMT3A) observed in acute myeloid leukemia patients disrupt processive methylation. *J Biol Chem,* 287**,** 30941-51.
HOVELMEYER, N., WUNDERLICH, F. T., MASSOUMI, R., JAKOBSEN, C. G., SONG, J., WORNS, M. A., MERKWIRTH, C., KOVALENKO, A., AUMAILLEY, M., STRAND, D., BRUNING, J. C., GALLE, P. R., WALLACH, D., FASSLER, R. & WAISMAN, A. 2007. Regulation of B cell homeostasis and activation by the tumor suppressor gene CYLD. *J Exp Med,* 204**,** 2615-27.
HRDINKA, M., FIIL, B. K., ZUCCA, M., LESKE, D., BAGOLA, K., YABAL, M., ELLIOTT, P. R., DAMGAARD, R. B., KOMANDER, D., JOST, P. J. & GYRD-HANSEN, M. 2016. CYLD Limits Lys63- and Met1-Linked Ubiquitin at Receptor Complexes to Regulate Innate Immune Signaling. *Cell Rep,* 14**,** 2846-58.

HU, H., BRITTAIN, G. C., CHANG, J. H., PUEBLA-OSORIO, N., JIN, J., ZAL, A., XIAO, Y., CHENG, X., CHANG, M., FU, Y. X., ZAL, T., ZHU, C. & SUN, S. C. 2013. OTUD7B controls non-canonical NF-kappaB activation through deubiquitination of TRAF3. *Nature,* 494**,** 371-4.

HU, Y., BAUD, V., DELHASE, M., ZHANG, P., DEERINCK, T., ELLISMAN, M., JOHNSON, R. & KARIN, M. 1999. Abnormal morphogenesis but intact IKK activation in mice lacking the IKKalpha subunit of IkappaB kinase. *Science,* 284**,** 316-20.

HU, Y., BAUD, V., OGA, T., KIM, K. I., YOSHIDA, K. & KARIN, M. 2001. IKKalpha controls formation of the epidermis independently of NF-kappaB. *Nature,* 410**,** 710-4.

HUTTI, J. E., SHEN, R. R., ABBOTT, D. W., ZHOU, A. Y., SPROTT, K. M., ASARA, J. M., HAHN, W. C. & CANTLEY, L. C. 2009. Phosphorylation of the tumor suppressor CYLD by the breast cancer oncogene IKKepsilon promotes cell transformation. *Mol Cell,* 34**,** 461-72.

HUYNH, K. D., FISCHLE, W., VERDIN, E. & BARDWELL, V. J. 2000. BCoR, a novel corepressor involved in BCL-6 repression. *Genes Dev,* 14**,** 1810-23.

HYMAN, D. M., SMYTH, L. M., DONOGHUE, M. T. A., WESTIN, S. N., BEDARD, P. L., DEAN, E. J., BANDO, H., EL-KHOUEIRY, A. B., PEREZ-FIDALGO, J. A., MITA, A., SCHELLENS, J. H. M., CHANG, M. T., REICHEL, J. B., BOUVIER, N., SELCUKLU, S. D., SOUMERAI, T. E., TORRISI, J., ERINJERI, J. P., AMBROSE, H., BARRETT, J. C., DOUGHERTY, B., FOXLEY, A., LINDEMANN, J. P. O., MCEWEN, R., PASS, M., SCHIAVON, G., BERGER, M. F., CHANDARLAPATY, S., SOLIT, D. B., BANERJI, U., BASELGA, J. & TAYLOR, B. S. 2017. AKT Inhibition in Solid Tumors With AKT1 Mutations. *J Clin Oncol,* 35**,** 2251-2259.

IMAI, K. & TAKAOKA, A. 2006. Comparing antibody and small-molecule therapies for cancer. *Nat Rev Cancer,* 6**,** 714-27.

ITO, T., ITO, N., SAATHOFF, M., BETTERMANN, A., TAKIGAWA, M. & PAUS, R. 2005. Interferon-gamma is a potent inducer of catagen-like changes in cultured human anagen hair follicles. *Br J Dermatol,* 152**,** 623-31.

JACOBS, J. F., NIERKENS, S., FIGDOR, C. G., DE VRIES, I. J. & ADEMA, G. J. 2012. Regulatory T cells in melanoma: the final hurdle towards effective immunotherapy? *Lancet Oncol,* 13**,** e32-42.

JAFFE, A. E., MURAKAMI, P., LEE, H., LEEK, J. T., FALLIN, M. D., FEINBERG, A. P. & IRIZARRY, R. A. 2012. Bump hunting to identify differentially methylated regions in epigenetic epidemiology studies. *Int J Epidemiol,* 41**,** 200-9.

JELTSCH, K. M., HU, D., BRENNER, S., ZÖLLER, J., HEINZ, G. A., NAGEL, D., VOGEL, K. U., REHAGE, N., WARTH, S. C., EDELMANN, S. L., GLOURY, R., MARTIN, N., LOHS, C., LECH, M., STEHKLEIN, J. E., GEERLOF, A., KREMMER, E., WEBER, A., ANDERS, H.-J., SCHMITZ, I., SCHMIDT-SUPPRIAN, M., FU, M., HOLTMANN, H., KRAPPMANN, D., RULAND, J., KALLIES, A., HEIKENWALDER, M. & HEISSMEYER, V. 2014. Cleavage of roquin and regnase-1 by the paracaspase MALT1 releases their cooperatively repressed targets to promote TH17 differentiation. *Nature Immunology,* 15**,** 1079-1089.

JIA, D., JURKOWSKA, R. Z., ZHANG, X., JELTSCH, A. & CHENG, X. 2007. Structure of Dnmt3a bound to Dnmt3L suggests a model for de novo DNA methylation. *Nature,* 449**,** 248-51.

JIN, W., CHANG, M., PAUL, E. M., BABU, G., LEE, A. J., REILEY, W., WRIGHT, A., ZHANG, M., YOU, J. & SUN, S. C. 2008. Deubiquitinating enzyme CYLD

negatively regulates RANK signaling and osteoclastogenesis in mice. *J Clin Invest,* 118**,** 1858-66.
JIN, W., REILEY, W. R., LEE, A. J., WRIGHT, A., WU, X., ZHANG, M. & SUN, S. C. 2007. Deubiquitinating enzyme CYLD regulates the peripheral development and naive phenotype maintenance of B cells. *J Biol Chem,* 282**,** 15884-93.
JIN, Y. J., WANG, S., CHO, J., SELIM, M. A., WRIGHT, T., MOSIALOS, G. & ZHANG, J. Y. 2016. Epidermal CYLD inactivation sensitizes mice to the development of sebaceous and basaloid skin tumors. *JCI Insight,* 1.
JOHNSON, S. C. & BENNETT, R. G. 1993. Occurrence of basal cell carcinoma among multiple trichoepitheliomas. *J Am Acad Dermatol,* 28**,** 322-6.
JONO, H., LIM, J. H., CHEN, L. F., XU, H., TROMPOUKI, E., PAN, Z. K., MOSIALOS, G. & LI, J. D. 2004. NF-kappaB is essential for induction of CYLD, the negative regulator of NF-kappaB: evidence for a novel inducible autoregulatory feedback pathway. *J Biol Chem,* 279**,** 36171-4.
JUNCO, SARAH E., WANG, R., GAIPA, JOHN C., TAYLOR, ALEXANDER B., SCHIRF, V., GEARHART, MICAH D., BARDWELL, VIVIAN J., DEMELER, B., HART, P. J. & KIM, CHONGWOO A. 2013. Structure of the Polycomb Group Protein PCGF1 in Complex with BCOR Reveals Basis for Binding Selectivity of PCGF Homologs. *Structure,* 21**,** 665-671.
JUNGEHULSING, M., WAGNER, M. & DAMM, M. 1999. Turban tumour with involvement of the parotid gland. *J Laryngol Otol,* 113**,** 779-83.
KALLAM, A. R., SATYANARAYANA, M. A., ARYASOMAYAJULA, S. & KRISHNA, B. A. 2016. Basal Cell Carcinoma Developing from Trichoepithelioma: Review of Three Cases. *J Clin Diagn Res,* 10**,** PD17-9.
KANITAKIS, J., ZAMBRUNO, G., VIAC, J., PANZINI, H. & THIVOLET, J. 1987. Expression of neural-tissue markers (S-100 protein and Leu-7 antigen) by sweat gland tumors of the skin. An immunohistochemical study. *J Am Acad Dermatol,* 17**,** 187-91.
KARATZAS, D. N., XANTHOPOULOS, K., KOTANTAKI, P., PSEFTOGAS, A., TELIOUSIS, K., HATZIVASSILIOU, E. G., KONTOYIANNIS, D. L., POUTAHIDIS, T. & MOSIALOS, G. 2016. Inactivation of CYLD in intestinal epithelial cells exacerbates colitis-associated colorectal carcinogenesis - a short report. *Cell Oncol (Dordr),* 39**,** 287-93.
KAZAKOV, D. V., ZELGER, B., RUTTEN, A., VAZMITEL, M., SPAGNOLO, D. V., KACEROVSKA, D., VANECEK, T., GROSSMANN, P., SIMA, R., GRAYSON, W., CALONJE, E., KOREN, J., MUKENSNABL, P., DANIS, D. & MICHAL, M. 2009. Morphologic diversity of malignant neoplasms arising in preexisting spiradenoma, cylindroma, and spiradenocylindroma based on the study of 24 cases, sporadic or occurring in the setting of Brooke-Spiegler syndrome. *Am J Surg Pathol,* 33**,** 705-19.
KEL, A. E., GOSSLING, E., REUTER, I., CHEREMUSHKIN, E., KEL-MARGOULIS, O. V. & WINGENDER, E. 2003. MATCH: A tool for searching transcription factor binding sites in DNA sequences. *Nucleic Acids Res,* 31**,** 3576-9.
KELLY, M. J., SO, J., ROGERS, A. J., GREGORY, G., LI, J., ZETHOVEN, M., GEARHART, M. D., BARDWELL, V. J., JOHNSTONE, R. W., VERVOORT, S. J. & KATS, L. M. 2019. Bcor loss perturbs myeloid differentiation and promotes leukaemogenesis. *Nature Communications,* 10**,** 1347.
KENT, W. J., SUGNET, C. W., FUREY, T. S., ROSKIN, K. M., PRINGLE, T. H., ZAHLER, A. M. & HAUSSLER, D. 2002. The human genome browser at UCSC. *Genome Res,* 12**,** 996-1006.

KERKELÄ, E. & SAARIALHO-KERE, U. 2003. Matrix metalloproteinases in tumor progression: focus on basal and squamous cell skin cancer. *Experimental Dermatology,* 12**,** 109-125.

KIM, D., PERTEA, G., TRAPNELL, C., PIMENTEL, H., KELLEY, R. & SALZBERG, S. L. 2013a. TopHat2: accurate alignment of transcriptomes in the presence of insertions, deletions and gene fusions. *Genome Biol,* 14**,** R36.

KIM, S. J., ZHAO, H., HARDIKAR, S., SINGH, A. K., GOODELL, M. A. & CHEN, T. 2013b. A DNMT3A mutation common in AML exhibits dominant-negative effects in murine ES cells. *Blood,* 122**,** 4086-4089.

KLEI, L. R., HU, D., PANEK, R., ALFANO, D. N., BRIDWELL, R. E., BAILEY, K. M., ORAVECZ-WILSON, K. I., CONCEL, V. J., HESS, E. M., VAN BEEK, M., DELEKTA, P. C., GU, S., WATKINS, S. C., TING, A. T., GOUGH, P. J., FOLEY, K. P., BERTIN, J., MCALLISTER-LUCAS, L. M. & LUCAS, P. C. 2016. MALT1 Protease Activation Triggers Acute Disruption of Endothelial Barrier Integrity via CYLD Cleavage. *Cell Rep,* 17**,** 221-232.

KNEE, D. A., HEWES, B. & BROGDON, J. L. 2016. Rationale for anti-GITR cancer immunotherapy. *Eur J Cancer,* 67**,** 1-10.

KNUDSON, A. G. 2001. Two genetic hits (more or less) to cancer. *Nat Rev Cancer,* 1**,** 157-62.

KNUPPEL, R., DIETZE, P., LEHNBERG, W., FRECH, K. & WINGENDER, E. 1994. TRANSFAC retrieval program: a network model database of eukaryotic transcription regulating sequences and proteins. *J Comput Biol,* 1**,** 191-8.

KOMANDER, D., LORD, C. J., SCHEEL, H., SWIFT, S., HOFMANN, K., ASHWORTH, A. & BARFORD, D. 2008. The structure of the CYLD USP domain explains its specificity for Lys63-linked polyubiquitin and reveals a B box module. *Mol Cell,* 29**,** 451-64.

KOMANDER, D. & RAPE, M. 2012. The ubiquitin code. *Annu Rev Biochem,* 81**,** 203-29.

KOMI, D. E. A. & REDEGELD, F. A. 2020. Role of Mast Cells in Shaping the Tumor Microenvironment. *Clin Rev Allergy Immunol,* 58**,** 313-325.

KOO, B. K., YOON, M. J., YOON, K. J., IM, S. K., KIM, Y. Y., KIM, C. H., SUH, P. G., JAN, Y. N. & KONG, Y. Y. 2007. An obligatory role of mind bomb-1 in notch signaling of mammalian development. *PLoS One,* 2**,** e1221.

KOPAN, R. & WEINTRAUB, H. 1993. Mouse notch: expression in hair follicles correlates with cell fate determination. *J Cell Biol,* 121**,** 631-41.

KOVALENKO, A., CHABLE-BESSIA, C., CANTARELLA, G., ISRAEL, A., WALLACH, D. & COURTOIS, G. 2003. The tumour suppressor CYLD negatively regulates NF-kappaB signalling by deubiquitination. *Nature,* 424**,** 801-5.

KRAMER, A., GREEN, J., POLLARD, J., JR. & TUGENDREICH, S. 2014. Causal analysis approaches in Ingenuity Pathway Analysis. *Bioinformatics,* 30**,** 523-30.

KRAPPMANN, D. & SCHEIDEREIT, C. 2005. A pervasive role of ubiquitin conjugation in activation and termination of IkappaB kinase pathways. *EMBO Rep,* 6**,** 321-6.

KUMAR, A., EBY, M. T., SINHA, S., JASMIN, A. & CHAUDHARY, P. M. 2001. The ectodermal dysplasia receptor activates the nuclear factor-kappaB, JNK, and cell death pathways and binds to ectodysplasin A. *J Biol Chem,* 276**,** 2668-77.

KUPKA, S., DE MIGUEL, D., DRABER, P., MARTINO, L., SURINOVA, S., RITTINGER, K. & WALCZAK, H. 2016. SPATA2-Mediated Binding of CYLD to HOIP Enables CYLD Recruitment to Signaling Complexes. *Cell Rep,* 16**,** 2271-80.

KUROSAKI, T., POPP, M. W. & MAQUAT, L. E. 2019. Quality and quantity control of gene expression by nonsense-mediated mRNA decay. *Nature Reviews Molecular Cell Biology,* 20**,** 406-420.

KUTSCHER, L. M., OKONECHNIKOV, K., BATORA, N. V., CLARK, J., SILVA, P. B. G., VOURI, M., VAN RIJN, S., SIEBER, L., STATZ, B., GEARHART, M. D., SHIRAISHI, R., MACK, N., ORR, B. A., KORSHUNOV, A., GUDENAS, B. L., SMITH, K. S., MERCIER, A. L., AYRAULT, O., HOSHINO, M., KOOL, M., VON HOFF, K., GRAF, N., FLEISCHHACK, G., BARDWELL, V. J., PFISTER, S. M., NORTHCOTT, P. A. & KAWAUCHI, D. 2020. Functional loss of a noncanonical BCOR-PRC1.1 complex accelerates SHH-driven medulloblastoma formation. *Genes Dev,* 34**,** 1161-1176.

KWACK, M. H., AHN, J. S., JANG, J. H., KIM, J. C., SUNG, Y. K. & KIM, M. K. 2016. SFRP2 augments Wnt/β-catenin signalling in cultured dermal papilla cells. *Experimental Dermatology,* 25**,** 813-815.

KWON, B., YU, K. Y., NI, J., YU, G. L., JANG, I. K., KIM, Y. J., XING, L., LIU, D., WANG, S. X. & KWON, B. S. 1999. Identification of a novel activation-inducible protein of the tumor necrosis factor receptor superfamily and its ligand. *J Biol Chem,* 274**,** 6056-61.

LAMBERTI, C., LIN, K. M., YAMAMOTO, Y., VERMA, U., VERMA, I. M., BYERS, S. & GAYNOR, R. B. 2001. Regulation of beta-catenin function by the IkappaB kinases. *J Biol Chem,* 276**,** 42276-86.

LANGBEIN, L., ROGERS, M. A., PRAETZEL, S., CRIBIER, B., PELTRE, B., GASSLER, N. & SCHWEIZER, J. 2005. Characterization of a novel human type II epithelial keratin K1b, specifically expressed in eccrine sweat glands. *J Invest Dermatol,* 125**,** 428-44.

LAURIKKALA, J., PISPA, J., JUNG, H. S., NIEMINEN, P., MIKKOLA, M., WANG, X., SAARIALHO-KERE, U., GALCERAN, J., GROSSCHEDL, R. & THESLEFF, I. 2002. Regulation of hair follicle development by the TNF signal ectodysplasin and its receptor Edar. *Development,* 129**,** 2541-53.

LAW, C. W., CHEN, Y., SHI, W. & SMYTH, G. K. 2014. voom: precision weights unlock linear model analysis tools for RNA-seq read counts. *Genome Biology,* 15**,** R29.

LEE, J., HYEON, D. Y. & HWANG, D. 2020. Single-cell multiomics: technologies and data analysis methods. *Experimental & Molecular Medicine,* 52**,** 1428-1442.

LEE, S. Y., REICHLIN, A., SANTANA, A., SOKOL, K. A., NUSSENZWEIG, M. C. & CHOI, Y. 1997. TRAF2 is essential for JNK but not NF-kappaB activation and regulates lymphocyte proliferation and survival. *Immunity,* 7**,** 703-13.

LEFEBVRE, S., FLINIAUX, I., SCHNEIDER, P. & MIKKOLA, M. L. 2012. Identification of ectodysplasin target genes reveals the involvement of chemokines in hair development. *J Invest Dermatol,* 132**,** 1094-102.

LEHMAN, T. A., MODALI, R., BOUKAMP, P., STANEK, J., BENNETT, W. P., WELSH, J. A., METCALF, R. A., STAMPFER, M. R., FUSENIG, N., ROGAN, E. M. & ET AL. 1993. p53 mutations in human immortalized epithelial cell lines. *Carcinogenesis,* 14**,** 833-9.

LEONARD, N., CHAGGAR, R., JONES, C., TAKAHASHI, M., NIKITOPOULOU, A. & LAKHANI, S. R. 2001. Loss of heterozygosity at cylindromatosis gene locus, CYLD, in sporadic skin adnexal tumours. *J Clin Pathol,* 54**,** 689-92.

LEONHARDT, H., PAGE, A. W., WEIER, H. U. & BESTOR, T. H. 1992. A targeting sequence directs DNA methyltransferase to sites of DNA replication in mammalian nuclei. *Cell,* 71**,** 865-73.

LI, N., LIU, S., ZHANG, H.-S., DENG, Z.-L., ZHAO, H.-S., ZHAO, Q., LEI, X.-H., NING, L.-N., CAO, Y.-J., WANG, H.-B., LIU, S. & DUAN, E.-K. 2016. Exogenous R-Spondin1 Induces Precocious Telogen-to-Anagen Transition in Mouse Hair Follicles. *International journal of molecular sciences,* 17**,** 582.

LI, Q., LU, Q., HWANG, J. Y., BUSCHER, D., LEE, K. F., IZPISUA-BELMONTE, J. C. & VERMA, I. M. 1999. IKK1-deficient mice exhibit abnormal development of skin and skeleton. *Genes Dev,* 13**,** 1322-8.

LI, S., ZHOU, J., BU, J., NING, K., ZHANG, L., LI, J., GUO, Y., HE, X., HE, H., CAI, X., CHEN, Y., REINACH, P. S., LIU, Z. & LI, W. 2017. Ectodysplasin A protein promotes corneal epithelial cell proliferation. *The Journal of biological chemistry,* 292**,** 13391-13401.

LI, Y.-H., ZHANG, K., YANG, K., YE, J.-X., XING, Y.-Z., GUO, H.-Y., DENG, F., LIAN, X.-H. & YANG, T. 2013. Adenovirus-Mediated Wnt10b Overexpression Induces Hair Follicle Regeneration. *Journal of Investigative Dermatology,* 133**,** 42-48.

LIANG, C., ZHANG, M. & SUN, S. C. 2006. beta-TrCP binding and processing of NF-kappaB2/p100 involve its phosphorylation at serines 866 and 870. *Cell Signal,* 18**,** 1309-17.

LIM, J. H., JONO, H., KOMATSU, K., WOO, C. H., LEE, J., MIYATA, M., MATSUNO, T., XU, X., HUANG, Y., ZHANG, W., PARK, S. H., KIM, Y. I., CHOI, Y. D., SHEN, H., HEO, K. S., XU, H., BOURNE, P., KOGA, T., XU, H., YAN, C., WANG, B., CHEN, L. F., FENG, X. H. & LI, J. D. 2012. CYLD negatively regulates transforming growth factor-beta-signalling via deubiquitinating Akt. *Nat Commun,* 3**,** 771.

LIPPENS, S., LEFEBVRE, S., GILBERT, B., SZE, M., DEVOS, M., VERHELST, K., VEREECKE, L., MC GUIRE, C., GUÉRIN, C., VANDENABEELE, P., PASPARAKIS, M., MIKKOLA, M. L., BEYAERT, R., DECLERCQ, W. & VAN LOO, G. 2011. Keratinocyte-specific ablation of the NF-κB regulatory protein A20 (TNFAIP3) reveals a role in the control of epidermal homeostasis. *Cell death and differentiation,* 18**,** 1845-1853.

LO, P.-K. & ZHOU, Q. 2018. Emerging techniques in single-cell epigenomics and their applications to cancer research. *Journal of clinical genomics,* 1**,** 10.4172/JCG.1000103.

LORENZ, V. N., SCHON, M. P. & SEITZ, C. S. 2016. c-Rel in Epidermal Homeostasis: A Spotlight on c-Rel in Cell Cycle Regulation. *J Invest Dermatol,* 136**,** 1090-6.

LORK, M., VERHELST, K. & BEYAERT, R. 2017. CYLD, A20 and OTULIN deubiquitinases in NF-kappaB signaling and cell death: so similar, yet so different. *Cell Death Differ,* 24**,** 1172-1183.

LOVE, M. I., HUBER, W. & ANDERS, S. 2014. Moderated estimation of fold change and dispersion for RNA-seq data with DESeq2. *Genome Biol,* 15**,** 550.

MANZONI, C., KIA, D. A., VANDROVCOVA, J., HARDY, J., WOOD, N. W., LEWIS, P. A. & FERRARI, R. 2018. Genome, transcriptome and proteome: the rise of omics data and their integration in biomedical sciences. *Briefings in bioinformatics,* 19**,** 286-302.

MASSOUMI, R., CHMIELARSKA, K., HENNECKE, K., PFEIFER, A. & FASSLER, R. 2006a. Cyld inhibits tumor cell proliferation by blocking Bcl-3-dependent NF-kappaB signaling. *Cell,* 125**,** 665-77.

MASSOUMI, R., KUPHAL, S., HELLERBRAND, C., HAAS, B., WILD, P., SPRUSS, T., PFEIFER, A., FASSLER, R. & BOSSERHOFF, A. K. 2009. Down-

regulation of CYLD expression by Snail promotes tumor progression in malignant melanoma. *J Exp Med,* 206**,** 221-32.
MASSOUMI, R., PODDA, M., FASSLER, R. & PAUS, R. 2006b. Cylindroma as tumor of hair follicle origin. *J Invest Dermatol,* 126**,** 1182-4.
MEYBEHM, M. & FISCHER, H. P. 1997. Spiradenoma and dermal cylindroma: comparative immunohistochemical analysis and histogenetic considerations. *Am J Dermatopathol,* 19**,** 154-61.
MICHAL M, L. J., MUKENSNABL P, PIZINGER K. 1999. Spiradenocylindromas of the skin: tumors with morphological features of spiradenoma and cylindroma in the same lesion: report of 12 cases. . *Pathology International,* 49**,** 419-425.
MIELE, L. 2006. Notch signaling. *Clin Cancer Res,* 12**,** 1074-9.
MILIANI DE MARVAL, P., LUTFEALI, S., JIN, J. Y., LESHIN, B., SELIM, M. A. & ZHANG, J. Y. 2011. CYLD inhibits tumorigenesis and metastasis by blocking JNK/AP1 signaling at multiple levels. *Cancer Prev Res (Phila),* 4**,** 851-9.
MOLL, R., DIVO, M. & LANGBEIN, L. 2008. The human keratins: biology and pathology. *Histochem Cell Biol,* 129**,** 705-33.
MORITA, K., WANG, F., JAHN, K., HU, T., TANAKA, T., SASAKI, Y., KUIPERS, J., LOGHAVI, S., WANG, S. A., YAN, Y., FURUDATE, K., MATTHEWS, J., LITTLE, L., GUMBS, C., ZHANG, J., SONG, X., THOMPSON, E., PATEL, K. P., BUESO-RAMOS, C. E., DINARDO, C. D., RAVANDI, F., JABBOUR, E., ANDREEFF, M., CORTES, J., BHALLA, K., GARCIA-MANERO, G., KANTARJIAN, H., KONOPLEVA, M., NAKADA, D., NAVIN, N., BEERENWINKEL, N., FUTREAL, P. A. & TAKAHASHI, K. 2020. Clonal evolution of acute myeloid leukemia revealed by high-throughput single-cell genomics. *Nature communications,* 11**,** 5327-5327.
MORLON, A., MUNNICH, A. & SMAHI, A. 2005. TAB2, TRAF6 and TAK1 are involved in NF-kappaB activation induced by the TNF-receptor, Edar and its adaptator Edaradd. *Hum Mol Genet,* 14**,** 3751-7.
MOU, C., JACKSON, B., SCHNEIDER, P., OVERBEEK, P. A. & HEADON, D. J. 2006. Generation of the primary hair follicle pattern. *Proceedings of the National Academy of Sciences of the United States of America,* 103**,** 9075-9080.
MUSTONEN, T., PISPA, J., MIKKOLA, M. L., PUMMILA, M., KANGAS, A. T., PAKKASJÄRVI, L., JAATINEN, R. & THESLEFF, I. 2003. Stimulation of ectodermal organ development by Ectodysplasin-A1. *Developmental Biology,* 259**,** 123-136.
NAGY, N., FARKAS, K., KEMENY, L. & SZELL, M. 2015. Phenotype-genotype correlations for clinical variants caused by CYLD mutations. *Eur J Med Genet,* 58**,** 271-8.
NAITO, A., YOSHIDA, H., NISHIOKA, E., SATOH, M., AZUMA, S., YAMAMOTO, T., NISHIKAWA, S.-I. & INOUE, J.-I. 2002. TRAF6-deficient mice display hypohidrotic ectodermal dysplasia. *Proceedings of the National Academy of Sciences,* 99**,** 8766-8771.
NALLANTHIGHAL, S., HEISERMAN, J. P. & CHEON, D.-J. 2019. The Role of the Extracellular Matrix in Cancer Stemness. *Frontiers in Cell and Developmental Biology,* 7.
NEWMAN, A. M., LIU, C. L., GREEN, M. R., GENTLES, A. J., FENG, W., XU, Y., HOANG, C. D., DIEHN, M. & ALIZADEH, A. A. 2015. Robust enumeration of cell subsets from tissue expression profiles. *Nat Methods,* 12**,** 453-7.
NG, D., THAKKER, N., CORCORAN, C. M., DONNAI, D., PERVEEN, R., SCHNEIDER, A., HADLEY, D. W., TIFFT, C., ZHANG, L., WILKIE, A. O. M.,

VAN DER SMAGT, J. J., GORLIN, R. J., BURGESS, S. M., BARDWELL, V. J., BLACK, G. C. M. & BIESECKER, L. G. 2004. Oculofaciocardiodental and Lenz microphthalmia syndromes result from distinct classes of mutations in BCOR. *Nature Genetics,* 36**,** 411-416.

NGUYEN, L. S., WILKINSON, M. F. & GECZ, J. 2014. Nonsense-mediated mRNA decay: inter-individual variability and human disease. *Neurosci Biobehav Rev,* 46 Pt 2**,** 175-86.

NI, F., ZHAO, H., CUI, H., WU, Z., CHEN, L., HU, Z., GUO, C., LIU, Y., CHEN, Z., WANG, X., CHEN, D., WEI, H. & WANG, S. 2015. MicroRNA-362-5p promotes tumor growth and metastasis by targeting CYLD in hepatocellular carcinoma. *Cancer Lett,* 356**,** 809-18.

NICKOLOFF, B. J., QIN, J. Z., CHATURVEDI, V., DENNING, M. F., BONISH, B. & MIELE, L. 2002. Jagged-1 mediated activation of notch signaling induces complete maturation of human keratinocytes through NF-kappaB and PPARgamma. *Cell Death Differ,* 9**,** 842-55.

NIK-ZAINAL, S., DAVIES, H., STAAF, J., RAMAKRISHNA, M., GLODZIK, D., ZOU, X., MARTINCORENA, I., ALEXANDROV, L. B., MARTIN, S., WEDGE, D. C., VAN LOO, P., JU, Y. S., SMID, M., BRINKMAN, A. B., MORGANELLA, S., AURE, M. R., LINGJAERDE, O. C., LANGEROD, A., RINGNER, M., AHN, S. M., BOYAULT, S., BROCK, J. E., BROEKS, A., BUTLER, A., DESMEDT, C., DIRIX, L., DRONOV, S., FATIMA, A., FOEKENS, J. A., GERSTUNG, M., HOOIJER, G. K., JANG, S. J., JONES, D. R., KIM, H. Y., KING, T. A., KRISHNAMURTHY, S., LEE, H. J., LEE, J. Y., LI, Y., MCLAREN, S., MENZIES, A., MUSTONEN, V., O'MEARA, S., PAUPORTE, I., PIVOT, X., PURDIE, C. A., RAINE, K., RAMAKRISHNAN, K., RODRIGUEZ-GONZALEZ, F. G., ROMIEU, G., SIEUWERTS, A. M., SIMPSON, P. T., SHEPHERD, R., STEBBINGS, L., STEFANSSON, O. A., TEAGUE, J., TOMMASI, S., TREILLEUX, I., VAN DEN EYNDEN, G. G., VERMEULEN, P., VINCENT-SALOMON, A., YATES, L., CALDAS, C., VAN'T VEER, L., TUTT, A., KNAPPSKOG, S., TAN, B. K., JONKERS, J., BORG, A., UENO, N. T., SOTIRIOU, C., VIARI, A., FUTREAL, P. A., CAMPBELL, P. J., SPAN, P. N., VAN LAERE, S., LAKHANI, S. R., EYFJORD, J. E., THOMPSON, A. M., BIRNEY, E., STUNNENBERG, H. G., VAN DE VIJVER, M. J., MARTENS, J. W., BORRESEN-DALE, A. L., RICHARDSON, A. L., KONG, G., THOMAS, G. & STRATTON, M. R. 2016. Landscape of somatic mutations in 560 breast cancer whole-genome sequences. *Nature,* 534**,** 47-54.

NIKOLAOU, K., TSAGARATOU, A., EFTYCHI, C., KOLLIAS, G., MOSIALOS, G. & TALIANIDIS, I. 2012. Inactivation of the deubiquitinase CYLD in hepatocytes causes apoptosis, inflammation, fibrosis, and cancer. *Cancer Cell,* 21**,** 738-50.

O'DONNELL, M. A., PEREZ-JIMENEZ, E., OBERST, A., NG, A., MASSOUMI, R., XAVIER, R., GREEN, D. R. & TING, A. T. 2011. Caspase 8 inhibits programmed necrosis by processing CYLD. *Nat Cell Biol,* 13**,** 1437-42.

O'REILLY, S., CANT, R., CIECHOMSKA, M., FINNIGAN, J., OAKLEY, F., HAMBLETON, S. & VAN LAAR, J. M. 2014. Serum amyloid A induces interleukin-6 in dermal fibroblasts via Toll-like receptor 2, interleukin-1 receptor-associated kinase 4 and nuclear factor-κB. *Immunology,* 143**,** 331-340.

OKANO, M., BELL, D. W., HABER, D. A. & LI, E. 1999. DNA Methyltransferases Dnmt3a and Dnmt3b Are Essential for De Novo Methylation and Mammalian Development. *Cell,* 99**,** 247-257.

OKANO, M., XIE, S. & LI, E. 1998. Cloning and characterization of a family of novel mammalian DNA (cytosine-5) methyltransferases. *Nature Genetics,* 19**,** 219-220.

OLDFORD, S. A. & MARSHALL, J. S. 2015. Mast cells as targets for immunotherapy of solid tumors. *Molecular Immunology,* 63**,** 113-124.

OOI, S. K., QIU, C., BERNSTEIN, E., LI, K., JIA, D., YANG, Z., ERDJUMENT-BROMAGE, H., TEMPST, P., LIN, S. P., ALLIS, C. D., CHENG, X. & BESTOR, T. H. 2007. DNMT3L connects unmethylated lysine 4 of histone H3 to de novo methylation of DNA. *Nature,* 448**,** 714-7.

OOSTERKAMP, H. M., NEERING, H., NIJMAN, S. M., DIRAC, A. M., MOOI, W. J., BERNARDS, R. & BRUMMELKAMP, T. R. 2006. An evaluation of the efficacy of topical application of salicylic acid for the treatment of familial cylindromatosis. *Br J Dermatol,* 155**,** 182-5.

PANNEM, R. R., DORN, C., AHLQVIST, K., BOSSERHOFF, A. K., HELLERBRAND, C. & MASSOUMI, R. 2014. CYLD controls c-MYC expression through the JNK-dependent signaling pathway in hepatocellular carcinoma. *Carcinogenesis,* 35**,** 461-8.

PARK, S. G., CHUNG, C., KANG, H., KIM, J. Y. & JUNG, G. 2006. Up-regulation of cyclin D1 by HBx is mediated by NF-kappaB2/BCL3 complex through kappaB site of cyclin D1 promoter. *J Biol Chem,* 281**,** 31770-7.

PASPARAKIS, M., COURTOIS, G., HAFNER, M., SCHMIDT-SUPPRIAN, M., NENCI, A., TOKSOY, A., KRAMPERT, M., GOEBELER, M., GILLITZER, R., ISRAEL, A., KRIEG, T., RAJEWSKY, K. & HAASE, I. 2002. TNF-mediated inflammatory skin disease in mice with epidermis-specific deletion of IKK2. *Nature,* 417**,** 861-6.

PENNEYS, N. S. & KAISER, M. 1993. Cylindroma expresses immunohistochemical markers linking it to eccrine coil. *Journal of Cutaneous Pathology,* 20**,** 40-43.

PETERS, E. M., STIEGLITZ, M. G., LIEZMAN, C., OVERALL, R. W., NAKAMURA, M., HAGEN, E., KLAPP, B. F., ARCK, P. & PAUS, R. 2006. p75 Neurotrophin Receptor-Mediated Signaling Promotes Human Hair Follicle Regression (Catagen). *Am J Pathol,* 168**,** 221-34.

PETERS, E. M. J., HANDJISKI, B., KUHLMEI, A., HAGEN, E., BIELAS, H., BRAUN, A., KLAPP, B. F., PAUS, R. & ARCK, P. C. 2004. Neurogenic inflammation in stress-induced termination of murine hair growth is promoted by nerve growth factor. *The American journal of pathology,* 165**,** 259-271.

PFALTZ, M., BRUCKNER-TUDERMAN, L. & SCHNYDER, U. W. 1989. Type VII collagen is a component of cylindroma basement membrane zone. *J Cutan Pathol,* 16**,** 388-95.

PIDSLEY, R., ZOTENKO, E., PETERS, T. J., LAWRENCE, M. G., RISBRIDGER, G. P., MOLLOY, P., VAN DJIK, S., MUHLHAUSLER, B., STIRZAKER, C. & CLARK, S. J. 2016. Critical evaluation of the Illumina MethylationEPIC BeadChip microarray for whole-genome DNA methylation profiling. *Genome Biology,* 17**,** 208.

PORTELA, A. & ESTELLER, M. 2010. Epigenetic modifications and human disease. *Nature Biotechnology,* 28**,** 1057-1068.

PUI, J. C., ALLMAN, D., XU, L., DEROCCO, S., KARNELL, F. G., BAKKOUR, S., LEE, J. Y., KADESCH, T., HARDY, R. R., ASTER, J. C. & PEAR, W. S. 1999. Notch1 expression in early lymphopoiesis influences B versus T lineage determination. *Immunity,* 11**,** 299-308.

R CORE TEAM 2019. R: A language and environment for statistical computing. Vienna, Austria.

RAHIGHI, S., IKEDA, F., KAWASAKI, M., AKUTSU, M., SUZUKI, N., KATO, R., KENSCHE, T., UEJIMA, T., BLOOR, S., KOMANDER, D., RANDOW, F., WAKATSUKI, S. & DIKIC, I. 2009. Specific recognition of linear ubiquitin chains by NEMO is important for NF-kappaB activation. *Cell,* 136**,** 1098-109.

RAINE, K. M., VAN LOO, P., WEDGE, D. C., JONES, D., MENZIES, A., BUTLER, A. P., TEAGUE, J. W., TARPEY, P., NIK-ZAINAL, S. & CAMPBELL, P. J. 2016. ascatNgs: Identifying Somatically Acquired Copy-Number Alterations from Whole-Genome Sequencing Data. *Curr Protoc Bioinformatics,* 56**,** 15 9 1-15 9 17.

RAJAN, N., ANDERSSON, M. K., SINCLAIR, N., FEHR, A., HODGSON, K., LORD, C. J., KAZAKOV, D. V., VANECEK, T., ASHWORTH, A. & STENMAN, G. 2016. Overexpression of MYB drives proliferation of CYLD-defective cylindroma cells. *J Pathol,* 239**,** 197-205.

RAJAN, N. & ASHWORTH, A. 2015. Inherited cylindromas: lessons from a rare tumour. *Lancet Oncol,* 16**,** e460-e469.

RAJAN, N., BURN, J., LANGTRY, J., SIEBER-BLUM, M., LORD, C. J. & ASHWORTH, A. 2011a. Transition from cylindroma to spiradenoma in CYLD-defective tumours is associated with reduced DKK2 expression. *J Pathol,* 224**,** 309-21.

RAJAN, N., ELLIOTT, R., CLEWES, O., MACKAY, A., REIS-FILHO, J. S., BURN, J., LANGTRY, J., SIEBER-BLUM, M., LORD, C. J. & ASHWORTH, A. 2011b. Dysregulated TRK signalling is a therapeutic target in CYLD defective tumours. *Oncogene,* 30**,** 4243-60.

RAJAN, N., ELLIOTT, R. J., SMITH, A., SINCLAIR, N., SWIFT, S., LORD, C. J. & ASHWORTH, A. 2014. The cylindromatosis gene product, CYLD, interacts with MIB2 to regulate notch signalling. *Oncotarget,* 5**,** 12126-40.

RAJAN, N., LANGTRY, J. A., ASHWORTH, A., ROBERTS, C., CHAPMAN, P., BURN, J. & TRAINER, A. H. 2009. Tumor mapping in 2 large multigenerational families with CYLD mutations: implications for disease management and tumor induction. *Arch Dermatol,* 145**,** 1277-84.

RAMADASS, V., VAIYAPURI, T. & TERGAONKAR, V. 2020. Small Molecule NF-κB Pathway Inhibitors in Clinic. *International journal of molecular sciences,* 21**,** 5164.

RAMSAY, R. G. 2005. c-Myb a stem-progenitor cell regulator in multiple tissue compartments. *Growth Factors,* 23**,** 253-61.

RAMSAY, R. G. & GONDA, T. J. 2008. MYB function in normal and cancer cells. *Nat Rev Cancer,* 8**,** 523-34.

RAPE, M. 2017. Ubiquitylation at the crossroads of development and disease. *Nat Rev Mol Cell Biol*.

RASHID, M., VAN DER HORST, M., MENTZEL, T., BUTERA, F., FERREIRA, I., PANCE, A., RUTTEN, A., LUZAR, B., MARUSIC, Z., DE SAINT AUBAIN, N., KO, J. S., BILLINGS, S. D., CHEN, S., ABI DAOUD, M., HEWINSON, J., LOUZADA, S., HARMS, P. W., CERRETELLI, G., ROBLES-ESPINOZA, C. D., PATEL, R. M., VAN DER WEYDEN, L., BAKAL, C., HORNICK, J. L., ARENDS, M. J., BRENN, T. & ADAMS, D. J. 2019. ALPK1 hotspot mutation as a driver of human spiradenoma and spiradenocarcinoma. *Nat Commun,* 10**,** 2213.

RAUDVERE, U., KOLBERG, L., KUZMIN, I., ARAK, T., ADLER, P., PETERSON, H. & VILO, J. 2019. g:Profiler: a web server for functional enrichment analysis and conversions of gene lists (2019 update). *Nucleic Acids Research,* 47**,** W191-W198.

REILEY, W., ZHANG, M. & SUN, S. C. 2004. Negative regulation of JNK signaling by the tumor suppressor CYLD. *J Biol Chem,* 279**,** 55161-7.

REILEY, W., ZHANG, M., WU, X., GRANGER, E. & SUN, S. C. 2005. Regulation of the deubiquitinating enzyme CYLD by IkappaB kinase gamma-dependent phosphorylation. *Mol Cell Biol,* 2*5***,** 3886-95.

REILEY, W. W., JIN, W., LEE, A. J., WRIGHT, A., WU, X., TEWALT, E. F., LEONARD, T. O., NORBURY, C. C., FITZPATRICK, L., ZHANG, M. & SUN, S.-C. 2007a. Deubiquitinating enzyme CYLD negatively regulates the ubiquitin-dependent kinase Tak1 and prevents abnormal T cell responses. *The Journal of experimental medicine,* 204**,** 1475-1485.

REILEY, W. W., JIN, W., LEE, A. J., WRIGHT, A., WU, X., TEWALT, E. F., LEONARD, T. O., NORBURY, C. C., FITZPATRICK, L., ZHANG, M. & SUN, S. C. 2007b. Deubiquitinating enzyme CYLD negatively regulates the ubiquitin-dependent kinase Tak1 and prevents abnormal T cell responses. *J Exp Med,* 204**,** 1475-85.

REILEY, W. W., ZHANG, M., JIN, W., LOSIEWICZ, M., DONOHUE, K. B., NORBURY, C. C. & SUN, S. C. 2006. Regulation of T cell development by the deubiquitinating enzyme CYLD. *Nat Immunol,* 7**,** 411-7.

RINALDI, L., AVGUSTINOVA, A., MARTIN, M., DATTA, D., SOLANAS, G., PRATS, N. & BENITAH, S. A. 2017. Loss of Dnmt3a and Dnmt3b does not affect epidermal homeostasis but promotes squamous transformation through PPAR-gamma. *Elife,* 6.

RINALDI, L., DATTA, D., SERRAT, J., MOREY, L., SOLANAS, G., AVGUSTINOVA, A., BLANCO, E., PONS, J. I., MATALLANAS, D., VON KRIEGSHEIM, A., DI CROCE, L. & BENITAH, S. A. 2016. Dnmt3a and Dnmt3b Associate with Enhancers to Regulate Human Epidermal Stem Cell Homeostasis. *Cell Stem Cell,* 19**,** 491-501.

RITCHIE, M. E., PHIPSON, B., WU, D., HU, Y., LAW, C. W., SHI, W. & SMYTH, G. K. 2015. limma powers differential expression analyses for RNA-sequencing and microarray studies. *Nucleic Acids Res,* 43**,** e47.

ROBINSON, J. T., THORVALDSDÓTTIR, H., WINCKLER, W., GUTTMAN, M., LANDER, E. S., GETZ, G. & MESIROV, J. P. 2011. Integrative genomics viewer. *Nat Biotechnol,* 29**,** 24-6.

ROBINSON, M. D., MCCARTHY, D. J. & SMYTH, G. K. 2010. edgeR: a Bioconductor package for differential expression analysis of digital gene expression data. *Bioinformatics,* 26**,** 139-40.

ROBINSON, M. D. & OSHLACK, A. 2010. A scaling normalization method for differential expression analysis of RNA-seq data. *Genome Biology,* 11**,** R25.

RODRIGUEZ-MEIRA, A., BUCK, G., CLARK, S.-A., POVINELLI, B. J., ALCOLEA, V., LOUKA, E., MCGOWAN, S., HAMBLIN, A., SOUSOS, N., BARKAS, N., GIUSTACCHINI, A., PSAILA, B., JACOBSEN, S. E. W., THONGJUEA, S. & MEAD, A. J. 2019. Unravelling Intratumoral Heterogeneity through High-Sensitivity Single-Cell Mutational Analysis and Parallel RNA Sequencing. *Molecular cell,* 73**,** 1292-1305.e8.

ROGERS, M. A., WINTER, H., SCHWEIZER, J., LANGBEIN, L. & PRAETZEL, S. 2003. K6irs1, K6irs2, K6irs3, and K6irs4 Represent the Inner-Root-Sheath-Specific Type II Epithelial Keratins of the Human Hair Follicle¹. *Journal of Investigative Dermatology,* 120**,** 512-522.

RONCHESE, F., HILLIGAN, K. L. & MAYER, J. U. 2020. Dendritic cells and the skin environment. *Current Opinion in Immunology,* 64**,** 56-62.

SAITO, K., KIGAWA, T., KOSHIBA, S., SATO, K., MATSUO, Y., SAKAMOTO, A., TAKAGI, T., SHIROUZU, M., YABUKI, T., NUNOKAWA, E., SEKI, E., MATSUDA, T., AOKI, M., MIYATA, Y., HIRAKAWA, N., INOUE, M., TERADA, T., NAGASE, T., KIKUNO, R., NAKAYAMA, M., OHARA, O., TANAKA, A. & YOKOYAMA, S. 2004. The CAP-Gly domain of CYLD associates with the proline-rich sequence in NEMO/IKKgamma. *Structure,* 12**,** 1719-28.

SÁNCHEZ-PAULETE, A. R., TEIJEIRA, A., CUETO, F. J., GARASA, S., PÉREZ-GRACIA, J. L., SÁNCHEZ-ARRÁEZ, A., SANCHO, D. & MELERO, I. 2017. Antigen cross-presentation and T-cell cross-priming in cancer immunology and immunotherapy. *Annals of Oncology,* 28**,** xii44-xii55.

SARKAR, H., MITSIOS, A., SMART, M., SKINNER, J., WELCH, A. A., KALATZIS, V., COFFEY, P. J., DUBIS, A. M., WEBSTER, A. R. & MOOSAJEE, M. 2019. Nonsense-mediated mRNA decay efficiency varies in choroideremia providing a target to boost small molecule therapeutics. *Hum Mol Genet,* 28**,** 1865-1871.

SATO, H., SUZUKI, H., TOYOTA, M., NOJIMA, M., MARUYAMA, R., SASAKI, S., TAKAGI, H., SOGABE, Y., SASAKI, Y., IDOGAWA, M., SONODA, T., MORI, M., IMAI, K., TOKINO, T. & SHINOMURA, Y. 2007. Frequent epigenetic inactivation of DICKKOPF family genes in human gastrointestinal tumors. *Carcinogenesis,* 28**,** 2459-66.

SCHLICHER, L., BRAUNS-SCHUBERT, P., SCHUBERT, F. & MAURER, U. 2017. SPATA2: more than a missing link. *Cell Death Differ,* 24**,** 1142-1147.

SCHLICHER, L., WISSLER, M., PREISS, F., BRAUNS-SCHUBERT, P., JAKOB, C., DUMIT, V., BORNER, C., DENGJEL, J. & MAURER, U. 2016. SPATA2 promotes CYLD activity and regulates TNF-induced NF-kappaB signaling and cell death. *EMBO Rep,* 17**,** 1485-1497.

SCHMIDT-SUPPRIAN, M., BLOCH, W., COURTOIS, G., ADDICKS, K., ISRAEL, A., RAJEWSKY, K. & PASPARAKIS, M. 2000. NEMO/IKK gamma-deficient mice model incontinentia pigmenti. *Mol Cell,* 5**,** 981-92.

SCHMIDT-ULLRICH, R., AEBISCHER, T., HULSKEN, J., BIRCHMEIER, W., KLEMM, U. & SCHEIDEREIT, C. 2001. Requirement of NF-kappaB/Rel for the development of hair follicles and other epidermal appendices. *Development,* 128**,** 3843-53.

SCHRODER, K., HERTZOG, P. J., RAVASI, T. & HUME, D. A. 2004. Interferon-γ: an overview of signals, mechanisms and functions. *Journal of Leukocyte Biology,* 75**,** 163-189.

SCHWALBE, E. C., LINDSEY, J. C., NAKJANG, S., CROSIER, S., SMITH, A. J., HICKS, D., RAFIEE, G., HILL, R. M., ILIASOVA, A., STONE, T., PIZER, B., MICHALSKI, A., JOSHI, A., WHARTON, S. B., JACQUES, T. S., BAILEY, S., WILLIAMSON, D. & CLIFFORD, S. C. 2017. Novel molecular subgroups for clinical classification and outcome prediction in childhood medulloblastoma: a cohort study. *Lancet Oncol,* 18**,** 958-971.

SCOTT, A. R., FAQUIN, W. C. & DESCHLER, D. G. 2010. Parotid mass in a woman with multiple cutaneous cylindromas. *Head & Neck,* 32**,** 684-687.

SELLHEYER, K. 2015. Spiradenoma and cylindroma originate from the hair follicle bulge and not from the eccrine sweat gland: an immunohistochemical study with CD200 and other stem cell markers. *J Cutan Pathol,* 42**,** 90-101.

SEN, R. & BALTIMORE, D. 1986a. Inducibility of kappa immunoglobulin enhancer-binding protein Nf-kappa B by a posttranslational mechanism. *Cell,* 47**,** 921-8.

SEN, R. & BALTIMORE, D. 1986b. Multiple nuclear factors interact with the immunoglobulin enhancer sequences. *Cell,* 46**,** 705-16.

SIMA, J., PIAO, Y., CHEN, Y. & SCHLESSINGER, D. 2016. Molecular dynamics of Dkk4 modulates Wnt action and regulates meibomian gland development. *Development,* 143**,** 4723-4735.

SIMA, J., YAN, Z., CHEN, Y., LEHRMANN, E., ZHANG, Y., NAGARAJA, R., WANG, W., WANG, Z. & SCHLESSINGER, D. 2018. Eda-activated RelB recruits an SWI/SNF (BAF) chromatin-remodeling complex and initiates gene transcription in skin appendage formation. *Proc Natl Acad Sci U S A,* 115**,** 8173-8178.

SISTO, M., BARCA, A., LOFRUMENTO, D. D. & LISI, S. 2016. Downstream activation of NF-κB in the EDA-A1/EDAR signalling in Sjögren's syndrome and its regulation by the ubiquitin-editing enzyme A20. *Clin Exp Immunol,* 184**,** 183-96.

SKAPER, S. D. 2012. The neurotrophin family of neurotrophic factors: an overview. *Methods Mol Biol,* 846**,** 1-12.

SMALE, S. T. 2012. Dimer-specific regulatory mechanisms within the NF-kappaB family of transcription factors. *Immunol Rev,* 246**,** 193-204.

SMYTH, L. M., TAMURA, K., OLIVEIRA, M., CIRUELOS, E. M., MAYER, I. A., SABLIN, M. P., BIGANZOLI, L., AMBROSE, H. J., ASHTON, J., BARNICLE, A., CASHELL, D. D., CORCORAN, C., DE BRUIN, E. C., FOXLEY, A., HAUSER, J., LINDEMANN, J. P. O., MAUDSLEY, R., MCEWEN, R., MOSCHETTA, M., PASS, M., ROWLANDS, V., SCHIAVON, G., BANERJI, U., SCALTRITI, M., TAYLOR, B. S., CHANDARLAPATY, S., BASELGA, J. & HYMAN, D. M. 2020. Capivasertib, an AKT Kinase Inhibitor, as Monotherapy or in Combination with Fulvestrant in Patients with AKT1 (E17K)-Mutant, ER-Positive Metastatic Breast Cancer. *Clin Cancer Res,* 26**,** 3947-3957.

SOMASUNDARAM, R., CONNELLY, T., CHOI, R., CHOI, H., SAMARKINA, A., LI, L., GREGORIO, E., CHEN, Y., THAKUR, R., ABDEL-MOHSEN, M., BEQIRI, M., KIERNAN, M., PEREGO, M., WANG, F., XIAO, M., BRAFFORD, P., YANG, X., XU, X., SECRETO, A., DANET-DESNOYERS, G., TRAUM, D., KAESTNER, K. H., HUANG, A. C., HRISTOVA, D., WANG, J., FUKUNAGA-KALABIS, M., KREPLER, C., PING-CHEN, F., ZHOU, X., GUTIERREZ, A., REBECCA, V. W., VONTEDDU, P., DOTIWALA, F., BALA, S., MAJUMDAR, S., DWEEP, H., WICKRAMASINGHE, J., KOSSENKOV, A. V., REYES-ARBUJAS, J., SANTIAGO, K., NGUYEN, T., GRISS, J., KEENEY, F., HAYDEN, J., GAVIN, B. J., WEINER, D., MONTANER, L. J., LIU, Q., PEIFFER, L., BECKER, J., BURTON, E. M., DAVIES, M. A., TETZLAFF, M. T., MUTHUMANI, K., WARGO, J. A., GABRILOVICH, D. & HERLYN, M. 2021. Tumor-infiltrating mast cells are associated with resistance to anti-PD-1 therapy. *Nat Commun,* 12**,** 346.

SRINIVASAN, R. S., ERKENEZ, A. C. D. & HEMENWAY, C. S. 2003. The mixed lineage leukemia fusion partner AF9 binds specific isoforms of the BCL-6 corepressor. *Oncogene,* 22**,** 3395-3406.

SRIVASTAVA, A. K., PISPA, J., HARTUNG, A. J., DU, Y., EZER, S., JENKS, T., SHIMADA, T., PEKKANEN, M., MIKKOLA, M. L., KO, M. S., THESLEFF, I., KERE, J. & SCHLESSINGER, D. 1997. The Tabby phenotype is caused by mutation in a mouse homologue of the EDA gene that reveals novel mouse and human exons and encodes a protein (ectodysplasin-A) with collagenous domains. *Proc Natl Acad Sci U S A,* 94**,** 13069-74.

STAAL, J., DRIEGE, Y., BEKAERT, T., DEMEYER, A., MUYLLAERT, D., VAN DAMME, P., GEVAERT, K. & BEYAERT, R. 2011. T-cell receptor-induced

JNK activation requires proteolytic inactivation of CYLD by MALT1. *EMBO J,* 30**,** 1742-52.

STEEN, C. B., LIU, C. L., ALIZADEH, A. A. & NEWMAN, A. M. 2020. Profiling Cell Type Abundance and Expression in Bulk Tissues with CIBERSORTx. *Methods Mol Biol,* 2117**,** 135-157.

STEENTOFT, C., VAKHRUSHEV, S. Y., JOSHI, H. J., KONG, Y., VESTER-CHRISTENSEN, M. B., SCHJOLDAGER, K. T., LAVRSEN, K., DABELSTEEN, S., PEDERSEN, N. B., MARCOS-SILVA, L., GUPTA, R., BENNETT, E. P., MANDEL, U., BRUNAK, S., WANDALL, H. H., LEVERY, S. B. & CLAUSEN, H. 2013. Precision mapping of the human O-GalNAc glycoproteome through SimpleCell technology. *Embo j,* 32**,** 1478-88.

STEGMEIER, F., SOWA, M. E., NALEPA, G., GYGI, S. P., HARPER, J. W. & ELLEDGE, S. J. 2007. The tumor suppressor CYLD regulates entry into mitosis. *Proc Natl Acad Sci U S A,* 104**,** 8869-74.

STEPHENS, P. J., DAVIES, H. R., MITANI, Y., VAN LOO, P., SHLIEN, A., TARPEY, P. S., PAPAEMMANUIL, E., CHEVERTON, A., BIGNELL, G. R., BUTLER, A. P., GAMBLE, J., GAMBLE, S., HARDY, C., HINTON, J., JIA, M., JAYAKUMAR, A., JONES, D., LATIMER, C., MCLAREN, S., MCBRIDE, D. J., MENZIES, A., MUDIE, L., MADDISON, M., RAINE, K., NIK-ZAINAL, S., O'MEARA, S., TEAGUE, J. W., VARELA, I., WEDGE, D. C., WHITMORE, I., LIPPMAN, S. M., MCDERMOTT, U., STRATTON, M. R., CAMPBELL, P. J., EL-NAGGAR, A. K. & FUTREAL, P. A. 2013. Whole exome sequencing of adenoid cystic carcinoma. *J Clin Invest,* 123**,** 2965-8.

STIRZAKER, C., TABERLAY, P. C., STATHAM, A. L. & CLARK, S. J. 2014. Mining cancer methylomes: prospects and challenges. *Trends in Genetics,* 30**,** 75-84.

STRUDWICK, X. L., LANG, D. L., SMITH, L. E. & COWIN, A. J. 2015. Combination of low calcium with Y-27632 rock inhibitor increases the proliferative capacity, expansion potential and lifespan of primary human keratinocytes while retaining their capacity to differentiate into stratified epidermis in a 3D skin model. *PLoS One,* 10**,** e0123651.

SUETAKE, I., SHINOZAKI, F., MIYAGAWA, J., TAKESHIMA, H. & TAJIMA, S. 2004. DNMT3L stimulates the DNA methylation activity of Dnmt3a and Dnmt3b through a direct interaction. *J Biol Chem,* 279**,** 27816-23.

SUN, S. C. 2010. CYLD: a tumor suppressor deubiquitinase regulating NF-kappaB activation and diverse biological processes. *Cell Death Differ,* 17**,** 25-34.

SUN, S. C. 2011. Non-canonical NF-kappaB signaling pathway. *Cell Res,* 21**,** 71-85.

TAKEDA, K., TAKEUCHI, O., TSUJIMURA, T., ITAMI, S., ADACHI, O., KAWAI, T., SANJO, H., YOSHIKAWA, K., TERADA, N. & AKIRA, S. 1999. Limb and skin abnormalities in mice lacking IKKalpha. *Science,* 284**,** 313-6.

TAMBURRI, S., LAVARONE, E., FERNANDEZ-PEREZ, D., CONWAY, E., ZANOTTI, M., MANGANARO, D. & PASINI, D. 2020. Histone H2AK119 Mono-Ubiquitination Is Essential for Polycomb-Mediated Transcriptional Repression. *Mol Cell,* 77**,** 840-856 e5.

TARA, S., ISSHIKI, Y., NAKAJIMA-TAKAGI, Y., OSHIMA, M., AOYAMA, K., TANAKA, T., SHINODA, D., KOIDE, S., SARAYA, A., MIYAGI, S., MANABE, I., MATSUI, H., KOSEKI, H., BARDWELL, V. J. & IWAMA, A. 2018. Bcor insufficiency promotes initiation and progression of myelodysplastic syndrome. *Blood,* 132**,** 2470-2483.

TATTON-BROWN, K., SEAL, S., RUARK, E., HARMER, J., RAMSAY, E., DEL VECCHIO DUARTE, S., ZACHARIOU, A., HANKS, S., O'BRIEN, E., AKSGLAEDE, L., BARALLE, D., DABIR, T., GENER, B., GOUDIE, D.,

HOMFRAY, T., KUMAR, A., PILZ, D. T., SELICORNI, A., TEMPLE, I. K., VAN MALDERGEM, L., YACHELEVICH, N., CHILDHOOD OVERGROWTH, C., VAN MONTFORT, R. & RAHMAN, N. 2014. Mutations in the DNA methyltransferase gene DNMT3A cause an overgrowth syndrome with intellectual disability. *Nat Genet,* 46**,** 385-8.

TATTON-BROWN, K., ZACHARIOU, A., LOVEDAY, C., RENWICK, A., MAHAMDALLIE, S., AKSGLAEDE, L., BARALLE, D., BARGE-SCHAAPVELD, D., BLYTH, M., BOUMA, M., BRECKPOT, J., CRABB, B., DABIR, T., CORMIER-DAIRE, V., FAUTH, C., FISHER, R., GENER, B., GOUDIE, D., HOMFRAY, T., HUNTER, M., JORGENSEN, A., KANT, S. G., KIRALLY-BORRI, C., KOOLEN, D., KUMAR, A., LABILLOY, A., LEES, M., MARCELIS, C., MERCER, C., MIGNOT, C., MILLER, K., NEAS, K., NEWBURY-ECOB, R., PILZ, D. T., POSMYK, R., PRADA, C., RAMSEY, K., RANDOLPH, L. M., SELICORNI, A., SHEARS, D., SURI, M., TEMPLE, I. K., TURNPENNY, P., VAL MALDERGEM, L., VARGHESE, V., VEENSTRA-KNOL, H. E., YACHELEVICH, N., YATES, L., CLINICAL ASSESSMENT OF THE UTILITY OF, S., EVALUATION AS A SERVICE RESEARCH, S., DECIPHERING DEVELOPMENTAL DISORDERS, S. & RAHMAN, N. 2018. The Tatton-Brown-Rahman Syndrome: A clinical study of 55 individuals with de novo constitutive DNMT3A variants. *Wellcome Open Res,* 3**,** 46.

TAURIELLO, D. V., HAEGEBARTH, A., KUPER, I., EDELMANN, M. J., HENRAAT, M., CANNINGA-VAN DIJK, M. R., KESSLER, B. M., CLEVERS, H. & MAURICE, M. M. 2010. Loss of the tumor suppressor CYLD enhances Wnt/beta-catenin signaling through K63-linked ubiquitination of Dvl. *Mol Cell,* 37**,** 607-19.

THOME, M., CHARTON, J. E., PELZER, C. & HAILFINGER, S. 2010. Antigen receptor signaling to NF-kappaB via CARMA1, BCL10, and MALT1. *Cold Spring Harb Perspect Biol,* 2**,** a003004.

THU, Y. M., SU, Y., YANG, J., SPLITTGERBER, R., NA, S., BOYD, A., MOSSE, C., SIMONS, C. & RICHMOND, A. 2012. NF-kappaB inducing kinase (NIK) modulates melanoma tumorigenesis by regulating expression of pro-survival factors through the beta-catenin pathway. *Oncogene,* 31**,** 2580-92.

TORMOEN, G. W., CRITTENDEN, M. R. & GOUGH, M. J. 2018. Role of the immunosuppressive microenvironment in immunotherapy. *Advances in radiation oncology,* 3**,** 520-526.

TRAPNELL, C., ROBERTS, A., GOFF, L., PERTEA, G., KIM, D., KELLEY, D. R., PIMENTEL, H., SALZBERG, S. L., RINN, J. L. & PACHTER, L. 2012. Differential gene and transcript expression analysis of RNA-seq experiments with TopHat and Cufflinks. *Nat Protoc,* 7**,** 562-78.

TROMPOUKI, E., HATZIVASSILIOU, E., TSICHRITZIS, T., FARMER, H., ASHWORTH, A. & MOSIALOS, G. 2003. CYLD is a deubiquitinating enzyme that negatively regulates NF-kappaB activation by TNFR family members. *Nature,* 424**,** 793-6.

TROMPOUKI, E., TSAGARATOU, A., KOSMIDIS, S. K., DOLLE, P., QIAN, J., KONTOYIANNIS, D. L., CARDOSO, W. V. & MOSIALOS, G. 2009. Truncation of the catalytic domain of the cylindromatosis tumor suppressor impairs lung maturation. *Neoplasia,* 11**,** 469-76.

TROWBRIDGE, I. S. & THOMAS, M. L. 1994. CD45: an emerging role as a protein tyrosine phosphatase required for lymphocyte activation and development. *Annu Rev Immunol,* 12**,** 85-116.

TRZECIAK, W. H. & KOCZOROWSKI, R. 2016. Molecular basis of hypohidrotic ectodermal dysplasia: an update. *Journal of applied genetics,* 57**,** 51-61.
UEMATSU, A., KIDO, K., TAKAHASHI, H., TAKAHASHI, C., YANAGIHARA, Y., SAEKI, N., YOSHIDA, S., MAEKAWA, M., HONDA, M., KAI, T., SHIMIZU, K., HIGASHIYAMA, S., IMAI, Y., TOKUNAGA, F. & SAWASAKI, T. 2019. The E3 ubiquitin ligase MIB2 enhances inflammation by degrading the deubiquitinating enzyme CYLD. *J Biol Chem,* 294**,** 14135-14148.
VAN BALKOM, I. D. & HENNEKAM, R. C. 1994. Dermal eccrine cylindromatosis. *J Med Genet,* 31**,** 321-4.
VAN DIJK, E. L., AUGER, H., JASZCZYSZYN, Y. & THERMES, C. 2014. Ten years of next-generation sequencing technology. *Trends in Genetics,* 30**,** 418-426.
VARRICCHI, G., GALDIERO, M. R., MARONE, G., GRANATA, F., BORRIELLO, F. & MARONE, G. 2017. Controversial role of mast cells in skin cancers. *Experimental Dermatology,* 2*6***,** 11-17.
VIAL, J., ROYET, A., CASSIER, P., TORTEREAU, A., DINVAUT, S., MAILLET, D., GRATADOU-HUPON, L., CREVEAUX, M., SADIER, A., TONDEUR, G., LÉON, S., DEPAEPE, L., PANTALACCI, S., DE LA FOUCHARDIÈRE, A., MICHEAU, O., DALLE, S., LAUDET, V., MEHLEN, P. & CASTETS, M. 2019. The Ectodysplasin receptor EDAR acts as a tumor suppressor in melanoma by conditionally inducing cell death. *Cell Death & Differentiation,* 2*6***,** 443-454.
VISSERS, J. H. A., NICASSIO, F., VAN LOHUIZEN, M., DI FIORE, P. P. & CITTERIO, E. 2008. The many faces of ubiquitinated histone H2A: insights from the DUBs. *Cell Division,* 3**,** 8.
WAGNER, S. A., SATPATHY, S., BELI, P. & CHOUDHARY, C. 2016. SPATA2 links CYLD to the TNF-alpha receptor signaling complex and modulates the receptor signaling outcomes. *EMBO J,* 35**,** 1868-84.
WALLACE L., R. J. 2013. *Using 3D Culture to Investigate the Role of Mechanical Signaling in Keratinocyte Stem Cells.*, Humana Press, Totowa, NJ.
WANG, B., LIANG, Y., CHAI, X., CHEN, S., YE, Z., LI, R., LI, X., KONG, G., LI, Y., ZHANG, X., CHE, Z., YOU, Y., YE, S., LI, L., LIN, B., HUANG, J., HUANG, M., ZHANG, X., QIU, X. & ZENG, J. 2020. Ectodysplasin A receptor (EDAR) promotes colorectal cancer cell proliferation via regulation of the Wnt/beta-catenin signaling pathway. *Exp Cell Res,* 395**,** 112170.
WANG, C., DENG, L., HONG, M., AKKARAJU, G. R., INOUE, J. & CHEN, Z. J. 2001. TAK1 is a ubiquitin-dependent kinase of MKK and IKK. *Nature,* 412**,** 346-51.
WANG, J., DEVGAN, V., CORRADO, M., PRABHU, N. S., EL-DEIRY, W. S., RICCARDI, C., PANDOLFI, P. P., MISSERO, C. & DOTTO, G. P. 2005. Glucocorticoid-induced tumor necrosis factor receptor is a p21Cip1/WAF1 transcriptional target conferring resistance of keratinocytes to UV light-induced apoptosis. *J Biol Chem,* 280**,** 37725-31.
WANG, S., SUN, H., MA, J., ZANG, C., WANG, C., WANG, J., TANG, Q., MEYER, C. A., ZHANG, Y. & LIU, X. S. 2013. Target analysis by integration of transcriptome and ChIP-seq data with BETA. *Nat Protoc,* 8**,** 2502-15.
WANG, Z., GEARHART, M. D., LEE, Y. W., KUMAR, I., RAMAZANOV, B., ZHANG, Y., HERNANDEZ, C., LU, A. Y., NEUENKIRCHEN, N., DENG, J., JIN, J., KLUGER, Y., NEUBERT, T. A., BARDWELL, V. J. & IVANOVA, N. B. 2018. A Non-canonical BCOR-PRC1.1 Complex Represses Differentiation Programs in Human ESCs. *Cell Stem Cell,* 22**,** 235-251.e9.
WANG, Z., GERSTEIN, M. & SNYDER, M. 2009. RNA-Seq: a revolutionary tool for transcriptomics. *Nature Reviews Genetics,* 10**,** 57-63.

WEGNER, K. A., MEHTA, V., JOHANSSON, J. A., MUELLER, B. R., KEIL, K. P., ABLER, L. L., MARKER, P. C., TAKETO, M. M., HEADON, D. J. & VEZINA, C. M. 2019. Edar is a downstream target of beta-catenin and drives collagen accumulation in the mouse prostate. *Biol Open,* 8.

WEINBERG, D. N., PAPILLON-CAVANAGH, S., CHEN, H., YUE, Y., CHEN, X., RAJAGOPALAN, K. N., HORTH, C., MCGUIRE, J. T., XU, X., NIKBAKHT, H., LEMIESZ, A. E., MARCHIONE, D. M., MARUNDE, M. R., MEINERS, M. J., CHEEK, M. A., KEOGH, M.-C., BAREKE, E., DJEDID, A., HARUTYUNYAN, A. S., JABADO, N., GARCIA, B. A., LI, H., ALLIS, C. D., MAJEWSKI, J. & LU, C. 2019. The histone mark H3K36me2 recruits DNMT3A and shapes the intergenic DNA methylation landscape. *Nature,* 573**,** 281-286.

WICKHAM, H. 2016. *ggplot2: Elegant Graphics for Data Analysis*, Springer-Verlag New York.

WICKSTROM, S. A., MASOUMI, K. C., KHOCHBIN, S., FASSLER, R. & MASSOUMI, R. 2010. CYLD negatively regulates cell-cycle progression by inactivating HDAC6 and increasing the levels of acetylated tubulin. *EMBO J,* 29**,** 131-44.

WIESMANN, C., LEDER, L., BLANK, J., BERNARDI, A., MELKKO, S., DECOCK, A., D'ARCY, A., VILLARD, F., ERBEL, P., HUGHES, N., FREULER, F., NIKOLAY, R., ALVES, J., BORNANCIN, F. & RENATUS, M. 2012. Structural Determinants of MALT1 Protease Activity. *Journal of Molecular Biology,* 419**,** 4-21.

WILGUS, T. A. & WULFF, B. C. 2014. The Importance of Mast Cells in Dermal Scarring. *Adv Wound Care (New Rochelle),* 3**,** 356-365.

WILLIAMS, E. A., MONTESION, M., ALEXANDER, B. M., RAMKISSOON, S. H., ELVIN, J. A., ROSS, J. S., WILLIAMS, K. J., GLOMSKI, K., BLEDSOE, J. R., TSE, J. Y. & MOCHEL, M. C. 2021. CYLD mutation characterizes a subset of HPV-positive head and neck squamous cell carcinomas with distinctive genomics and frequent cylindroma-like histologic features. *Mod Pathol,* 34**,** 358-370.

WISNIEWSKI, S. A. & TRZECIAK, W. H. 2012. A rare heterozygous TRAF6 variant is associated with hypohidrotic ectodermal dysplasia. *Br J Dermatol,* 166**,** 1353-6.

WOODFORD-THOMAS, T. & THOMAS, M. L. 1993. The leukocyte common antigen, CD45 and other protein tyrosine phosphatases in hematopoietic cells. *Seminars in Cell Biology,* 4**,** 409-418.

WRIGHT, A., REILEY, W. W., CHANG, M., JIN, W., LEE, A. J., ZHANG, M. & SUN, S. C. 2007. Regulation of early wave of germ cell apoptosis and spermatogenesis by deubiquitinating enzyme CYLD. *Dev Cell,* 13**,** 705-16.

WU, X., FUKUSHIMA, H., NORTH, B. J., NAGAOKA, Y., NAGASHIMA, K., DENG, F., OKABE, K., INUZUKA, H. & WEI, W. 2014. SCFbeta-TRCP regulates osteoclastogenesis via promoting CYLD ubiquitination. *Oncotarget,* 5**,** 4211-21.

XIA, J. T., CHEN, L. Z., JIAN, W. H., WANG, K. B., YANG, Y. Z., HE, W. L., HE, Y. L., CHEN, D. & LI, W. 2014. MicroRNA-362 induces cell proliferation and apoptosis resistance in gastric cancer by activation of NF-kappaB signaling. *J Transl Med,* 12**,** 33.

XIAO, G., HARHAJ, E. W. & SUN, S. C. 2001. NF-kappaB-inducing kinase regulates the processing of NF-kappaB2 p100. *Mol Cell,* 7**,** 401-9.

XIE, S., CHEN, M., GAO, S., ZHONG, T., ZHOU, P., LI, D., ZHOU, J., GAO, J. & LIU, M. 2017. The B-box module of CYLD is responsible for its intermolecular interaction and cytoplasmic localization. *Oncotarget,* 8**,** 50889-50895.

XU, T.-H., LIU, M., ZHOU, X. E., LIANG, G., ZHAO, G., XU, H. E., MELCHER, K. & JONES, P. A. 2020a. Structure of nucleosome-bound DNA methyltransferases DNMT3A and DNMT3B. *Nature,* 586**,** 151-155.

XU, W., LI, J., RONG, B., ZHAO, B., WANG, M., DAI, R., CHEN, Q., LIU, H., GU, Z., LIU, S., GUO, R., SHEN, H., WU, F. & LAN, F. 2020b. DNMT3A reads and connects histone H3K36me2 to DNA methylation. *Protein & Cell,* 11**,** 150-154.

YAMAMOTO, Y., ABE, A. & EMI, N. 2014. Clarifying the impact of polycomb complex component disruption in human cancers. *Mol Cancer Res,* 12**,** 479-84.

YANG, L., RAU, R. & GOODELL, M. A. 2015. DNMT3A in haematological malignancies. *Nature reviews. Cancer,* 15**,** 152-165.

YANG, Y., RAN, J., LIU, M., LI, D., LI, Y., SHI, X., MENG, D., PAN, J., OU, G., ANEJA, R., SUN, S. C. & ZHOU, J. 2014. CYLD mediates ciliogenesis in multiple organs by deubiquitinating Cep70 and inactivating HDAC6. *Cell Res,* 24**,** 1342-53.

YANG, Y., WU, J. & WANG, J. A database and functional annotation of NF-ʃB target genes. 2016.

YANG, Y. & ZHOU, J. 2016. CYLD – a deubiquitylase that acts to fine-tune microtubule properties and functions. *Journal of Cell Science,* 129**,** 2289-2295.

YE, H., LIU, X., LV, M., WU, Y., KUANG, S., GONG, J., YUAN, P., ZHONG, Z., LI, Q., JIA, H., SUN, J., CHEN, Z. & GUO, A. Y. 2012a. MicroRNA and transcription factor co-regulatory network analysis reveals miR-19 inhibits CYLD in T-cell acute lymphoblastic leukemia. *Nucleic Acids Res,* 40**,** 5201-14.

YE, J., COULOURIS, G., ZARETSKAYA, I., CUTCUTACHE, I., ROZEN, S. & MADDEN, T. L. 2012b. Primer-BLAST: a tool to design target-specific primers for polymerase chain reaction. *BMC Bioinformatics,* 13**,** 134.

YIN, Y., MORGUNOVA, E., JOLMA, A., KAASINEN, E., SAHU, B., KHUND-SAYEED, S., DAS, P. K., KIVIOJA, T., DAVE, K., ZHONG, F., NITTA, K. R., TAIPALE, M., POPOV, A., GINNO, P. A., DOMCKE, S., YAN, J., SCHÜBELER, D., VINSON, C. & TAIPALE, J. 2017. Impact of cytosine methylation on DNA binding specificities of human transcription factors. *Science,* 356**,** eaaj2239.

YOSHIDA, H., JONO, H., KAI, H. & LI, J. D. 2005. The tumor suppressor cylindromatosis (CYLD) acts as a negative regulator for toll-like receptor 2 signaling via negative cross-talk with TRAF6 AND TRAF7. *J Biol Chem,* 280**,** 41111-21.

ZANDI, E., ROTHWARF, D. M., DELHASE, M., HAYAKAWA, M. & KARIN, M. 1997. The IkappaB kinase complex (IKK) contains two kinase subunits, IKKalpha and IKKbeta, necessary for IkappaB phosphorylation and NF-kappaB activation. *Cell,* 91**,** 243-52.

ZHANG, J., STIRLING, B., TEMMERMAN, S. T., MA, C. A., FUSS, I. J., DERRY, J. M. & JAIN, A. 2006. Impaired regulation of NF-kappaB and increased susceptibility to colitis-associated tumorigenesis in CYLD-deficient mice. *J Clin Invest,* 116**,** 3042-9.

ZHANG, Q., LENARDO, M. J. & BALTIMORE, D. 2017. 30 Years of NF-kappaB: A Blossoming of Relevance to Human Pathobiology. *Cell,* 168**,** 37-57.

ZHANG, X. J., LIANG, Y. H., HE, P. P., YANG, S., WANG, H. Y., CHEN, J. J., YUAN, W. T., XU, S. J., CUI, Y. & HUANG, W. 2004. Identification of the

cylindromatosis tumor-suppressor gene responsible for multiple familial trichoepithelioma. *J Invest Dermatol,* 122**,** 658-64.

ZHANG, Y., TOMANN, P., ANDL, T., GALLANT, N. M., HUELSKEN, J., JERCHOW, B., BIRCHMEIER, W., PAUS, R., PICCOLO, S., MIKKOLA, M. L., MORRISEY, E. E., OVERBEEK, P. A., SCHEIDEREIT, C., MILLAR, S. E. & SCHMIDT-ULLRICH, R. 2009. Reciprocal requirements for EDA/EDAR/NF-kappaB and Wnt/beta-catenin signaling pathways in hair follicle induction. *Dev Cell,* 17**,** 49-61.

ZHANG, Y. E. 2009. Non-Smad pathways in TGF-beta signaling. *Cell Res,* 19**,** 128-39.

ZHAO, Y., THORNTON, A. M., KINNEY, M. C., MA, C. A., SPINNER, J. J., FUSS, I. J., SHEVACH, E. M. & JAIN, A. 2011. The deubiquitinase CYLD targets Smad7 protein to regulate transforming growth factor beta (TGF-beta) signaling and the development of regulatory T cells. *J Biol Chem,* 286**,** 40520-30.

ZHOU, S.-L., DAI, Z., ZHOU, Z.-J., CHEN, Q., WANG, Z., XIAO, Y.-S., HU, Z.-Q., HUANG, X.-Y., YANG, G.-H., SHI, Y.-H., QIU, S.-J., FAN, J. & ZHOU, J. 2013. CXCL5 contributes to tumor metastasis and recurrence of intrahepatic cholangiocarcinoma by recruiting infiltrative intratumoral neutrophils. *Carcinogenesis,* 35**,** 597-605.

ZHU, J., ZHANG, S., GU, L. & DI, W. 2012. Epigenetic silencing of DKK2 and Wnt signal pathway components in human ovarian carcinoma. *Carcinogenesis,* 33**,** 2334-43.

ZUO, Y. G., XU, Y., WANG, B., LIU, Y. H., QU, T., FANG, K. & HO, M. G. 2007. A novel mutation of CYLD in a Chinese family with multiple familial trichoepithelioma and no CYLD protein expression in the tumour tissue. *Br J Dermatol,* 157**,** 818-21.